Marco Hofer, B.Sc.

KIM – Numerical studies on parameter determination and grain crushing effects

Master Thesis

to achieve the university degree of

Diplom-Ingenieur

submitted to

Graz University of Technology

Supervisor

Ass. Prof. Dipl.-Ing. Dr.techn., Franz Tschuchnigg

Institute of Soil Mechanics, Foundation Engineering and Computational Geotechnics

Graz, January 2020

Declaration of Authorship

I declare that I have authored this thesis independently, that I have not used other that the declared sources/resources, and that I have explicitly indicated all material which has been quoted either literally or by content from the sources used. The text document uploaded to TUGRAZonline is identical to the present master's thesis.

....

Date   Signature

Acknowledgements

First of all, I would like to give my thanks to my academic supervisor from my university, Franz Tschuchnigg, of the Institute of Soil Mechanics and Foundation Engineering, for the great guidance and support. He was always immediately available whenever I needed advice for my thesis, and with his interest in this topic he always guided me in the right direction. Furthermore, I would like to thank him for giving me a lot of freedom regarding the writing of this thesis, because it was never a problem to put the thesis aside for a certain amount of time. I have learned a lot from him, and I am grateful that he was able to greatly increase my interest in soil mechanics and especially in this specific topic.

I would also like to thank my friends and fellow students who accompanied me for last few years and always supported my way of life. Also, I will always appreciate the newfound friends that I have made within the master’s program who made my time as a student in Graz unforgettable.

Finally, I would like to give my deepest thanks to my family, and especially to my parents, who made me the person that I am today. They have sincerely supported me throughout my entire life and also during my study time in Graz. Without their support, I could not had completed my studies the way I did it. Thank you so much, Mum and Dad.

Without all the named persons on this page, this thesis would not have been accomplished.

Thank you.

Abstract

KIM – Numerical studies on parameter determination and grain crushing effects

The compaction process of reclaimed land is indispensable but comprises several challenges as its quality control. The aim of compaction work is to densify the fill to a certain relative density I_D. Since the quality control of compaction work is an important contractual issue, it must be defined in technical terms, such as the relative density I_D or the maximum dry density (MDD). This thesis focuses on the quality control of compaction works by means of the relative density I_D which can be measured indirectly by performing cone penetration tests (CPT).

However, to determine the actual relative density I_D from the results obtained from cone penetration tests, appropriate correlation methods between the relative density and the cone resistance q_c are required. The most commonly used interpretation methods are purely empirical and further derived only from silica sands. Therefore, such interpretation methods are not suitable to apply for other materials, such as calcareous sands, which show a totally different soil behavior under the same conditions. Due to the different soil characteristics, calcareous sands show a significantly higher tendency towards grain crushing. A possible correlation method that considers the behavior of calcareous sands is given by the semi-empirical correlation method, the Karlsruhe Interpretation Method (KIM). Furthermore, with the application of cone penetration tests, very high pressures are usually occurring which could cause grain crushing of the soil, which is not considered by the commonly used interpretation methods. By means of numerical modelling, a possible approach to take grain crushing into account is the application of constitutive soil models that consider grain crushing effects.

This thesis begins by focusing on the determination of the hypoplastic soil parameters by means of the automatic calibration with ExCalibre, which enables an easy and fast parameter determination. Following that, a relatively new constitutive soil model, namely the hypoplastic soil model for crushable sand, is investigated to show the different soil behavior under high pressures. The thesis continues onto the spherical cavity expansion, as an important part of the KIM by applying different constitutive soil models and analyze the influence of single soil parameter on the results. The work contains additionally a full KIM analysis, as well as a description of the full automation of the KIM analysis. Finally, the Press-Replace method is presented as an alternative approach to model cone penetration tests by means of finite element analysis.

Kurzfassung

KIM – Numerical studies on parameter determination and grain crushing effects

Im Zuge der Landgewinnung ist der Verdichtungsprozess unerlässlich und bringt auch einige Herausforderungen mit sich, wie zum Beispiel das Sicherstellen der Bemessungskriterien. Das Ziel des Verdichtungsprozesses ist, den Boden bis zu einer vordefinierten Lagerungsdichte I_D zu verdichten, um ihn in Bezug auf Festigkeit und Steifigkeit damit zu stärken. Die Bemessungskriterien für den Verdichtungsprozess sind fixer Bestandteil der vertraglichen Vereinbarungen und müssen somit als technische Bodenkennwerte, wie zum Beispiel die relative Lagerungsdichte, angegeben werden, welche wiederum indirekt durch Ergebnisse von Drucksondierungen (CPT) bestimmt werden können.

Um jedoch die relative Lagerungsdichte eines Bodens mithilfe der aus Drucksondierungen erhaltenen Spitzendrücke q_c zu bestimmen, bedarf es einer geeigneten Korrelationsmethode. Die Standardkorrelationen sind hauptsächlich mithilfe empirischer Methoden entwickelt worden und auch nur auf Basis von Quarzsanden. Daher können diese Standardkorrelationen nicht für Kalksande angewendet werden, welche unter denselben Bedingungen ein deutlich anderes Materialverhalten zeigen als Quarzsande. Aufgrund unterschiedlicher Eigenschaften weisen Kalksande ein deutlich höheres Potential für Kornbruch auf. Eine mögliche Korrelationsmethode, die speziell dieses Materialverhalten berücksichtigt, ist die Karlsruhe Interpretations Methode (KIM). Außerdem entsteht bei Drucksondierungen zumeist ein sehr hoher Druck, welcher sich auch auf das Verhalten von Quarzsanden auswirkt, sprich zum Kornbruch führt. Ein möglicher Ansatz, der das Verhalten bei sehr hohen Drücken auch bei Quarzsanden berücksichtigt, ist durch das relativ neue Stoffmodell „Hypoplastic model for crushable sand" gegeben.

Zu Beginn liegt der Fokus der Arbeit auf der Bestimmung der Parameter für das hypoplastische Stoffgesetz unter der Verwendung der automatischen Kalibrierung mittels ExCalibre. Im Anschluss wird das schon zuvor erwähnte Stoffgesetz „Hypoplastic model for crushable sand" untersucht, um die Auswirkungen sehr hoher Drücke auf das Materialverhalten zu zeigen. Als ein sehr wichtiger und unersetzlicher Bestandteil der KIM wird dann die Aufweitung eines sphärischen Hohlraums im Hinblick auf die Anwendung unterschiedlicher Stoffgesetzte und den Einfluss einzelner Parameter auf die Ergebnisse untersucht. Eine vollständige KIM Analyse zeigt die Ergebnisse für die Anwendung unterschiedlicher Material Sets und auch die neuen Möglichkeiten, die die neue und wertvolle Automatisierung der KIM Analyse mit sich bringt. Zuletzt wird noch die „Press-Replace" Methode als alternative Methode zur Modellierung von Drucksondierungen mittels Finite-Elemente Methode präsentiert.

Content

List of Figures

Appendix

List of Tables

Appendix

List of Abbreviations

CPT	Cone Penetration Test
FEM	Finite Element Model
FEA	Finite Element Analysis
HS	Hardening Soil Model
HP	Hypoplastic Model
KIM	Karlsruhe Interpretation Method
MC	Mohr-Coulomb Model
MDD	Maximum Dry Density
OED	Oedometric Compression Test
PRM	Press Replace Method
SCE	Spherical Cavity Expansion
TSHD	Trail Suction Hopper Dredger
TRIAX	Triaxial Compression Test
UAE	United Arab Emirates

List of Notations

a_1, a_2, a_3	KIM parameters
b_1, b_2, b_3	KIM parameters
c	cohesion
c'	effective cohesion
d_{50}	mean grain size
e	void ratio
e_c	critical void ratio
e_{c0}	critical void ratio at zero pressure
e_d	lower limit void ratio
e_{d0}	lower limit void ratio at zero pressure
e_i	upper limit void ratio
e_{i0}	upper limit void ratio at zero pressure
e_{init}	initial void ratio
e_{max}	maximum void ratio from index test
e_{min}	minimum void ratio from index test
e_0	void ratio at zero pressure
h_s	granulate hardness – hypoplastic parameter
k_q	shape factor
n	hypoplastic parameter
p'	effective mean pressure
p_o'	effective mean pressure at zero pressure
p_{LS}	limit pressure
q	deviatoric stress
q_c	cone penetration resistance
q_t	corrected cone resitance
s_u	undrained shear strength
u_{tot}	total displacements
u_z	vertical displacements
w	water content

C_u	uniformity coefficient
E	Young’s modulus
E_{oed}^{ref}	reference oedometric Young’s modulus
E_{ur}^{ref}	reference unloading-reloading Young’s modulus
G	shear modulus
I_D	relative density
K	global stiffness matrix
K_0	lateral earth pressure coefficient
K_{0T}	lateral earth pressure coefficient (total stress)
N_c	theoretical cone factor

α	hypoplastic parameter
β	hypoplastic parameter
γ	unit weight
γ_w	unit weight of water
δ	interface friction angle
ε_{ax}	axial strain
ε_{eng}	engineering strain
ε_{true}	true strain
ε_v	volumetric strain
ν	Poisson’s ratio
ν_u	Poisson’s ratio (undrained total stress analysis)
ρ_d	dry density
ρ_s	grain density
ρ_{sat}	saturated density
ρ_w	density of water
σ_{ax}	axial stress
$\sigma_h{}'$	effective horizontal pressure
$\sigma_v{}'$	effective vertical pressure
φ'	effective friction angle
φ_c	critical friction angle
φ_p	peak friction angle
ψ	dilatancy angle

1 Introduction

It is possible that during the course of construction or land reclamation projects, masses of soil will have to be dug up in order to change the terrain. Subsequently, these new masses of soil must be compacted with the aim to strengthen the soil by means of densification. To ensure that the minimum requirements related to the variables of an already compacted soil are fulfilled, e.g. the strength and the stiffness, the quality control of compaction work is a key issue that incorporates several challenges.

The quality control of, e.g., deep vibro compaction works, is an important contractual issue, which is defined in technical terms as the relative density I_D or the maximum dry density (MDD). The density of already compacted soil can on the one hand be measured directly by the cutter cylinder or the sand replace method, and, on the other hand, an indirect determination can be applied by means of cone penetration tests (CPT). However, the latter case requires the application of appropriate correlation methods between the received cone resistance q_c and the relative density I_D. The most commonly used interpretation methods, such as correlations according to Schmertmann (1976) or Baldi et al. (1986), are purely empirical and further derived from series of calibration chamber tests based on a wide range of different silica sands. Hence, these correlations can be applied for quality control of compaction works in case of silica sands but may not be capable of reproducing the characteristics of calcareous sands due to the different soil behavior of calcareous sands.

Calcareous sands show significantly lower q_c-values than silica sands under the same conditions because of different soil characteristics. For example, calcareous sand shows a significantly higher tendency towards grain crushing than silica sands. This is related to the fact that $CaCO_3$ is classified by Mohs' scale of mineral hardness only by a value of approximately three, whereas silica sand reaches a value of approximately seven. Hence, it is a key issue to take the influence of the carbonate content on soil properties into account, when correlating q_c-values (obtained from CPT tests) to relative densities I_D.

Since it has been shown (Reinisch, 2018) that the commonly used and purely empirical correlations methods from Baldi et al. (1986) and Schmertmann (1976) are not the best choice to apply for calcareous sands, especially for the contractor, a first step taken to overcome this problem was the establishment of a so-called shell correlation factor (SCF). The purpose of its development was to take the influence of the carbonate content, and, therefore, the effect of grain crushing during cone penetration tests into account. The aim of the shell correction factor is to translate measured q_c-values of calcareous sands into appropriate silica q_c-values and to enable the application of the commonly used correlation methods (Baldi, et al., 1986; Schmertmann, 1976). The problem that comes along with the

SCE, is that its magnitude results more from negotiations between the contractor and the client and less from representing the real soil behavior on site.

Therefore, a new correlation method considering both silica and calcareous sands, or one especially for calcareous sands, is necessary. A possible solution to this problem is given by the semi-empirical correlation method known as the Karlsruhe Interpretation Method (KIM). This method was originally developed by Cudmani (2000) and, as an alternative to the purely empirical correlation methods (Baldi, et al., 1986; Schmertmann, 1976), the Karlsruhe Interpretation Method has the advantage of considering the behavior of calcareous sands. The key components of the KIM are numerical solutions of the spherical cavity expansion (SCE) problem and an empirically determined shape factor k_q. The original KIM method (Cudmani, 2000) uses the hypoplastic soil model according to Von Wolffersdorff (1996) to model the soil behavior, and Meier (2007) applied the KIM to investigate the soil behavior of calcareous sands. Meier (2007) showed that this semi empirical correlation method is capable of representing the complex material behavior of calcareous sand and, therefore, can be used to compute realistic values of q_c.

In the first part of this thesis, an overview of the background including land reclamation, carbonate sands and compaction works is briefly presented, followed by a more detailed presentation of the theory and the intention of the Karlsruhe Interpretation Method. This incorporates a general overview of the semi-empirical correlation method and the original hypoplastic soil model according to Von Wolffersdorff (1996), as well as a description of the calibration process for the hypoplastic soil parameters.

Due to the importance of the correct determination of the hypoplastic soil model parameters within the application of the KIM, the third part investigates the online automatic calibration tool, ExCalibre, and presents a relatively new hypoplastic soil model that takes the effect of grain crushing into account.

The main part of this thesis is then provided in chapters 5 and 6. Chapter 5 focuses on the solution of the spherical cavity expansion problem, consisting of a verification of the finite element model and the application of different constitutive models. Additionally, the numerical studies of the SCE investigate the influence of the dilatancy angle ψ and the initial stress state. Following that, chapter 6 shows the results and the single steps of a full KIM analysis including the full automation of the KIM using Python scripting. Finally, the Press-Replace-Method (PRM) is presented as an alternative approach to model cone-penetration tests by means of finite element-analysis.

The aim of this thesis is to further investigate the already established finite element model, to solve the spherical cavity expansion problem and to show the possibilities and limitations regarding the application of constitutive soil models other than the hypoplastic one. With the full automation of the KIM process, this correlation method will be applicable from a practical point of view, as it does not involve much effort.

2 Land reclamation in the UAE

This chapter should briefly introduce the issue of land reclamation in the United Arab Emirates and its challenges with respect to compaction works of calcareous sands. Because Reinisch (2018) and Winkler (2018) already described this topic in detail, only the main points are presented within this chapter. For more detailed information, reference is made to (Reinisch, 2018; Winkler, 2018).

2.1 Land reclamation

The creation of new land by raising the elevation of the seabed or, for example, other low-lying land can be described as land reclamation. Especially in the United Arab Emirates, big land reclamation projects, such as the Palm Jumeirah or the Palm Jebel Ali, are the pre-stages of big building projects and, therefore, the land reclamation is of particular significance. The main method to reclaiming land in the UAE is the hydraulic filling. The whole reclamation process usually consists of the three main processes as follows (Reinisch, 2018; Winkler, 2018):

- Dredging of desired material from a borrow area
- Transport of desired material from the borrow area to the reclamation area
- Placement of the desired material within the reclamation area

For each one of the above mentioned steps of a reclamation process, different methods and different equipment may be applied, which is then decisive for the feasibility as well as the cost efficiency of the overall land reclamation project. For the first step, the dredging process, two different methods can be applied, namely the suction dredging, which can again be subdivided into different methods, and the mechanical dredging. Then, the transport and the placement of the desired fill material is usually executed by hydraulic transport through a pipeline, transport by barge or transport by a trailing suction hopper dredger (TSHD). Because the fill material in this area is sand with varying amount of the carbonate content, its influence on the soil properties is an important issue and will be discussed in the following chapter (Reinisch, 2018; Winkler, 2018).

2.2 Calcareous sands

Calcareous sands, or carbonate sands, are mostly comprised of carbonate minerals, especially of calcite, also known as calcium carbonate ($CaCO_3$). A possible classification of carbonate sands according to Clark & Walker (1977) and Meigh (1987) is given as follows:

- Carbonate sand if carbonate content is above 90%
- Siliceous carbonate sand if carbonate content is between 50% and 90%
- Calcareous sand if carbonate content is between 10% and 50%

In this thesis, both designations, calcareous sand and carbonate sand are equal and hence describe the same carbonate content.

Carbonate sands in the UAE mostly consist of seashells and coral lumps with a varying concentration of the carbonate content. Due to its origin and mineralogy, these sands show a significantly higher tendency towards grain crushing than other sands (e.g. silica sands). This is also related to the fact that calcium carbonate ($CaCO_3$) is classified by a significant lower Mohs` scale of mineral hardness than silica sand. Hence, it is important to take the influence of the carbonate content on the mechanical soil behavior and, thus, on the soil properties into consideration, especially when correlating q_c-values (obtained from CPT tests) to relative densities I_D (Reinisch, 2018).

Based on detailed laboratory investigations on 11 soil samples with different carbonate content, Tschuchnigg et al. (2018) stated, that four geotechnical parameters, namely the limit void ratios e_{min} and e_{max}, the critical friction angle φ_c' and the grain density ρ_s are especially influenced by the carbonate content. The relation between these four soil parameters and the carbonate content are illustrated from Fig. 1 to Fig. 3.

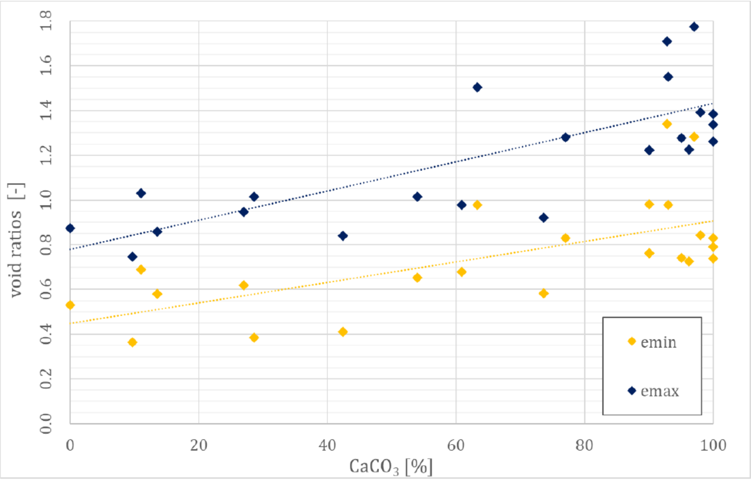

Fig. 1: Influence of carbonate content on the limit void ratios e_{max} and e_{min} (Reinisch, 2018)

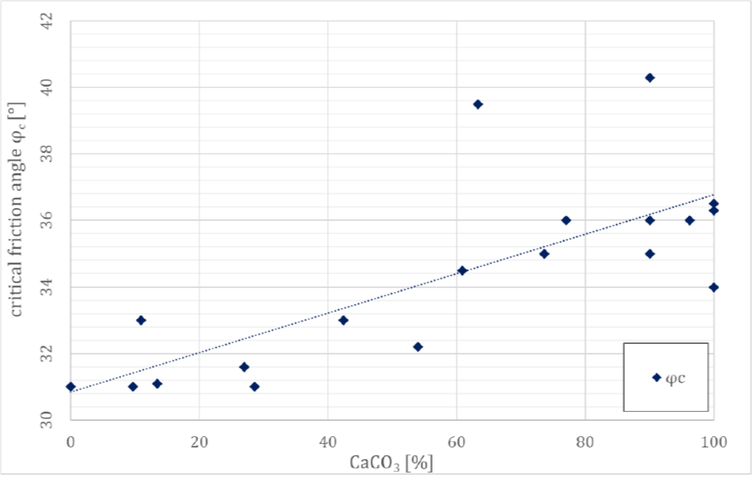

Fig. 2: Influence of carbonate content on the critical friction angle $\varphi_c{}'$ (Reinisch, 2018)

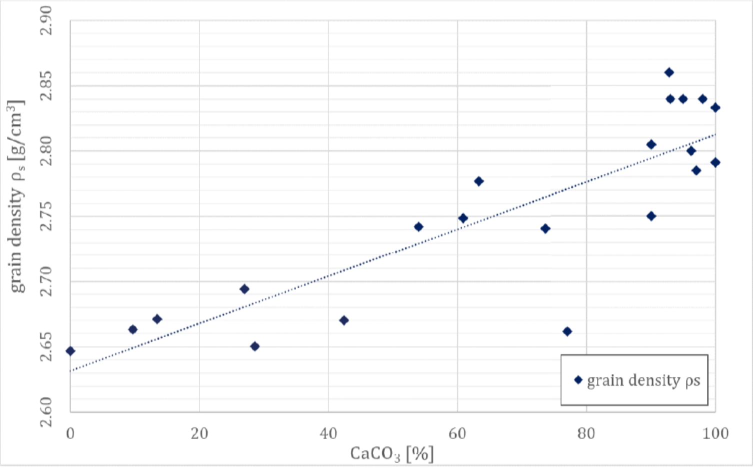

Fig. 3: Influence of carbonate content on the grain density ρ_s (Reinisch, 2018)

Fig. 1 to Fig. 3 show that the four parameters, namely the limit void ratios e_{min} and e_{max}, the critical friction angle $\varphi_c{}'$ and the grain density ρ_s, are all increasing with increasing carbonate content of sand. Furthermore, the carbonate content also influences the soil's unit weight γ and, consequently, the mean effective stress $p_0{}'$. Hence, with an increase of the carbonate content, γ and $p_0{}'$ decrease, which finally leads to lower cone resistances q_c.

2.3 Compaction works

Once the placement of the fill material is finished, the reclaimed land must be compacted to fulfill desired design criteria, especially regarding the soil's stiffness and strength. The state of an already compacted soil is mostly described in terms of the relative density I_D and, thus, the challenge is to compact the soil up to a contractually agreed minimum state of density. In the United Arab Emirates, the compaction works are usually performed by means of vibratory-compaction. For more details regarding the compaction process, as well as the limitations and used equipment of applying deep vibro compaction, reference is made to (Reinisch, 2018; Winkler, 2018).

To verify if the reclaimed soil land is sufficiently compacted, the quality control of deep vibro-compaction works is an important contractual issue, which is often defined in technical terms such as the relative density I_D. The density of an already compacted soil can be indirectly determined by means of cone penetration tests (CPT) and applying appropriate correlation methods between then received cone resistance q_c and the relative density I_D. Because commonly used and purely empirical correlations methods (Baldi, et al., 1986; Schmertmann, 1976) are not capable of reproducing the characteristics of carbonate sands, the next chapter introduces the Karlsruhe Interpretation Method, comprising of the advantage of considering the behavior of calcareous sands (Tschuchnigg & Winkler, 2019).

3 Karlsruhe Interpretation Method

The aim of Chapter 3 is to introduce the theoretical key issues of the Karlsruhe Interpretation Method (KIM). In order to apply the Karlsruhe Interpretation Method on geotechnical problems, a basic knowledge of hypoplasticity as well as of the cavity expansion theory is needed. Following the introduction, this chapter presents the hypoplasticity in general, followed by the description of the commonly used hypoplastic soil model according to Von Wolffersdorff (1996) and the standard calibration procedure of the model parameters to the reader. After the basics of hypoplasticity are given, the general aspects of the spherical cavity expansion theory are presented. Finally, the final KIM equation is shown.

3.1 Introduction

The Karlsruhe Interpretation Method is a semi-empirical method used to correlate the cone resistance q_c with the relative density I_D. This method was originally developed by Cudmani (2000) and is different to the commonly used and well established empirical CPT interpretation methods (Baldi, et al., 1986; Schmertmann, 1976). The Karlsruhe Interpretation Method consists of both an empirical part and a numerical part. Therefore, the key components of the KIM are the numerical solutions of the spherical cavity expansion (SCE) problem and the empirically determined shape factor k_q. The KIM, as developed by Cudmani (2000), uses the hypoplastic soil model according to Von Wolffersdorff (1996). More recently, Meier (2007) applied the KIM to investigate calcareous sands and showed that the KIM method is capable of representing the material’s behavior on site.

3.2 Hypoplasticity

The very first appearance of a hypoplastic constitutive soil model and the historical development up to the generally used hypoplastic soil model according to von Wolffersdorff are already part of the former theses regarding the Karlsruhe Interpretation Method from Reinisch (2018) and Winkler (2018).

Generally, it can be concluded that one big advantage of applying the hypoplastic soil model is that it forgoes the definition of a flow rule and a yield surface. Therefore, different to elasto-plastic constitutive modelling, the mechanical behavior of the material is solely based on one complex tensorial equation. Furthermore, the consideration of pyknotropy (dependency on the density), as well as barotropy (dependency on the stress) allows describing the mechanical behavior of a cohesionless granular material by the application of only one hypoplastic parameter set for a wide range of soil states (Meier, 2007).

3.2.1 Hypoplastic model according to Von Wolffersdorff

The hypoplastic constitutive model according to Von Wolffersdorff (1996) is considered the standard hypoplastic soil model for cohesionless granular material (sands and gravels) and is also the constitutive soil model that the Karlsruhe Interpretation Method was originally developed for (Cudmani, 2000). As previously mentioned, hypoplastic constitutive modelling requires only one tensorial equation where the stress rate tensor $\dot{\sigma}$ can be determined by the stress state σ, the strain rate $\dot{\varepsilon}$ and the void ratio e (density). The general form of the hypoplastic constitutive equation can be formulated as follows (Meier, 2007; Herle & Gudehus, 1999):

$$\dot{\sigma} = f(\sigma, \dot{\varepsilon}, e) \tag{3.1}$$

According to Von Wolffersdorff (1996), the basic concept is then to separate pyknotropy and barotropy from the tensorial formulation of the function f, such that both, pyknotropy and barotropy are described by different factors, which are scalar functions of the current void ratio e and the stress state σ (Von Wolffersdorff, 1996). For a comprehensive description and formulation of the hypoplastic constitutive equation, see (Herle & Gudehus, 1999; Niemunis & Herle, 1997; Von Wolffersdorff, 1996).

Furthermore, the application of hypoplasticity requires the assumption of a so-called simple grain skeleton. Hence, effects that influence the soil behavior, such as crushing effects or physico-chemical effects, are not taken into account with the hypoplastic constitutive modelling according to Von Wolffersdorff (1996). With the assumption of a simple grain skeleton, the following material properties can be derived (Herle & Gudehus, 1999):

- The stress tensor σ and the void ratio e are sufficient to describe the stress state, and deviations from such states are not considered.

- There is an upper limit void ratio (e_i), which decreases with an increase of the mean skeleton pressure p_s. e_{i0} is the void ratio at mean skeleton pressure of $p_s = 0$ and represents the void ratio of a simple grain skeleton at the loosest possible state (see Fig. 4 (left)). If $e > e_{i0}$, the skeleton could no longer exist because there would be macro-voids in the grain skeleton or grain contacts would be opened.

- There is also a lower limit void ratio (e_d), which decreases with an increase of the mean skeleton pressure p_s. If $e < e_d$, a kind of dry masonry would exist (see Fig. 4 (right)).

- The third limit void ratio is given by the critical void ratio e_c, which decreases with increasing pressure p_s, similar to e_i and e_d. The critical void ratio e_c is reached after large monotonic shear deformations.

- The stress-strain behavior of a simple grain skeleton does not change with strain or stress rate, hence the behavior is rate-independent.

- Independent from the initial state, proportional strain paths lead to proportional stress paths. This asymptotic behavior of granular materials is known as the so-called SOM (Swept Out of Memory) behavior.

- The principle of effective stress is valid (Terzaghi's principle).

- Attractive forces of the grain contacts and cementation can be neglected.

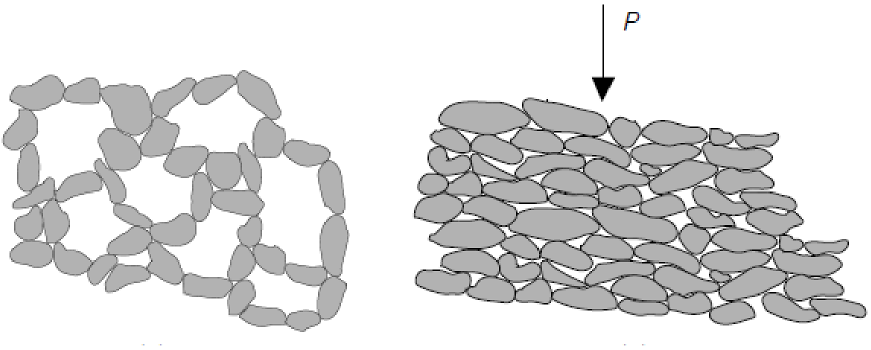

Fig. 4: macro-voids if $e > e_i$ (left) and dry masonry if $e < e_d$ (right) (Herle & Gudehus, 1999)

All together, the hypoplastic constitutive soil model according to Von Wolffersdorff (1996) consists of 8 model parameters. Four of them are material parameters, which can be simply determined by executing standard laboratory tests, and the remaining 4 model parameters have to be calibrated. Tab. 1 lists all of the hypoplastic model parameters.

Tab. 1: Hypoplastic parameters acc. to Von Wolffersdorff (1996)

parameter		laboratory test
	material parameters	
critical friction angle	φ_c	angle of repose test
limit void ratios	e_{d0} e_{i0} e_{c0}	densest and loosest packing (DIN 18126)
	calibration parameters	
granulate hardness exponent	h_s n	high-pressure oedometer (DIN 18135)
exponent exponent	α β	drained triaxial test (DIN 18137-2)

3.2.2 Standard model parameter calibration

For every applied constitutive soil model, an accurate determination of the respective model parameters is an essential part for a description of a material's mechanical behavior. Especially in the case of the hypoplastic soil model being used to describe a soil's behavior, a correct parameter determination is very important due to the fact that only one parameter set is used to describe the behavior of one soil at different density states. In the following, the determination processes for every hypoplastic parameter are shortly presented. For a more detailed description, reference is made to (Herle, 2000; Herle & Gudehus, 1999).

Critical friction angle φ_c

The critical friction angle is one of the two hypoplastic parameters related to the critical state. The critical friction angle represents the resistance of a granulate material, and, in case of large monotonic shearing in critical state, therefore, both the stress rate ($\dot{\sigma}$) and the volumetric deformation rate ($\dot{\varepsilon}$) becomes zero. The determination of the critical friction angle can be done by appropriate laboratory tests as drained or undrained triaxial tests, simple or direct shear tests on initially very loose specimens ($e \approx e_{max}$), or by the angle of repose test. Regarding the advantages with respect to required duration, costs and effort, the angle of repose is potentially the best choice to determine the critical friction angle, because many experimental studies also proved the reliability of the obtained values of φ_c (Herle & Gudehus, 1999; Meier, 2007).

The aim of the angle of repose test is to obtain a cone of the used material in its loosest state, such that, only a hopper must be filled with granular material, and then said hopper is lifted slowly without losing contact between the hopper and the arising cone of the granular material. Due to the steady flow of the grains, a quasi-critical state is reached, and the critical friction angle can be determined by measuring the inclination of the cone (increments of 0.5 ° are enough) or by measuring the diameter and height of the cone and then calculating the critical friction angle with $\varphi_c = \tan^{-1}(2h/d)$. A schematical representation of the angle of repose test is shown in Fig. 5 (Herle & Gudehus, 1999; Meier, 2007).

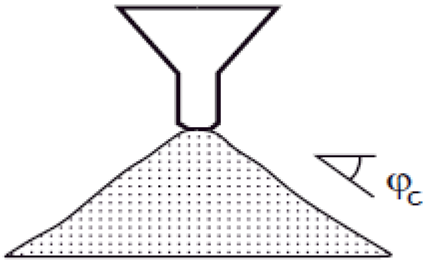

Fig. 5: Angle of repose test (Herle & Gudehus, 1999)

Herle & Gudehus (1999) stated that the critical friction angle φ_c is mainly influenced by the grain size and the angularity, whereas the uniformity coefficient C_u shows less influence on φ_c (see Fig. 6 (left)). Reinisch (2018) also investigated the effects of changing C_u on the critical friction angle, with the results shown in Fig. 6 (right).

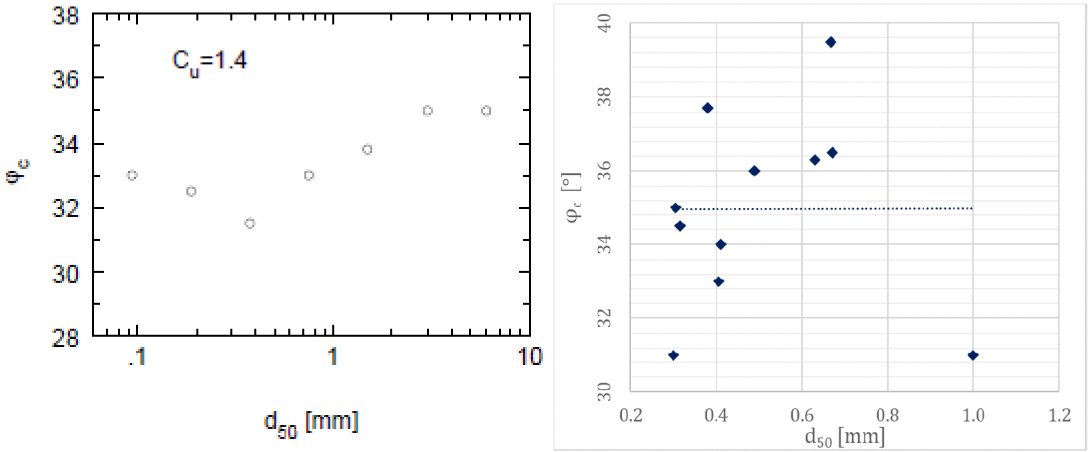

Fig. 6: Relation between critical friction angle φ_c and the d_{50} after Herle & Gudehus (1999) (left) and Reinisch (2018) (right)

It can be seen that the critical friction angle increases with an increase of the grain size (increasing d_{50}), due to the fact that larger grains have to overcome higher stresses when rolling downwards. In Fig. 6 (right), the trendline is only horizontal because of one single outlier.

Limit void ratios e_{d0}, e_{i0} and e_{c0}

Overall, the hypoplastic soil model consists of three limit void ratios, which all decrease with an increase of the effective mean pressure p'. The relation between the limit void ratios and the pressure is shown in Fig. 7, and according to the compression law developed by Bauer (1996), the relation is formulated as shown in equation (3.2). In Fig. 7, as well as in equation (3.2), the limit void ratios at a certain pressure p' are presented by e_d, e_i and e_c and hence e_{d0}, e_{i0} and e_{c0} all present the limit void ratios at zero pressure. The shadowed part in Fig. 7 shows the inadmissible zones for the void ratios of a simple grain skeleton (Herle & Gudehus, 1999).

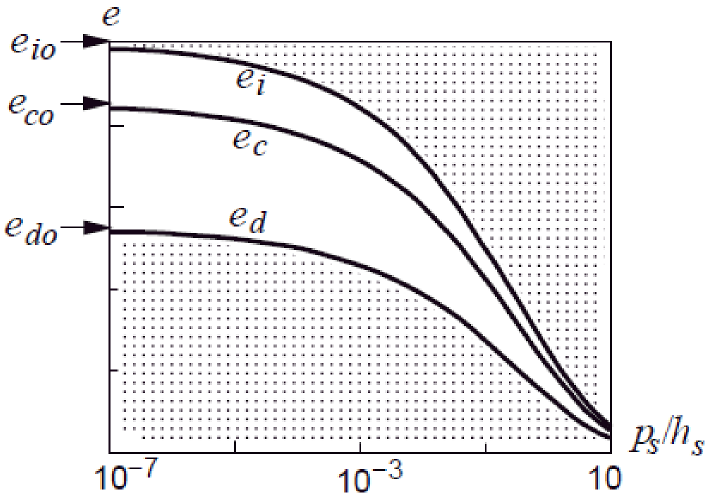

Fig. 7: Relation between limit void ratios and pressure p_s (Herle & Gudehus, 1999)

$$\frac{e_d}{e_{d0}} = \frac{e_i}{e_{i0}} = \frac{e_c}{e_{c0}} = exp\left[-\left(\frac{3p'}{h_s}\right)\right]^n \tag{3.2}$$

As previously stated within Tab. 1, the minimum and maximum void ratio at zero pressure can be determined by standard index tests (DIN 18126). The lower limit of void ratios is given by the limit void ratio e_d, which can be determined by the standard index test, “densest packing”, in practice. The index test is performed at a certain pressure level, and the received minimum void ratio e_{min} is always above the theoretical limit void ratio e_d. However, the difference between the measure e_{min} and e_d is negligibly small, so the relation $e_{d0} \approx e_{min}$ can exist (Herle & Gudehus, 1999).

In practice, it is almost impossible to determine the maximum limit void ratio at zero pressure e_{i0} experimentally. However, the maximum void ratio e_{max} can be determined by the index test, “loosest packing”, and after comparing the differences between determined e_{max}-values and theoretical maximum limit void ratios e_{i0}, the relation $e_{i0} \approx 1.15 * e_{max}$ can be assumed for well-graded granular materials (Herle, 2000).

The critical void ratio e_c corresponds to the critical state, and according to Herle & Gudehus (1999), it can be determined by a shear test on a soil element. Former experimental studies regarding the critical void ratio e_c also stated that $e_{c0} \approx e_{max}$ is a valid assumption, because during the index test for e_{max}, a state close to the critical state is reached (large shear deformations at low pressures close to zero).

Herle & Gudehus (1999) showed the influence of C_u on the limit void ratios e_d and the maximum void ratio e_{max}, and, therefore, also the critical void ratio e_c due to the relation between e_{max} and e_c. Reinisch (2018) also investigated the influence of C_u on the limit void ratios in his thesis, and both Herle & Gudehus (1999) and Reinisch (2018) stated that the limit void ratios are increasing with increasing angularity and decreasing C_u (see Fig. 8 and Fig. 9) (Herle & Gudehus, 1999; Reinisch, 2018).

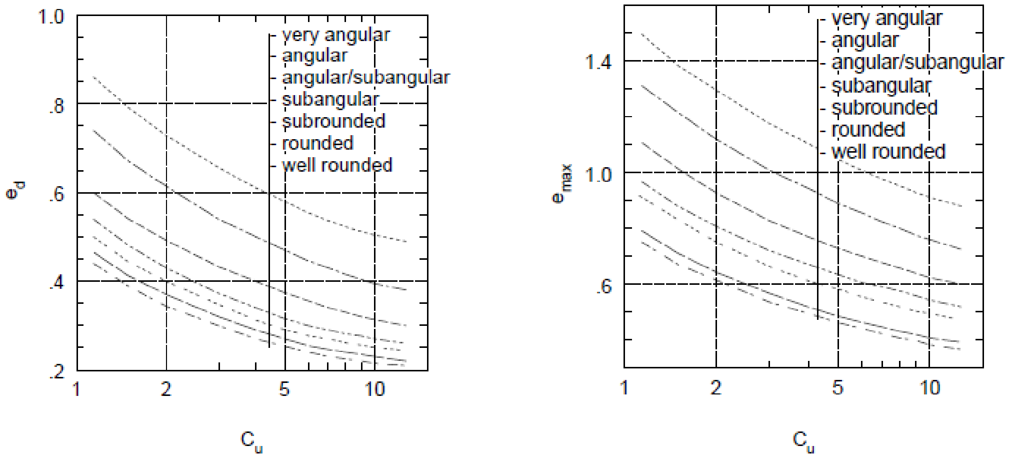

Fig. 8: Relation between e_d (left) and e_{max} (right) on C_u and grain angularity (Herle & Gudehus, 1999)

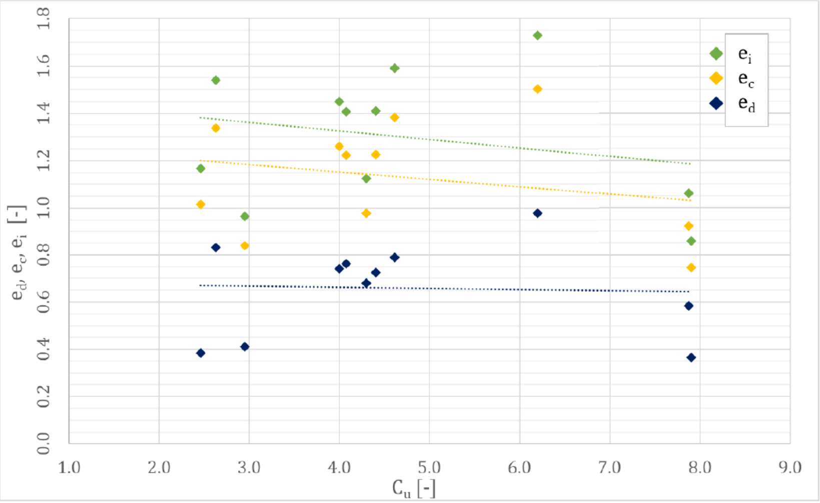

Fig. 9: Dependency of limit void ratios on C_u (Reinisch, 2018)

Granulate hardness h_s and exponent n

The granulate hardness h_s is the only hypoplastic parameter in the dimension of stress, and hence is used as a reference pressure. However, it must not be related to the hardness of the single grains of a material. Regarding equation (3.2), the compression behavior of a loose specimen during isotropic compression depends only on h_s when keeping n constant. Therefore, the exponent n can be seen as the parameter that takes the pressure-sensitivity of the grain skeleton into account.

The parameters h_s and n can be obtained by performing a compression test on specimen that are initially very loose (but not collapsible). Generally, oedometric compression tests that are performed on dry or water-saturated samples eliminate physico-chemical effects. For a void ratio e_p during proportional compression (starting from e_{p0}) and using the granulate hardness h_s and the exponent n, the compression law according to Bauer (1996) reduces as follows:

$$e_p = e_{p0} * exp\left[-\left(\frac{3p'}{h_s}\right)\right]^n \tag{3.3}$$

In principle, the parameters h_s and n can be determined by numerical regression of the measured data which is not recommended due to the high nonlinearity of equation (3.3). For the three unknown parameters (h_s, n, e_{p0}), several solutions are possible, which is not acceptable regarding the requirements of an explicit determination of constitutive soil model parameters. For this reason, n should be determined independently of h_s by applying the following two equations (Herle & Gudehus, 1999).

$$h_s = 3p_s \left({}^{ne_p}/_{C_c} \right)^{1/n} \tag{3.4}$$

$$n = \frac{ln\left(\frac{e_{p1}C_{c2}}{e_{p2}C_{c1}}\right)}{ln\left(\frac{p_{s2}}{p_{s1}}\right)} \tag{3.5}$$

Where C_c is representing the compression index, and p_{s1} and p_{s2} specify a certain pressure range with the appropriate void ratios e_{p1} and e_{p2}. The necessary values for a determination of n from the measured data are schematically shown in Fig. 10 (Herle & Gudehus, 1999; Herle, 2000).

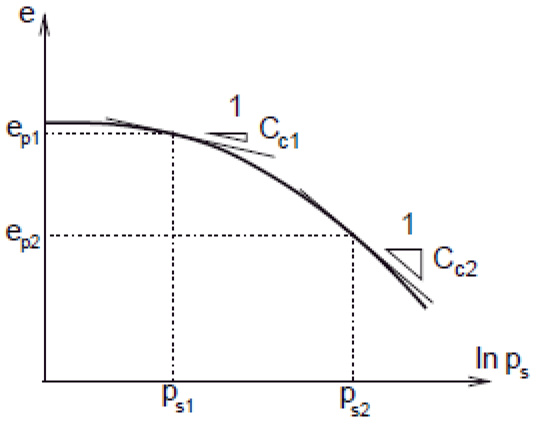

Fig. 10: Parameters for determination of n for a certain pressure range p_{s1} and p_{s2} (Herle & Gudehus, 1999)

Equation (3.4) and (3.5) show that the exponent n can be determined independently from the granulate hardness h_s whereas for the determination of h_s the exponent n must be known. Fig. 11 shows the influence of h_s and n on the resulting compression curves and it can be seen that n influences the curvature of the curve, whereas h_s reflects the slope of it.

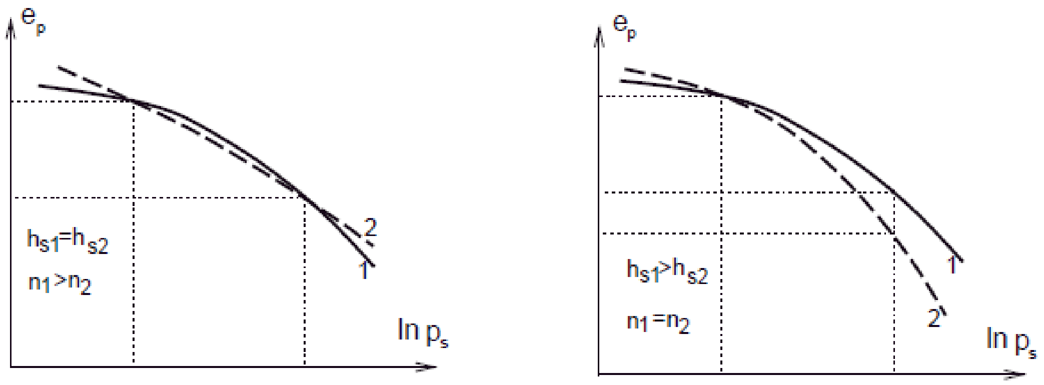

Fig. 11: Influence of n (left) and h_s (right) on the resulting compression curves (Herle & Gudehus, 1999)

Exponent α

The exponent alpha is related to the peak state in a triaxial compression test on an initially dense sample. It controls the dependency of the peak friction angle φ_P, and hence the dilatancy behavior on the relative void ratio of the considered soil sample. For that reason, alpha can be calibrated by fitting results obtained from simulations applying the hypoplastic constitutive equation to the results of measured curves. Thereby it is important to mention that the granulate hardness h_s and the exponent n also influence the results of triaxial test simulations (including the hypoplastic constitutive equation). Therefore, it is necessary to adjust also h_s and n. The increase of the friction angle up to the peak friction angle ($\varphi_P > \varphi_c$) during the shearing of a dense sample is shown in Fig. 12 (Masin, 2019; Meier, 2007; Herle & Gudehus, 1999).

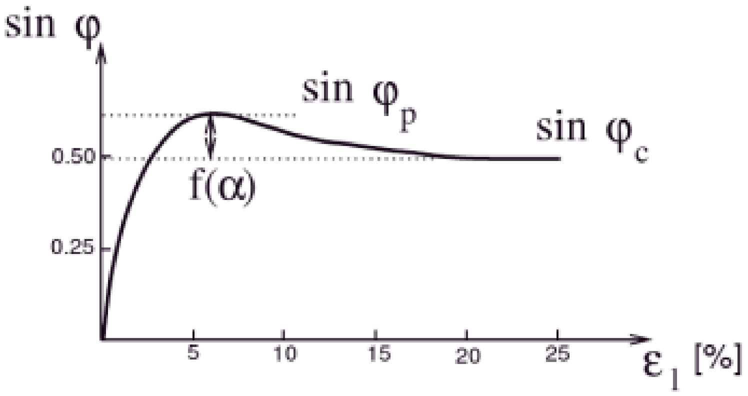

Fig. 12: Results of a triaxial test (shearing) on a dense soil sample (Masin, 2019)

Exponent β

With the exponent beta, the stiffness of a grain skeleton can be adjusted in the case that $e < e_c$ (Meier, 2007). Beta is of especially high importance for dense samples, thus the void ratio e lies significantly below e_i. This fact can be seen in Fig. 13, where an increase of beta of 100% results in similar compression curves on a loose sample, whereas the same change in beta results in a significant difference of the resulting compression curves for a dense sample (Herle & Gudehus, 1999).

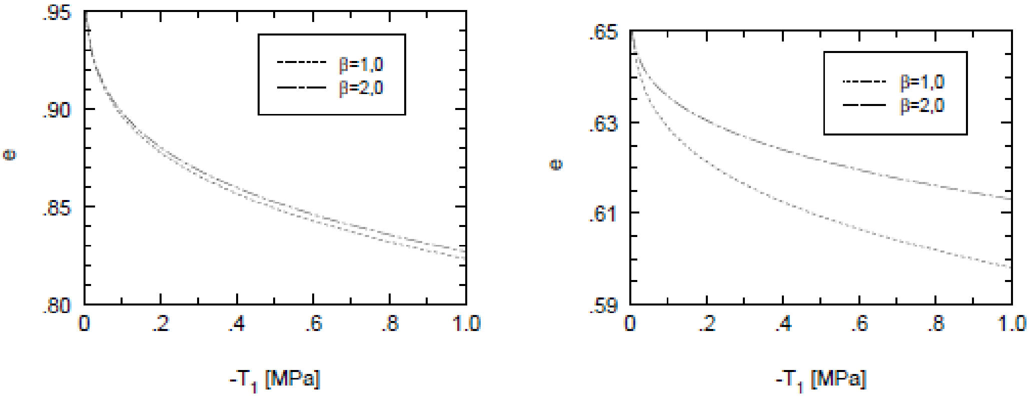

Fig. 13: Resulting compression curves for different β-values on a loose (left) and a dense (right) soil sample (Herle & Gudehus, 1999)

In case of isotropic compression β can be obtained from equation (3.6).

$$\beta = \frac{ln\left(\beta_0 \frac{E_2}{E_1}\right)}{ln\left(\frac{e_1}{e_2}\right)} \tag{3.6}$$

For the determination of beta with equation (3.6), the influence of the pressure p_s can be eliminated if the ratio of the stiffness moduli E_2/E_1 is related to the density states given by the void ratios e_1 and e_2, but at the same pressure T_1. The parameter β_0 consists again of different factors of the hypoplastic constitutive equation. For a detailed determination of β_0, see Herle & Gudehus (1999). Experimental studies showed that to assume exponent beta with $\beta \approx 1$ is sufficient for a first approximation (Herle, 2000).

Regarding the determination of the 8 hypoplastic parameters, it was shown that all parameters are influenced by the grain shape, the mean grain diameter d_{50} and the uniformity coefficient C_u (Herle, 2000). According to Meier (2007), the final calibration parameters (h_s, n, α and β) should be obtained by an iterative process due to the fact that they are all interrelated. Furthermore, Meier (2007) stated that the engineer is responsible to define the “abort-criterion” adjusted for the respective application. In the case of the hypoplastic parameter set is applied within CPT interpretation methods, such as the Karlsruhe Interpretation Method, it is important to correctly reproduce the compressibility of dense samples at very high pressures ($p' \geq 10MPa$) (Meier, 2007).

After the first important issue regarding the Karlsruhe Interpretation Method, the hypoplastic soil model, is presented, the next chapter introduces the spherical cavity expansion theory, which is an unconditional requirement of the KIM.

3.3 The spherical cavity expansion

This chapter will introduce the theoretical background of the spherical cavity expansion and the determination of the limit pressure p_{LS}, due to its importance regarding the Karlsruhe Interpretation Method. Mathematical formulations are not given within this chapter and, therefore, for a detailed description of the analytical solution of the spherical cavity expansion, reference is made to Cudmani (2000).

The spherical cavity expansion is one particular theory within the general cavity expansion theory that can be applied to different geotechnical problems and is considered as a one-dimensional boundary problem. Different analytical solutions of the cavity expansion theory are already published, but most solutions are based on the assumption that during the expansion of the cavity, only small deformations occur near the cavity. Because solutions based on this assumption are not capable of being applied for geotechnical application where large deformations occur, Cudmani & Osinov (2001) developed a cavity expansion theory for large deformations that is applicable to cohesionless soils by applying the hypoplastic constitutive soil model. A schematic representation of the spherical cavity expansion and its boundary value problem is shown in Fig. 14 (Cudmani, 2000).

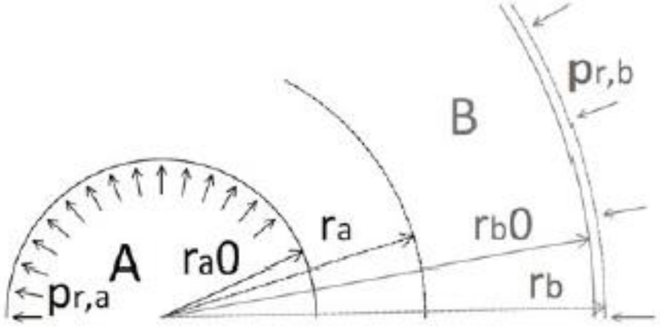

Fig. 14: Schematic representation of the SCE and its boundary value problem (Uhlig & Herle, 2015)

Fig. 14 shows the boundary value problem of the spherical cavity expansion where a sphere A expands quasi-statically inside of a sphere B, in case of an expansion within a drained body with finite expansion. The initial radius of sphere A is denoted with r_a^0, and for sphere B the initial radius is given with r_b^0. The symmetric expansion is described by the temporal development of the velocity, stress components and the void ratio e using spherical coordinates (Cudmani, 2000).

According to Cudmani (2000), the initial radius of sphere B must be chosen as large enough to obtain sufficiently accurate results of the spherical cavity expansion. It is recommended to apply a ratio of $r_a^0/r_b^0 \geq 30$ for loose soils ($I_D \approx 0$) and $r_a^0/r_b^0 \geq 90$ for dense soils ($I_D \approx 0.9$). Furthermore, Cudmani (2000) stated that the limit values are reached after the sphere undergoes an expansion of $r_a \approx 2r_a^0$ for loose soils and $r_a \approx 3r_a^0$ for dense soils (Cudmani, 2000).

The process of the spherical cavity expansion starts with loading the sphere B with the initial mean pressure $p_{r,b}$, and is followed by the expansion of sphere A. During this expansion, the cavity pressure $p_{r,a}$ is increased up to a certain threshold value, denoted as limit pressure p_{LS}. If this limit pressure is reached, it remains the same even though sphere A experiences ongoing expansion. The expansion curves for the two stress components (radial and tangential stress) are shown in Fig. 15 (Cudmani, 2000).

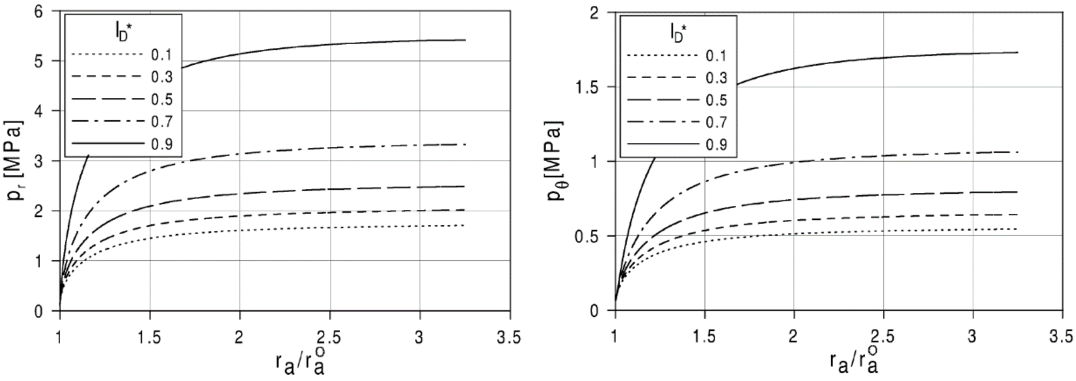

Fig. 15: Expansion curves of Ticino sand for radial stress (left) and tangential stress (right) versus the normalized deformation r_a/r_a^0 (Cudmani, 2000)

The relationship between the limit pressure p_{LS} and the initial mean pressure p_0 depends on the density state of the considered soil. An increase of the relative density causes the limit pressure to increase as well. An example of the relationship between the limit pressure and the initial mean pressure is shown in Fig. 16 for Ticino sand at different density states (Cudmani, 2000).

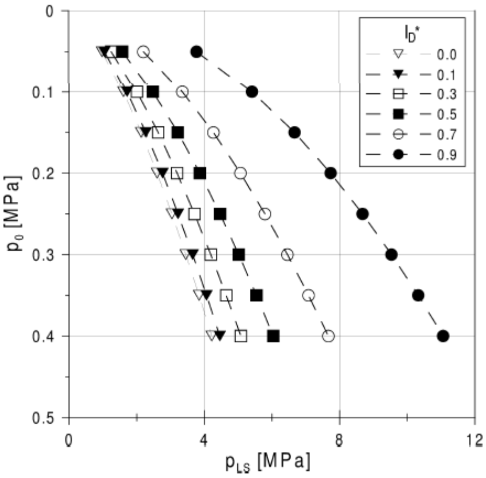

Fig. 16: Limit pressure p_{LS} versus initial mean pressure p_0 for Ticino sand and different density states (Cudmani, 2000)

With regards to the functional relation, depending on the initial state of a soil (I_D and p_0) shown below, the limit pressure can be approximately determined (Cudmani, 2000).

$$p_{LS} = a * {p_0}^b \tag{3.7}$$

Where p_0 is the initial mean effective pressure, and the parameters a and b are only depending on the density state (I_D) and can be calculated as follows (Cudmani, 2000):

$$a = a_1 + \frac{a_2}{a_3 + I_D} \tag{3.8}$$

$$b = b_1 + \frac{b_2}{b_3 + I_D} \tag{3.9}$$

The parameters a_i and b_i are known as the KIM-parameters and are determined by a curve fitting procedure, which is presented in chapter 6. Hence, after the KIM parameters for an analyzed material are determined, the limit pressure can be calculated for any initial state (I_D and p_0) by applying equation (3.7) (Cudmani, 2000).

To model a cone penetration test by means of the spherical cavity expansion Cudmani showed that directly modelling the cone resistance q_c by the limit pressure p_{LS} received from a spherical cavity expansion is not possible. However, several performed calibration tests of cone penetrations showed a similar qualitative dependency of the cone resistance on the initial mean pressure, as the limit pressure does. Therefore, Cudmani (2000) investigated the so-called shape factor k_q to correlate the cone resistance q_c and the limit pressure p_{LS} as it is shown in equation (3.10). Fig. 17 shows the qualitative similarities of the dependency of the cone resistance on the initial mean pressure, as well as the relation between the limit pressure and the initial mean pressure.

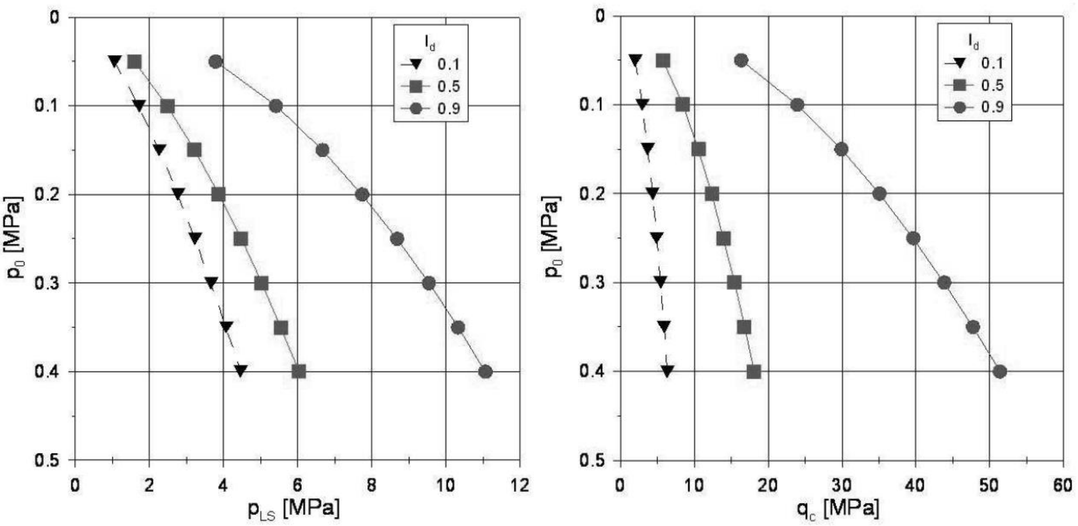

Fig. 17: Dependency of limit pressure p_{LS} (left) and cone resistance q_c (right) of the initial mean pressure p_0 (Meier, 2007)

$$q_c = k_q * p_{LS} \tag{3.10}$$

After many investigations, Cudmani (2000) concluded that the shape factor k_q only depends on the relative density and can be calculated by applying equation (3.11). For a detailed description of the establishment of the formulation for the shape factor, see (Cudmani, 2000).

$$k_q = 1.5 + \frac{5.8(I_D)^2}{(I_D)^2 + 0.11} \tag{3.11}$$

Regarding equation (3.10), it can be seen that the shape factor is a very important part, with respect to the determination of the cone resistance q_c. Therefore, it may be useful to investigate the shape factor more to see if a sole dependency on the relative density is sufficiently accurate or if influencing parameter, such as the mean pressure, have to be added. This investigations are part of current research at the Institute of Soil Mechanics, Foundation Engineering and Computational Geotechnics at the Technical University of Graz.

3.4 The final KIM equation

By combining the equations from (3.7) to (3.11) and the definition of the mean effective pressure $p_0{}'$,

$$p_0' = \frac{1}{3} * \sigma_v' * (1 + 2 * K_0) \tag{3.12}$$

the final KIM equation is given as follows:

$$q_c = \left(1.5 + \frac{5.8(I_D)^2}{(I_D)^2 + 0.11}\right) * \left(a_1 + \frac{a_2}{a_3 + I_D}\right) * \left(\frac{1}{3} * \sigma_v' * (1 + 2 * K_0)\right)^{b_1 + \frac{b_2}{b_3 + I_D}} \tag{3.13}$$

where $\sigma_v{}'$ is the effective vertical stress, and the empirical part of KIM is given by the shape factor k_q. The numerical part of the KIM (second part of the KIM) is related to the calculation of the limit pressure (p_{LS}) obtained from the solution of a spherical cavity expansion problem (Cudmani, 2000). Once the KIM parameters a_i and b_i for a certain material are known, the cone resistances for every desired relative density I_D and every effective mean pressure p_0 can be determined. An exemplary plot of q_c-curves for different relative densities is shown in Fig. 18.

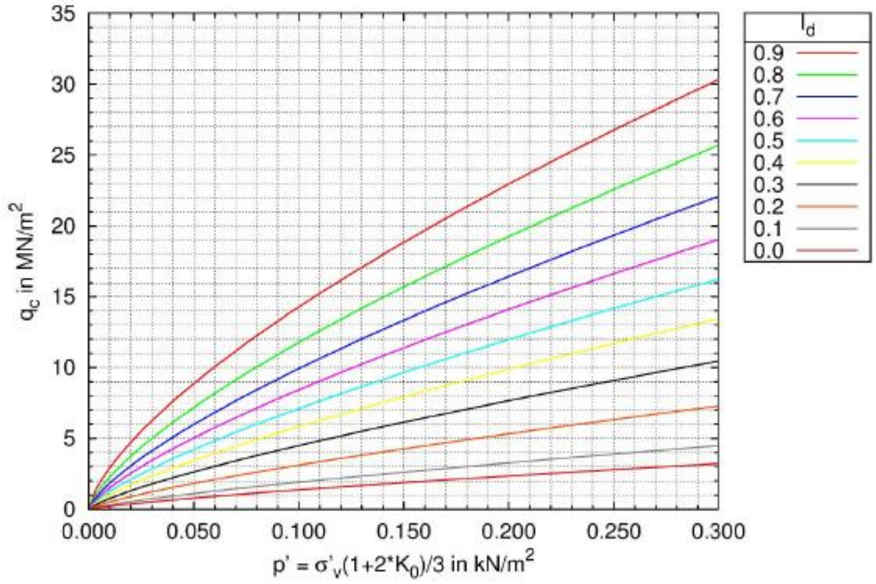

Fig. 18: q_c-curves for different density states for one investigated calcareous sand (Winkler, 2018)

4 Investigations on hypoplastic soil model

This chapter firstly introduces the online tool ExCalibre, which enables an automatic calibration of all hypoplastic parameters based only on laboratory soil test results, and then discusses its advantages and disadvantages compared to the standard parameter determination presented in chapter 3.2.2. Furthermore, the application of a relatively new hypoplastic soil model, which takes grain crushing into account, is presented.

4.1 Introduction

Regarding the Karlsruhe Interpretation Method and, with this, the determination of the limit pressure p_{LS} of a spherical cavity expansion analysis, the calibration of the hypoplastic soil parameters entails a certain sensitivity, and hence is one of the most influential factors. A proper calibration of the hypoplastic parameters (based on laboratory tests of the materials found on site) is indispensable to model a realistic material behavior. The challenge of the calibration process is minimizing the sensitivity that the calibration of the hypoplastic parameters entails, in order to produce satisfying KIM results.

With respect to the calibration of the hypoplastic parameters, the four parameters h_s, n, α and β are of importance and are generally calibrated by fitting the measurement curves of oedometric compression tests and triaxial compression tests with the results of simulated laboratory soil tests performed with the hypoplastic soil model. Due to the high relevance of a proper parameter calibration, different investigations related to alternative approaches of calibrating hypoplastic parameters are analyzed.

4.2 Calibration tool ExCalibre

The online tool ExCalibre is provided by the website “soilmodels.com”, and it enables the user to calibrate advanced constitutive soil models, such as the hypoplastic sand model according to Von Wolffersdorff (1996). A model-specific calibration algorithm is responsible for achieving a reliable set of parameters. After finishing the calibration process, users can change single hypoplastic parameters manually to do a kind of fine-tuning and evaluate the influence of the parameter change on the resulting lab test simulations. ExCalibre can also be used as an element test to simulate standard laboratory test.

4.2.1 General aspects of ExCalibre

Absolute preconditioning is a proper application of the input-file and is provided as a simply constructed Excel-worksheet, which must be uploaded to the website in order to start the calibration process. Without the essential input parameters listed below, ExCalibre always return an error, and the calibration process cannot be started.

- Specific gravity, angle of repose, sieve-passing
- Lab data of oedometric compression test(s)
- Lab data of triaxial compression test(s)

A template for the input-file is provided on the website “soilmodels.com”, and the next chapter details how it must be edited in order to enable a successful calibration of the hypoplastic parameters.

Input-file – ExCalibre

The input worksheet consists of several tab-sheets containing information about the considered soil that is to be calibrated by ExCalibre. Before presenting the different tab-sheets in more detail, it must be mentioned that a prerequisite to starting the calibration process is, the correct designation and order of all tab-sheets.

In the first tab-sheet, denoted as “NOTES”, the user can provide general information on the material about the soil type, environment, sampling depth, sampling method and add any other comments. It must be mentioned that this tab-sheet is not used within the calibration process of ExCalibre. Hence, the user does not have to consider this tab-sheet in anyway and can also add more information regarding the material.

On the second tab-sheet, called “IDX AND GRAD”, the user must provide the specific gravity, the angle of repose and the sieve passing. Additionally, the USCS classification and the liquid limit, as well as the plastic limit can be added, but it is not necessary to do so. Based on the provided information, the grading curves for the considered material are generated, as seen in Fig. 19.

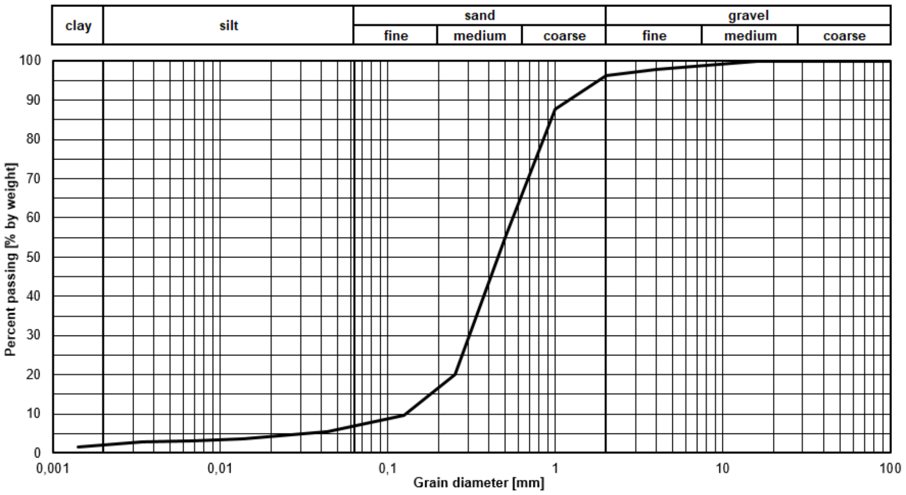

Fig. 19: Grading curve – ExCalibre input

The following tab-sheets consider laboratory test results of oedometric compression and triaxial compression tests. First, the user must provide the lab test data of at least one oedometric compression test in the tab-sheet named “OED-REC-1”. Test data of a second oedometric compression test can then be provided within the tab-sheet “OED-REC-2”. For the oedometer test, the initial void ratio (at the start of the shear), the vertical stresses σ_{ax} [kPa] and the corresponding vertical strain ε_{ax} [-] must be inserted. A compression curve, as shown in Fig. 20, is automatically generated after the lab test data is added. With respect to the definition of the calibration of the hypoplastic parameter β, an oedometric compression test performed on an initially very loose sample should be added (Meier, 2007). Additionally, the influence of providing different types and a different number of lab test data within the input file for ExCalibre on the calibration results is shown later in chapter 4.2.2.

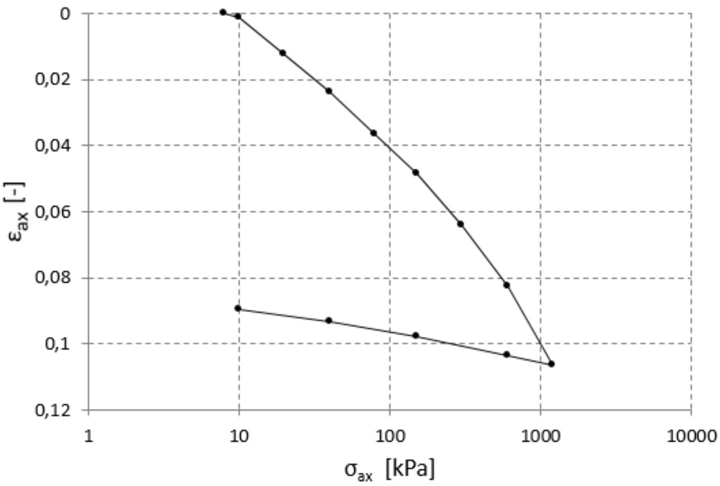

Fig. 20: Compression curve of oedometer test – ExCalibre input

After all available lab test data of oedometric compression tests is inserted into an input file, the lab test data of triaxial compression tests must be finally added to the tab-sheet called “CID-REC-1”. Again, the user has the possibility to provide more than just one triaxial compression test. The tab-sheet for lab test data of a second triaxial compression test must be denoted as “CID-REC-2”, for example. The generated curves shown in Fig. 21 are based on the provided results of the initial void ratio (at the beginning of the shear), vertical strains ε_{ax} [kPa], the confining pressure σ'_{rad} (σ'_3) [kPa], the deviatoric stress $q = \sigma_1 - \sigma_3$ [kPa] and the volumetric strains ε_v [%]. It is further important to state that dilatancy is defined as negative in ExCalibre.

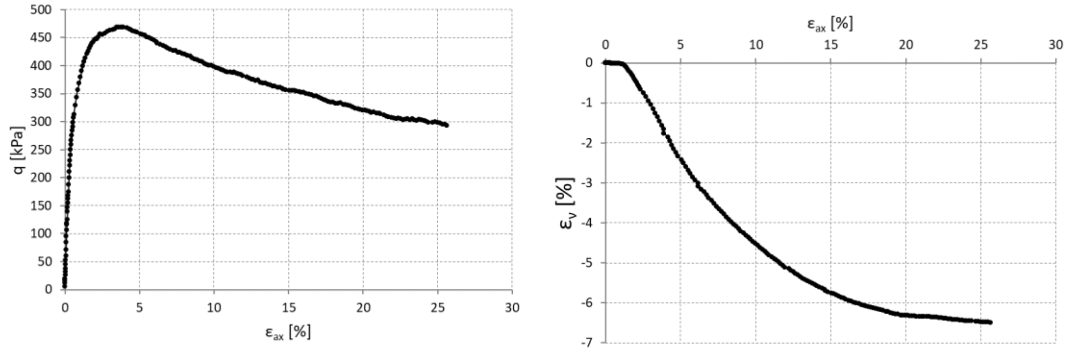

Fig. 21: Triaxial soil test curves – ExCalibre input

The volumetric behavior (Fig. 21 (right)) shows that negative volumetric strains result and, according to the definition of ExCalibre, this indicates that the soil sample undergoes a volume increase.

Results of ExCalibre calibration

After successfully uploading the input files on the website “soilmodels.com”, ExCalibre presents the calibrated parameters, as well as the option to recalculate the soil tests by changing single hypoplastic parameters. The aim of this recalculation option is that the user can do a kind of fine-tuning of the hypoplastic parameter set. Furthermore, the automatic calibration process updates the initial void ratios of the triaxial compression tests. The initial void ratios of the oedometric compression tests remain the same. According to a personal conversation with David Masin, the reason for that is the inconsistency between measured void ratios in triaxial tests and oedometer tests. This may also lead to an inconsistent model calibration and, therefore, the initial void ratios are updated, but just for the triaxial test. The resulting soil test curves (after the calibration) for the oedometric compression test and the triaxial compression test are shown in Fig. 22 and Fig. 23 respectively.

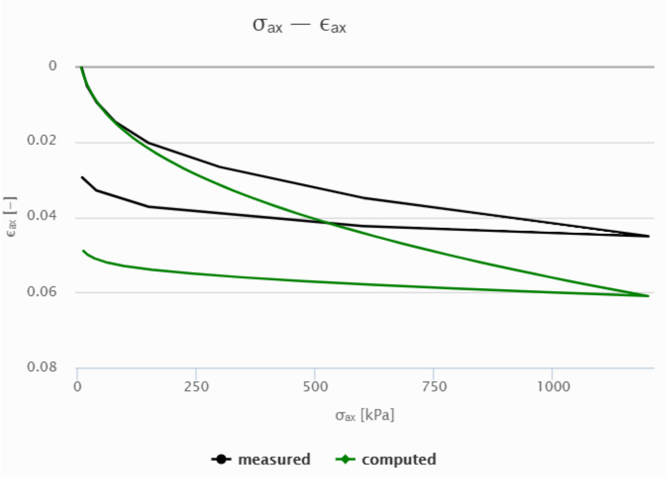

Fig. 22: Calibration results – oedometric compression test

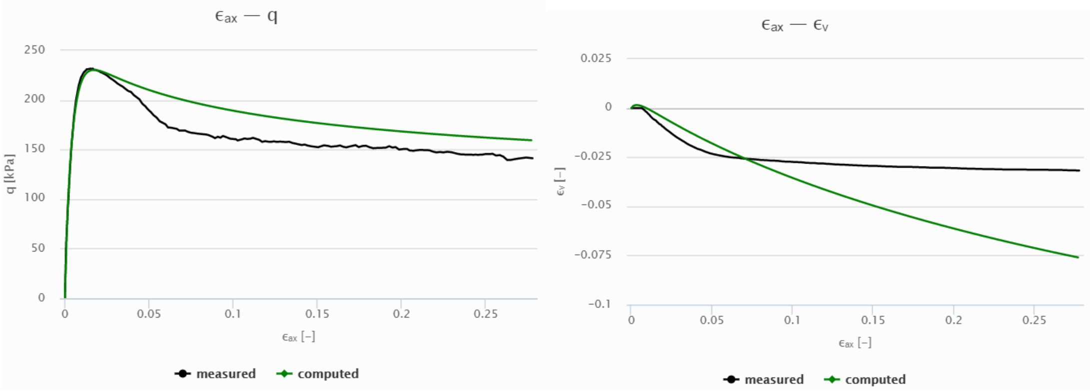

Fig. 23: Calibration results – triaxial compression test

The results of Fig. 22 show a relativly high discrepancy between the lab test results and the calibrated results of ExCalibre, whereas the stress-strain behavior of the triaxial compression test shown in Fig. 23 (left) matches better between the lab test results and the calibrated results. The volumetric behavior (see Fig. 23 (right)) shows, again, higher deviations between both of the considered results. It also must be noted that the calibration process of ExCalibre changes the strains of the lab test results from engineering strains $\varepsilon_{\text{eng}} = dL/L_0$ to true strains $\varepsilon_{\text{true}}$ by applying equation (4.1).

$$\varepsilon_{true} = -ln(1 - \varepsilon_{eng}) \tag{4.1}$$

The next chapter investigates the influence of different input files on the calibration results of ExCalibre.

4.2.2 Influence of different input data

Due to the fact that ExCalibre provides the possibility to change the type and amount of soil test data in the input file, this chapter will show the influence on the calibrating hypoplastic parameters of uploading different input files of the same soil sample on the website. For example, it is possible to use only one oedometric compression test (loose or dense sample) as well as only one triaxial compression test (loose or a dense sample, with any confining pressure). For this investigation, three soil samples from the "soilmodels.com" website were used again and can be seen in Tab. 2. The three materials of Tab. 2 were selected, because for all of them, two oedometric compression tests and three triaxial compression tests with confining pressures of 50, 100 and 200 kPa were provided. To investigate the influence of the input tab-sheet on the resulting hypoplastic parameters, different combinations of the input were created, which can be seen in Tab. 4, and were then uploaded for the calibration with ExCalibre. After the calibration process for each input file was finished, the resulting hypoplastic parameters were noted, and the relative difference [%] related to input set a (see Tab. 4), which contains all available soil tests, was calculated. For a better representation of the results, the differences to the reference set a were plotted for every hypoplastic parameter (see Fig. 24 to Fig. 27), and the magnitudes of the differences presented within tables can be seen in the appendix.

Tab. 2 Parameters of three different materials

Material	φ_c [°]	h_s $[kPa]$	n [-]	e_{d0} [-]	e_{c0} [-]	e_{i0} [-]	α [-]	β [-]
Rohatec sand	34.3	61,377	0.462	0.379	0.757	0.909	0.11	3.3
Kralupy sand	36.3	3810	0.165	0.758	1.517	1.820	0.12	4.3
Motol sand	35.3	987	0.193	0.594	1.188	1.426	0.01	1.7

Tab. 3: Initial void ratios of the soil tests

	Initial void ratios of input file		
Soil test	Rohatec sand	Kralupy sand	Motol sand
Oed 1	0.741	0.997	0.7615
Oed 2	0.721	1.017	0.743
Triax 1 ($\sigma_3 = 50\ kPa$)	0.520	0.637	0.313
Triax 2 ($\sigma_3 = 100\ kPa$)	0.467	0.625	0.306
Triax 3 ($\sigma_3 = 200\ kPa$)	0.469	0.525	0.281

Tab. 4: Different combinations of input files for ExCalibre

Input set	Oed 1	Oed 2	Triax 1 ($\sigma_3 = 50\ kPa$)	Triax 2 ($\sigma_3 = 50\ kPa$)	Triax 3 ($\sigma_3 = 50\ kPa$)
a	●	●	●	●	●
b	●		●	●	●
c	●		●	●	
d	●		●		●
e	●			●	●
f	●		●		
g	●			●	
h	●				●
i	●	●	●	●	
j	●	●	●		●
k	●	●		●	●
l	●	●	●		
m	●	●		●	
n	●	●			●

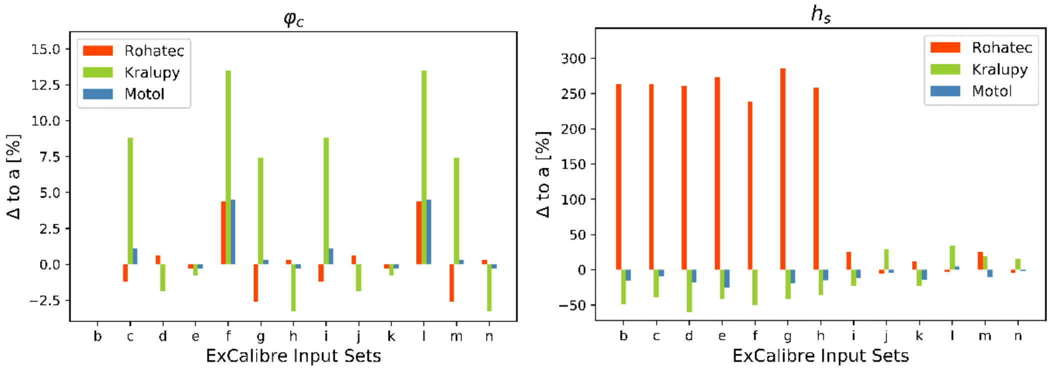

Fig. 24: Resulting φ_c-values (left) and h_s-values (right) for the different input files

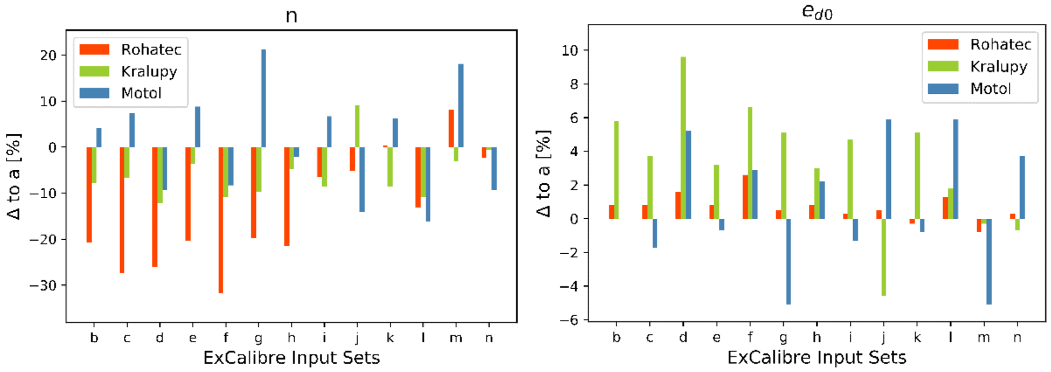

Fig. 25: Resulting n-values (left) and e_{d0}-values (right) for the different input files

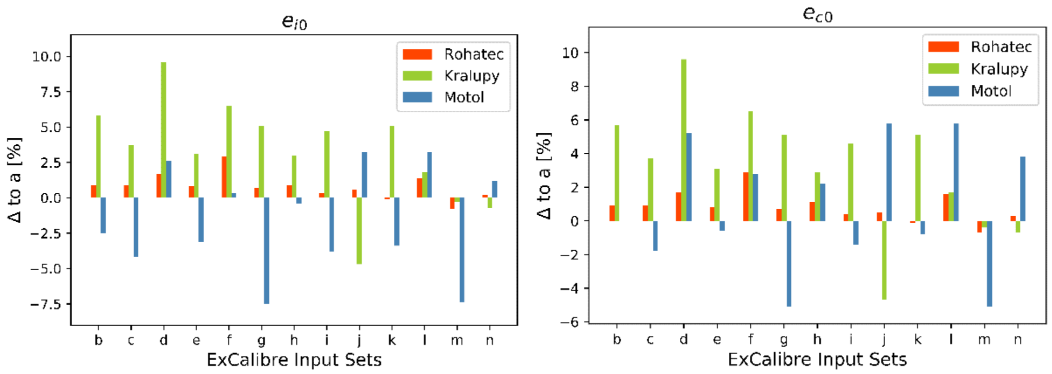

Fig. 26: Resulting e_{i0}-values (left) and e_{c0}-values (right) for the different input files

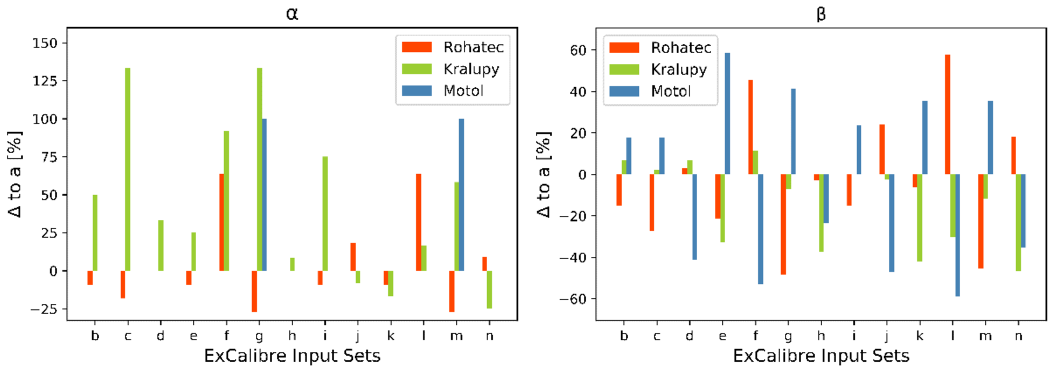

Fig. 27: Resulting α-values (left) and β-values (right) for the different input files

Fig. 24 (left) shows that the critical friction angle φ_c shows the highest magnitudes in the case that only one triaxial compression test with a low confining pressure (here $\sigma_3 = 50\ kPa$) is used, which can particularly be seen for the Motol sand. Furthermore, it can be observed that the amount of applied oedometric compression tests within the input file does not have much influence on the resulting critical friction angle. Also, with respect to the initial void ratios of the different soil tests of the input file, it can be seen that the Kralupy sand has the highest void ratios and also shows the highest deviations for φ_c. However, for most of the used input sets, the deviations of the critical friction angle are in an acceptable range. For the h_s parameter (see Fig. 24 right), it can be seen that adding a second oedometric compression test has a significant influence on the resulting calibrated h_s parameter, although for all soil samples, the initial void ratios of the second oedometer test are similar to the first one. So, for the Rohatec sand, the relative changes of h_s decrease at an extreme rate from a very high magnitude. For the Motol sand, it seems that the relative changes decrease, and for the Kralupy sand, the relative changes of h_s went from negative to positive deviations by adding a second oedometric compression test.

For the hypoplastic parameter n (see Fig. 25 left), the relative deviations show no clear trend between the different soil samples and the different input sets. For example, the Motol sand shows only negative deviations if the triaxial compression tests with a confining pressure of $\sigma_3 = 100\ kPa$ is missing, and for the Kralupy sand, all combinations show negative deviations, except for set j. All initial void ratios (Fig. 25 right and Fig. 26 left and right) show the same behavior of deviations but gain no consistent behavior that can be observed between the different applied input sets and the different soil samples. But for the Motol sand, again the triaxial compression test at a confining pressure of $\sigma_3 = 100\ kPa$ show significant influence on the resulting calibration parameters. If this test is missing, or if only this test is used as triaxial compression test within the input file, the deviations are highest.

The deviations of the hypoplastic parameter α (see Fig. 27 left) seem to be mostly influenced by the triaxial compression tests of the input file. The Rohatec sand shows the highest deviations if only one triaxial compression test with a low confining pressure of $\sigma_3 = 50\ kPa$ is used. The results of the Motol sand are again, significantly influenced by the triaxial test with a confining pressure of $\sigma_3 = 100\ kPa$, and the deviations for the Kralupy sand are highest in the case of the triaxial compression test with $\sigma_3 = 200\ kPa$ missing.

The hypoplastic parameter β presented within Fig. 27 (right) shows the strongest scattering effect by applying different input files. Again, no real consistent behavior between changing the input files and the different soil samples can be found.

In general, it can be concluded that, although the initial void ratios for each soil samples are similar for the different oedometric compression tests, as well as for the different triaxial compression tests, the amount of soil test data applied within the input file can have significant influence on the resulting calibration parameters. A reason for this could not be found until this part of the work, and to investigate this issue in more detail, the calibration process must be analyzed more, because there may be an influence from the different applied triaxial compression tests with respect to the confining pressure. But, the calibration process is also surely influenced by the initial void ratios of each soil test.

4.2.3 Updating initial void ratios of input

As already stated within chapter 4.2.1, the initial void ratios are updated during the calibration process, but only for the triaxial compression test. Due to importance of the initial void ratio e_{init} connected with the application of the hypoplastic soil model, the idea was to change the initial void ratios in the input files for ExCalibre to the updated ones of the first calibration process. Hence, a kind of iterative process is performed and the aim is to see the influence of updating the initial void ratios on the calibrated hypoplastic parameters. The first investigations regarding the updated initial void ratios were performed for the Motol sand from the “soilmodels.com” website (see Tab. 2).

As provided, the input dataset, denoted as “Set 1”, was uploaded to ExCalibre, the updated void ratios (“Set 2”) were noted and the relative difference between both was calculated. Furthermore, the hypoplastic parameters were taken, and for input set “Set 1”, the hypoplastic parameter set was denoted as “Set a”.

In the second step, the initial void ratios of input set 1 were updated to the magnitudes of set 2, and the calibration was started. The resulting updated void ratios then present “Set 3”, and the obtained hypoplastic parameters (from input set 2) present “Set b”.

This process was rerun several times in order to see how ExCalibre reacted to the change of the initial void ratios in the input files. The initial void ratios of the oedometric compression tests were not considered, due to the fact that only the initial void ratios of the triaxial compression tests were updated.

Tab. 5 to Tab. 7 show the different sets of initial void ratios and their differences and Tab. 8 to Tab. 10 show the associated obtained hypoplastic parameters.

Tab. 5: Initial void ratios of set 1 and set 2 – Motol sand

	Initial void ratios		
Test	Input dataset (set 1)	ExCalibre output (set 2)	Difference [%]
Triax 50 kPa	0.313	0.375	+19.8
Triax 100 kPa	0.306	0.306	0
Triax 200 kPa	0.281	0.308	+9.6

Tab. 6: Initial void ratios of set 2 and set 3 – Motol sand

	Initial void ratios		
Test	Input dataset (set 2)	ExCalibre output (set 3)	Difference [%]
Triax 50 kPa	0.375	0.406	+8.3
Triax 100 kPa	0.306	0.282	-7.8
Triax 200 kPa	0.308	0.329	+6.8

Tab. 7: Initial void ratios of set 3 and set 4 – Motol sand

	Initial void ratios		
Test	Input dataset (set 3)	ExCalibre output (set 4)	Difference [%]
Triax 50 kPa	0.406	0.410	+1.0
Triax 100 kPa	0.282	0.276	**-2.0**
Triax 200 kPa	0.329	0.330	+0.3

Tab. 8: Hypoplastic parameters for input set 1 and input set 2 – Motol sand

Set (input)	φ_c [°]	h_s $[kPa]$	n [-]	e_{d0} [-]	e_{c0} [-]	e_{i0} [-]	α [-]	β [-]
Set a (set 1)	35.3	987	0.193	0.594	1.188	1.426	0.01	1.7
Set b (set 2)	35.3	867	0.198	0.595	1.191	1.429	0.01	2
Difference [%]	0	-12.2	+2.6	+0.2	+0.3	+0.2	0	+17.7

Tab. 9: Hypoplastic parameters for input set 2 and input set 3 – Motol sand

Set (input)	φ_c [°]	h_s $[kPa]$	n [-]	e_{d0} [-]	e_{c0} [-]	e_{i0} [-]	α [-]	β [-]
Set b (set 2)	35.3	867	0.198	0.595	1.191	1.429	0.01	2
Set c (set 3)	35.3	928	0.206	0.583	1.166	1.399	0.01	2
Difference [%]	0	+7.0	+4.0	-2.0	-2.1	-2.1	0	0

Tab. 10: Hypoplastic parameters for input set 3 and input set 4 – Motol sand

Set (input)	φ_c [°]	h_s $[kPa]$	n [-]	e_{d0} [-]	e_{c0} [-]	e_{i0} [-]	α [-]	β [-]
Set c (set 3)	35.3	928	0.206	0.583	1.166	1.399	0.01	2
Set d (set 4)	35.3	601	0.184	0.631	1.262	1.515	0.01	2
Difference [%]	0	**-35.2**	-10.7	+8.2	+8.2	+8.3	0	0

Also, after updating the initial void ratios of the input file twice, there is still a maximum change of $|\Delta| = 2\%$ (see Tab. 7). Even though the changes of the initial void ratios are relatively small, the hypoplastic parameters show significant changes, with a maximum change of $|\Delta| > 35\%$ (see Tab. 10). The same investigations were performed for the Dobrany sand (see Tab. 11), and the results are given within the appendix A.

In the next chapter, the performance of the automatic hypoplastic parameter calibration tool ExCalibre is validated by performing the soil tests, which are used as inputs for ExCalibre, along with the PLAXIS (Brinkgreve, et al., 2018) Soil Test Tool.

4.2.4 Comparison of ExCalibre and PLAXIS Soil Test Tool

Regarding the investigations within this chapter, two soil samples from the database provided by the website, “soilmodels.com”, were used. For all of the materials of the database, the input-template for ExCalibre, including different lab test data and all further necessary information, can simply be downloaded from the website. In addition, the already calibrated hypoplastic parameter set for every material is provided. The hypoplastic parameters for the two soil samples are given in Tab. 11, and the settings for the oedometric and triaxial compression test are given in Tab. 12 and Tab. 13. The settings for the Dobrany sand are shown in the appendix A.

Tab. 11: Hypoplastic parameters for Dobrany and Rohatec sand

Material	φ_c [°]	h_s $[kPa]$	n [-]	e_{d0} [-]	e_{c0} [-]	e_{i0} [-]	α [-]	β [-]
Rohatec sand	34.3	61,377	0.462	0.379	0.757	0.909	0.11	3.3
Dobrany sand	36.5	49846	0.243	0.572	1.144	1.372	0.09	4.5

Tab. 12: Settings for oedometric compression test – Rohatec sand

Soil test	e_{init}	Pressure-steps [kPa]
Oedometer 1	0.741	8 – 10 – 20 – 40 – 80 – 150 – 300 – 600 – 1200 – 600 – 150 – 40 - 10
Oedometer 2	0.721	8 – 10 – 20 – 40 – 80 – 150 – 300 – 600 – 1200 – 600 – 150 – 40 - 10

Tab. 13: Settings for triaxial compression test – Rohatec sand

Soil test	e_{init}	Confining pressure σ_3 $[kPa]$
Triax 1	0.440	50
Triax 2	0.521	100
Triax 3	0.458	200

First, the corresponding input file was uploaded to ExCalibre, and after the calibration was successfully completed, the results of all soil tests were transferred to a new Excel worksheet.

Then, the results of lab tests were copied from the input file to the new worksheet, and the strains of both the oedometric and the triaxial compression tests were changed from engineering strains ε_{eng} into true strains ε_{true} with equation (4.1). Due to the reason that PLAXIS also uses true strains (ε_{true}), for the figures Fig. 28 to Fig. 30 only true strains were applied.

The third and last step is to perform the same soil tests using the Soil Test Tool within PLAXIS. For this, two important points must be considered before starting the lab tests. The first is the correct determination of the parameter p_t in the “Parameter” sheet in PLAXIS, which is especially important for the oedometric compression test. According to Masin (2010), the p_t-value is defined as *the shift of the mean stress due to cohesion. The effective stress* σ *used in the model formulation is replaced by* $\sigma - 1p_t$. *Non-zero value of* p_t *is needed to overcome problems with stress-free state. If* $p_t = 0$*, it will be replaced by a default value of 1 kPa. Any other value can be input by user (for basic hypoplasticity, set* p_t *to very low number, e.g.* $p_t = 1.e\text{-}5$*).* Due to the fact that the oedometer lab tests given in the input file all start at a magnitude of 8 kPa, and the PLAXIS soil test simulations start at 0 kPa, the p_t value has to be taken into account with a magnitude of $p_t = 8$ kPa.

Furthermore, it is important that the initial stress increment be chosen with -1 kPa and 10,000 steps for the oedometric compression test, otherwise the strains will be induced, but the stresses will not be updated and will remain at 0 kPa (Winkler, 2018). All other load increments can be chosen as desired. The second point regarding the simulation of soil tests with PLAXIS is related to the initial void ratios. For the triaxial tests, the updated initial void ratios after the calibration process were taken and converted to initial void ratios at zero pressure using Bauer’s compression law (Bauer, 1996) (see equation 3.2), as this is necessary for PLAXIS. According to Winkler (2018), the initial void ratios of the oedometric compression tests provided in the input-file were assumed to be the void ratio at zero pressure, due to a lack of information regarding the isotropic pressure level, for which the initial void ratio was determined.

Additionally, it has to be mentioned that regarding the volumetric behavior, the same sign convention as defined in ExCalibre is used, with dilatancy being negative. The results of two oedometric compression tests and two triaxial compression tests for Rohatec sand are shown from Fig. 28 to Fig. 30. For the Dobrany sand tests, the results are given within the appendix A.

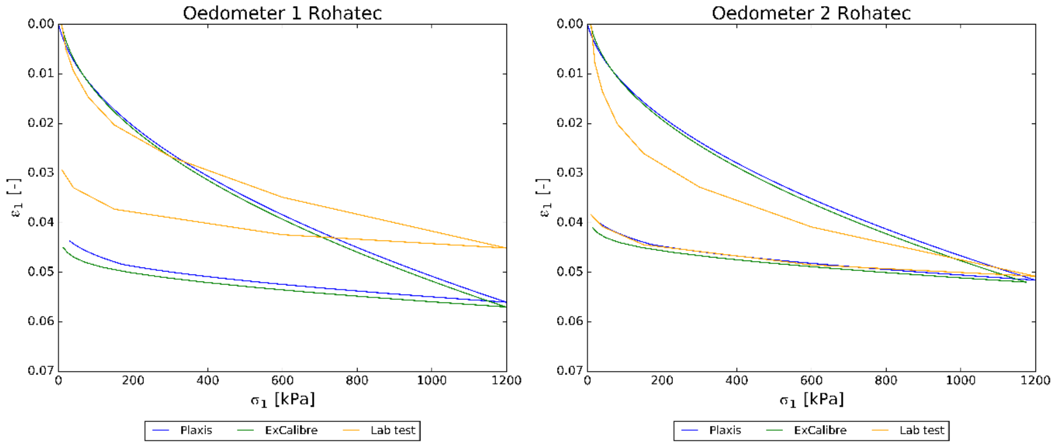

Fig. 28: Oedometric compression tests – Rohatec sand

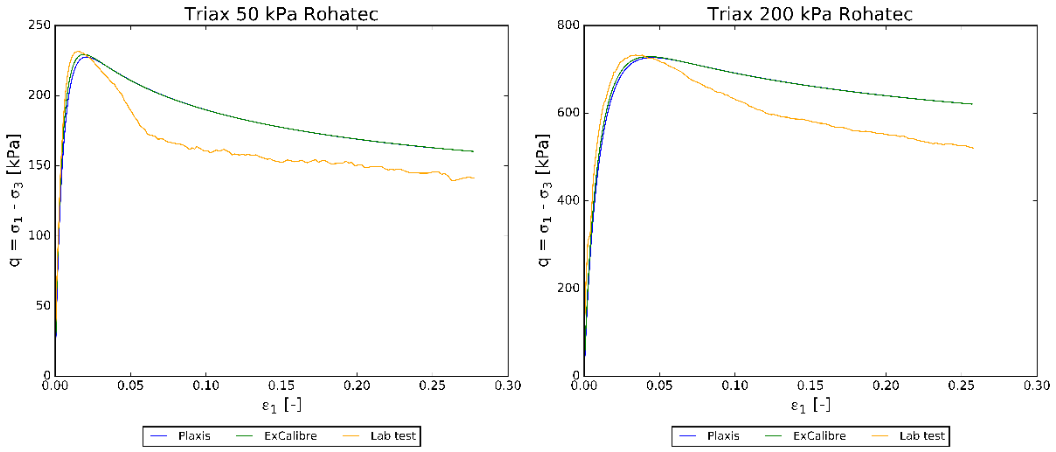

Fig. 29: Triaxial compression tests (q-ε_1-diagrams) – Rohatec sand

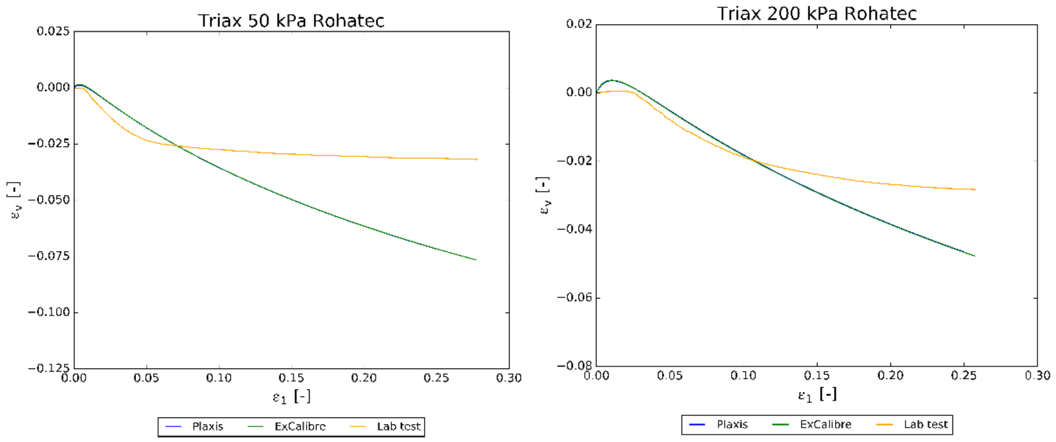

Fig. 30: Triaxial compression tests (ε_v-ε_1-diagrams) – Rohatec sand

For the oedometric compression test results of Fig. 28, it can be seen that the resulting curves from ExCalibre and PLAXIS are very similar but show significant deviations from the lab test data, whereas the stress-strain response of the triaxial compression tests shown in Fig. 29 match up to the peak stress very well with the lab test results. It is also true that after the peak stress is reached, the stress-strain response of ExCalibre and PLAXIS results show deviations from the lab test data. The situation for the volumetric behavior is different, since the results obtained with PLAXIS and ExCalibre are not able to reproduce the real soil behavior of the lab test results (see Fig. 30).

4.2.5 p_t-value of hypoplastic soil model in PLAXIS (connected to ExCalibre)

In all studies where the hypoplastic soil model was used, the p_t value was set to a very low number of p_t = 1E-5, as recommended by Masin (2010). But, since the p_t-value had to be changed for the simulations of the oedometric compression tests within the PLAXIS Soil Test Tool this chapter will present some of these investigations with respect to p_t-value. The Motol soil sample from Tab. 2 is used for these investigations. First, with regards to the material of Tab. 2 (Motol sand), an oedometric compression test was simulated with the PLAXIS Soil Test Tool and different magnitudes for the p_t-value were applied. The resulting oedometer curves are shown in Fig. 31.

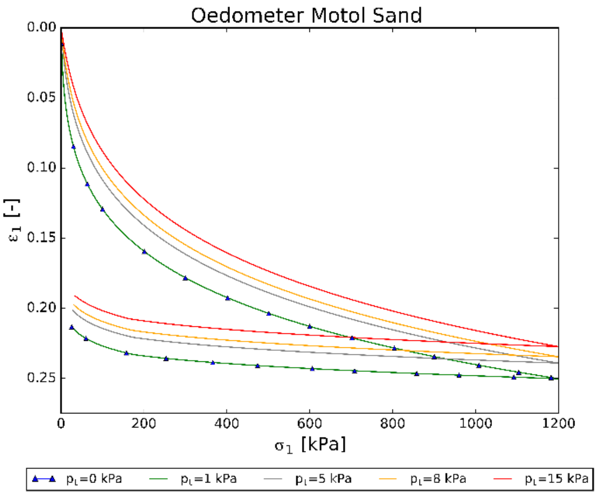

Fig. 31: Oedometer test with different p_t-values – Motol sand

Fig. 31 illustrates the significant influence of the p_t-value very well. It can also be seen that the compression curves for p_t = 0 kPa and p_t = 1 kPa are exactly the same, due to the definition of the p_t-value. According to the definition given in (Masin, 2010), p_t must be unequal to 0, and if it is applied as 0 kPa, its default value of 1 kPa is used.

Additional investigations were executed with respect to ExCalibre, and it was discovered, that ExCalibre only takes the first pressure increment into account if $\sigma_{ax} \geq 5kPa$ for the oedometric compression test. To prove this statement, the first pressure increment of the ExCalibre input files was varied, and then the calibrated compression results were again transferred to an Excel worksheet, and the same oedometric compression tests were simulated within PLAXIS. This was done by applying the p_t-values at the same time as the same magnitude as the first pressure increment of the input file was used. In Fig. 32, it is schematically shown, which value of the input file is changed.

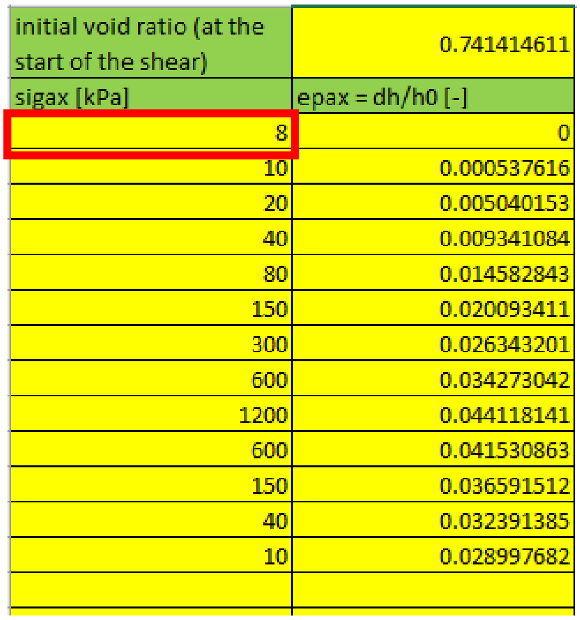

initial void ratio (at the start of the shear)	0.741414611
sigax [kPa]	epax = dh/h0 [-]
8	0
10	0.000537616
20	0.005040153
40	0.009341084
80	0.014582843
150	0.020093411
300	0.026343201
600	0.034273042
1200	0.044118141
600	0.041530863
150	0.036591512
40	0.032391385
10	0.028997682

Fig. 32: Changing first stress increment of ExCalibre input

The following Fig. 33 and Fig. 34 show, with the appropriate PLAXIS Soil Test Tool curves, the oedometric compression curves for the different ExCalibre input files where only the first stress increment is different.

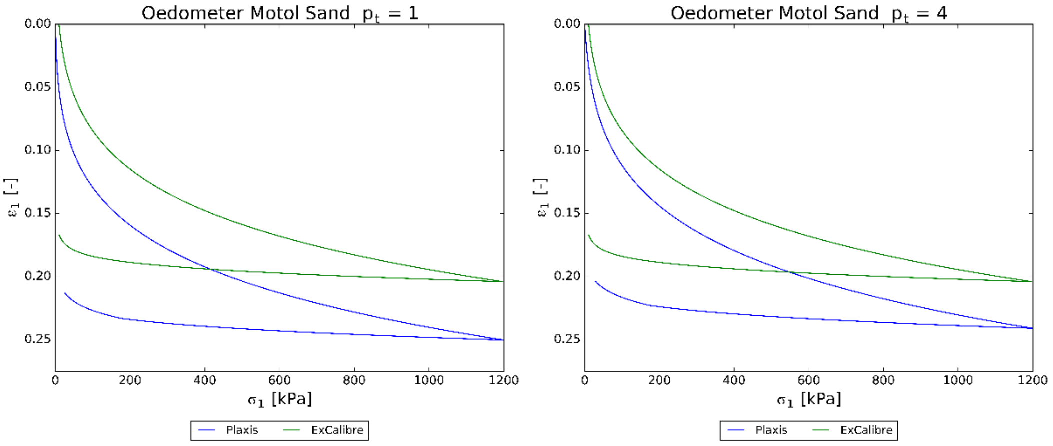

Fig. 33: Oedometer curves for different p_t-values: $p_t = 1$ (left) and $p_t = 4$ (right) – Motol sand

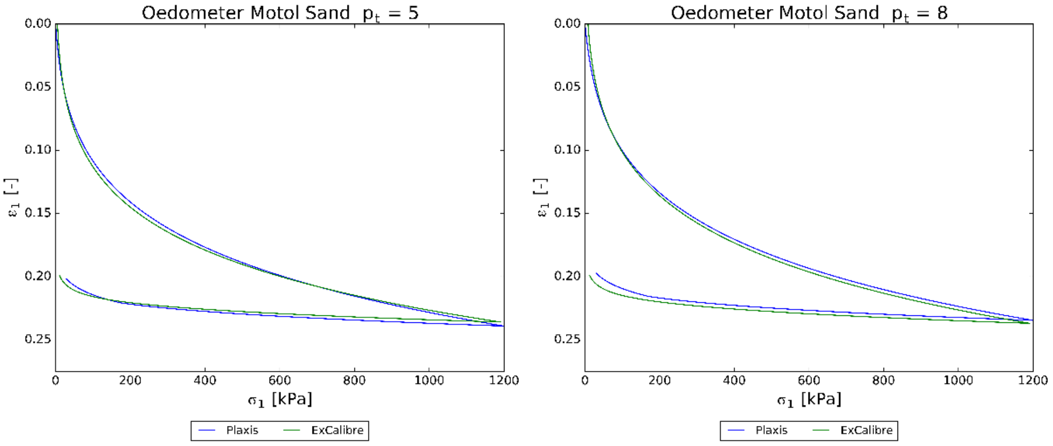

Fig. 34: Oedometer curves for different p_t-values: $p_t = 5$ (left) and $p_t = 8$ (right) – Motol sand

Fig. 33 shows that applying the first pressure increment of the oedometric compression test for the ExCalibre input file smaller than 5 kPa always results in ExCalibre taking the next pressure increment $\geq 5\ kPa$ into account, and so the PLAXIS curves with the appropriate p_t-values exhibit very large deviations. Using the first pressure increment with 5 kPa or higher, Fig. 33 shows that ExCalibre does actually take this first pressure increment into account, and that the simulations executed with PLAXIS including the appropriate p_t-values only show small differences. With respect to this particular issue regarding the p_t-value for PLAXIS simulations that apply the hypoplastic soil model, and the way ExCalibre takes the lab test data from oedometric compression tests into account, more investigations have to be done.

4.3 Hypoplastic model for crushable sand

This chapter discusses first the effect of grain crushing on the mechanical behavior of soils, as well as on the soil properties. This is followed by a presentation of a hypoplastic soil model that takes grain crushing into account. Moreover, the application and performance of this relatively new soil model within PLAXIS is shown.

4.3.1 Grain breakage

Introduction

Depending on soil properties, grain breakage usually occurs at high pressures, and, whereas many geotechnical applications are related to low stress levels, several geotechnical problems have to deal with high stresses. For example, the penetration of a cone, stability of earth dams or the bearing capacity of piles all demonstrate geotechnical problems that deal with high stresses. Hence, for granular materials considered at high confining stress levels, grain breakage could occur. Furthermore, the soil's mechanical behavior could be significantly influenced. In general, the problem of grain breakage is considered at a micro-scale that is, besides the micro-scale properties, also strongly influenced by macro-scale properties and external forces. Furthermore, the influencing parameters can be distinguished between nature parameters that characterize the discontinuous medium, and mechanical or state parameters. With respect to soil mechanics, several performed studies showed that, for example, parameters like the grain mechanical resistance, the grain size, the grain angularity and the grain size distribution have a significant influence on the amount of grain breakage. Besides these main influencing parameters, which are necessary by means of geotechnical applications, further parameters may have an influence on the amount of grain breakage. These further parameters include, for example, the agitation intensity, mineralogical composition of the grains and also the grain's state of alteration. Overall, grain breakage can be classified by distinguishing between the three different modes shown in Fig. 35 (Daouadji & Hicher, 2010; Engin, et al., 2014; Phuong, et al., 2018).

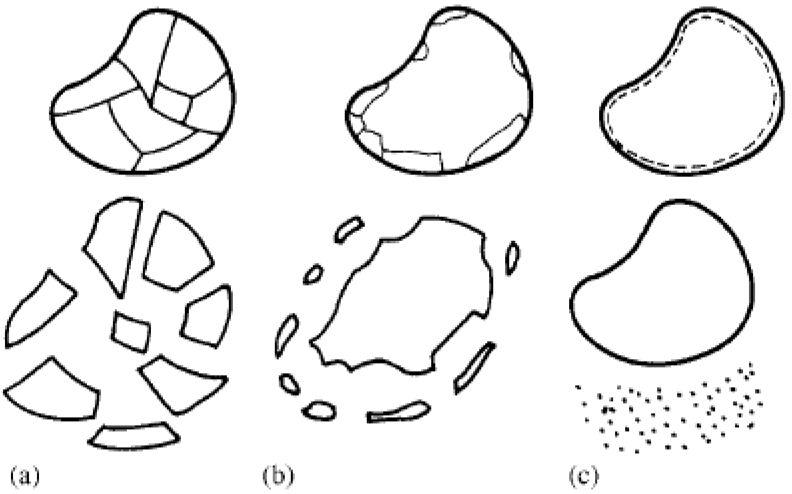

Fig. 35: Modes of grain breakage: (a) fracture, (b) attrition and (c) abrasion (Daouadji & Hicher, 2010)

The three different modes of grain breakage (see Fig. 35) can be described as follows (Daouadji & Hicher, 2010):

- (a) fracture: this mode can be seen as a splitting (breaking) of the grain into similar sizes

- (b) attrition: the results of this breakage mode are a single grain with an smaller size and several grains with a significantly smaller size

- (c) abrasion: the break of the grain asperities results in the production of fine particles ($\% < d_{10}$)

With respect to geotechnical applications, the first two grain breakage modes (fracture and attrition) are of the most relevance, because they show a more significant influence on nature and mechanical parameters (Daouadji & Hicher, 2010).

The performance of soil tests on granular materials shows that the constitutive behavior of soil during loading is affected by the stress level. With regards to triaxial compression tests, is can be seen that the peak strength, and also the dilation, show significant changes between the different stress levels. Fig. 36 shows, that this dilation is suppressed, even though dense sand normally tends to show dilation behavior at high confining pressure. In addition to this, it can be seen that with an increase of the confining pressure, the peak friction also significantly decreases. One possible reason for such behavior may be the problem of grain breakage occurring at higher pressure levels (Loung & Touati, 1983). Therefore, it is important to incorporate the main influencing characteristics, such as stress dependency, hardening and softening, dilation, and contraction in a constitutive soil model for a proper modelling of the soil behavior. The following points present the stress dependency of the most relevant soil parameters with respect to the amount of grain crushing (Engin, et al., 2014).

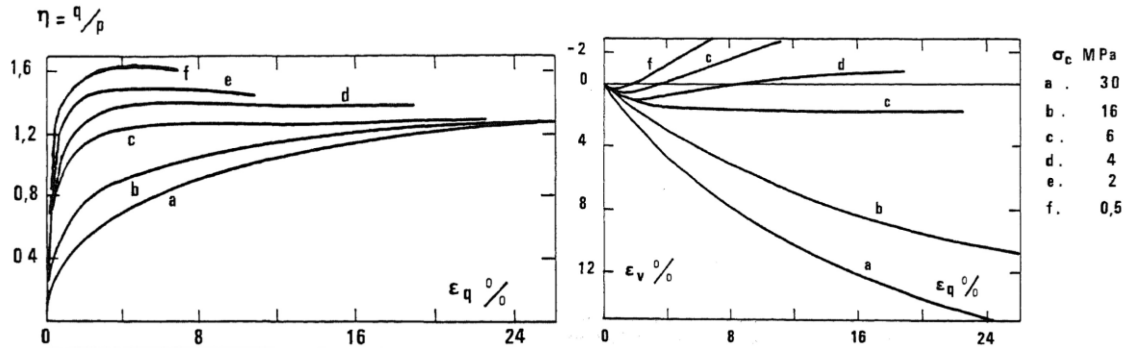

Fig. 36: triaxial tests at different confining pressures σ_c (Fontainbleau with $I_D = 0.95$) (Loung & Touati, 1983)

Uniformity coefficient C_u

Grain breakage causes a change of the grain sizes of a material (see Fig. 35) and hence also the grain size distribution changes. An inidcator for the grain size distribution is the so called uniformity coefficient C_u, which can be calculated as shown in equation (4.2), where d_{10} defines the particel size at which 10% of all particels are finer and 90% are coarser than d_{10}. Equally, d_{60} defines the particel size at which 60% of all particels are finer and 40% are coarser than d_{60}.

$$C_u = {}^{d_{60}}/_{d_{10}} \tag{4.2}$$

Nakata et al. (2001) performed oedometric compression tests on a dense silica sand ($e_0 \approx 0.6$) for two different initial gradings (uniformly and well-graded). The results of the oedometer tests are shown in Fig. 37. Furthermore, for different considered stress levels (see legend Fig. 37), the related grain size distributions are shown within Fig. 38. It can be seen that the change in the grain size distribution caused by grain breakage can be characterized by the uniformity coefficient C_u. Hence, Rohe et al. (2014) formulated the dependency of C_u on the stress level based on the results provided by (Nakata, et al., 2001), as shown in equation (4.3).

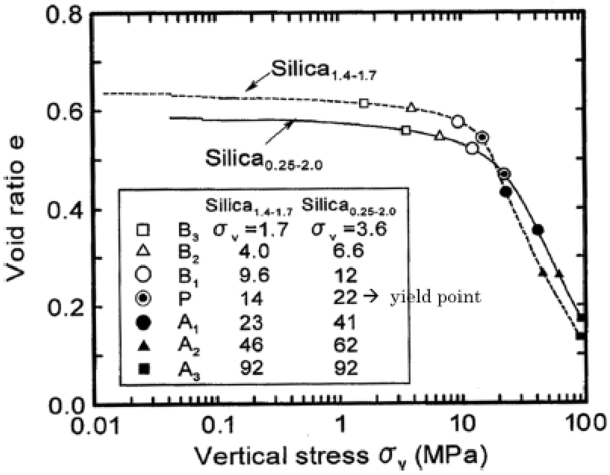

Fig. 37: Results of oedometric compression tests on dense silica sand for different initial gradings (Nakata, et al., 2001)

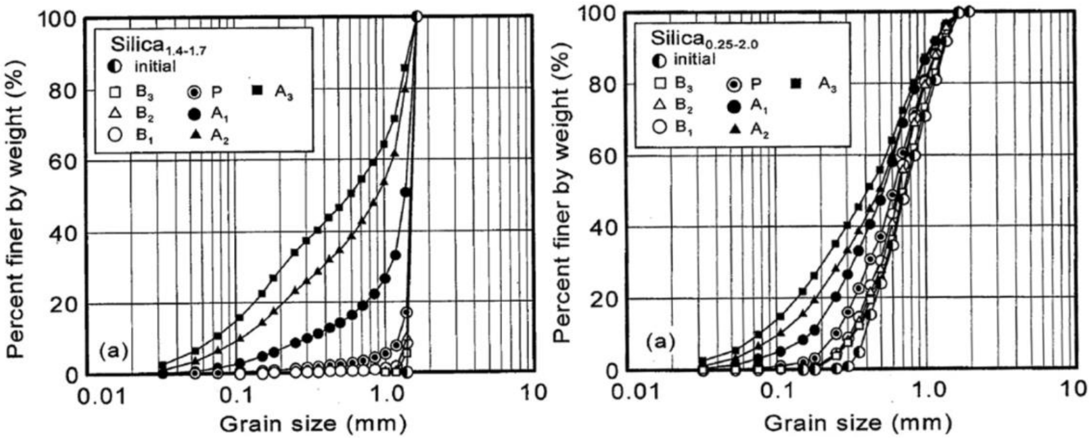

Fig. 38: Grain size distributions for stress levels according to Fig. 37 (Nakata, et al., 2001)

$$C_u = f(p', q) = \alpha_p p'^2 - \alpha_q q^2 + \beta_p p' - \beta_q q + C_{u0} \tag{4.3}$$

Equation (4.3) shows the dependency of the uniformity coefficient C_u on the vertical stress by taking into account the mean effective stress p' (negative in compression) and the deviatoric stress q. Furthermore, the factors α_p and α_q control the quadratic, and the factors β_p and β_q control the linear change of the uniformity coefficient due to the mean effective and deviatoric stress. All four factors can be determined by means of a curve-fitting procedure (Engin, et al., 2014; Phuong, et al., 2018). Because the determination of the different factors incorporated within equation (4.3) was not further explained and suggested values were only valid for one-dimensional compression, Phuong et al. (2018) generalized the stress dependency of C_u for both, one-dimensional and triaxial compression by collecting data from literature. The results taken from literature are shown in Fig. 39, where the horizontal axis represents a non-dimensional stress (vertical effective stress for oedometer test and cell pressure for triaxial test), and the vertical axis represents the difference between the uniformity coefficient C_u and the reference value C_{u0}. Fig. 39 clearly shows that for triaxial compression (red curve), the amount of grain crushing is higher than for oedometric compression (blue curve) due to the additional shearing during triaxial loading.

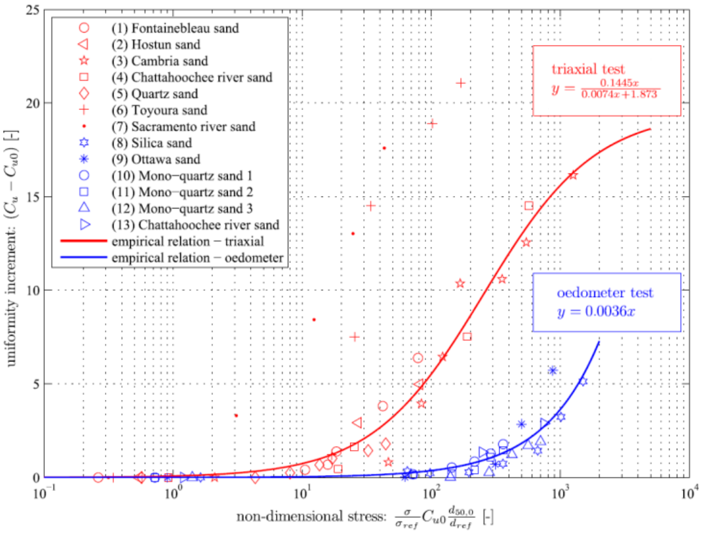

Fig. 39: Dependency of uniformity coefficient C_u on stress level for oedometric and triaxial compression tests (Phuong, et al., 2018)

The dependency of C_u on the stress level (see Fig. 39) for triaxial compression and for oedometric compression can be formulated as follows (Phuong, et al., 2018):

- Triaxial compression:

$$C_u = \frac{0.1445x}{0.0074x + 1.873} + C_{u0} \tag{4.4}$$

- Oedometric compression:

$$C_u = 0.0036x + C_{u0} \tag{4.5}$$

For both formulas, the variable x is defined as shown in equation (4.6), however, for triaxial compression, the cell pressure must be taken into account, with $\sigma = \sigma_{tx}$, and for oedometric compression, the applied effective vertical stress is considered, with $\sigma = \sigma_{oed}$ (Phuong, et al., 2018).

$$x = \frac{\sigma}{\sigma_{ref}} * C_{u0} * \frac{d_{50,0}}{d_{ref}} \tag{4.6}$$

The reference uniformity coefficient is taken into account with the variable C_{u0} and the reference mean grain size with $d_{50,0}$. Furthermore, σ_{ref} represents a reference stress level of 100 kPa, and d_{ref} represents the reference grain diameter of 1 mm. It is also important to mention that, to find the correlations of (4.4) and (4.5), mainly quartz sands were considered, and, therefore, the relation may not be applicable for calcareous sands. The consideration of different sand may also show deviations to the generalized correlation due to, for example, effects of different grain shapes, grain sizes or different initial gradings (Phuong, et al., 2018). These uncertainties should be part of further research.

Minimum and maximum void ratio

As already shown in Fig. 39, the stress dependency of the void ratios must also be considered because the effect and the amount of grain crushing also have a significant influence on the void ratio. And, especially with respect to hypoplasticity, the void ratios are very important in predicting the soil's behavior. In general, it can be stated that both the minimum and the maximum void ratio (e_{min} and e_{max}) decrease with an increase of the uniformity coefficient C_u. Phuong et al. (2018) used the same collected data from the aforementioned literature and illustrated the dependency of the minimum and maximum void ratio on the stress applied stress level, as shown in Fig. 40 (Phuong, et al., 2018).

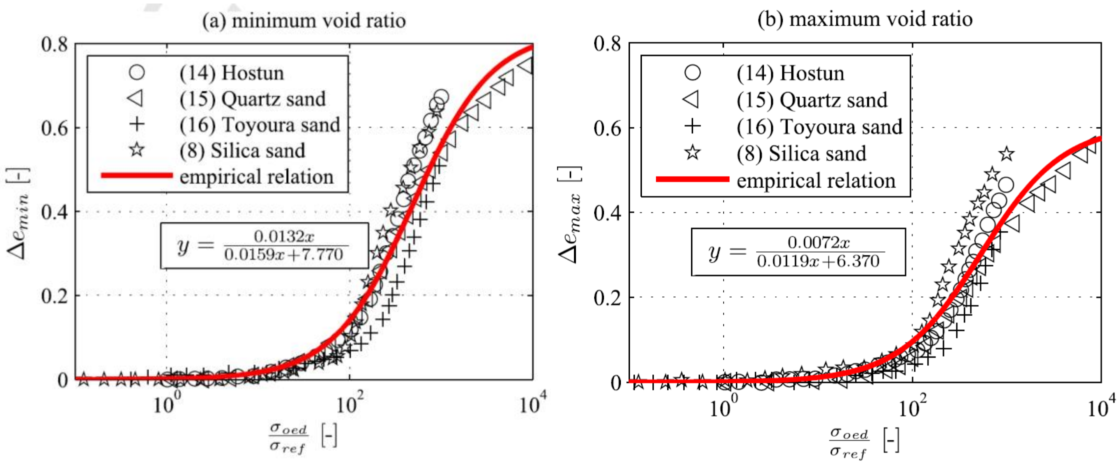

Fig. 40: Change of minimum void ratio e_{min} (left) and maximum void ratio e_{max} (right) with stress (Phuong, et al., 2018)

Fig. 40 shows that the minimum and maximum void ratio decrease with an increase of the stress level, and the correlations are formulated as shown in equation (4.7) and (4.8) (Phuong, et al., 2018).

$$\triangle\, e_{min} = \frac{0.0132\,\frac{\sigma_{oed}}{\sigma_{ref}}}{0.0159\,\frac{\sigma_{oed}}{\sigma_{ref}} + 7.77} \tag{4.7}$$

$$\triangle\, e_{max} = \frac{0.0072\,\frac{\sigma_{oed}}{\sigma_{ref}}}{0.0119\,\frac{\sigma_{oed}}{\sigma_{ref}} + 6.37} \tag{4.8}$$

Again, the relations presented by equation (4.7) and (4.8) are only valid for Quartz sands due to the collected results from literature, and are also only applicable for one-dimensional loading processes. However, it will be an unconditional issue of future research to build up such relations for a wider range of different sand and triaxial loading modes (Phuong, et al., 2018).

Strength parameters

Several investigations related to the stress dependency were performed in the past, especially for the friction angle and the dilatancy angle, and, it can be stated that the friction angle, as well as the dilatancy angle, decrease with an increase in the stress level. Phuong et al. (2018) applied the empirical relations after Bolton (1986) and Schanz & Vermeer (1996) and compared the results with the laboratory triaxial tests performed by Loung & Touati (1983). The comparison between the laboratory results and the results obtained from the empirical relation for the friction angle and the dilatancy angle are shown in Fig. 41. It can be easily seen that the friction angle and the dilatancy angle show a significant decrease with respect to an increasing stress level, and Fig. 41 also shows that the empirical relations (Bolton, 1986; Schanz & Vermeer, 1996) strongly support the laboratory results. Hence, the empirical relations according to Bolton (1986) and Schanz & Vermeer (1996) can be applied to describe the influence of the stress level on the soil's strength (Phuong, et al., 2018).

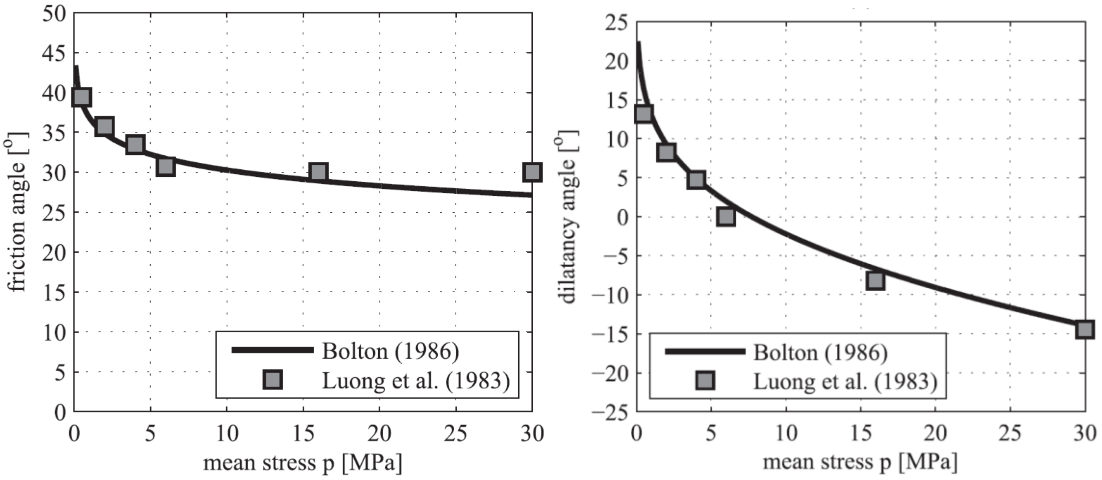

Fig. 41: Dependency of friction angle (left) and dilatancy angle (right) on the mean stress (laboratory test results (Loung & Touati, 1983) and empirical relations (Schanz & Vermeer, 1996)

Stress dependency of Stiffness

According to Ohde (1939), the dependency of the stiffness on the stress level can be determined as follows:

$$E = E_{ref} \left(\frac{p}{p_{ref}} \right)^{w} \tag{4.9}$$

Where the stress-dependent oedometer modulus is E_{ref}, which is the reference value of E_{50} corresponding to a reference pressure p_{ref}. The determination of w, which is dependent on the stress level, is divided into three different zones, which are not presented at great detail in this thesis. For a more detailed description, reference is made to (Phuong, et al., 2018).

4.3.2 Hypoplastic model taking grain breakage into account

The aim of many researchers is then to implement the relations shown in the chapter 4.3.1 into a constitutive soil model that considers grain breakage. This chapter will introduce to the user a hypoplastic model for crushable sand. First, the theory of the relatively new constitutive soil model and the expansion of the original hypoplastic model (Von Wolffersdorff, 1996) are presented, and this is followed by the application within PLAXIS 2D.

According to Von Wolffersdorff (1996), the hypoplastic constitutive soil model is applied as the basic model for modifying different parameters and, therefore, for accounting for grain breakage. The original hypoplastic soil model already incorporates dilation, contraction and the stress dependency of stiffness. Only the main mathematical formulations of the adaption of the constitutive soil model are shown in this thesis, and for more detailed descriptions see (Phuong, et al., 2018). Firstly, the modified minimum and maximum void ratios are presented (Phuong, et al., 2018).

Modified minimum and maximum void ratio

As shown in chapter 4.3.1, the minimum and maximum void ratio decrease with an increasing stress level caused by grain crushing effects. Hence, the reference void ratios should be adapted at each stress level based on the relation shown in the following equations (Phuong, et al., 2018).

$$e_{d0}^{m} = e_{d0} - \Delta e_{min} \tag{4.10}$$

$$e_{c0}^{m} = e_{c0} - \Delta e_{max} \tag{4.11}$$

$$e_{i0}^{m} = 1.15 * e_{c0}^{m} \tag{4.12}$$

Where the determination of Δe_{min} and Δe_{max} follows equations (4.7) and (4.8). The dependency of the reference void ratios (e_{d0}, e_{c0} and e_{i0}) on the stress level is shown in Fig. 42 (Phuong, et al., 2018).

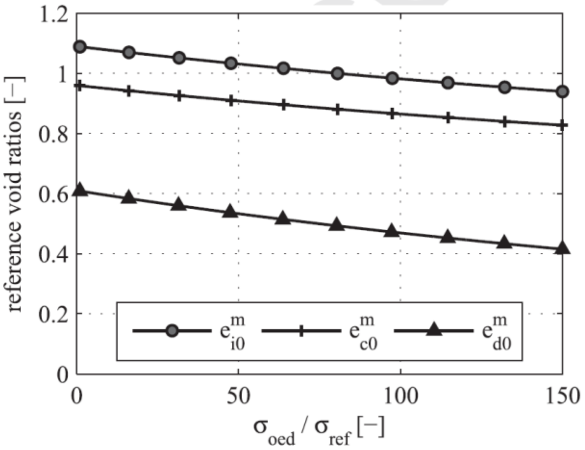

Fig. 42: Influence of stress level on the reference void ratios (Hostun sand, $I_D = 0.90$) (Phuong, et al., 2018)

Modified parameter α

According to Herle & Gudehus (1999), the hypoplastic parameter α controls the peak state of triaxial compression test that applies the hypoplastic soil model, and the peak strength is determined according to Bolton (1986). So, Phuong et al. (2018) stated that it must also be possible to determine an α-value that is dependent on the stress level. In Fig. 43, the stress dependency of the peak friction angle, as well as the parameter α, are both shown, where σ_{ref} indicates the reference pressure of 100 kPa. Fig. 43 shows a significant influence of the stress level on the parameter α, which may also reach a negative magnitude (Phuong, et al., 2018).

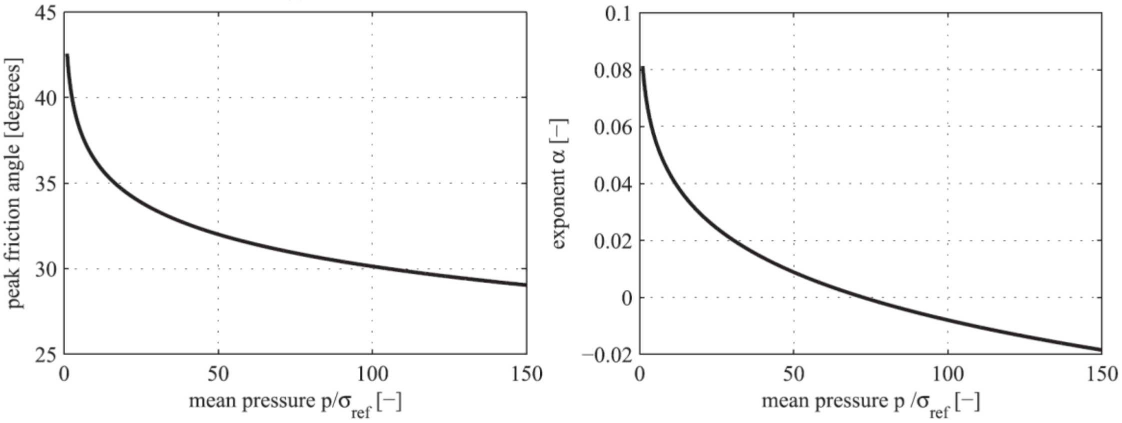

Fig. 43: Stress-dependent behavior of the peak friction angle (left) and the hypoplastic parameter α (right) (Phuong, et al., 2018)

Modified parameter β

According to Herle & Gudehus (1999), the hypoplastic parameter β should be determined by considering two different stiffness moduli at different density states (void ratios) but the same stress level. As mentioned before, the hypoplastic soil model already incorporates the stress-dependency of stiffness, as well as the modified parameter β, which is dependent on the stress level. The stress-dependent behavior of the exponent w (see equation 4.8) and the hypoplastic parameter β are shown in Fig. 44. It can be seen that the parameter β increases up to a peak value at low stress levels and then decreases to negative magnitudes for high stress levels (Phuong, et al., 2018).

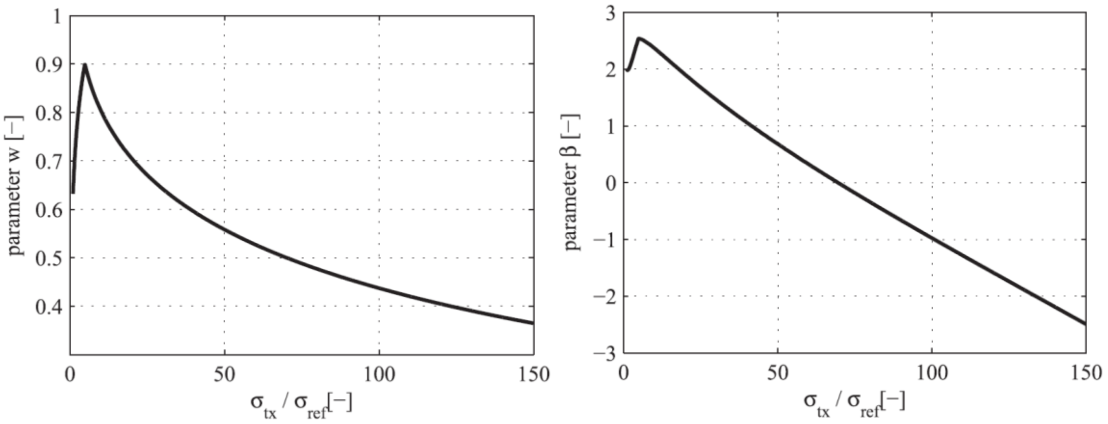

Fig. 44: Stress-dependent behavior of exponent w (left) and the hypoplastic parameter β (right) (Phuong, et al., 2018)

Remarks on the modified hypoplastic soil model

In the modified model, the five parameters, e_{d0}, e_{c0}, e_{i0}, α and β, are stress dependent. Overall, this modified model consists of nine parameters that need to be determined, namely the critical friction angle φ_c, the limit void ratios e_{d0}, e_{c0} and e_{i0}, the granulate hardness h_s, the exponents n and β_{ref}, the uniformity coefficient C_{u0} and the mean grain size d_{50}. C_{u0} and d_{50} are two additional physical parameters, whereas the parameter α can be neglected because it can be directly determined from the stress level. All standard hypoplastic parameters should still be determined as proposed within chapter 3.2.2 (Phuong, et al., 2018).

Application of hypoplastic model for crushable sand within PLAXIS 2D

To apply the hypoplastic model for crushable sand as presented above for geotechnical calculations, it must be correctly used within PLAXIS 2D. Therefore, the dll-file firstly must be copied into the directory of PLAXIS 2D and when adding a new material in PLAXIS the material model has to be set to “User-defined”. If the dll-file was copied into the right directory, the appropriate soil model can be chosen in PLAXIS as seen in Fig. 45.

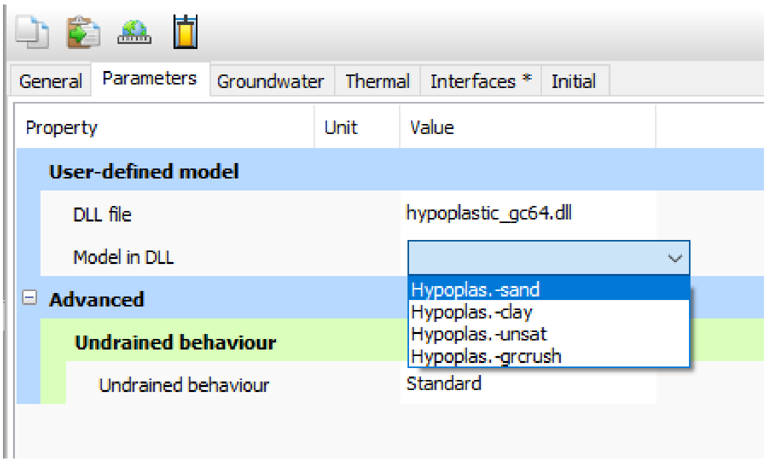

Property	Unit	Value
User-defined model		
DLL file		hypoplastic_gc64.dll
Model in DLL		Hypoplas.-sand Hypoplas.-clay Hypoplas.-unsat Hypoplas.-grcrush
Advanced		
Undrained behaviour		
Undrained behaviour		Standard

Fig. 45: Application of grain crushing model within PLAXIS

The hypoplastic model for crushable sand has to be chosen as “Model in DLL” (“Hypoplas.-gcrush”) and then the parameter tab-sheet looks as follows (see Fig. 46).

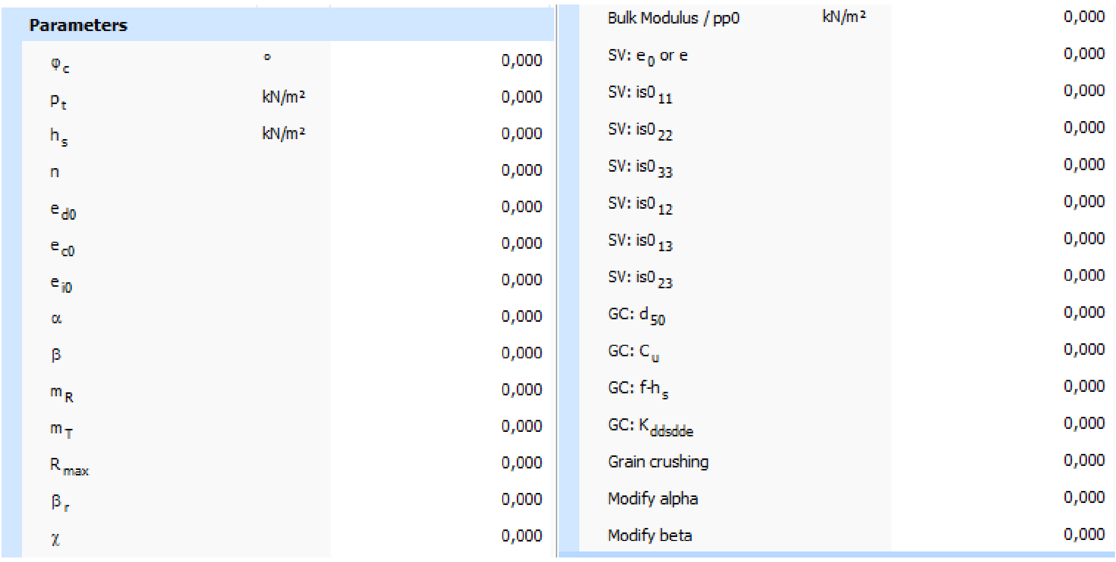

Parameters		
φ_c	°	0,000
p_t	kN/m²	0,000
h_s	kN/m²	0,000
n		0,000
e_{d0}		0,000
e_{c0}		0,000
e_{i0}		0,000
α		0,000
β		0,000
m_R		0,000
m_T		0,000
R_{max}		0,000
β_r		0,000
χ		0,000

Bulk Modulus / pp0	kN/m²	0,000
SV: e_0 or e		0,000
SV: $is0_{11}$		0,000
SV: $is0_{22}$		0,000
SV: $is0_{33}$		0,000
SV: $is0_{12}$		0,000
SV: $is0_{13}$		0,000
SV: $is0_{23}$		0,000
GC: d_{50}		0,000
GC: C_u		0,000
GC: $f\text{-}h_s$		0,000
GC: K_{ddsdde}		0,000
Grain crushing		0,000
Modify alpha		0,000
Modify beta		0,000

Fig. 46: Parameter tab-sheet of hypoplastic model for crushable sand

As Fig. 46 shows, most of the parameters are the same as for the original hypoplastic soil model according to Von Wolffersdorff (1996) however, the new parameters have to applied as follows (Phuong, 2018):

- all eight original hypoplastic parameters has to be taken the same magnitude as for the original hypoplastic soil model
- the d_{50} is the mean grain size of the material and has to added in [mm]
- for the C_u the reference value of the uniformity coefficient C_{u0} has to be taken

- the parameter f-h_s and K_{ddsdde} are not considered in this modified hypoplastic soil model
- the parameters "Grain crushing", "Modify alpha" and "Modify beta" are all set to 1 to be activated and to take into account their pressure-dependency

With the new parameters d_{50} and C_{u0} this soil model takes the pressure dependency of the parameters e_d, e_c, e_i, α and β into account. In the next chapter the triaxial response of two materials is shown for once applying the original hypoplastic model and once for the application of the grain crushing model.

4.3.3 Application of grain crushing model – triaxial response

In this chapter triaxial compression tests are performed (modelled) using Hostun sand and Toyoura sand with the appropriate parameters given in Tab. 14. To see the influence of considering the pressure dependency of the single parameters, at first a triaxial compression test with an initial cell pressure of 10 MPa is performed for the Hostun sand by a stepwise application of the grain crushing model. Thus, at the beginning only the "grain crushing" is activated to only consider the pressure dependency of the void ratios (e_d, e_c and e_i) followed by also activating "modify alpha" to take also the pressure dependency of the parameter α into account. Finally, also "modify beta" is activated to consider the pressure dependency of β. The results (see Fig. 47) are compared to the curves obtained from the application of the original hypoplastic model and test results from Colliat-Dangus et al. (1988).

Tab. 14: Hypoplastic parameters for Hostun sand and Toyoura sand

Material	φ_c [°]	h_s $[MPa]$	n [-]	e_{d0} [-]	e_{c0} [-]	e_{i0} [-]	α [-]	β [-]	C_{u0} [-]	d_{50} [mm]
Hostun sand	32	1000	0.29	0.61	0.96	1.09	0.13	2.0	1.69	0.32
Toyoura sand	32	120	0.69	0.61	0.98	1.13	0.12	1.0	1.50	0.23

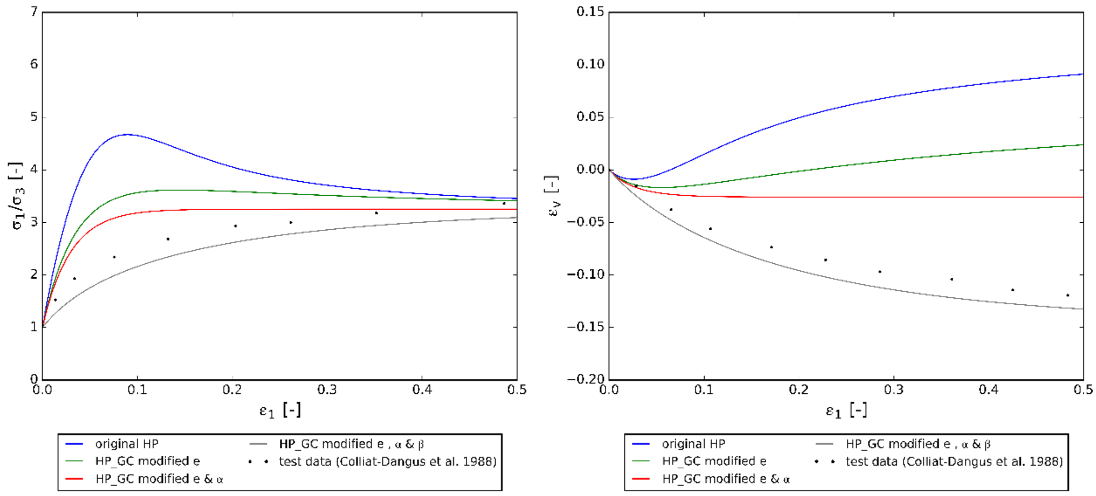

Fig. 47: Triaxial response of Hostun sand at an initial cell pressure of 10 MPa and a relative density of $I_D = 0.9$ (stress ratio vs axial strain (left) and volumetric strain vs axial strain (right))

In Fig. 47 it can be seen, that at a cell pressure of 10 MPa the original hypoplastic model predicts too high peak friction angle and too much dilatancy compared to the laboratory results. With each modification of the hypoplastic model (e, α and β) the obtained results match better with the laboratory test results.

In the following for both materials from Tab. 14 several triaxial tests with different initial cell pressures were performed and compared to laboratory test results. The laboratory test results for Hostun sand (Colliat-Dangus, et al., 1988) are shown in Fig. 48 and the ones for Toyoura sand (Miura & Yamanouchi, 1973) can be seen in Fig. 51. The results obtained from the application of the original hypoplastic model (Von Wolffersdorff, 1996) as well as the hypoplastic model for crushable sand (Phuong, et al., 2018) are presented in Fig. 49 and Fig. 50 for Hostun sand and for Toyoura sand see Fig. 52 and Fig. 53.

Triaxial response of Hostun sand at different initial cell pressures and a relative density of $I_D = 0.9$

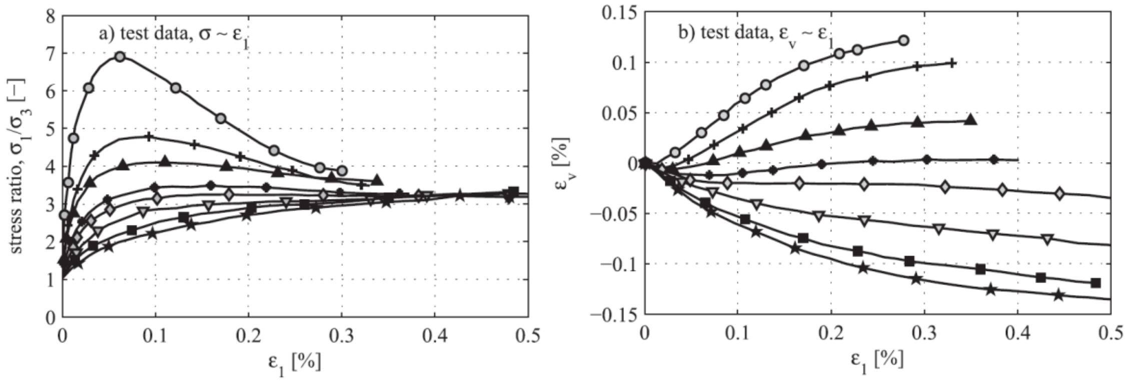

Fig. 48: test data - stress ratio vs axial strain (left) and volumetric strain vs axial strain (right) (Phuong, et al., 2018)

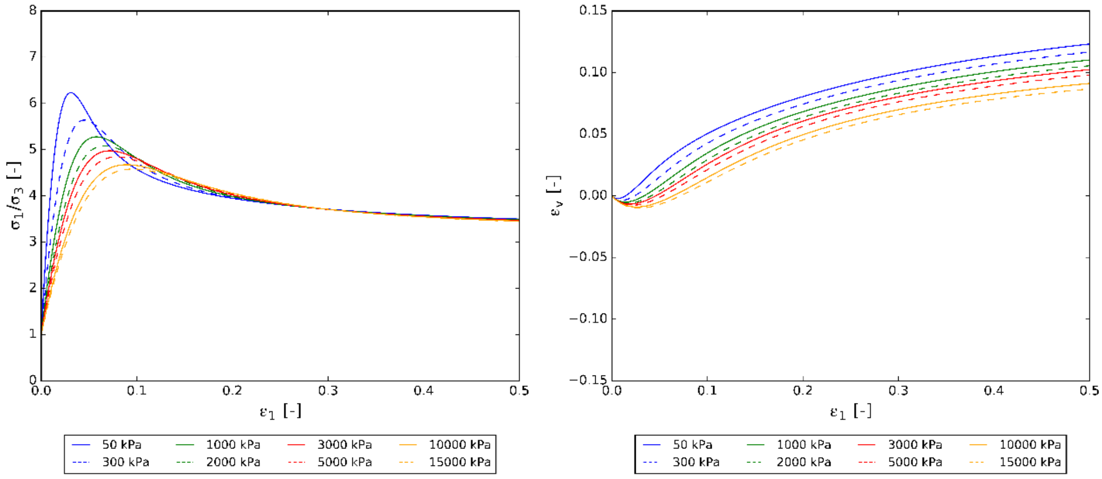

Fig. 49: PLAXIS Soil Test tool original hypoplastic model - stress ratio vs axial strain (left) and volumetric strain vs axial strain (right)

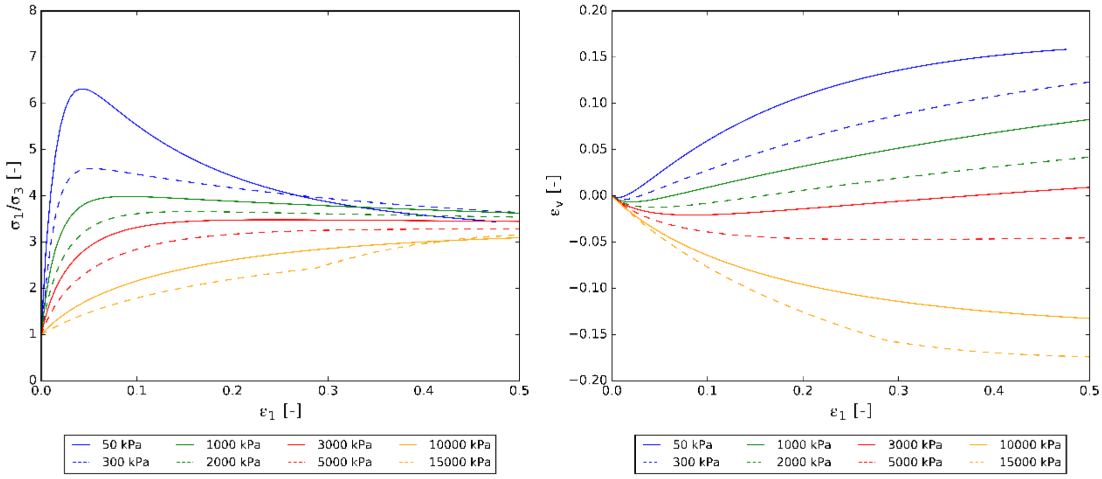

Fig. 50: PLAXIS Soil Test tool grain crushing model - stress ratio vs axial strain (left) and volumetric strain vs axial strain (right)

Triaxial response of Toyoura sand at different initial cell pressures and a relative density of $I_D = 0.97$

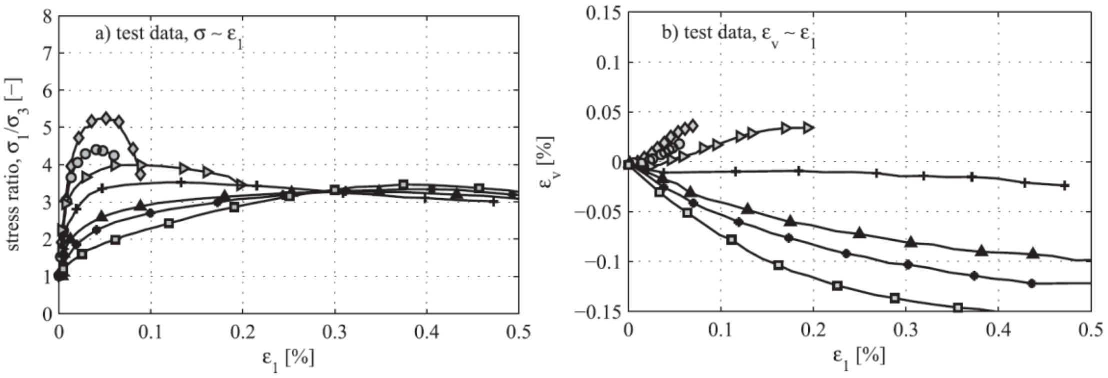

Fig. 51: test data - stress ratio vs axial strain (left) and volumetric strain vs axial strain (right) (Phuong, et al., 2018)

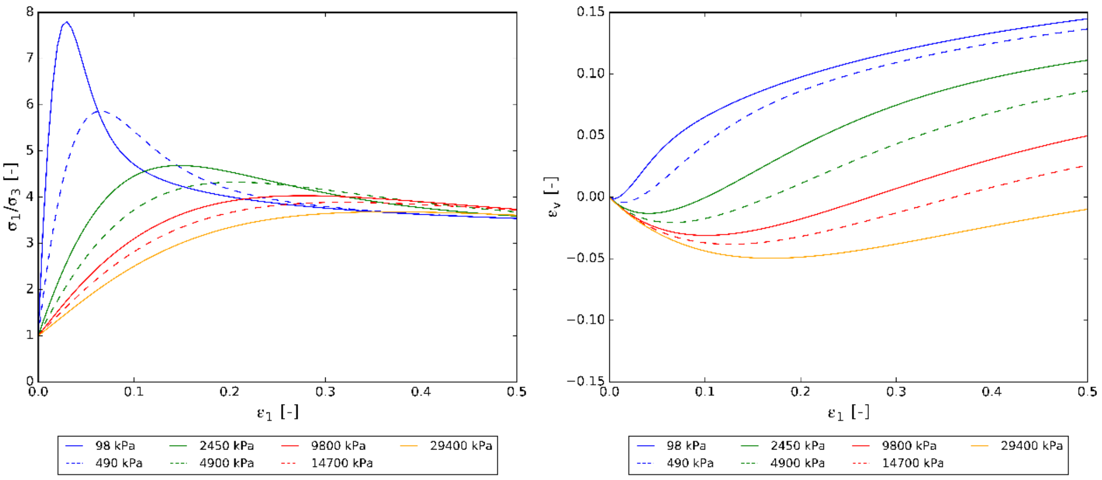

Fig. 52: PLAXIS Soil Test tool original hypoplastic model - stress ratio vs axial strain (left) and volumetric strain vs axial strain (right)

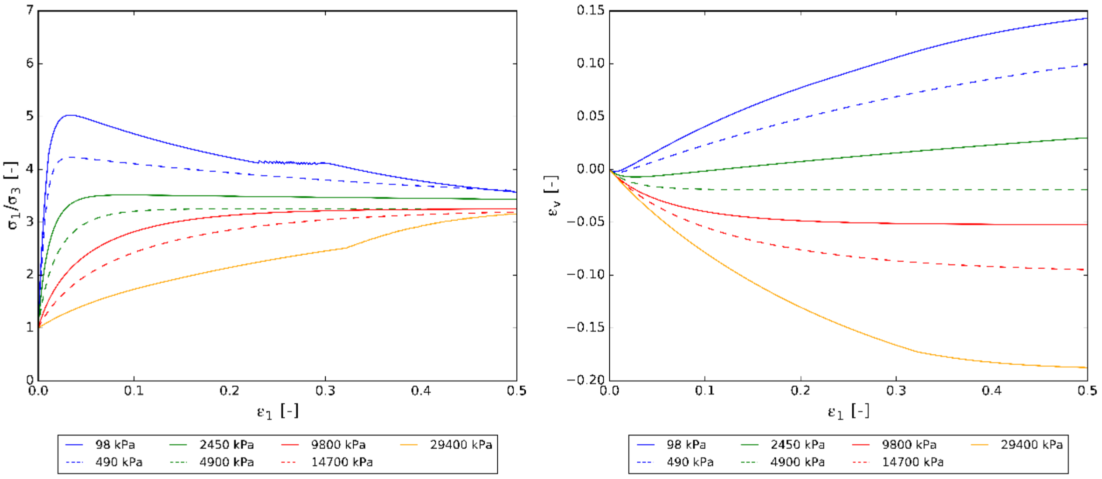

Fig. 53: PLAXIS Soil Test tool grain crushing model - stress ratio vs axial strain (left) and volumetric strain vs axial strain (right)

When applying the original hypoplastic model according to Von Wolffersdorff (1996) (see Fig. 49 and Fig. 52) no contractive behavior can be observed even at very high cell pressures. Furthermore, applying a constant α-value leads to an overestimation of the peak friction angle. In contrast, the results obtained from applying the hypoplastic model for crushable sand (see Fig. 50 and Fig. 53) show a much softer soil stiffness response which is similar to the test data (see Fig. 48 and Fig. 51).

During the performance of triaxial compression tests some problems occurred for Hostun sand at an initial cell pressure of 15 MPa (see Fig. 50 (left)) and for Toyoura sand at initial cell pressures of 98 kPa and 29.4 MPa (see Fig. 53 (left)). Therefore, the next chapter deals with the problems of this grain crushing model at very high pressures.

4.3.4 Problems with actual grain crushing dll-file

Based on a correspondence with Phuong Nguyen (main author of paper related to grain crushing model) it was concluded, that she had the same problems at very high pressures and therefore she adapted the code a little bit. The latest version of the code Phuong used to apply the grain crushing model is unfortunately not available anymore and thus, the dll-file applied within this thesis must be adapted. The change of the code could not be done within the framework of this thesis. This improvement is an important issue of further research (see chapter 8.2).

According to Phuong the problems occurred because at high pressures sometimes the calculated current void ratio (based on the current stress level) is smaller than the minimum void ratio which further causes incorrect α-values. To investigate the stress level from which on the problems occur, two materials of Tab. 14 and one carbonate sand (see Tab. 15) were used for further triaxial compression tests on only high pressures were performed (see Fig. 54 to Fig. 56).

Tab. 15: Parameters for a carbonate sand

Material	φ_c [°]	h_s $[MPa]$	n [-]	e_{d0} [-]	e_{c0} [-]	e_{i0} [-]	α [-]	β [-]	C_{u0} [-]	d_{50} [mm]
Carbonate sand	36.3	39	0.53	0.74	1.26	1.45	0.05	1.97	4.0	0.63

Triaxial response of Hostun sand at different initial cell pressures and a relative density of I_D = 0.9

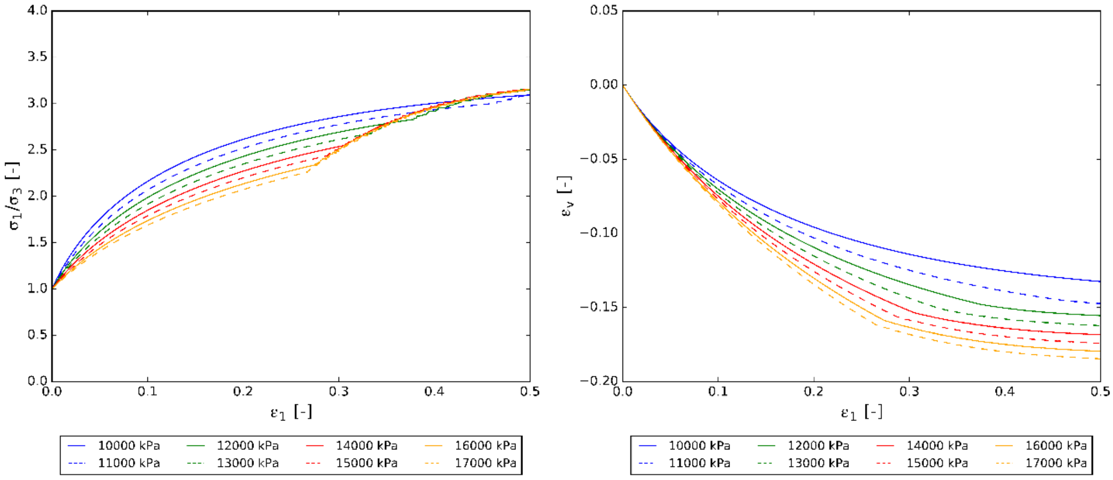

Fig. 54: PLAXIS Soil Test tool grain crushing model - stress ratio vs axial strain (left) and volumetric strain vs axial strain (right)

Triaxial response of Toyoura sand at different initial cell pressures and a relative density of I_D = 0.97

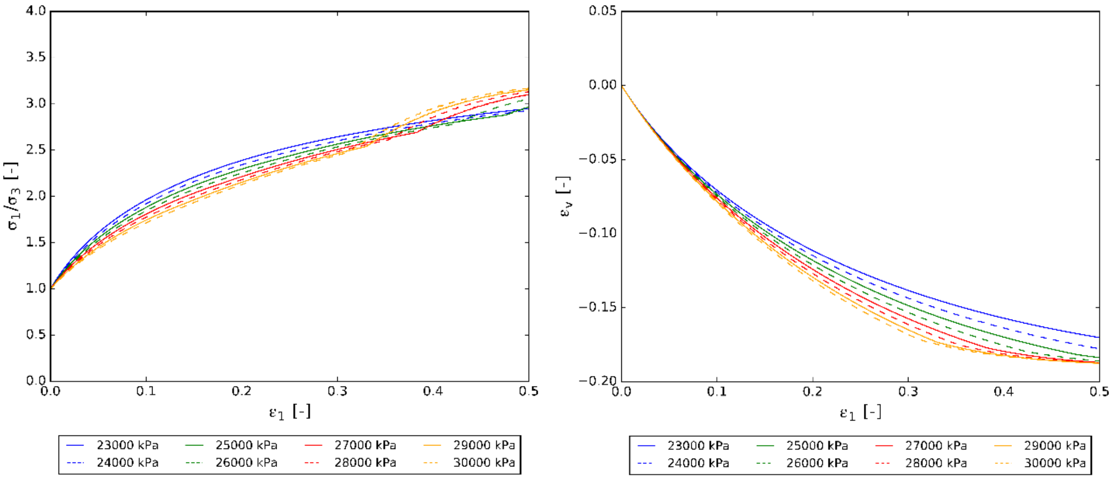

Fig. 55: PLAXIS Soil Test tool grain crushing model - stress ratio vs axial strain (left) and volumetric strain vs axial strain (right)

Triaxial response of carbonate sand at different initial cell pressures and a relative density of I_D = 0.9

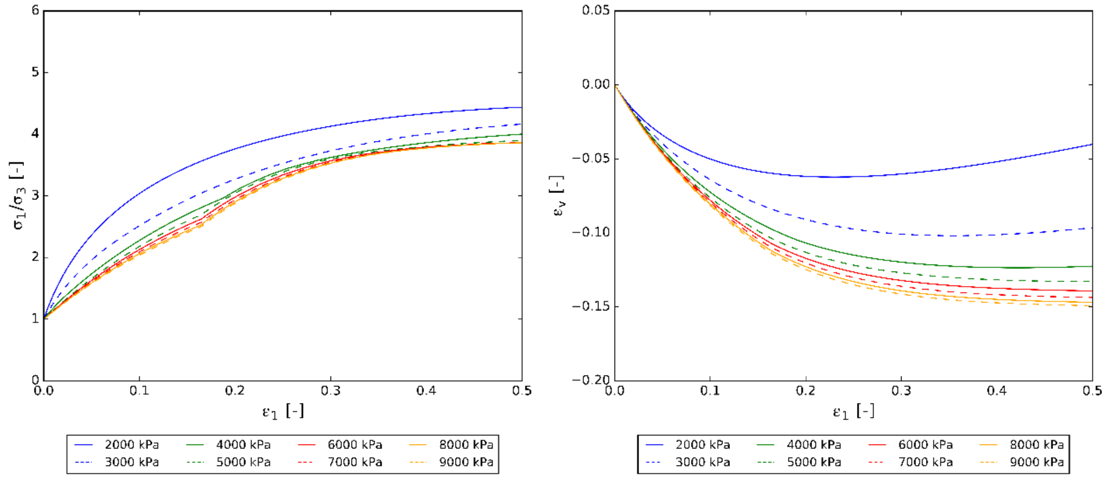

Fig. 56: PLAXIS Soil Test tool grain crushing model - stress ratio vs axial strain (left) and volumetric strain vs axial strain (right)

From Fig. 54 to Fig. 56 it can be seen, that stress level from which on problems start to occur are very different. For Hostun sand the problems start at an initial cell pressure of 11 MPa, for Toyoura sand at 25 MPa at for the given carbonate sand sample already at 4 MPa. It also can be seen, that the kink in the obtained curves occurs for the carbonate sand sample at a much lower strain than for the silica sands (Hostun and Toyoura). Thereby, it has to be stated that the grain crushing model was developed on the basis of soil tests performed on only silica sands. However, the performance of the grain crushing model applied for calcareous sand is presented in chapter 6.5 where a full KIM analysis is performed once on the basis of the original hypoplastic soil model and once on the basis of the hypoplastic model for crushable sand.

5 Spherical cavity expansion

This chapter focuses on the finite element model in order to solve the spherical cavity expansion problem, using both a hypoplastic and an elasto-plastic constitutive soil model. First, the final FE model, proposed by Winkler (2018), is presented, along with all of its characteristics. This is followed by additional investigations regarding different boundary conditions and the influence of applying different calculation phases. Additionally, this chapter investigates the sensitivity of soil parameters on the results of a spherical cavity expansion analysis and comprises a model verification, where computed results are compared with closed form solutions.

5.1 Final PLAXIS model

In accordance with several studies that Winkler (2018) performed to investigate the influence of different settings, the improved FE model presented within this chapter was applied for all calculations of the spherical cavity expansion problem.

Firstly, an axisymmetric model type was used with 15-noded elements. The model's dimension included a width of b = 20 m and a height of h = 41 m (incorporating a 1 m surcharge layer) in combination with the deformation boundaries y_{min} and y_{max} set to "fully fixed" and x_{min} and x_{max} set to "normally fixed". Moreover, different deformation boundaries are investigated in chapter 5.1.1. The initial radius of the cavity was considered with $a_0 = 0.1$ m, and two concentric half circles around the cavity were added for a finer mesh generation (Winkler, 2018).

The final FE model has, in total, 740 elements and includes a 4-element discretization of the cavity. The chosen nodes and stress points for the output were taken as proposed by Xu (2007). In Fig. 57, the model dimensions, as well as the final mesh, are shown, and Fig. 58 shows the mesh discretization around and within the cavity including the selected output nodes (A to I) and stress points (K to T) (Winkler, 2018).

Independent from the material applied to the continuum, the cavity and the surcharge layer are modeled with the linear-elastic constitutive soil model and the parameter given in Tab. 16 (Winkler, 2018).

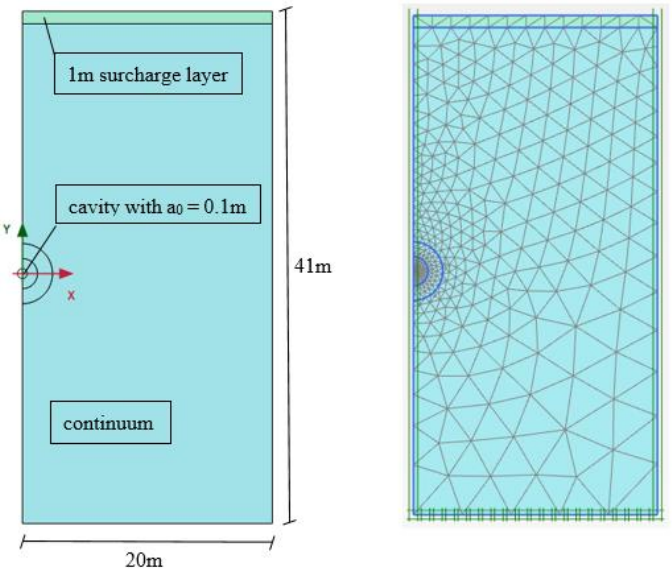

Fig. 57: Model dimensions (left) and final mesh (right) of improved FE model

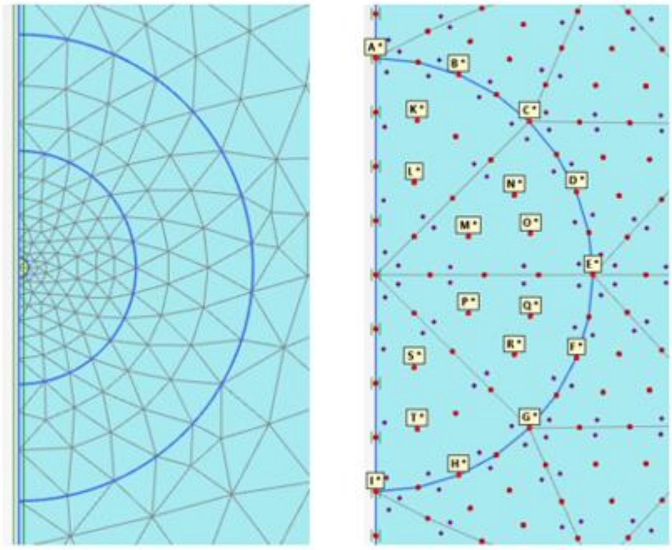

Fig. 58: Mesh discretization around and within the cavity (left), including the selected output nodes and stress points (right)

Tab. 16: Proposed cavity and surcharge layer materials of improved FE model (Winkler, 2018)

Material	Soil parameters			Constitutive model
Cavity	E'	1/5 continuum E	[kPa]	Linear elastic
	ν	0.0	[-]	
	γ'	0.0	[kN/m^3]	
	K_0	1.0	[-]	
Surcharge layer	E'	20,000	[kPa]	Linear elastic
	ν	0.2	[-]	

The initial stress state is generated by applying the K_0 procedure within the initial phase, and, for the first calculation phase, the option to reset displacements to zero is selected. As shown in Fig. 59, the updated mesh option is selected, the arch-length control is deselected, the number of maximum steps is chosen with the maximum value of 1,000 and the maximum load fraction per step was decreased to 0.05. All of this was done for all phases. The magnitudes of volumetric strains applied to the cavity for the different calculation phases are discussed in chapter 5.3 (Winkler, 2018).

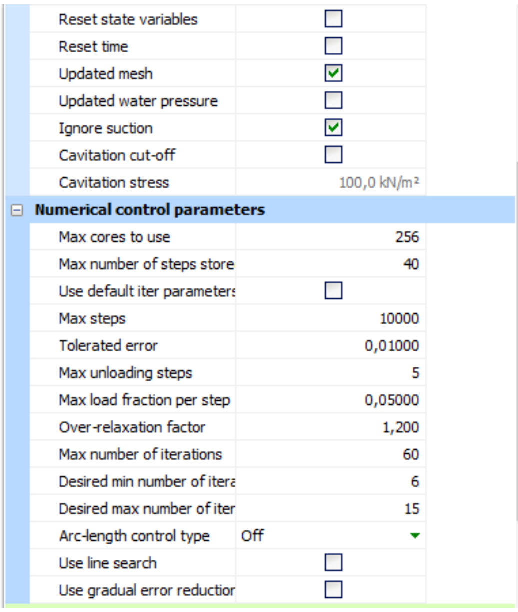

Reset state variables	☐
Reset time	☐
Updated mesh	☑
Updated water pressure	☐
Ignore suction	☑
Cavitation cut-off	☐
Cavitation stress	100,0 kN/m²
Numerical control parameters	
Max cores to use	256
Max number of steps store	40
Use default iter parameters	☐
Max steps	10000
Tolerated error	0,01000
Max unloading steps	5
Max load fraction per step	0,05000
Over-relaxation factor	1,200
Max number of iterations	60
Desired min number of itera	6
Desired max number of iter	15
Arc-length control type	Off
Use line search	☐
Use gradual error reductior	☐

Fig. 59: Proposed settings for calculation phases

5.1.1 Influence of different boundary conditions

As a result of several finite element analyses of the spherical cavity expansion problem that were performed, Winkler (2018) proposed to choose the deformation boundaries as follows:

- x_{min} & x_{max} normally fixed
- y_{min} & y_{max} fully fixed

This chapter aims to show how changing the boundary conditions (applying load boundary conditions) will influence the results of the spherical cavity expansion using the material set MC 1 from Tab. 18. Therefore, all deformation boundaries (x_{min}, y_{min}, x_{max} & y_{max}) were set to “free”, and two line loads, dependent on the applied lateral earth pressure coefficient and the initial stress field (see chapter 5.6), were created, as shown in Fig. 60.

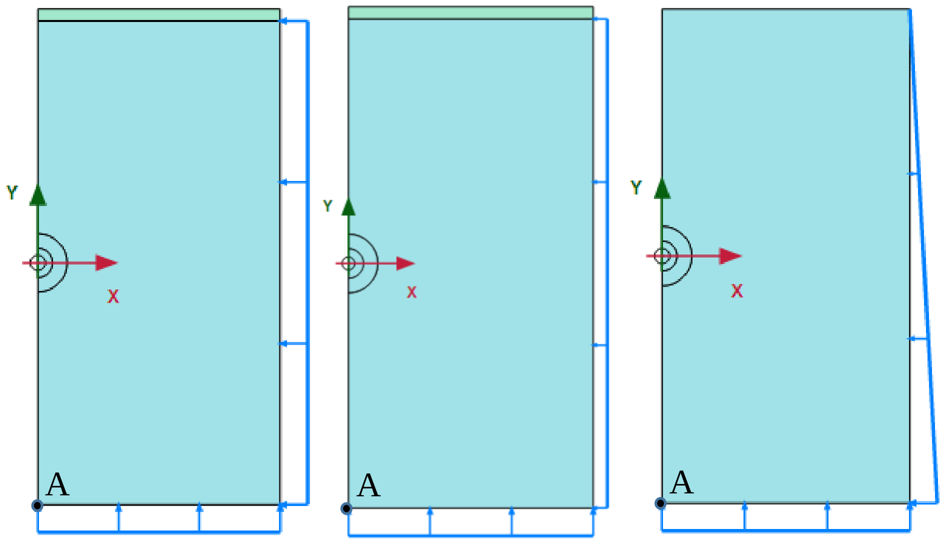

Fig. 60: Load boundary conditions for $K_0 = 1.0$ / uniform (left), $K_0 = 0.5$ / uniform (middle) and $K_0 = 1.0$ / non-uniform (right)

Because of the application of only the load boundary conditions (with all deformation boundaries set to “free”), as illustrated in Fig. 60, several numerical problems occurred during the finite element analyses. To solve that issue, a fixed point at the symmetry axis (A) was defined. By fixing point A, a point displacement was created, which enables three different settings (free, fixed and prescribed) in both the x- and y-directions. At first, prescribed displacements with $|u| = 0\ m$ in both directions (x & y) were applied, followed by changing the point displacement in the x-direction to “free” and keeping the prescribed displacement with $|u| = 0\ m$ for the y-direction. In order to see if there is a difference between the different boundary conditions, the initial stress state $(p', \sigma_1' \ \& \ \sigma_3')$, the final deformations, the final stresses $(p', q \ \& \ \sigma_1')$ and the pressure expansion curves are plotted for both situations. The denotation for the different applied boundary conditions within the following figures is given in Tab. 17.

Tab. 17: Denotations for different analyzed boundary conditions

denotation	deformation boundaries	point displacements A
boundary condition 1	x_{min}, x_{max} normally fixed y_{min}, y_{max} fully fixes	-
boundary condition 2	x_{min}, x_{max}, y_{min} & y_{max} free	both prescribed: u_x and $u_y = 0$ m
boundary condition 3		x-direction free and y-direction prescribed: $u_y = 0$ m

Initial stress conditions (p', σ_1' & σ_3') for K₀ = 1.0 / uniform

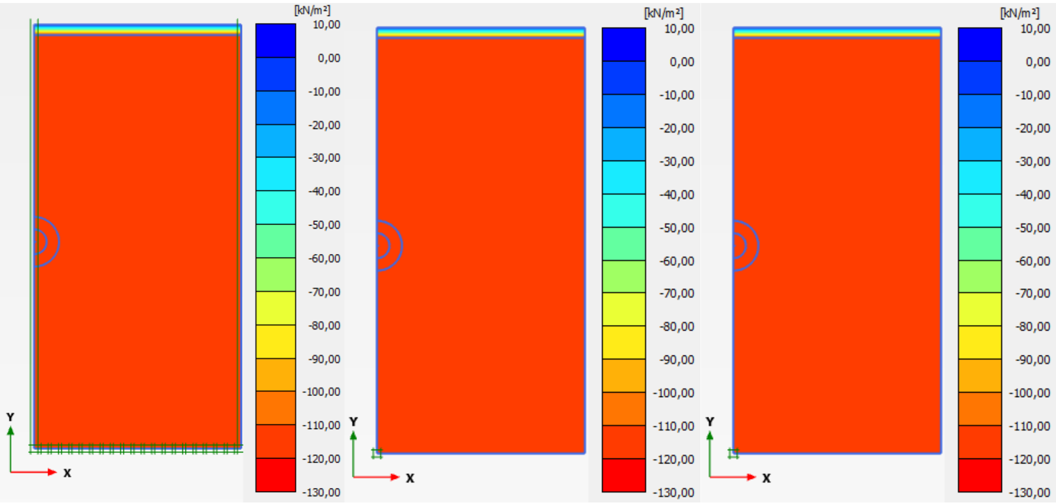

Fig. 61: Initial stress situation (p', σ_1' & σ_3') for boundary condition 1 (left), boundary condition 2 (middle) and boundary condition 3 (right)

Final stresses (p', q & σ_1') and deformations ($|u|$) for K₀ = 1.0 / uniform

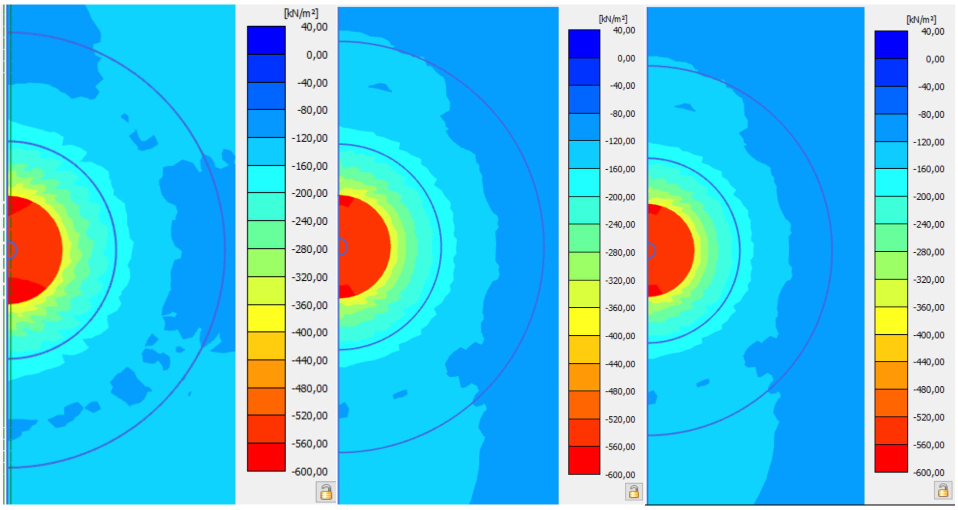

Fig. 62: Final p' for boundary condition 1 (left), boundary condition 2 (middle) and boundary condition 3 (right)

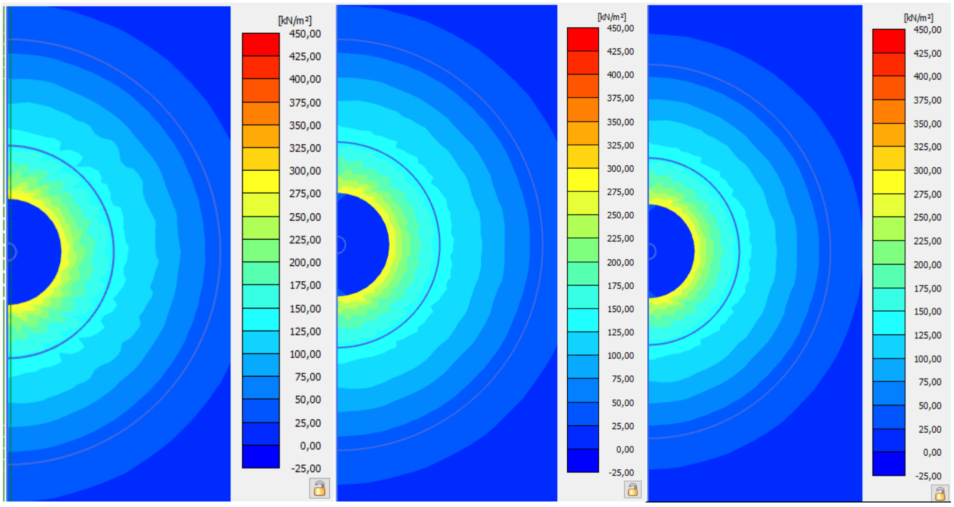

Fig. 63: Final q for boundary condition 1 (left), boundary condition 2 (middle) and boundary condition 3 (right)

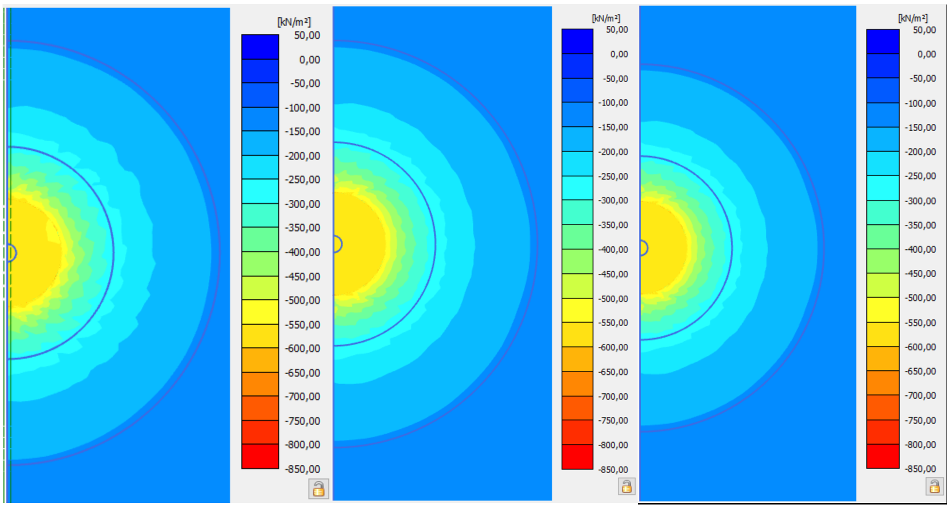

Fig. 64: Final $\sigma_1{}'$ for boundary condition 1 (left), boundary condition 2 (middle) and boundary condition 3 (right)

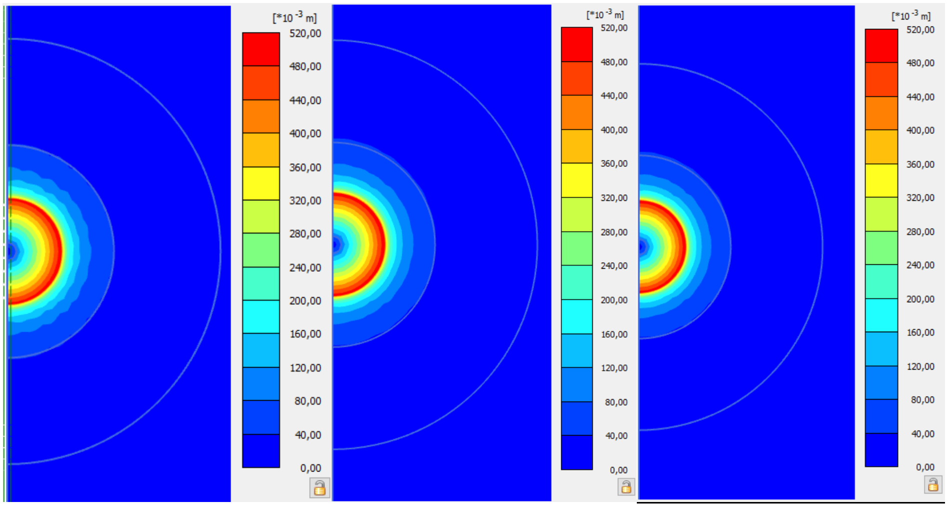

Fig. 65: Final $|u|$ for boundary condition 1 (left), boundary condition 2 (middle) and boundary condition 3 (right)

Pressure-expansion curves for K_0 = 1.0 / uniform

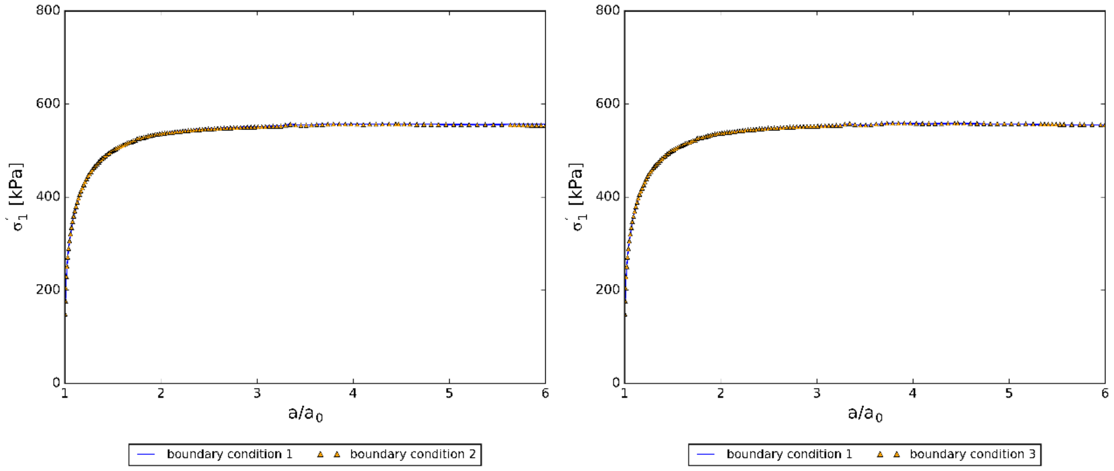

Fig. 66: Pressure-expansion curves for boundary condition 2 (left) and boundary condition 3 (right) compared to boundary condition 1

The results presented from Fig. 61 to Fig. 66 show that there is no difference between the applied boundary conditions. It must be mentioned that there is no difference between applying a point displacement as "prescribed" with $|u| = 0\ m$ and applying a point displacement as "fixed". Furthermore, it is irrelevant if the fixed point is on the lower end of the symmetry axis or anywhere else on the symmetry axis. The same results were obtained for the other two investigated scenarios (K_0 = 0.5 and K_0 = 1.0 / non-uniform). The results for K_0 = 1.0 / non-uniform are given within appendix B.

5.2 Necessity of averaging process

Preliminary studies showed that the flow rule (when using elasto-plastic constitutive soil models) has a significant influence on the results of the finite element analysis. Different from the application of an associated flow rule, the application of a non-associated flow results in slightly non-uniform deformation behavior of the cavity. Winkler (2018) already showed that averaging the received pressure-expansion curves delivers satisfying results when compared with the closed-form solution of Yu & Houlsby (1991). The arrangement of the nodes (A to I) and stress points (K to T) of the finite element model, which are used for the averaging procedure, are already shown in Fig. 58 (right) (Winkler, 2018).

To visualize the resulting pressure-expansion curves, principle effective stresses $\sigma_1{}'$ are plotted against the normalized deformations (a/a_0) of the sphere. The results of the spherical cavity expansion (as illustrated in Fig. 67) show the stresses ($\sigma_1{}'$) for each stress point (K to T) as consequences of the normalized deformations a/a_0 of the related nodes (A to I).

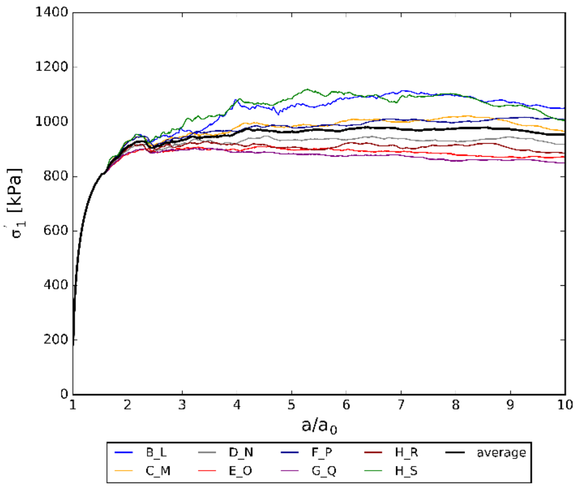

Fig. 67: Pressure-expansion curves for all output nodes and stress points including the averaged solution (MC 3 material set and non-associated flow rule with $\psi = 0$ °)

The studies to investigate the averaging procedure of the SCE results were performed with material set MC 3 of Tab. 18. The results showed (when using the MC 3 material with a non-associated flow rule) high scattering of the pressure-expansion curves of the output nodes and stress points. On the contrary, applying an associated flow rule with $\psi = 30$ ° results in a uniform deformation behavior of all nodes and stress points. Hence, when applying a non-associated flow rule, an averaging process is required. The resulting averaged $\sigma_1{}'$- a/a$_0$ curve and the computed results from the different pairs of nodes and stress points (e.g. A & K) can be seen in Fig. 67.

Based on numerical investigations, Winkler (2018) further suggested the exclusion of the results of the southern- and northern-most selected nodes (A and I) and stress points (K and T). This approach can be confirmed by comparing the averaged $\sigma_1{}'$- a/a$_0$ curves using all nodes and stress points and the averaged solution with the results of the closed-form solution of Yu & Houlsby (1991) (see Fig. 68), where the nodes (A and I) and the stress points (K and T) are neglected.

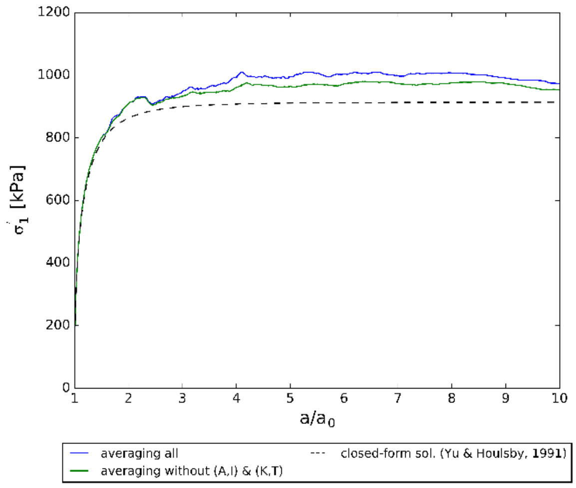

Fig. 68: Average approaches and closed-form solution (Yu & Houlsby, 1991) (MC 3 material set and non-associated flow rule with $\psi = 0°$)

5.3 Studies regarding the calculation phases

In the following, the influence of the calculation procedure (different volumetric strains applied inside the cavity) on the resulting limit pressure, applying different soil models, materials and initial stress situations, is investigated. For each of the three constitutive soil models, Mohr-Coulomb (MC), Hardening Soil (HS) (Schanz, et al., 1996) and hypoplastic soil model (HP) (Von Wolffersdorff, 1996), one example of the resulting pressure-expansion curves is shown for various applied volumetric strains. The used input parameters for the FEA are given within every figure (Fig. 69 and Fig. 70). The value within the brackets shows the applied volumetric strain inside the cavity, and the number of applied calculation phases differs between the applied volumetric strains and the different constitutive soil models.

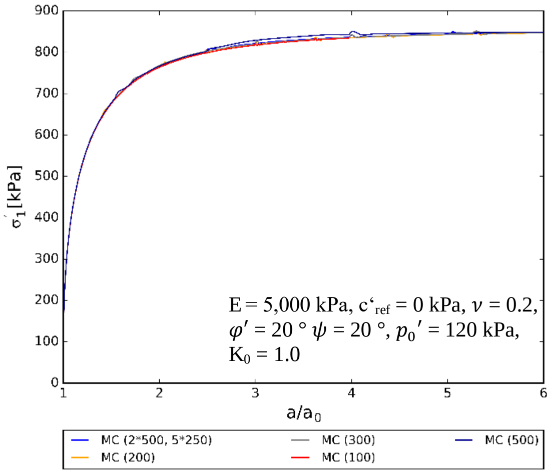

Fig. 69: Pressure-expansion curves (MC soil model) for different calculation procedures (applied volumetric strains)

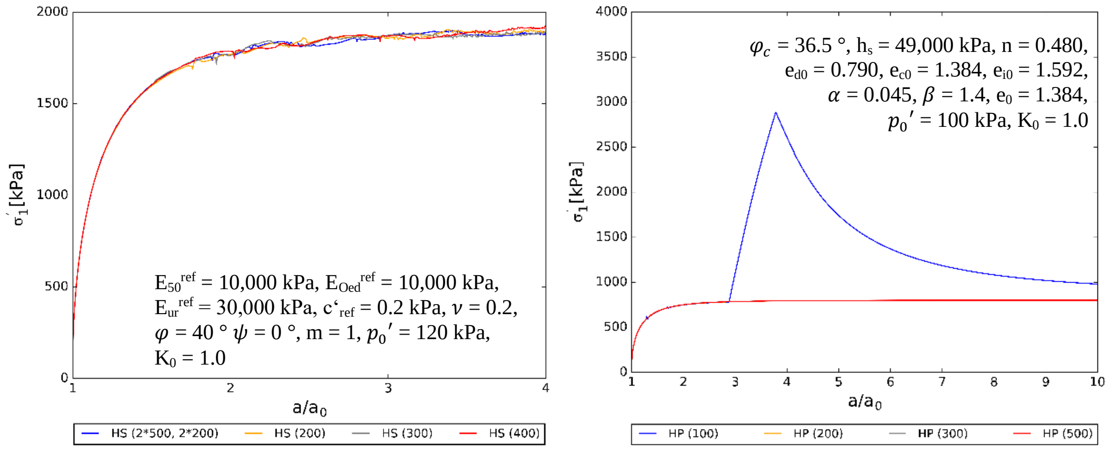

Fig. 70: Pressure-expansion curves (HS left and HP right) for different calculation procedures (applied volumetric strains)

Fig. 69 and Fig. 70 clearly show that there is almost no difference between the curves. One exception, which was found during these studies is that the application of the hypoplastic soil model shows problems, when for all calculation phases, a volumetric strain of 100% was applied inside the cavity. However, it must be mentioned that for low initial stress states ($p'_0 = 25\ kPa$), no problems occurred with an applied volumetric strain of 100%. Thus, independent from the applied constitutive soil model, it can be concluded that the numerical model is very robust. Based on the studies, it is recommended to apply volumetric strains between 300% and 400% for each calculation phase. Applying too small volumetric strains may cause numerical problems (see Fig. 70 right) and require a higher number of calculation phases. Similarly, applying too high volumetric strains may also cause numerical problems and cause the simulations to abort.

5.4 Model verification

The materials shown in Tab. 18 and Tab. 19 were used for the following investigations regarding the performance of the FE model to solve the spherical cavity expansion problem. For all Mohr-Coulomb materials of Tab. 18, an effective cohesion of $c' = 0kPa$ and a Poisson's ratio of $\nu = 0.2$ were defined, and for the Hardening Soil material sets of Tab. 19, $c' = 0.2\ kPa$ and $\nu = 0.2$ were used.

Tab. 18: Material parameters for Mohr-Coulomb material

Material	E [kPa]	φ' [°]	ψ [°]	K_0 [-]	p'_0[kPa]
MC 1	5,000	20	[0, 20]	1.0	120
MC 2	10,000	42	[0, 5, 12, 17]	1.0	120
MC 3	25,000	30	[0, 30]	1.0	50

Tab. 19: Material parameters for Hardening Soil material

Material	HS 1	HS 2	HS 3	HS 4
E_{50}^{red} [MPa]	10	50	50	30
E_{ur}^{ref} [MPa]	30	150	150	90
E_{Oed}^{ref} [MPa]	10	50	50	30
φ' [°]	40	20	40	33
ψ [°]	0	0	10	3
m [-]	1	1	0.5	1
e_{min} [-]	0.49	0.49	0.49	0.49
e_{max} [-]	0.78	0.78	0.78	0.78
e_{init} [-]	0.68	0.68	0.5	0.68

To verify the performance of the improved FE model solutions, curves found in literature were taken as reference. Therefore, the solutions obtained by applying the Mohr-Coulomb model were verified with the closed-form solution of Yu & Houlsby (1991), and for the FEA with the Hardening Soil model, the solutions from Xu (2007) were taken as references. Winkler (2018) implemented the analytical solution (Yu & Houlsby, 1991) with Matlab to obtain the resulting pressure-expansion curves. A big advantage of this closed-form solution is that it allows one to consider different magnitudes of the dilatancy angle, thus accounting for non-associated plasticity.

Mohr-Coulomb model

For the verification of the FEA applying the Mohr-Coulomb soil model, the pressure-expansion curves obtained from the finite element analysis and the closed form solution were illustrated for all Mohr-Coulomb material sets shown in Tab. 18. For each material set, a dilatancy angle of $\psi = 0°$ was applied to consider non-associated plasticity. From Fig. 71 and Fig. 72, it can be concluded that the solutions obtained from the improved finite element model are in agreement with the closed-form solution.

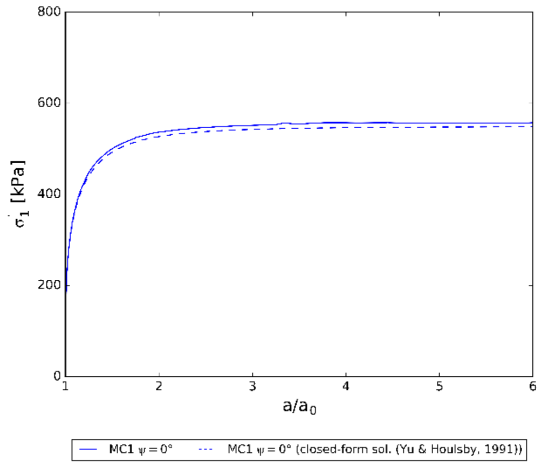

Fig. 71: Pressure-expansion curves (MC 1 material set) of FEA and closed-form solution (Yu & Houlsby, 1991)

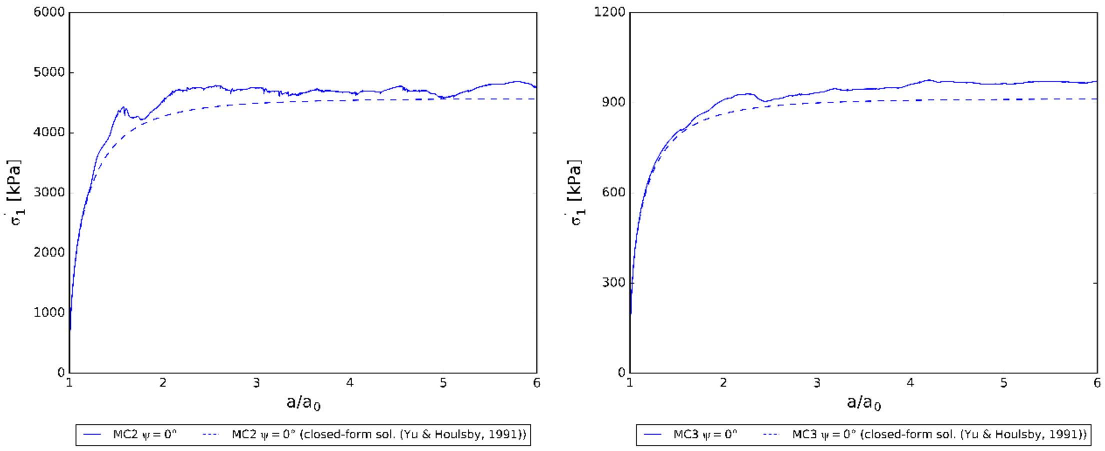

Fig. 72: Pressure-expansion curves for MC 2 (left) and MC 3 (right) of FEA and closed-form solution (Yu & Houlsby, 1991)

Hardening Soil model

For the verification of the FE model applying the Hardening Soil model, results from literature (Xu, 2007) were taken and compared to the results obtained from the FEA of the Hardening Soil parameter sets of Tab. 19. For the finite element analyses, a lateral earth pressure coefficient of $K_0 = 1.0$ and an initial effective mean pressure of $p'_0 = 120kPa$ were considered. For all investigated materials, the obtained results are in agreement with the results from Xu (2007) (see Fig. 73 and Fig. 74).

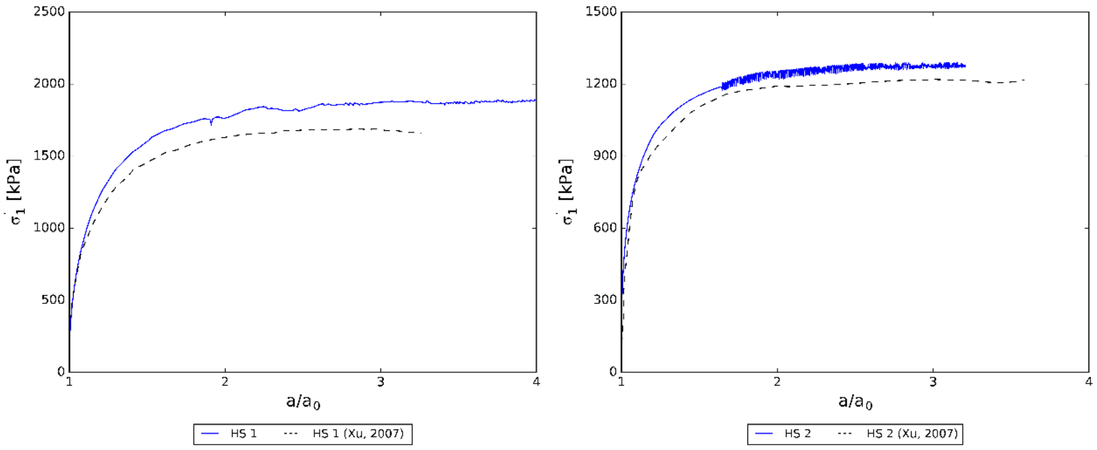

Fig. 73: Pressure-expansion curves for HS 1 (left) and HS 2 (right) of FEA and results from Xu (2007)

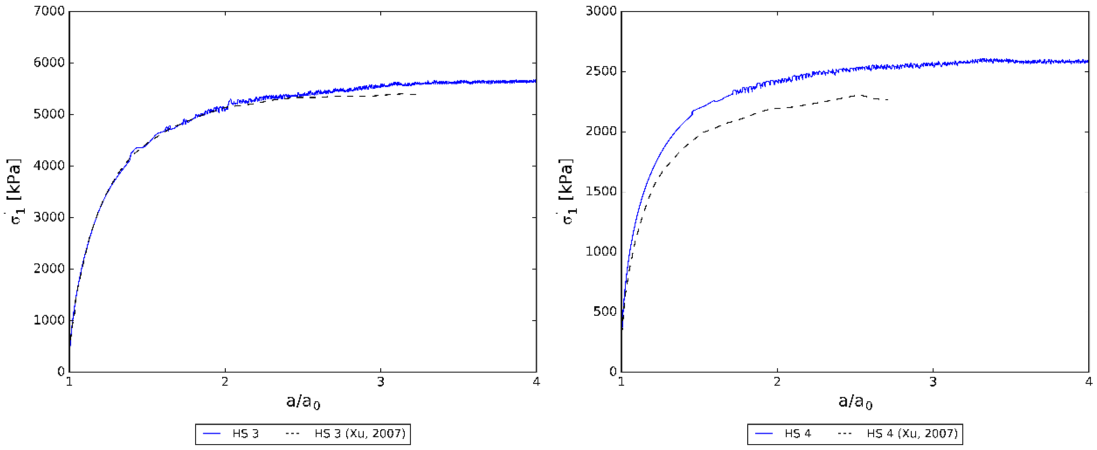

Fig. 74: Pressure-expansion curves for HS 3 (left) and HS 4 (right) of FEA and results from Xu (2007)

Numerical studies confirmed that the problem of the continuous increase of the limit pressure p_{LS} during the spherical cavity expansion process (see FEA with associated plasticity in Fig. 78 (right)) can be controlled by use of a dilatancy-cut-off, as available in the Hardening Soil model. This option sets the mobilized dilatancy angle ψ_m to zero at the point where the maximum void ratio e_{max} (which is an input parameter) is reached. But, it must be mentioned that the change of void ratio e is related to the change of volumetric strain ε_v (see equation (5.1)). A schematical representation of the dilatancy-cut-off can be seen in Fig. 75 (Brinkgreve, et al., 2010). The necessity of selecting the dilatancy-cut-off when using the Hardening Soil model for a proper determination of the limit pressure p_{LS} can be seen in Fig. 76, which shows that with the application of the dilatancy-cut-off, the pressure-expansion curves will become horizontal for large values of a/a_0, hence a clear limit pressure is computed.

$$-(\varepsilon_v - \varepsilon_v^{init}) = ln\left(\frac{1-e}{1+e_{init}}\right) \tag{5.1}$$

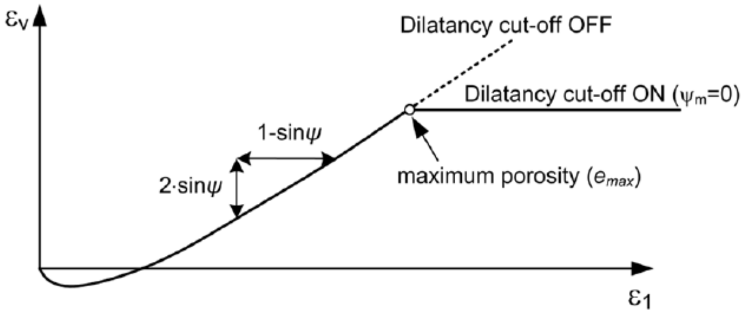

Fig. 75: Dilatancy-cut-off principle of the HS model (Brinkgreve, et al., 2010; Tschuchnigg, 2012)

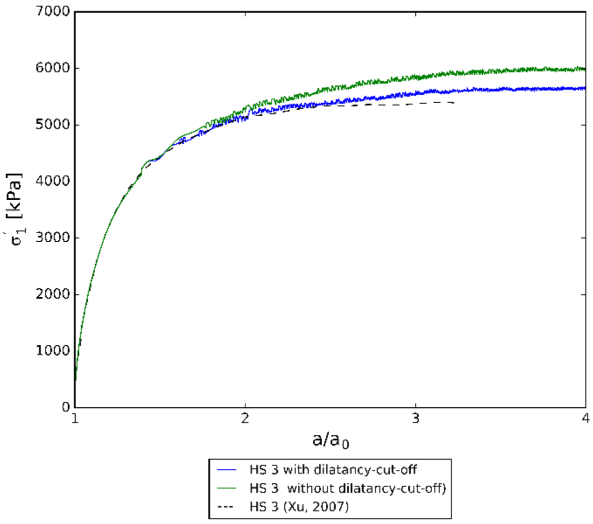

Fig. 76: Pressure-expansion curves for HS 3 material set with and without applying the dilatancy-cut-off and results from Xu (2007)

5.5 Influence of dilatancy angle

For the investigations regarding the influence of the dilatancy angle on the computed pressure-expansion curves, the Mohr-Coulomb material sets from Tab. 18 and two HS material sets from Tab. 19 were used with different magnitudes of the dilatancy angle (see Fig. 77 and Fig. 78). For the solutions of the MC material sets, the closed-form solutions (Yu & Houlsby, 1991) are again added to investigate the performance of the finite element model, in case that different amounts of non-associativity $(\varphi' - \psi)$ are applied.

Mohr-Coulomb model

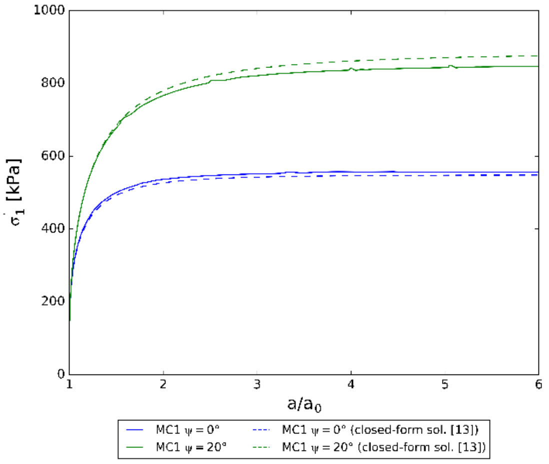

Fig. 77: Pressure-expansion curves: MC 1 material set and different dilatancy angles ψ

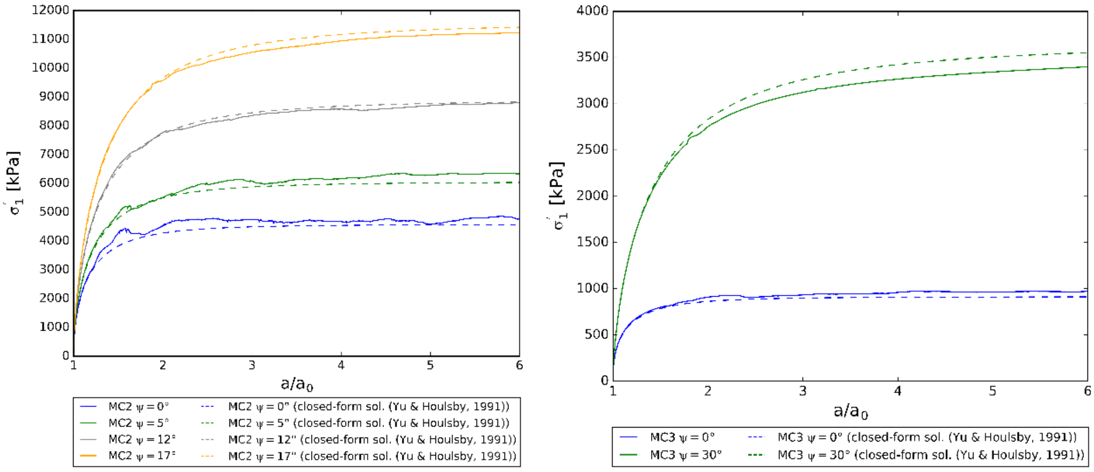

Fig. 78: Pressure-expansion curves: MC 2 (left) and MC 3 (right) for different dilatancy angles ψ

From Fig. 77 and Fig. 78, it can be concluded that, independent from the magnitude of the dilatancy angle, all curves are in agreement with the closed-form solution (Yu & Houlsby, 1991), even though the pressure-expansion curves using a non-associated flow rule show a small amount of scattering. Fig. 78 (left) confirms the impact of non-associated plasticity and indicates that the resulting $\sigma_1{}'$- a/a$_0$ become smoother with an increase of the dilatancy angle. The solution for the non-associated material with $\psi = 0°$ represented in Fig. 77 is already very smooth, which is due to the relatively low amount of non-associativity $(\varphi' - \psi)$ of material set MC 1.

Furthermore, when using an associated flow rule the pressure-expansion curves tend to increase further eventhough large strains are applied to the model, what can be seen best in Fig. 78 (right & $\psi = 30°$). In other words, a horizontal tangent and a well defined limit pressure cannot be achieved when using the Mohr-Coulomb model.

Generally, it can be concluded that a high amount of non-associativity causes a small amount of scattering of the computed pressure-expansion curves, and an increasing dilatancy angle causes the pressure expansion-curves to increase. Hence higher limit pressures can also be reached. However, an increase of the dilatancy angle causes the pressure-expansion curve to always increase, and, therefore, no proper limit pressure can be determined.

Hardening Soil model

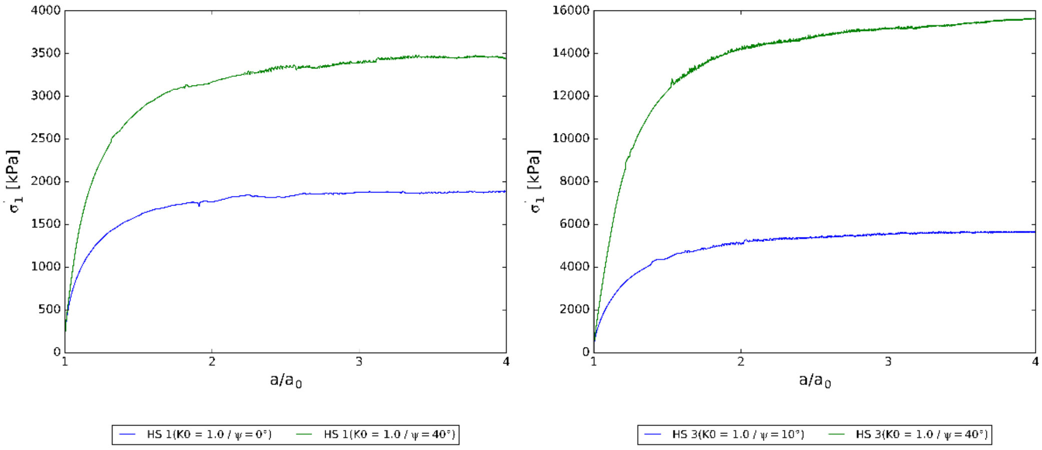

Fig. 79: Pressure-expansion curves: HS 1 (left) and HS 3 (right) for different dilatancy angles ψ

In Fig. 79 the same influence of the dilatancy angle on the computed pressure-expansion curves can be seen as previously shown in Fig. 77 and Fig. 78. An increase of the dilatancy angle causes the pressure-expansion curve to also increase, however, the difference between an associated flow rule ($\psi = 40°$) and a non-associated flow rule ($\psi = 0° \, (left) \, \& \, \psi = 10° \, (right)$) can be significantly different. For example, the HS 1 material set shows a difference of less than 100%, whereas the HS 3 material shows a difference of more than 250% between an dilatancy angle of $\psi = 10°$ and $\psi = 40°$. However, the Hardening Soil model has the advantage to apply the dilatancy-cut-off principle (contrary to the MC-model) which enables a more proper determination of the limit pressure.

5.6 Influence of initial stress state

This chapter presents additional studies that have been performed to investigate the effect of the initial stress field on p_{LS}. In the FE model, the initial stress field is generally generated by means of a surcharge layer ($\gamma_{surcharge}$), while the unit weight of the continuum ($\gamma_{continuum}$) is set to zero. First, in order to analyze the influence of the initial stress field, lateral earth pressure coefficients of $K_0 \neq 1.0$ are used for the finite element analyses. Finally, the effect of a non-uniform stress field is investigated by deactivating the surcharge layer and considering the continuum with a unit weight of $\gamma_{continuum} \neq 0$.

5.6.1 Influence of K_0-value

To investigate the impact of a non-isotropic initial stress state, the finite element analyses using material sets MC 1 and MC 3 (see Tab. 18) and all HS material sets (see Tab. 19) were firstly repeated with a K_0-value according to Jaky (1944) ($K_0 = 1 - sin\varphi'$). When considering a $K_0 \neq 1.0$, two different situations must be considered in order to enable a meaningful comparison between the different finite element analyses. Therefore, the unit weight of the surcharge layer was defined with the same value as the FEA, with $K_0 = 1.0$, to model the situation with the same initial effective vertical pressure $\sigma_v{}'$. In another FEA, the unit weight of the surcharge layer was increased to model the situation where the initial mean effective pressure $p_0{}'$ is the same as in the case $K_0 = 1.0$. It must be mentioned that within chapter 5.6.1, all FEA were performed with a unit weight of the continuum of zero.

For example, the FEA using the MC 3 material set is calculated with $p_0' = 50kPa$, $K_0 = 1.0$, $\gamma_{surcharge} = 50kN/m^3$ and $\sigma_v' = 50kPa$. Now, in order to investigate the effect of the initial stress field, K_0 was set to $1 - sin\varphi' = 0.5$, and the following two situations were considered:

- same $\sigma_v{}'$ as with $K_0 = 1.0$ → $\gamma_{surcharge} = 50kN/m^3$
- same $p_0{}'$ as with $K_0 = 1.0$ → $\gamma_{surcharge} = 75kN/m^3$

For the determination of the initial mean effective pressure, equation (5.2) was used.

$$p' = \frac{1}{3} * \sigma_v' * (1 + 2 * K_0) \tag{5.2}$$

For the considered MC material sets, different values were again considered for the dilatancy angle, in order to account for associated and non-associated plasticity. The results for the MC material sets are presented in Fig. 80, followed by the obtained pressure-expansion curves using the HS material sets (see Fig. 81 and Fig. 82).

Results MC material sets

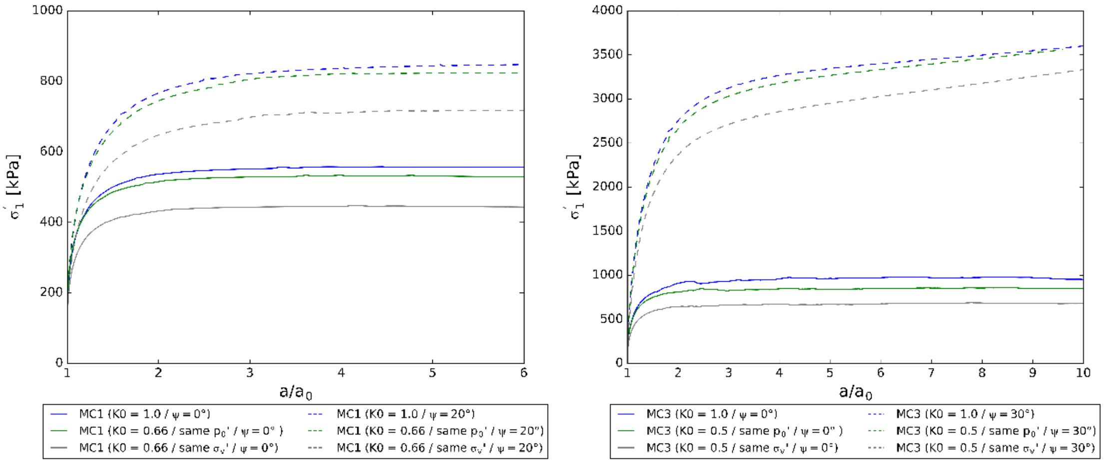

Fig. 80: Pressure-expansion curves for MC material sets (MC 1 (left) and MC 3 (right)) and different K_0-values

Fig. 80 shows that the limit pressure increases as expected with increasing K_0-values. It also can be seen that the difference between the pressure-expansion curves applying $K_0 = 1.0$ and $K_0 = 1 - sin\varphi'$ with the same initial mean effective pressure $p_0{}'$ are relatively small, whereas the difference between the results for $K_0 = 1.0$ and $K_0 = 1 - sin\varphi'$ with the same vertical effective pressure $\sigma_v{}'$ are significantly larger. Similar observations are obtained with an associated flow rule.

Results HS material sets

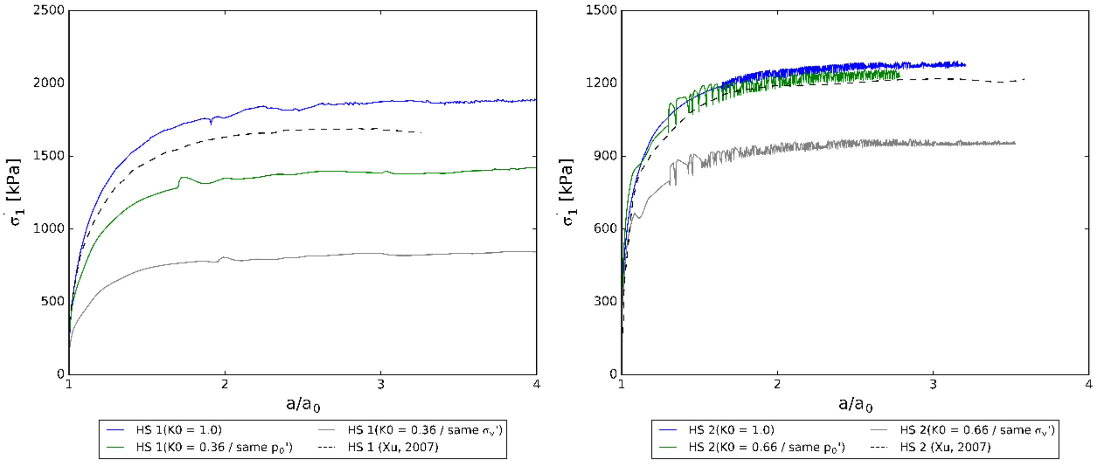

Fig. 81: Pressure-expansion curves for HS material sets (HS 1 (left) and HS 2 (right)) and different K_0-values

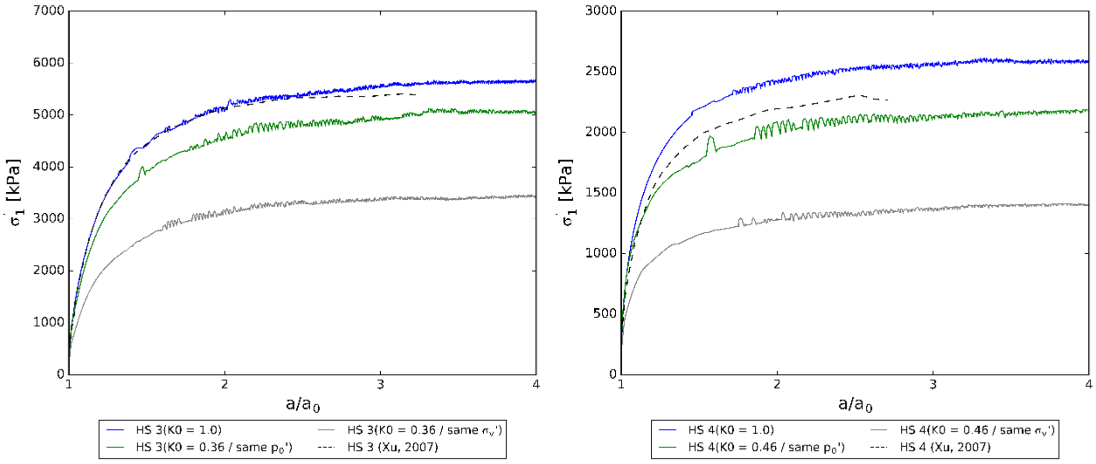

Fig. 82: Pressure-expansion curves for HS material sets (HS 3 (left) and HS 4 (right)) and different K_0-values

Fig. 81 and Fig. 82 show almost the same behavior of the calculated pressure-expansion curves due to a change of the K_0-values. This means that an increase of K_0 causes an increase of the limit pressure, and, again, the differences between $K_0 = 1.0$ and $K_0 = 1 - sin\varphi'$ with the same p_0' are smaller than the differences between $K_0 = 1.0$ and $K_0 = 1 - sin\varphi'$ with the same σ_0'. However, for the HS material sets the differences between the pressure-expansion curves for $K_0 = 1.0$ and $K_0 = 1 - sin\varphi'$ with the same p_0' are larger than the differences for the Mohr-Coulomb model, except for the HS 2 material set (see Fig. 81 (right)). Also, the differences between $K_0 = 1.0$ and $K_0 = 1 - sin\varphi'$ with the same σ_0' are significantly larger for the HS material sets than for the Mohr-Coulomb ones. Hence, it can be concluded that the magnitude of the lateral earth pressure shows more influence for the Hardening Soil model than for the Mohr-Coulomb model.

5.6.2 Uniform and non-uniform stress state

The previously performed analyses considered a zero unit weight of the continuum ($\gamma_{continuum} = 0$) to account for a uniform stress field within the continuum, independent of the applied K_0-value. This chapter now investigates the influence of a non-uniform stress state of the continuum. For these finite element analyses, the surcharge layer was deactivated and the continuum was modelled with a non-zero unit weight. The FEA, using a lateral earth pressure coefficient of $K_0 = 1 - sin\varphi'$, are defined once with the same initial mean effective pressure p_0' (as in the FEA with $K_0 = 1.0$) at the center of the cavity and once with the same effective vertical pressure σ_v' (as discussed in chapter 5.6.1) at the center of the cavity. A schematic representation of the uniform and non-uniform initial stress field is shown in Fig. 83.

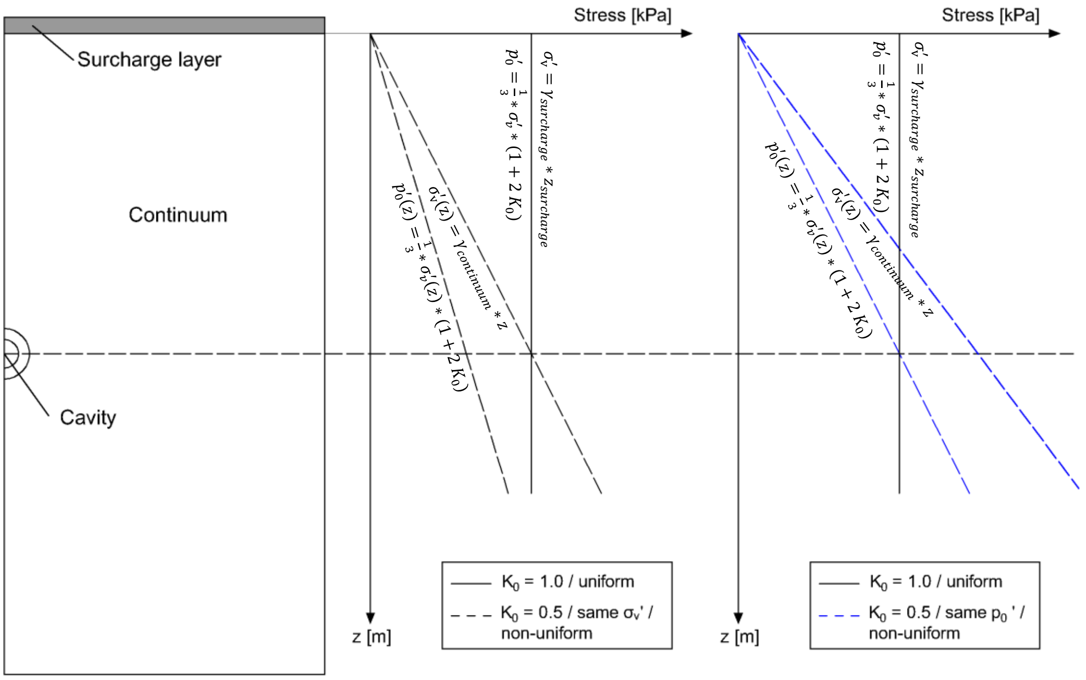

Fig. 83: Schematical representation of different initial stress fields: uniform with $K_0 = 1.0$ and non-uniform with $K_0 \neq 1.0$ (same $\sigma_v{}'$ and same $p_0{}'$)

For the finite element analyses investigating the influence of a non-uniform stress field, all HS material sets from Tab. 19 were used. For all materials (HS 1 to HS 4), the calculated pressure-expansion curves for a uniform, as well as for a non-uniform stress field, both comprising of different values for K_0 ($K_0 = 1.0$; $K_0 = 1 - sin\varphi'$ & $same\ \sigma_v'$; $K_0 = 1 - sin\varphi'$ & $same\ p_0{}'$), are illustrated in Fig. 84 and Fig. 85.

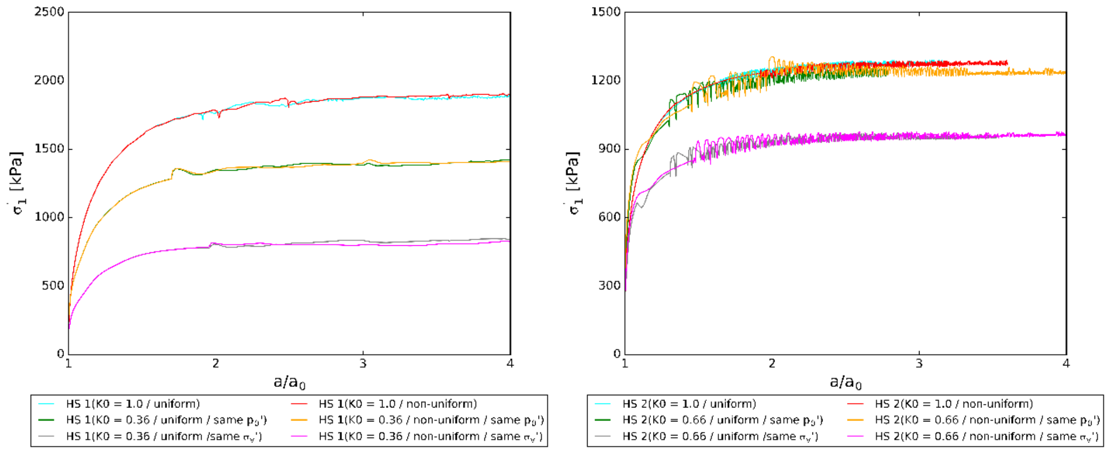

Fig. 84: Pressure-expansion curves for HS material sets (HS 1 (left) and HS 2 (right)) and different initial stress fields

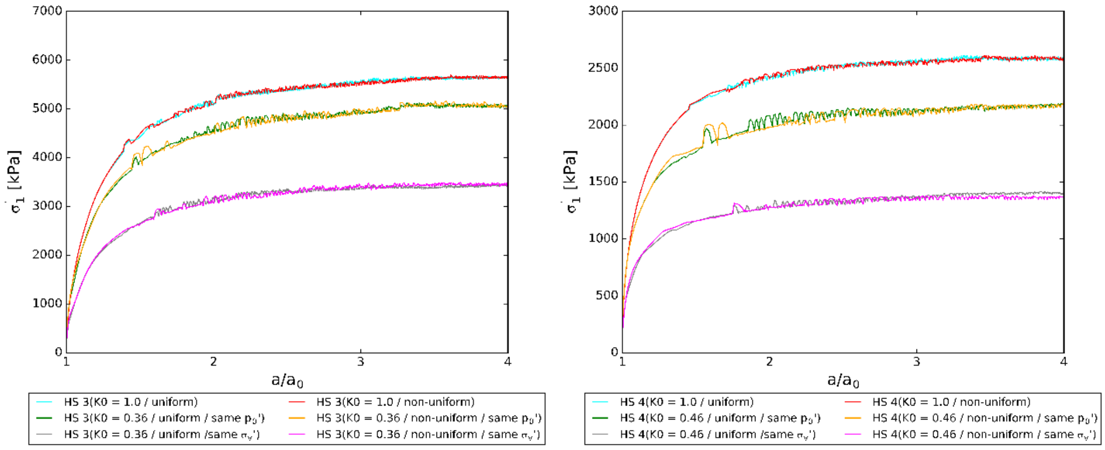

Fig. 85: Pressure-expansion curves for HS material sets (HS 3 (left) and HS 4 (right)) and different initial stress fields

Fig. 84 and Fig. 85 clearly show that there is almost no difference between the application of a uniform stress state and a non-uniform stress state, where the continuum is modeled with a non-zero unit weight and without the requirement of a surcharge layer. Hence, the conclusions made for a uniform stress state regarding the influence of the dilatancy angle and the lateral earth pressure coefficient on the results of the FEA also hold for the application of a non-uniform initial stress field.

5.7 Contour plots of stress and strain development

The contour plots created within the PLAXIS Output manager were investigated to show the stress and strain development of the cavity after each calculation phase (phase 1 to phase 4). The figures are arranged from left to right where the most left figure represents the first calculation phase and the most right figure shows the results for calculation phase 4. Phase 1 is the first calculation phase following the initial phase, where volumetric strains are applied inside the cavity. Similarly phase 2 to phase 4 represent the remaining calculation phases, where all of them contain volumetric strains inside the cavity. For the Mohr-Coulomb constitutive soil model, MC 3 material set from Tab. 18 was used, and for the Hardening Soil model, HS 1 from Tab. 19 was used. For both material sets, the contour plots were created for an associated flow rule, and a non-associated flow rule as well as for a K_0-value of $K_0 = 1.0$ and $K_0 = 1 - sin\varphi$. Additionally, for the Hardening Soil material set (HS 1), the contour plots were made for a non-uniform initial stress field.

Mohr-Coulomb model / contour plots for σ_1'

- $K_0 = 1.0$ / $\psi = 0°$

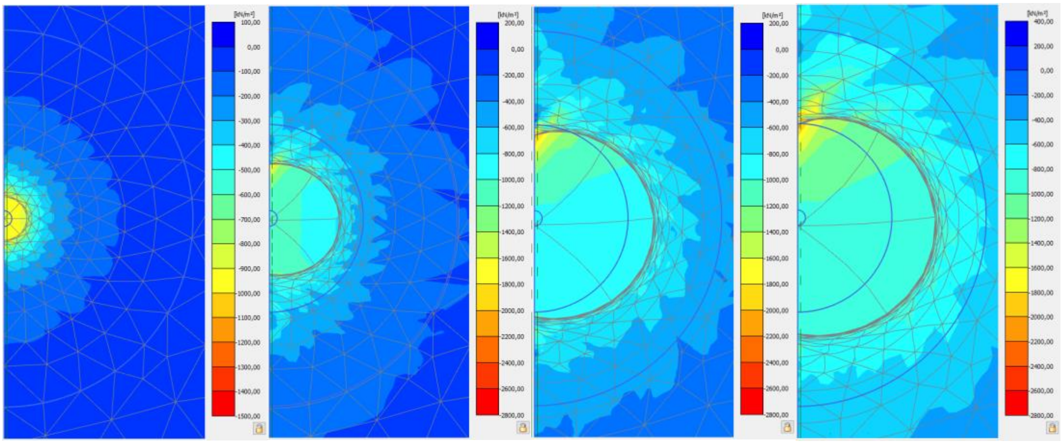

Fig. 86: Contour plots for σ_1': MC 3 material set, $K_0 = 1.0$, $\psi = 0°$ (from phase 1 to phase 4)

- $K_0 = 1.0$ / $\psi = 30°$

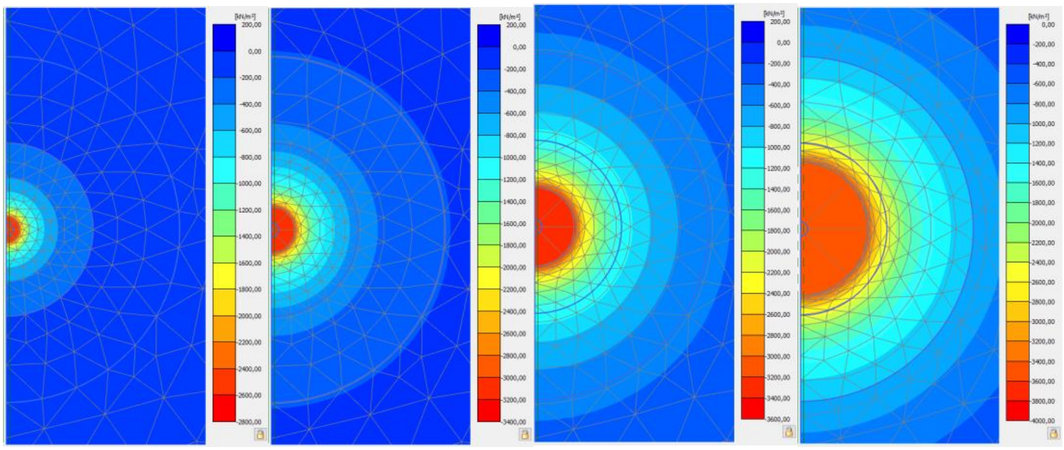

Fig. 87: Contour plots for σ_1': MC 3 material set, $K_0 = 1.0$, $\psi = 30°$ (from phase 1 to phase 4)

- $K_0 = 0.5$ / same p_0' / $\psi = 0°$

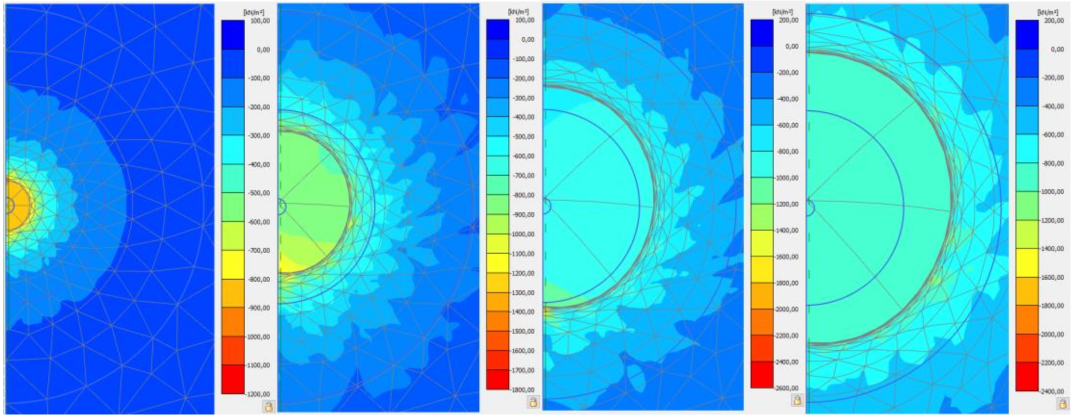

Fig. 88: Contour plots for σ_1': MC 3 material set, $K_0 = 0.5$ & same p_0', $\psi = 0°$ (from phase 1 to phase 4)

- $K_0 = 0.5$ / same $p_0{}'$ / $\psi = 30°$

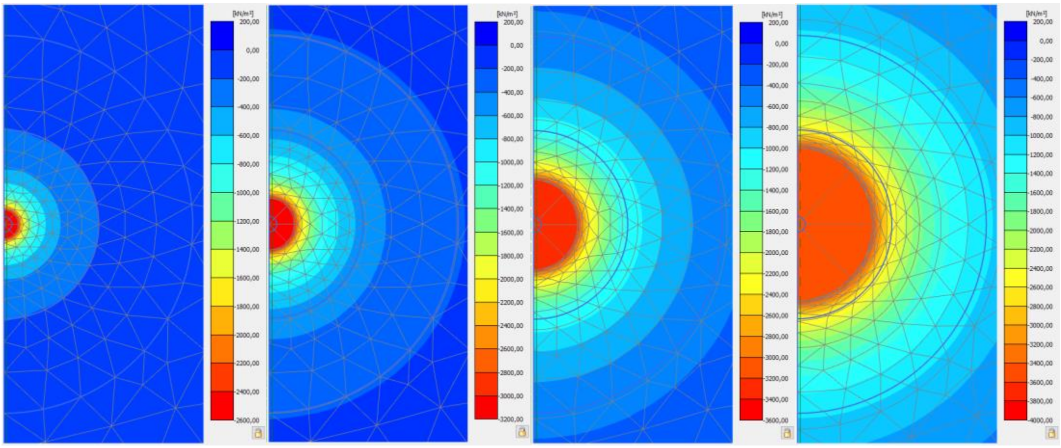

Fig. 89: Contour plots for $\sigma_1{}'$: MC 3 material set, $K_0 = 0.5$ & same $p_0{}'$, $\psi = 30°$ (from phase 1 to phase 4)

Mohr-Coulomb model / contour plots for u_{tot}

- $K_0 = 1.0$ / $\psi = 0°$

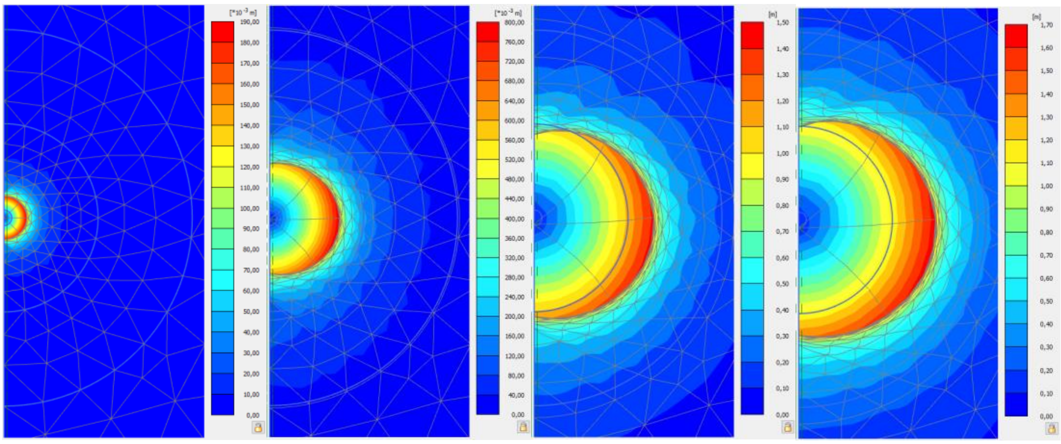

Fig. 90: Contour plots for u_{tot}: MC 3 material set, $K_0 = 1.0$, $\psi = 0°$ (from phase 1 to phase 4)

- $K_0 = 1.0$ / $\psi = 30°$

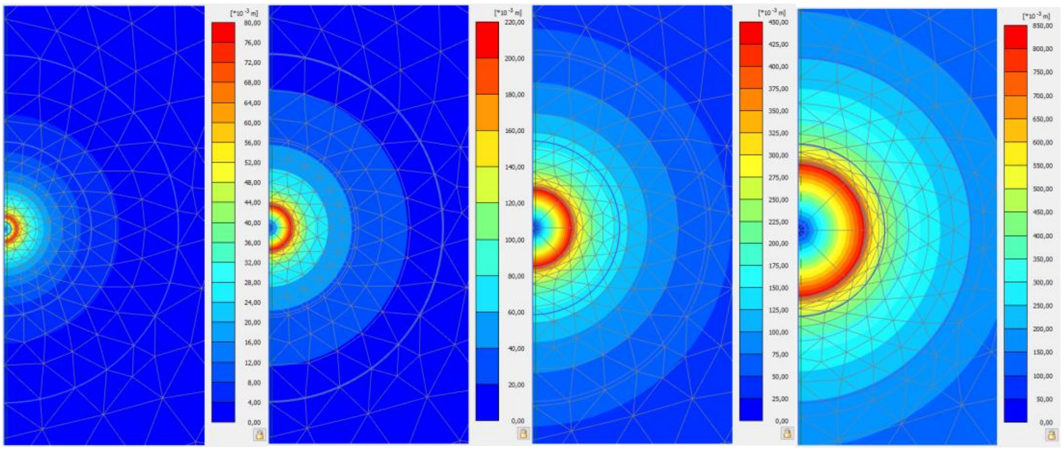

Fig. 91: Contour plots for u_{tot}: MC 3 material set, $K_0 = 1.0$, $\psi = 30°$ (from phase 1 to phase 4)

- $K_0 = 0.5$ / same p_0' / $\psi = 0°$

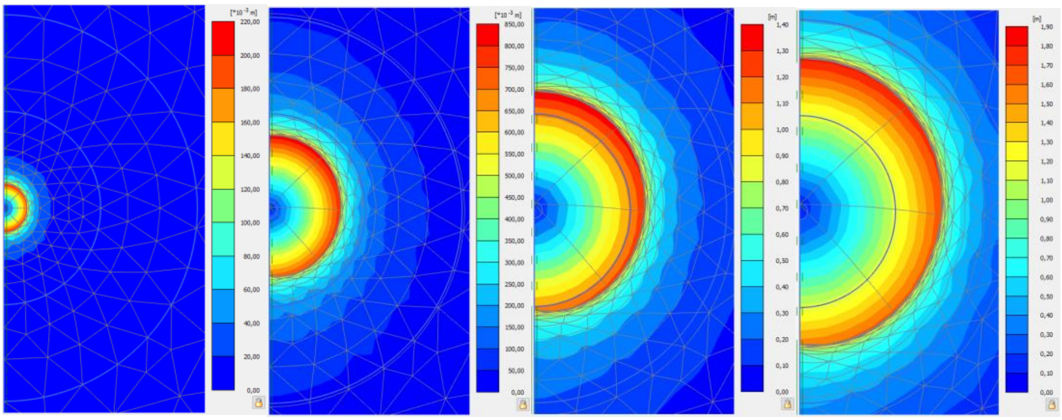

Fig. 92: Contour plots for u_{tot}: MC 3 material set, $K_0 = 0.5$ & same p_0', $\psi = 0°$ (from phase 1 to phase 4)

- $K_0 = 0.5$ / same p_0' / $\psi = 30°$

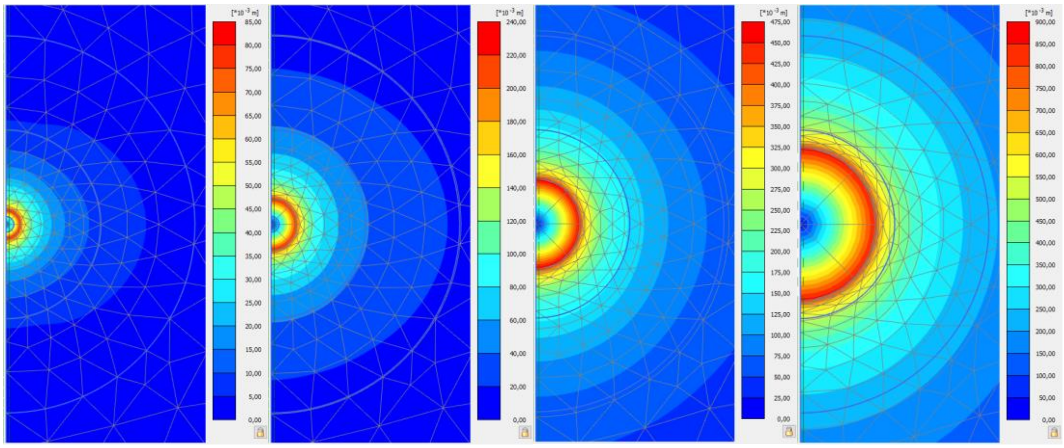

Fig. 93: Contour plots for u_{tot}: MC 3 material set, $K_0 = 0.5$ & same p_0', $\psi = 30°$ (from phase 1 to phase 4)

From Fig. 86 to Fig. 93, the effect of applying an associated flow rule can be easily seen. For an associated flow rule with ψ = 30°, both the stress and strain development of the cavity is totally uniform, whereas for a non-associated flow rule (here ψ = 0°), the situation is different. The stress distribution within the cavity is almost uniform (with some stress concentrations), whereas outside the cavity, it is non-uniform. The strain development shows more accordance to the application of an associated flow rule than the stress behavior does, however, it is also true that the strain development of the cavity shows a non-uniform behavior. When comparing the results obtained from K_0 = 1.0 and $K_0 = 1 - sin\varphi$ (for ψ = 0°) it can be seen, that in phase 4 the application of K_0 = 1.0 still shows some stress concentrations in the upper part whereas applying $K_0 = 1 - sin\varphi$ does not show any stress concentrations. Regarding the results of the total displacements it can be seen that the application of $K_0 = 1 - sin\varphi$ results in a more uniform deformation of the cavity than for the application of K_0 = 1.0.

Hardening Soil model

For the Hardening Soil model, the contour plots for a lateral earth pressure coefficient of K_0 = 1.0 and different dilatancy angles are shown below. Additionally, for the application of an associated flow rule (ψ = 40°), the contour plots for a non-uniform initial stress field ($\gamma_{continuum} \neq 0$ & no surcharge layer) are added. All other contour plots can be found within appendix B.

HS contour plots for $\sigma_1{}'$

- K_0 = 1.0 / uniform / ψ = 0°

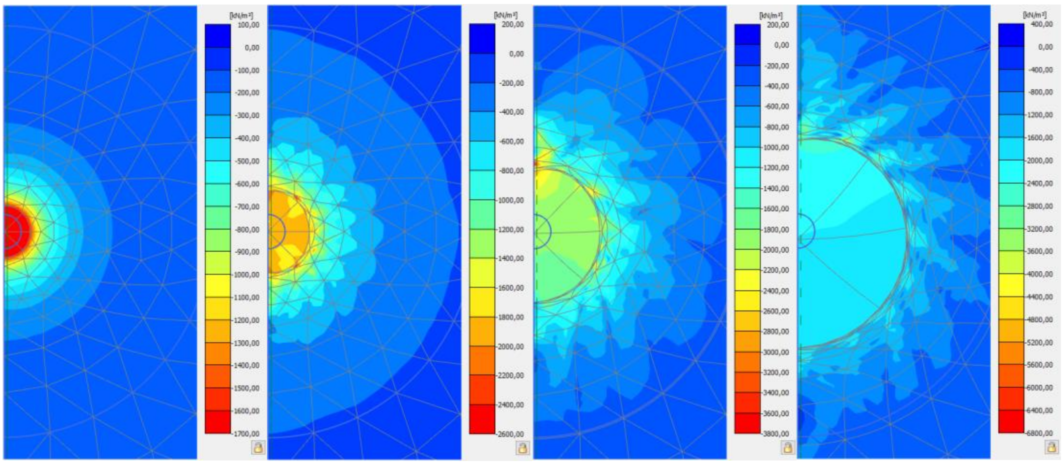

Fig. 94: Contour plots for $\sigma_1{}'$: HS 1 material set, K_0 = 1.0, ψ = 0°, uniform (from phase 1 to phase 4)

- $K_0 = 1.0$ / uniform/ $\psi = 40°$

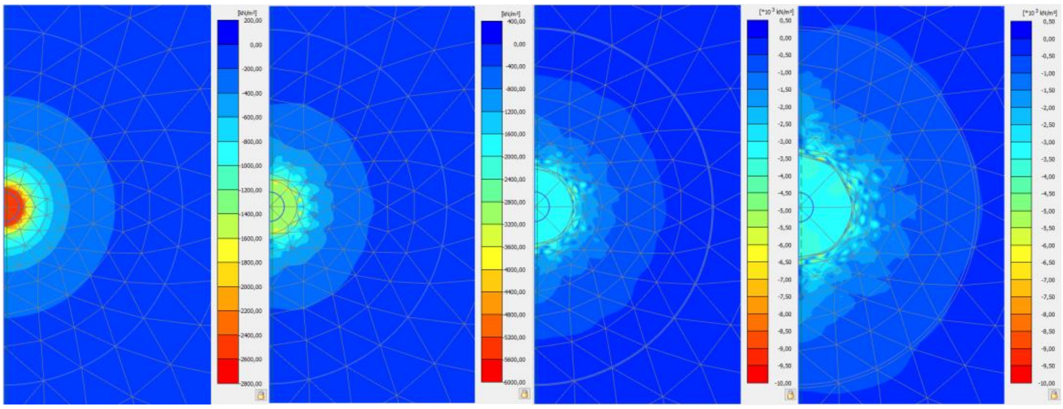

Fig. 95: Contour plots for σ_1': HS 1 material set, $K_0 = 1.0$, $\psi = 40°$, uniform (from phase 1 to phase 4)

- $K_0 = 1.0$ / non-uniform/ $\psi = 40°$

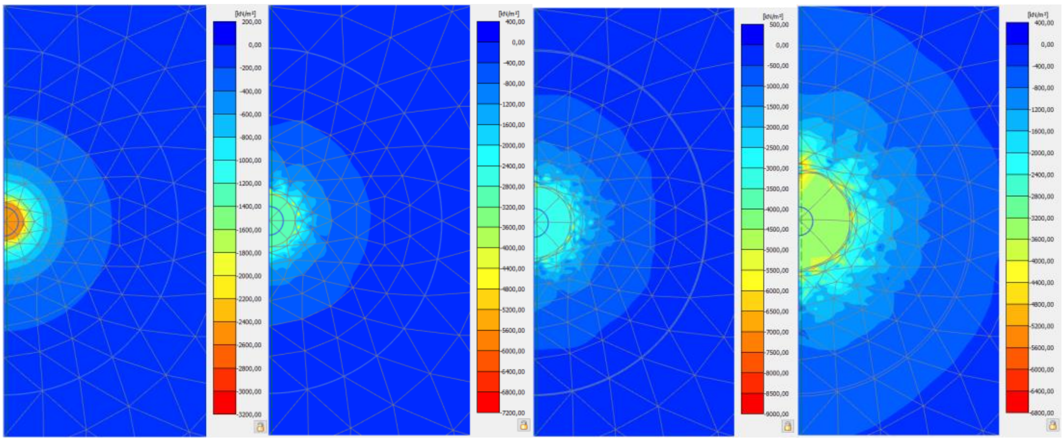

Fig. 96: Contour plots for σ_1': HS 1 material set, $K_0 = 1.0$, $\psi = 40°$, non-uniform (from phase 1 to phase 4)

HS contour plots for u_{tot}

- $K_0 = 1.0$ / uniform / $\psi = 0°$

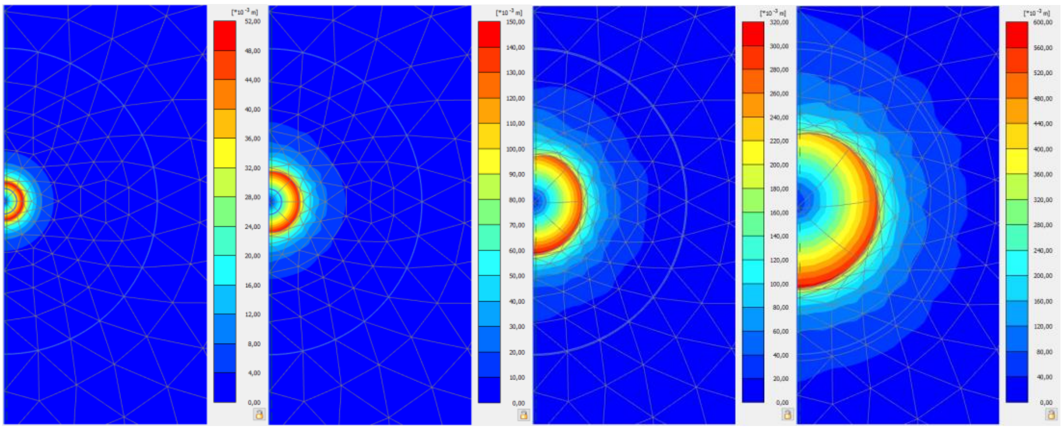

Fig. 97: Contour plots for u_{tot}: HS 1 material set, $K_0 = 1.0$, $\psi = 0°$, uniform (from phase 1 to phase 4)

- K_0 = 1.0 / uniform / ψ = 40°

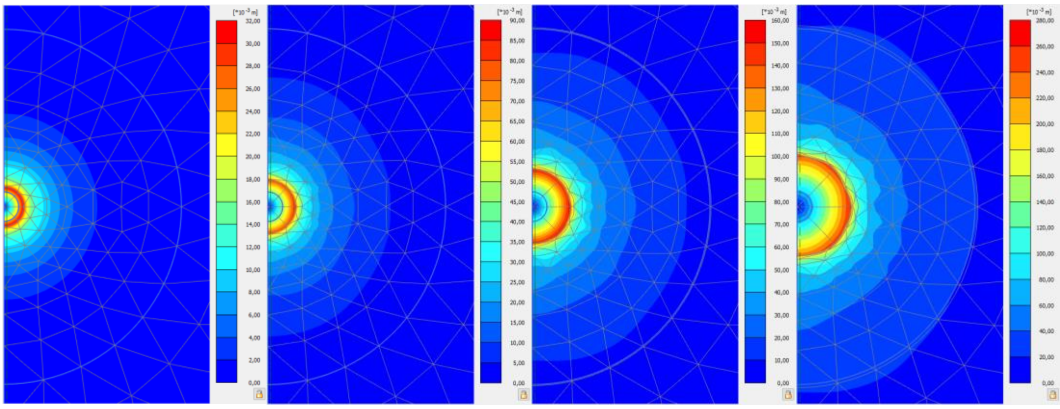

Fig. 98: Contour plots for u_{tot}: HS 1 material set, K_0 = 1.0, ψ = 40°, uniform (from phase 1 to phase 4)

- K_0 = 1.0 / non-uniform / ψ = 40°

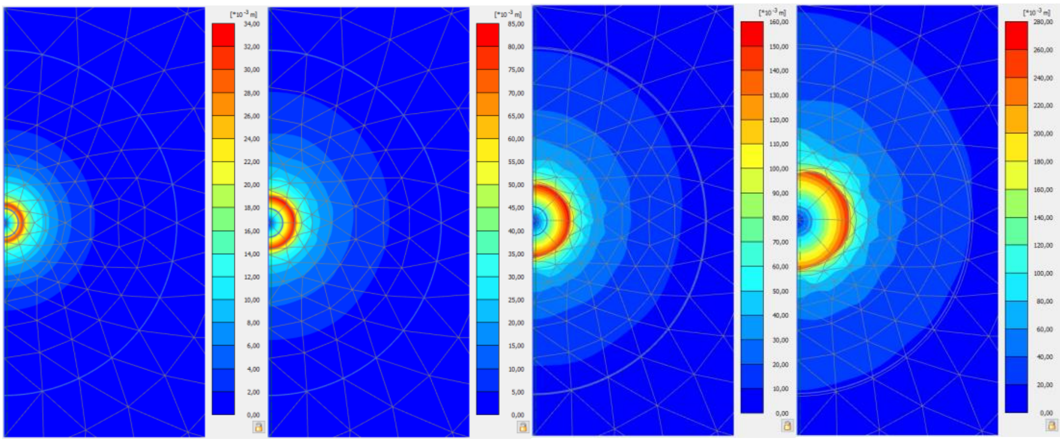

Fig. 99: Contour plots for u_{tot}: HS 1 material set, K_0 = 1.0, ψ = 40°, non-uniform (from phase 1 to phase 4)

For the Hardening Soil model (Fig. 94 to Fig. 99), similar conclusions can be made. However, when applying an associated flow rule (here ψ = 40°), the stress, as well as the strain development of the cavity, are not entirely uniform. But, it is still more uniform overall than if a non-associated flow rule were to be applied, and, further, it can be seen that there is no difference between the application of a uniform or a non-uniform initial stress field. The figures within appendix B (A-Fig. 10 to A-Fig. 19) clearly show that, different to the MC material set, applying a K_0-value with $K_0 = 1 - sin\varphi$ results in a significant non-uniform stress and strain development of the cavity.

5.8 Hardening Soil vs Mohr-Coulomb

In this chapter, the performance of the Hardening Soil model, as well as the Mohr-Coulomb soil model, will be investigated. Therefore, the HS material sets of Tab. 19 were taken, and the corresponding MC materials were simply determined as E' (MC) = E_{50}^{ref} (HS), φ' (MC) = φ' (HS), c' (MC) = c' (HS), ψ (MC) = ψ (HS) and ν (MC) = ν (HS). With these simple assumptions, four new MC material sets were created, as shown in Tab. 20.

Tab. 20: MC material sets according to HS materials (see Tab. 19)

Material	corresponding HS set	E [MPa]	φ' [°]	ψ [°]	ν [-]
MC 4	HS 1	10	40	0	0.2
MC 5	HS 2	50	20	0	0.2
MC 6	HS 3	50	40	10	0.2
MC 7	HS 4	30	33	3	0.2

For the investigations within this chapter, the HS materials sets are compared with the MC material sets from Tab. 20, which were obtained by applying simple assumptions, as mentioned above. For all calculations a cohesion of $c' = 0.2\ kPa$ and an initial mean effective pressure $p_0' = 120\ kPa$ were used. Furthermore, the pressure-expansion curves were calculated for K_0 = 1.0, $K_0 = 1 - sin\varphi'$ and same $\sigma_v{}'$, and a uniform initial stress field was assumed.

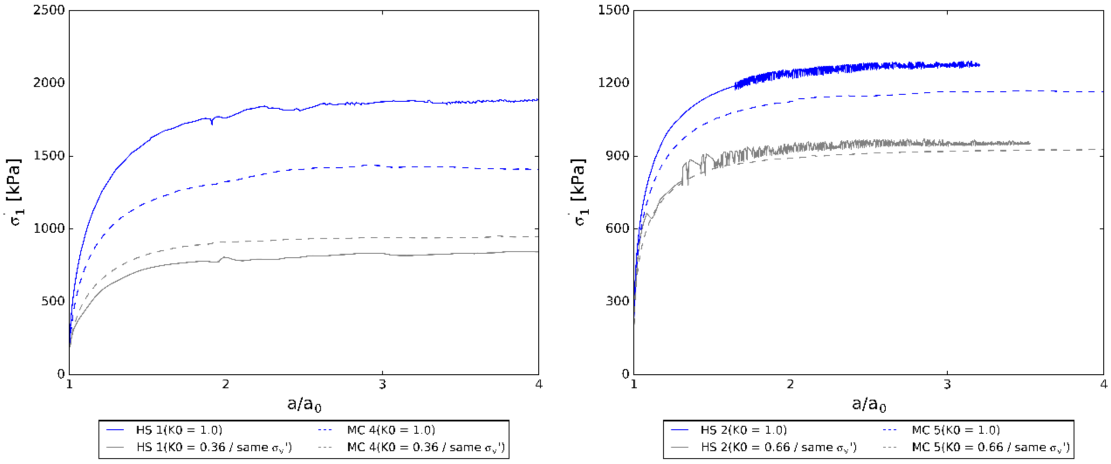

Fig. 100: Pressure expansion curves for HS material sets and corresponding MC material sets (HS 1 & MC 4 (left) and HS 2 & MC 5 (right)

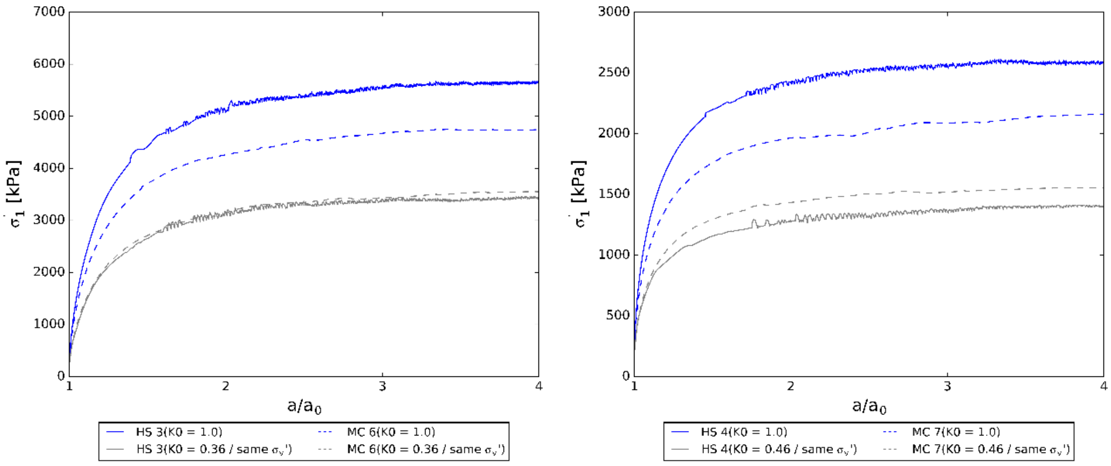

Fig. 101: Pressure expansion curves for HS material sets and corresponding MC material sets (HS 3 & MC 6 (left) and HS 4 & MC 7 (right)

Fig. 100 and Fig. 101 show the significant difference between the computed pressure-expansion curves for $K_0 = 1.0$, which indicates that the assumptions above are not sufficient. The reason for the relatively small differences between the pressure-expansion curves for the HS material set and the corresponding MC material set for a $K_0 = 1 - sin\varphi'$ and same σ_v' can be derived from the conclusions from chapter 5.6.1. Due to the fact that the influence of the lateral earth pressure is stronger for the HS model than for the MC model, the difference between the HS and MC models is larger for $K_0 = 1.0$ than for $K_0 = 1 - sin\varphi'$ and same σ_v'. The differences between the results of the FEA for $K_0 = 1.0$ clearly illustrate that the MC and the HS model compute different results of the spherical cavity expansion problem.

5.9 Hypoplastic soil model

The previous investigations of chapter 5 showed the performance of the finite element analyses to solve the spherical cavity expansion problem when applying an elasto-plastic constitutive soil model (Mohr-Coulomb and Hardening Soil). Since the originally developed Karlsruhe Interpretation Method used the hypoplastic soil model, this chapter shows the influence of the K_0-value and the initial stress state on the resulting pressure-expansion curves when applying the hypoplastic soil model (Fig. 102 to Fig. 104). As basis for the investigations, the hypoplastic parameter set HP 1 shown in Tab. 21 is used, and further, the indices i (see Tab. 22) define the density state, as well as the initial stress field.

Tab. 21: Hypoplastic parameters for material set HP 1

Material	φ_c [°]	h_s $[kPa]$	n [-]	e_{d0} [-]	e_{c0} [-]	e_{i0} [-]	α [-]	β [-]
HP 1	36.3	39,000	0.525	0.740	1.261	1.450	0.05	1.97

Tab. 22: I_D- and p_0-values for different indices

Index i	1	2	3	4	5	6
I_D	0.0	0.0	0.5	0.5	0.9	0.9
p_0 [kPa]	50	300	50	300	50	300

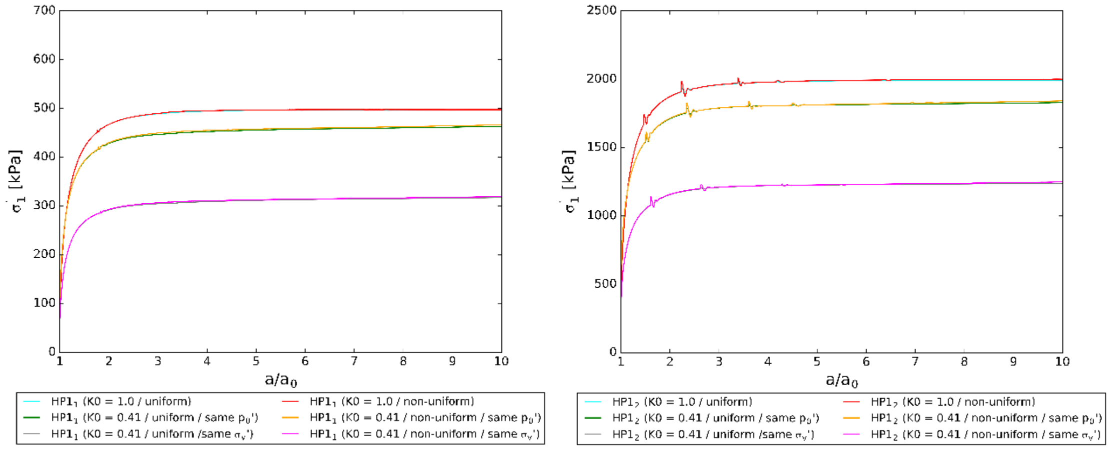

Fig. 102: Pressure-expansion curves for HP material sets (HP 1_1 (left) and HP 1_2 (right)) and different initial stress fields

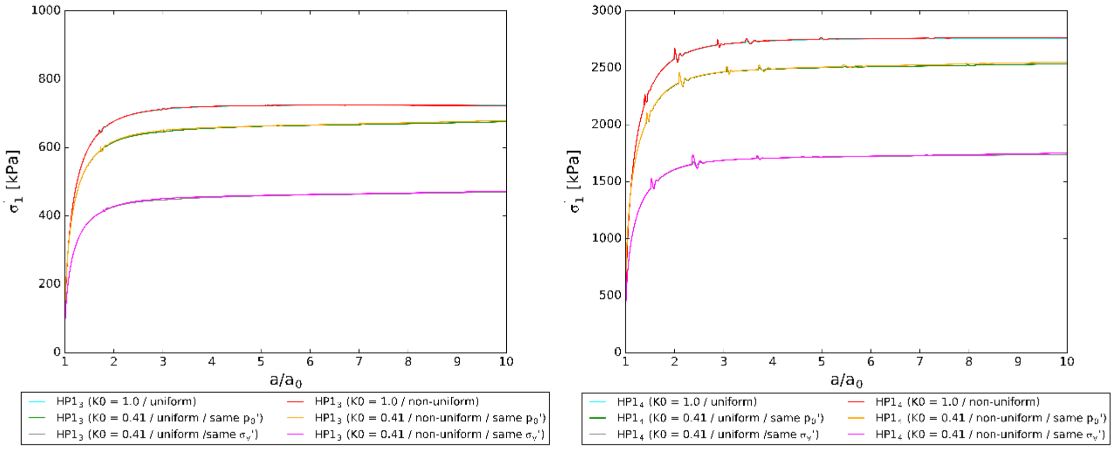

Fig. 103: Pressure-expansion curves for HP material sets (HP 1_3 (left) and HP 1_4 (right)) and different initial stress fields

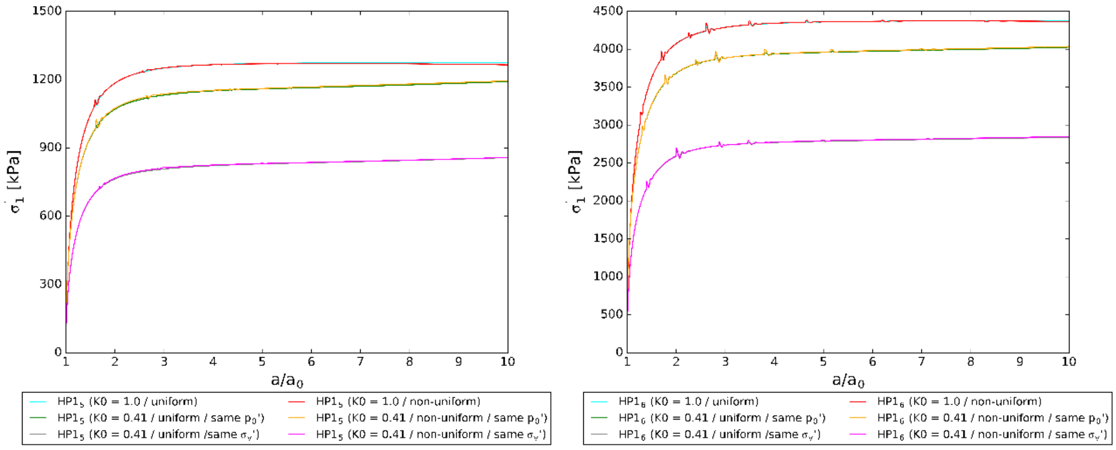

Fig. 104: Pressure-expansion curves for HP material sets (HP 1_5 (left) and HP 1_6 (right)) and different initial stress fields

From figures Fig. 102 to Fig. 104, it can be concluded that the pressure-expansion curves increase with an increasing K_0-value, just as they do for the MC material sets and HS material sets. Furthermore, it can again be concluded that the difference between the pressure-expansion curves for $K_0 = 1.0$ and $K_0 = 0.41$ with the same initial mean effective pressure p_0' are smaller than the differences between the results for $K_0 = 1.0$ and $K_0 = 0.41$ with the same initial vertical effective pressure σ_v'. Additionally, it can be seen that there is absolutely no difference between the application of a uniform initial stress field ($\gamma_{continuum} = 0$ & activated surcharge layer) and a non-uniform initial stress field ($\gamma_{continuum} \neq 0$ & deactivated surcharge layer).

HP contour plots

The contour plots were again created with the PLAXIS Output manager for the stress and strain development of the cavity after selected calculation phases. For these investigations the material HP 1_3 was used and due to the reason that in total 6 calculation phases were applied, the contour plots were created for the first, second, fifth and sixth calculation phase (were volumetric strains were applied inside the cavity).

HP contour plots for σ_1'

- $K_0 = 1.0$ / $I_D = 0.5$ / $p_0 = 50$ kPa

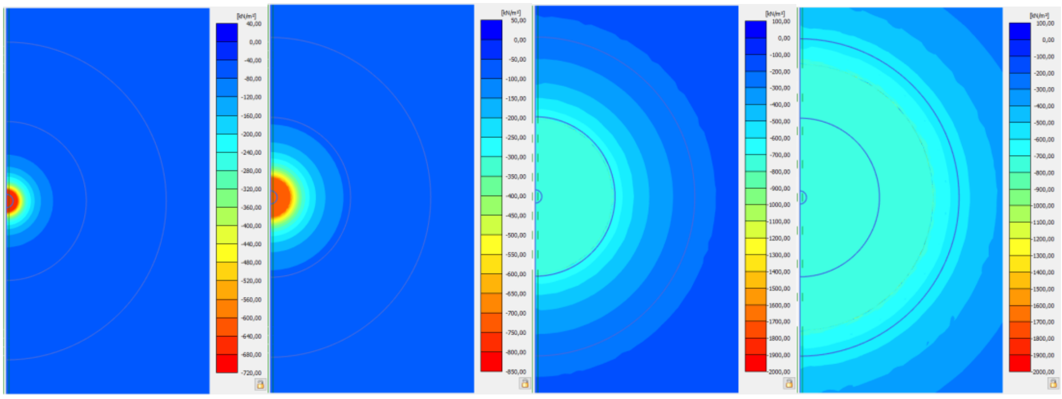

Fig. 105: Contour plots for σ_1': HP 1_3 material set, $K_0 = 1.0$, uniform (1st phase, 2nd phase, 5th phase, 6th phase)

- $K_0 = 0.41$ / $I_D = 0.5$ / $p_0 = 50$ kPa

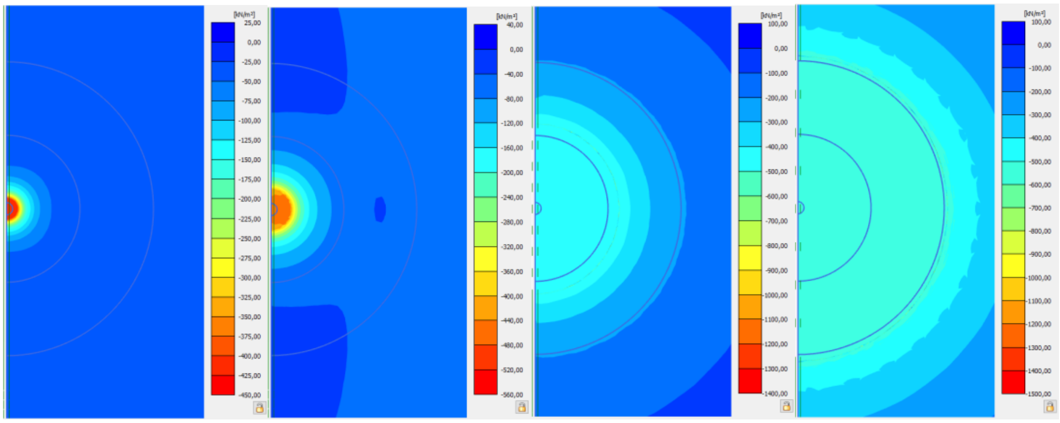

Fig. 106: Contour plots for σ_1': HP 1_3 material set, $K_0 = 0.41$, uniform (1st phase, 2nd phase, 5th phase, 6th phase)

HP contour plots for u_{tot}

- $K_0 = 1.0$ / $I_D = 0.5$ / $p_0 = 50$ kPa

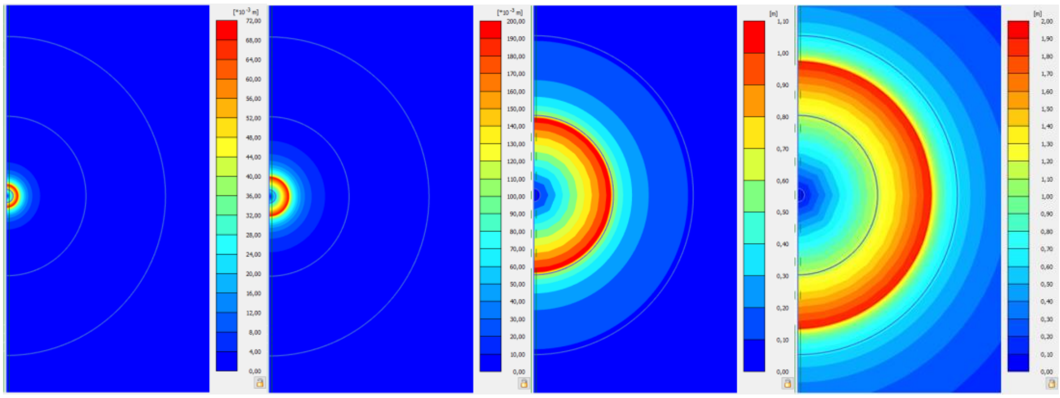

Fig. 107: Contour plots for u_{tot}: HP 1_3 material set, $K_0 = 1.0$, uniform (1st phase, 2nd phase, 5th phase, 6th phase)

- $K_0 = 0.41$ / $I_D = 0.5$ / $p_0 = 50$ kPa

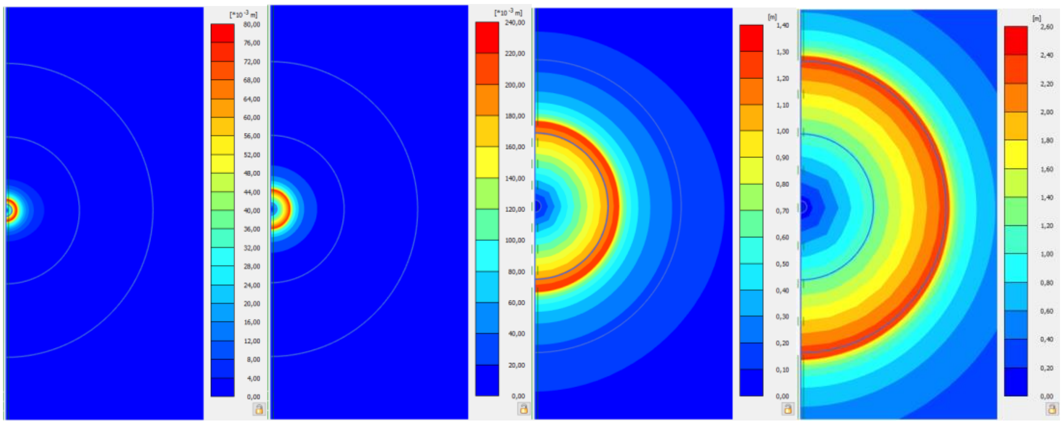

Fig. 108: Contour plots for u_{tot}: HP 1_3 material set, $K_0 = 1.0$, uniform (1st phase, 2nd phase, 5th phase, 6th phase)

From Fig. 105 to Fig. 108 it can be seen that the stress, as well as the strain development of the cavity is uniform, independent of the applied lateral earth pressure coefficient K_0. However, the stress development for an applied K_0-value of 0.41 shows some non-uniformity within the continuum. For the remaining density states and initial stress situation of material set HP 1, the contour plots are qualitative the same and therefore, the contour plots only for HP 1_3 are presented within this thesis.

5.9.1 Hardening Soil model vs hypoplastic soil model

In this chapter, the spherical cavity expansion is modelled with optimized HS-parameters based on a parameter set for a hypoplastic model. The aim of this study is to investigate the performance of an elasto-plastic constitutive model compared to hypoplasticity. For these investigations, a material set found in literature (Marcher, et al., 2000) was used. The Hardening Soil, as well as the hypoplastic (HP) soil parameters, can be found in Tab. 23 and Tab. 24.

Tab. 23: Hardening Soil parameters – Hostun sand

Material	E_{50}^{ref} $[MPa]$	E_{Oed}^{ref} $[MPa]$	E_{ur}^{ref} [MPa]	φ' [°]	ψ [°]	m [-]
Dense sand	30	28	90	44	14	0.55
Loose sand	12	12	36	34	0	0.75

Tab. 24: Hypoplastic soil parameters – Hostun sand

Material	φ_c [°]	h_s $[MPa]$	n [-]	e_{d0} [-]	e_{c0} [-]	e_{i0} [-]	α [-]	β [-]
Dense & loose sand	32	1000	0.29	0.61	0.91	1.09	0.19	2

Compared to the parameters given in (Marcher, et al., 2000), the stiffness parameters of the HS model for the loose Hostun sand were, slightly adjusted as follows:

- $E_{Oed}^{ref} = E_{50}^{ref}$ and $E_{ur}^{ref} = 3 * E_{50}^{ref}$.

For the different parameter sets, triaxial tests applying a confining pressure of $\sigma_3' = 100\,kPa$ were modelled with the PLAXIS Soil Test Tool. Finally, the obtained results were compared with the results given in (Marcher, et al., 2000), as shown in Fig. 109.

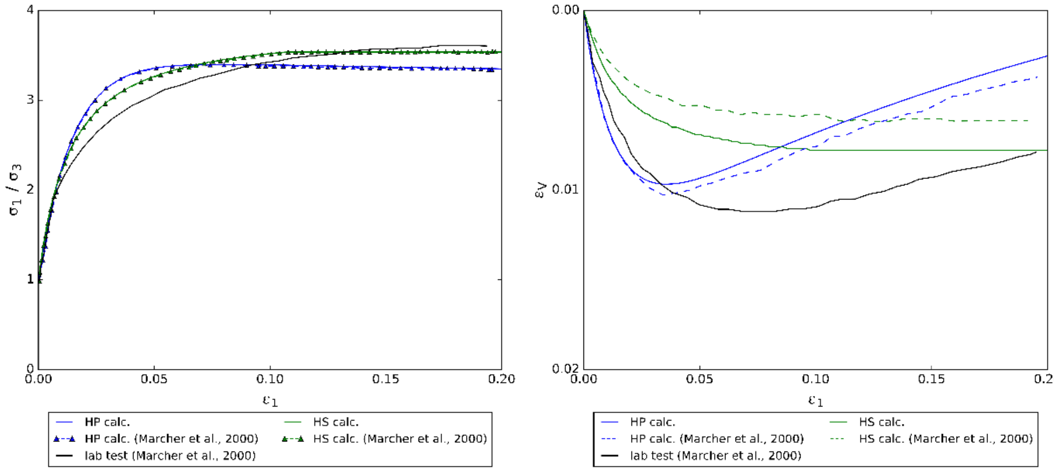

Fig. 109: Triaxial test on loose Hostun sand (confining pressure $\sigma_3 = 100kPa$)

The computed stress-strain curves (Fig. 109 (left)) of the triaxial compression test are in agreement with both the laboratory test results and the numerical results presented by Marcher et al. (2000). However, the volumetric behavior (Fig. 109 (right)) show deviations to both. For the hypoplastic soil model, only small differences can be seen between the numerical results that prove the correct application of the initial void ratios. The differences between the numerical results for applying the Hardening soil model may have resulted from the adjustment of the stiffness parameters.

For the HS model, the dilatancy-cut-off option was selected, but due to the fact that the limit void ratios, e_{min} and e_{max} were not explicitly given in (Marcher, et al., 2000), the hypoplastic parameter set was used to calculate the limit void ratio e_{max}

(using equation (3.2)). The computed pressure-expansion curves for the two density states and the different constitutive soil models are illustrated in Fig. 110. This figure shows that the Hardening Soil model calculates very similar results, thus similar limit pressures. However, a closer look indicates that for the loose material, the difference between the applied constitutive soil models is less than that of the dense material. Based on the performed numerical studies, it can be concluded that the Hardening Soil model is also able to provide satisfying results, but due to the fact that this constitutive soil model does not take pyknotropy into account, a new Hardening Soil parameter set must be generated for each density state. Thus, a great amount of effort is needed to complete this modelling task. The hypoplastic soil model, on the other hand, has the advantage of taking the influence of density (pyknotropy) into account. Fig. 111 shows example results of performed FEA to analyze the SCE problem using the hypoplastic soil model according to Von Wolffersdorff (1996). This figure illustrates the change of void ratio e with the pressure p' during the application of volumetric strains.

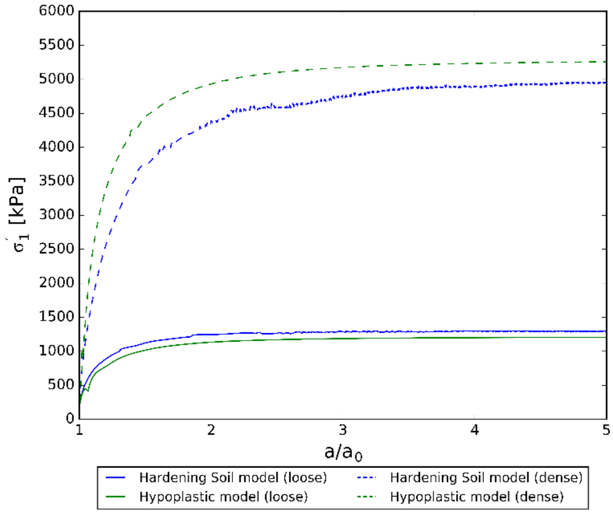

Fig. 110: Pressure-expansion curves for loose and dense Hostun sand with the Hardening Soil and the hypoplastic soil model

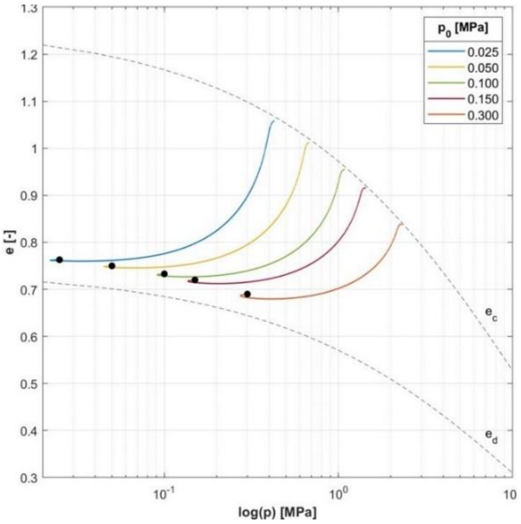

Fig. 111: FEA of the SCE problem: log (p') - e - diagram using a hypoplastic soil model (relative density I_D = 0.9) (Winkler, 2018)

6 Full KIM analysis

A full KIM analysis consists of several steps in order to finally come up with the calculated cone penetration resistance q_c for a certain density state. This chapter presents first each step of the KIM, including its results, and discusses in the following the full automation of the entire KIM analysis.

6.1 Hypoplastic parameter sets

The hypoplastic parameter set HP 1 from Tab. 21 is used for the full KIM analysis, because for this parameter set the KIM parameters a_i and b_i were already determined in Thurner et al. (2019), and hence can be used as reference for the calculations. This parameter set includes 6 laboratory tests (two oedometric compression tests: one on a loose soil sample and one on a dense soil sample; Furthermore, four triaxial compression tests with different confining pressures, with two being allocated to loose soil samples and two to dense soil samples), which can be used to calibrate the hypoplastic parameter with ExCalibre.

Preliminary studies related to ExCalibre (see chapter 4.2.2) already indicated the influence of the number and the type of laboratory tests (provided to the ExCalibre input file) on the resulting hypoplastic parameters. To enable a good comparison of a full KIM analysis between the hypoplastic parameter set HP 1 (Thurner, et al., 2019) and the corresponding parameter set obtained from the ExCalibre calibration, the same process was executed, as already presented within chapter 4.2.2.

Therefore, different combinations of the laboratory test results have been used as ExCalibre input sets (see Tab. 25). For every input set in ExCalibre, a hypoplastic parameter set was calibrated, and the differences of the calibrated parameters compared to the parameter set HP 1 (Thurner, et al., 2019) are exemplary shown in Fig. 112 (for h_s, α, β and e_{d0}).

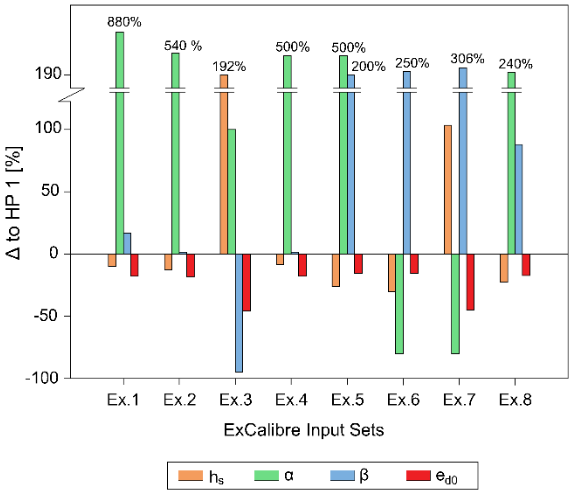

Fig. 112: Differences between HP 1 and ExCalibre results (for h_s, α, β and e_{d0})

Tab. 25: Different input sets for the calibration tool ExCalibre

Input set	Oed 1 (dense)	Oed 2 (loose)	Triax 100 (dense)	Triax 100 (loose)	Triax 600 (dense)	Triax 600 (loose)
Ex. 1	●	●	●	●	●	●
Ex. 2		●	●		●	
Ex. 3	●			●		●
Ex. 4	●	●	●		●	
Ex. 5	●	●	●			●
Ex. 6	●	●		●	●	
Ex. 7	●			●	●	
Ex. 8		●		●	●	

Fig. 112 indicates that the h_s parameter shows large deviations for the input sets where only one dense oedometric compression test was used. This result was expected, since h_s should be obtained from oedometric compression tests on initially very loose specimens. The parameter α can generally be calibrated by performing drained triaxial tests on initially dense samples (see chapter 3.2.2). ExCalibre input set Ex. 7 and Ex. 8 include triaxial test data of dense samples, but show a significant difference for the parameter α. These results indicate that the calibration of α is highly affected by the number and type of data used as an input for ExCalibre. Furthermore, it can be concluded that the input sets Ex. 1, Ex. 2 and Ex. 4 show very high deviations for α, coupled with only small deviations for all other hypoplastic parameters. The reason for such high deviations of α is not clear at the moment. Conversely, the limit void ratio e_{d0} shows significant deviations only for input sets Ex. 3 and Ex. 7, which include only one dense oedometric compression test result. Also, the deviations of β are very high for some input sets. However, no clear correlation between the different input sets and the impact on the parameter β could be found.

All calibrated hypoplastic parameter sets (obtained from the different input files) and the deviations from the parameter set HP 1 are given in appendix C for every hypoplastic parameter.

A full KIM analysis is performed both with the parameter set HP 1 given in (Thurner, et al., 2019) and with hypoplastic parameter obtained from the ExCalibre calibration. For this comparison, the input set Ex. 4 was taken, which is a result of a calibration using both oedometric compression tests and the triaxial tests of the dense soil sample as inputs for ExCalibre. Both parameter sets and their deviations from each other can be seen in Tab. 26. From this follows that the automatic calibration (with ExCalibre) is in agreement with the “manually” calibrated parameters given in (Thurner, et al., 2019), except for the α-value (which shows a difference ao approximately 500%). Due to this big deviation of the α-value, another full KIM analysis was performed using the calibrated parameters from ExCalibre set Ex. 4 in combination with a α-value of 0.05 (reference value of set HP 1). This parameter set is subsequently denoted as “Ex. 4b”.

Tab. 26: Hypoplastic parameters for set HP 1 and set Ex. 4

Material	φ_c [°]	h_s $[MPa]$	n [-]	e_{d0} [-]	e_{c0} [-]	e_{i0} [-]	α [-]	β [-]
HP 1	36.3	39,00	0.525	0.740	1.261	1.450	0.05	1.97
Ex. 4	34.2	35.72	0.452	0.607	1.215	1.458	0.30	2.00
$\lvert\triangle\rvert$[%]	5.8	8.4	13.9	18.0	3.7	0.6	500.0	1.5

6.2 SCE analyses and limit pressures

At first, 50 finite element analyses must be calculated in order to come up with 50 limit pressures. The 50 finite element models comprise 10 different density states of I_D = [0.0, 0.1, 0.2, 0.3, 0.4, 0.5, 0.6, 0.7, 0.8, 0.9] and 5 different initial effective mean pressures of $p_0{}'$ = [25 kPa, 50 kPa, 100 kPa, 150 kPa, 300 kPa]. All FEA consist of the same hypoplastic parameter set and only differ in the initial void ratio and the initial effective mean pressure. The results of this step are the pressure-expansion curves for every combination of I_D and p_0 and the calculated limit pressure. The pressure-expansion curves, as well as the limit pressures for the FEA applying the parameter set Ex. 4b, are shown below, whereas the results for the parameter set HP 1 and Ex. 4 can be seen within the appendix C.

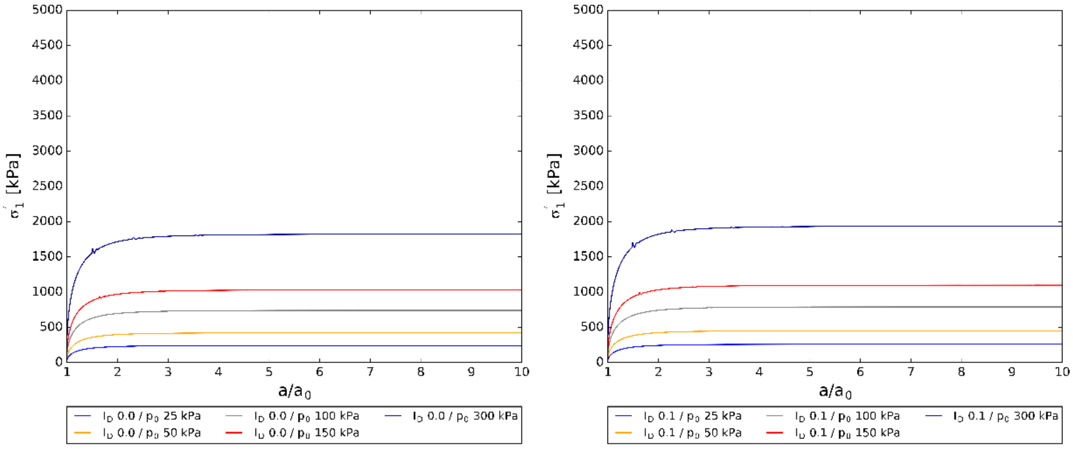

Fig. 113: Pressure-expansion curves for parameter set Ex. 4b and different density states (I_D 0.0 (left) and I_D 0.1 (right))

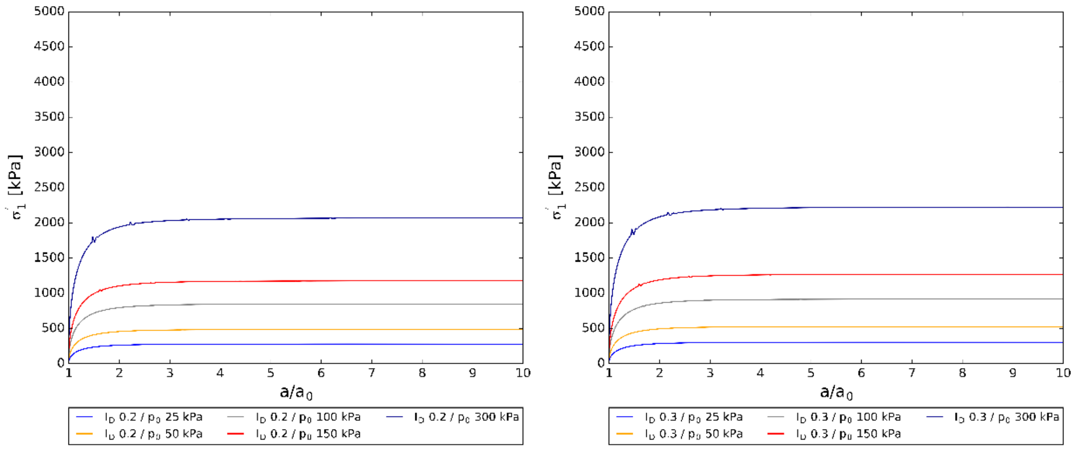

Fig. 114: Pressure-expansion curves for parameter set Ex. 4b and different density states (I_D 0.2 (left) and I_D 0.3 (right))

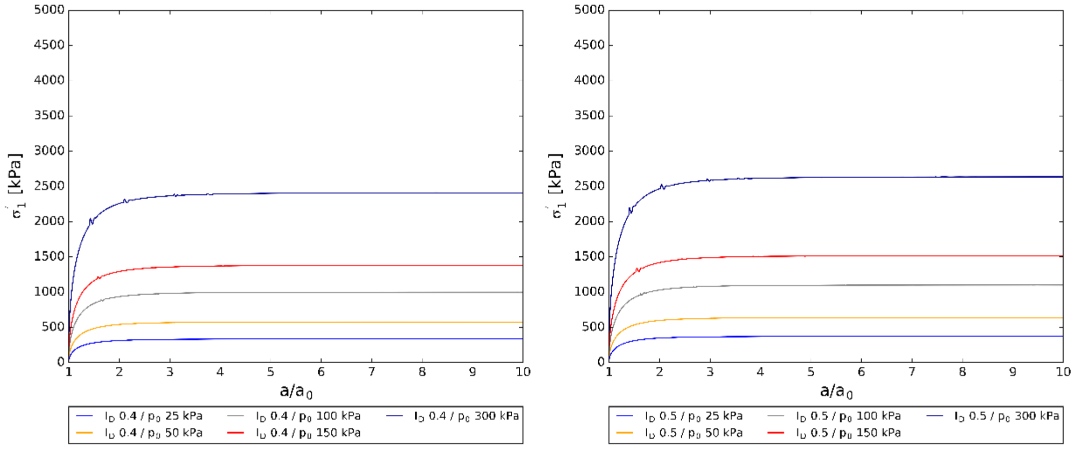

Fig. 115: Pressure-expansion curves for parameter set Ex. 4b and different density states (I_D 0.4 (left) and I_D 0.5 (right))

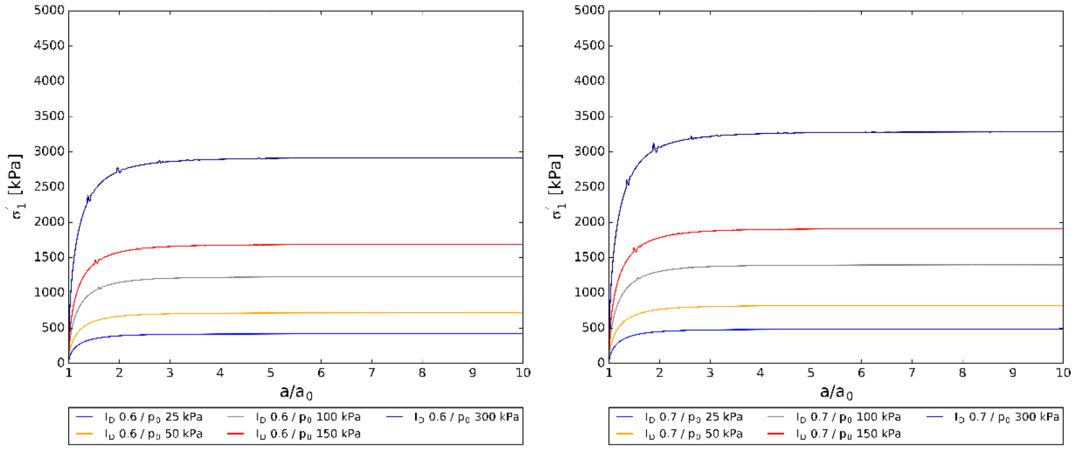

Fig. 116: Pressure-expansion curves for parameter set Ex. 4b and different density states (I_D 0.6 (left) and I_D 0.7 (right))

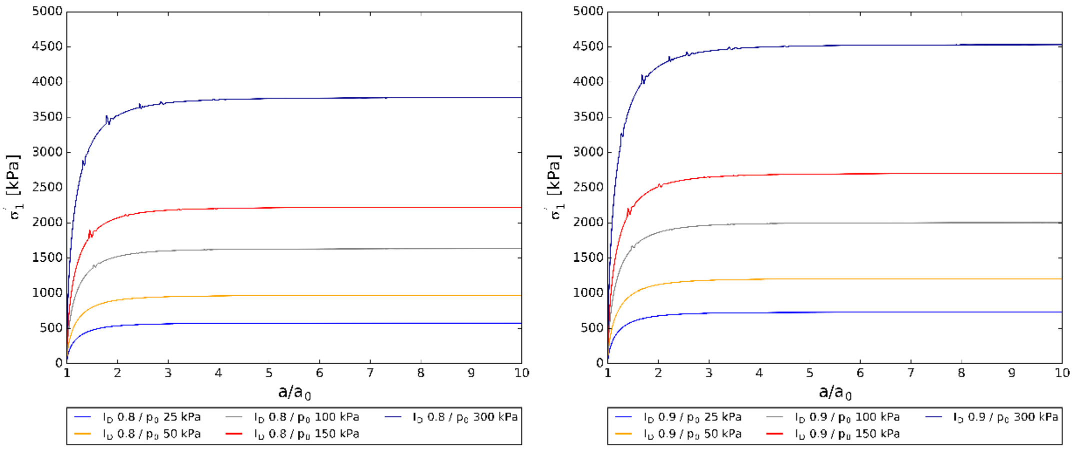

Fig. 117: Pressure-expansion curves for parameter set Ex. 4b and different density states (I_D 0.8 (left) and I_D 0.9 (right))

From Fig. 113 to Fig. 117, it can be seen that the computed pressure-expansion curves are increasing with an increase of relative density I_D and the initial effective mean pressure p_0'. Furthermore, only one parameter set (Ex. 4b) is used, and the only changing variables are the initial void ratio e_{init} and the initial effective mean pressure. In Tab. 27 below, the obtained limit pressure p_{LS} for every finite element analysis are presented.

Tab. 27: Calculated limit pressures for parameter set Ex. 4b

	Limit pressure p_{LS} [kPa]				
p_0 \ I_D	0.0	0.1	0.2	0.3	0.4
25 kPa	242	260	281	305	335
50 kPa	423	452	487	528	577
100 kPa	741	790	848	917	999
150 kPa	1031	1099	1177	1270	1380
300 kPa	1823	1937	2070	2225	2411
p_0 \ I_D	0.5	0.6	0.7	0.8	0.9
25 kPa	372	420	485	578	731
50 kPa	639	717	822	970	1207
100 kPa	1101	1229	1399	1634	2005
150 kPa	1517	1688	1913	223	2703
300 kPa	2636	2919	3283	3781	4532

When comparing the obtained pressure-expansion curves or the calculated limit pressures between the different parameter sets, it can be seen that the ExCalibre set with the reference value for α (Set Ex. 4b) and the "manually" calibrated parameter set HP 1 show similar results whereas, the "pure" ExCalibre set (Ex. 4) results in significantly higher limit pressures, which can be seen very well within the next chapter through the presentation of the p_{LS}-curves. The obtained limit pressures for each parameter set (see Tab. 27, A-Tab. 24 & A-Tab. 25) are necessary to be able to start with the next step of the KIM analysis, namely the determination of the so-called KIM parameters.

6.3 KIM parameters

The limit pressure p_{LS} obtained from the FEA of the spherical cavity expansions (using the three parameter sets) is used in the next step in order to determine the KIM parameters a_1, a_2, a_3, b_1, b_2, and b_3 (see equation (3.13)) through application of the curve fitting procedure developed by Winkler (2018). The obtained values of a_i and b_i for the three hypoplastic parameter sets (HP 1 according to (Thurner, et al., 2019), Ex. 4 and Ex. 4b) are then compared with the "reference" KIM parameters given in (Thurner, et al., 2019). This comparison can be seen in Tab. 28. The KIM parameters are then used to determine the parameters a and b for different relative densities, and subsequently to calculate the limit pressure for different relative densities and different effective mean pressures (as shown in equation (3.7), (3.8) and (3.9)). In order to evaluate the impact of the individual KIM parameters a_i and b_i, the a- and b-values were calculated for different relative densities (see

Fig. 118).

Tab. 28: Calculated KIM parameters for three different hypoplastic parameter sets and KIM parameters given in (Thurner, et al., 2019)

Parameter	KIM parameters (Thurner, et al., 2019)	Set HP 1	Set Ex. 4	Set Ex.4b
a_1	1.666	1.622	-1.520	1.294
a_2	-6.152	-5.330	-8.587	-5.139
a_3	-1.597	-1.535	-1.290	-1.429
b_1	0.835	0.829	1.037	0.860
b_2	0.073	0.078	0.302	0.060
b_3	-1.395	-1.459	-1.416	-1.404

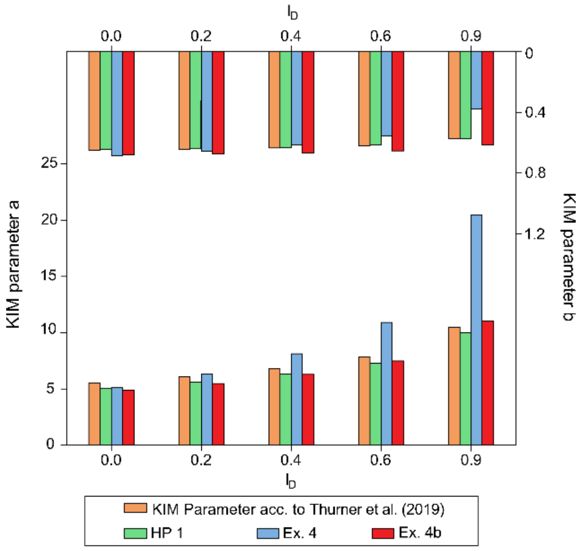

Fig. 118: KIM parameters a and b for selected relative densities

From

Fig. 118 follows that the parameters a and b resulting from the hypoplastic parameter set HP 1 and the set Ex. 4b (α-value of set HP 1) are in agreement with the values given in (Thurner, et al., 2019). For set Ex. 4, the values of a and b only agree for low relative densities, whereas for higher relative densities, both parameters (a and b) show high deviations, with a maximum of around 100%. The final p_{LS} - p_0' curves for different densities I_D (using the according KIM parameters for each parameter set) are shown in Fig. 119 and Fig. 120 below.

The limit pressures, denoted as “p_{LS} explicit”, are the respective results obtained from the spherical cavity expansion analyses for different relative densities and different mean effective pressure p_0'.

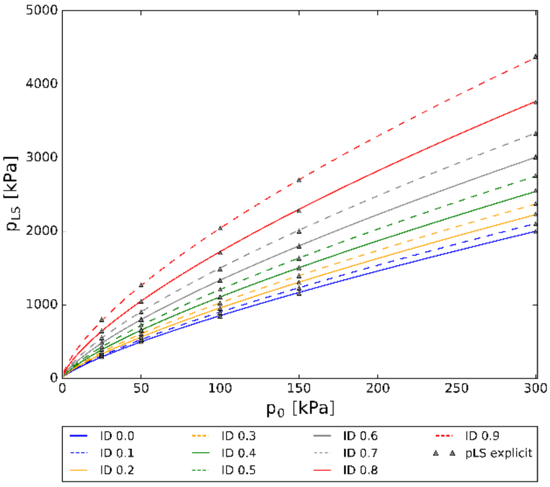

Fig. 119: p_{LS}-p_0' curves for parameter set HP 1

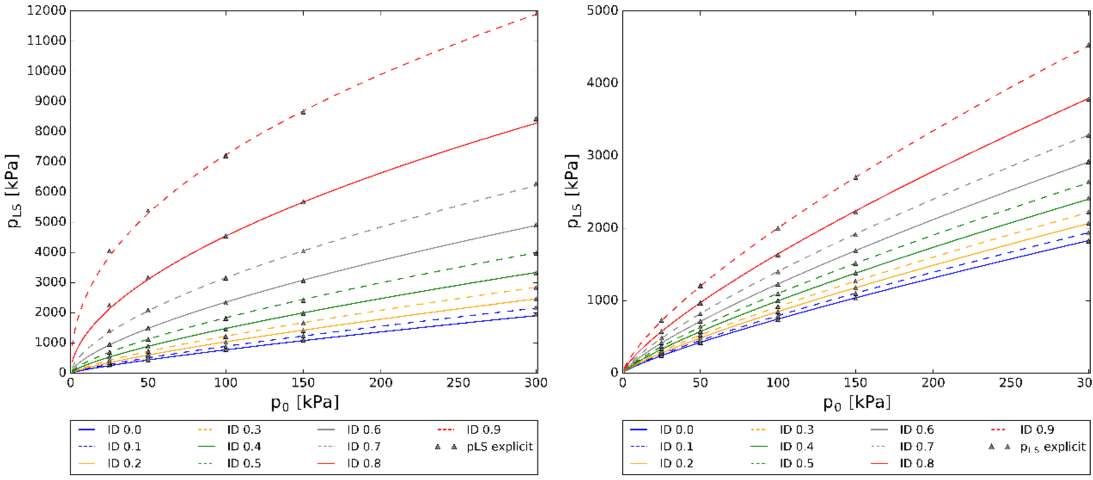

Fig. 120: p_{LS}-$p_0{}'$ curves for parameter sets Ex. 4 (left) and Ex. 4b (right)

Fig. 119 and Fig. 120 indicate that, as already seen from the results of the limit pressures, the p_{LS} curves for parameter sets HP 1 and Ex. 4b are very similar, and the parameter set Ex. 4b shows similar results for low relative densities. However, for I_D values larger than 0.3, the limit pressures show deviations of over 100% with respect to the other parameter sets (HP 1 and Ex. 4b). The last step of the KIM analysis, determination of the cone resistance q_c, is presented within the next chapter 6.4.

6.4 Calculation of cone resistance q_c

The final aim of the KIM is to provide the correlation between the cone resistance q_c and a certain relative density I_D. The first part of the final KIM equation (3.13) represents the shape factor k_q, which only depends on the relative density and the effective mean pressure $p'(z)$. The second part can be calculated using the effective vertical stress $\sigma_v{}'(z)$ and the lateral earth pressure coefficient K_0.

$$p'(z) = \frac{1}{3} * \sigma_v'(z) * (1 + 2 * K_0) \tag{6.1}$$

Because the mean effective pressure $p'(z)$ increases with depth, the calculated void ratios decrease with depth (for a certain relative density). The actual void ratio (related to a certain relative density) can be calculated with the limit void ratios e_c and e_d, where these limit void ratios are pressure-dependent. Hence, according to Bauer (1996), they must be determined through utilization of the effective mean pressure $p'(z)$ and the compression law (see equation (3.2)).

$$I_D = \frac{e_c - e(z)}{e_c - e_d} \rightarrow e(z) = e_c - I_D * (e_c - e_d) \tag{6.2}$$

A change in the void ratio will also affect the density, and subsequently the unit weight of the soil. Thus, a decrease in the void ratios causes an increase in the dry density, as shown below in equations (6.3) and (6.4).

$$\rho_d(z) = \frac{\rho_s}{1 - e(z)} \tag{6.3}$$

$$\gamma(z) = (1 + w) * \rho_d(z) * g \tag{6.4}$$

Where ρ_d is the dry density, ρ_s the grain density and w the assumed water content of the soil. The result of equation (6.4) is used in the next step to calculate the vertical effective pressure $\sigma_v{}'(z)$, which is required to determine the mean effective pressure $p'(z)$. And finally, by using equation (3.13), the cone resistance q_c can be calculated for different values of I_D.

The equations given above are only valid as long as the desired depth is above the ground water table. If the ground water table is above the desired depth that the cone resistance needs to be determined for, it is necessary to determine the saturated density, and, further, the buoyant unit weight γ' of the soil below the ground water table (see equation (6.5) and (6.6)).

$$\rho_{sat}(z) = \frac{\rho_s + (e(z) * \rho_w)}{1 + e(z)} \tag{6.5}$$

$$\gamma'^{(z)} = \rho_{sat}(z) * g - \gamma_w \tag{6.6}$$

In the following figures, the cone resistances for certain relative densities I_D are presented. The results, namely q_c over depth (for all four analyzed material sets), are plotted in Fig. 121 to Fig. 123. The q_c curves over depth for the remaining densities are given within appendix C. For all results, the water content was taken into account with w = 0.2, and the water level was assumed to be below the desired depth of 10 m.

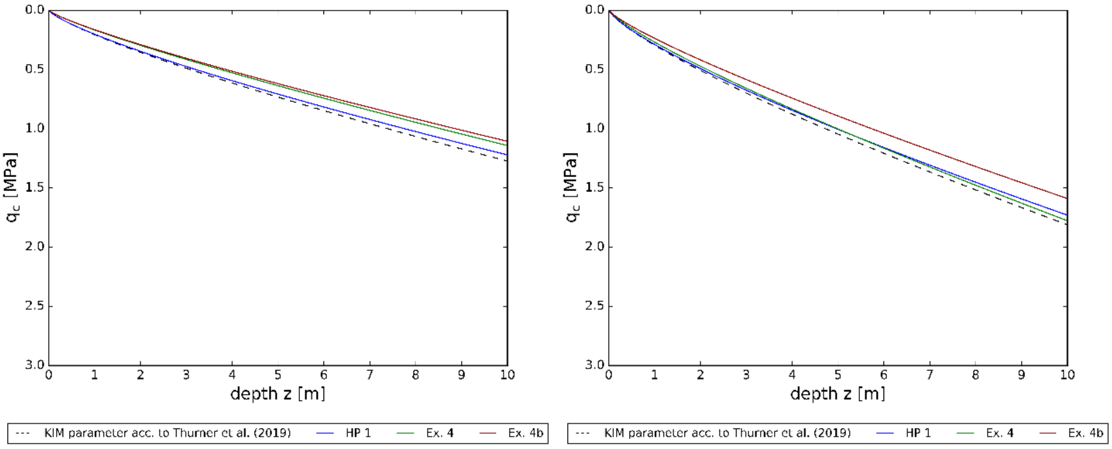

Fig. 121: q_c curves for relative densities I_D = 0.0 (left) and I_D = 0.1 (right)

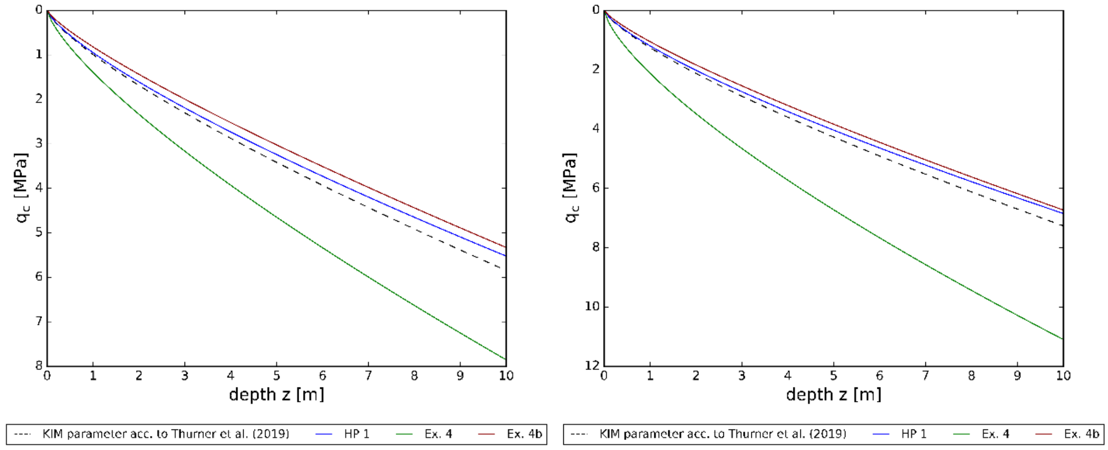

Fig. 122: q_c curves for relative densities I_D = 0.4 (left) and I_D = 0.5 (right)

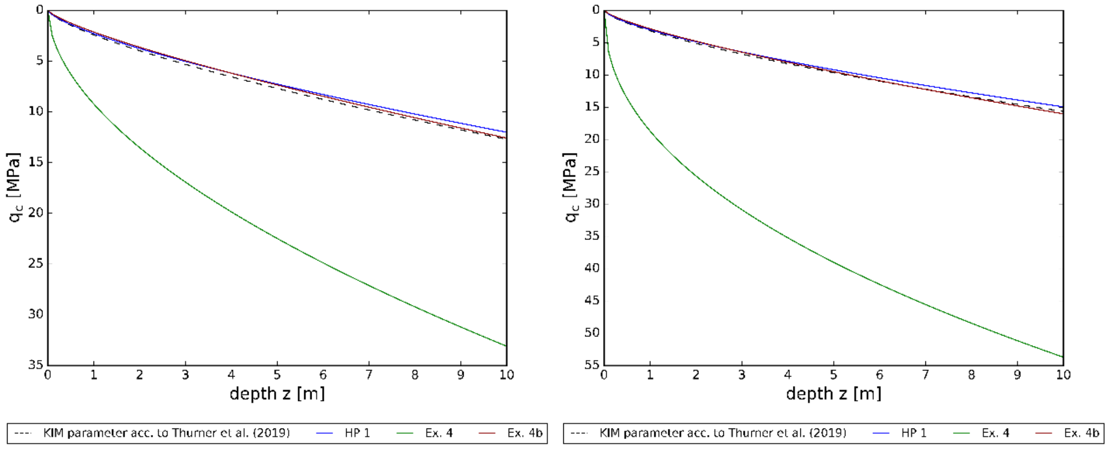

Fig. 123: q_c curves for relative densities I_D = 0.8 (left) and I_D = 0.9 (right)

Similar conclusions to the ones that have been made in chapter 6.2 and 6.3 can also be drawn from Fig. 121 to Fig. 123. The cone resistances obtained from the hypoplastic parameter set HP 1 show, as expected, similar results as obtained with the KIM parameters given in (Thurner, et al., 2019) for all investigated relative densities, whereas the calculated cone resistances for the hypoplastic parameter set of the ExCalibre calibration (Ex. 4) are only similar for low relative densities. With regards to ExCalibre set Ex. 4, significant deviations were found for higher I_D-values ($I_D > 0.3$). However, by changing the magnitude of the parameter α (Ex. 4b), the results again yield somewhat similar q_c-curves for all relative densities. These studies indicate the high sensitivity of the KIM to certain input parameters of the hypoplastic soil model!

6.5 Results of KIM analysis applying the hypoplastic model for crushable sand

Whereas the previous chapter presented a full KIM analysis for different parameter sets based on the original hypoplastic soil model (Von Wolffersdorff, 1996), this chapter presents the results from a full KIM analysis once applying the original hypoplastic soil model and once for the application of the grain crushing model. For these studies, the parameter set HP 1 from Tab. 26 and a second parameter set HP 2 (material parameters for Hokksund sand taken from Cudmani (2000)) was used. Both material parameters can be seen in Tab. 29 and in the following the results of the KIM analysis are presented. In this chapter the results obtained from the application of the original hypoplastic soil model are further denoted as “orig. HP X” and the results obtained from applying the grain cruhsing model are further denoted as “GC HP X”.

Tab. 29: Parameters for HP 1 and HP 2

Material	φ_c [°]	h_s $[MPa]$	n [-]	e_{d0} [-]	e_{c0} [-]	e_{i0} [-]	α [-]	β [-]	C_{u0} [-]	d_{50} [mm]
HP 1	36.3	39	0.53	0.74	1.26	1.45	0.05	1.97	4.0	0.63
HP 2	31	150	0.70	0.53	0.87	1.01	0.09	1.0	2.2	0.43

Before starting with the first step of the KIM analysis, triaxial tests were simulated with the PLAXIS Soil Test Tool for the material sets HP 1 and HP 2 applying both, the original hypoplastic model and the grain crushing model. The results for HP 2 and different applied confining pressures σ_3 are shown below and for material set HP 1 the triaxial test results can be seen in appendix C.

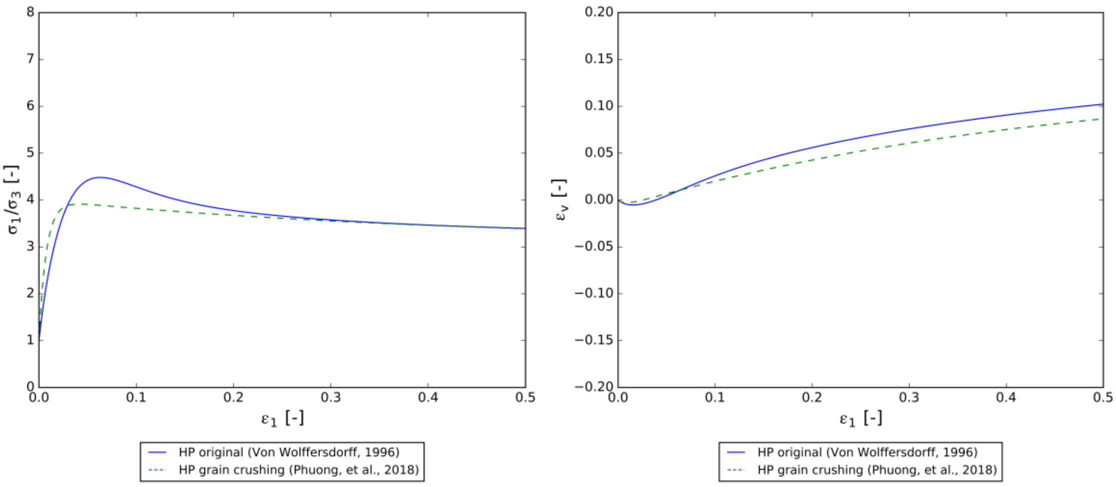

Fig. 124: Triaxial test results for material set HP 2 and σ_3 = 500 kPa – stress ratio vs axial strain (left) and volumetric strain vs axial strain (right)

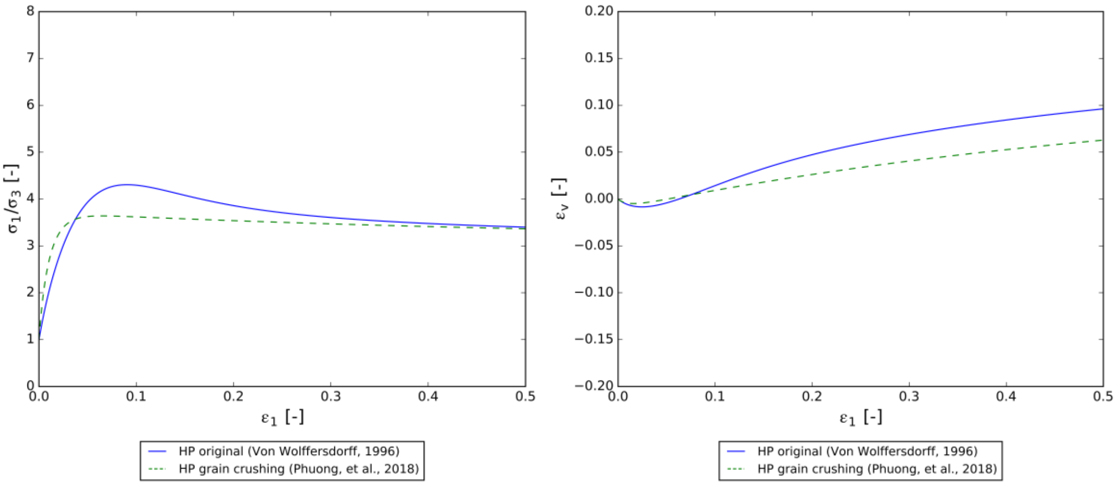

Fig. 125: Triaxial test results for material set HP 2 and σ_3 = 1000 kPa – stress ratio vs axial strain (left) and volumetric strain vs axial strain (right)

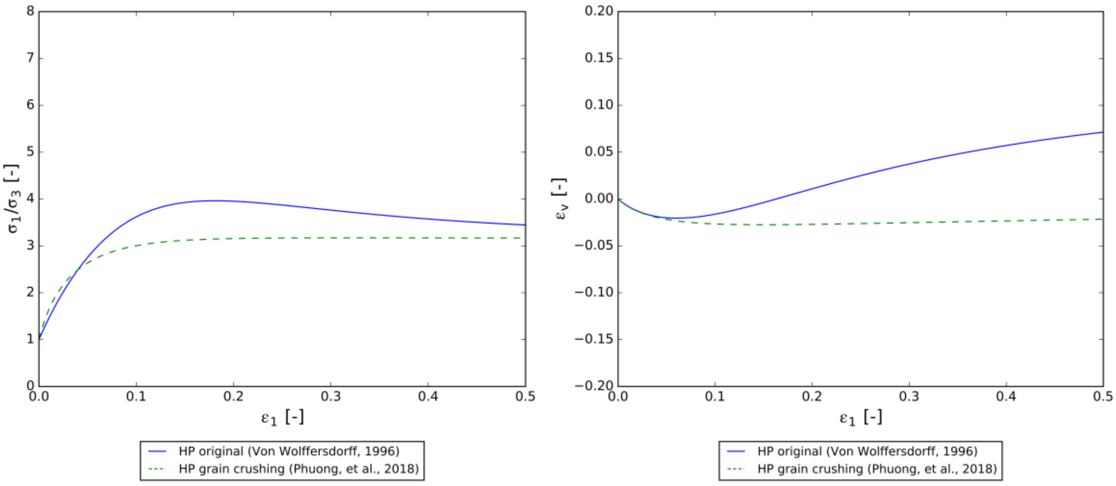

Fig. 126: Triaxial test results for material set HP 2 and σ_3 = 4000 kPa – stress ratio vs axial strain (left) and volumetric strain vs axial strain (right)

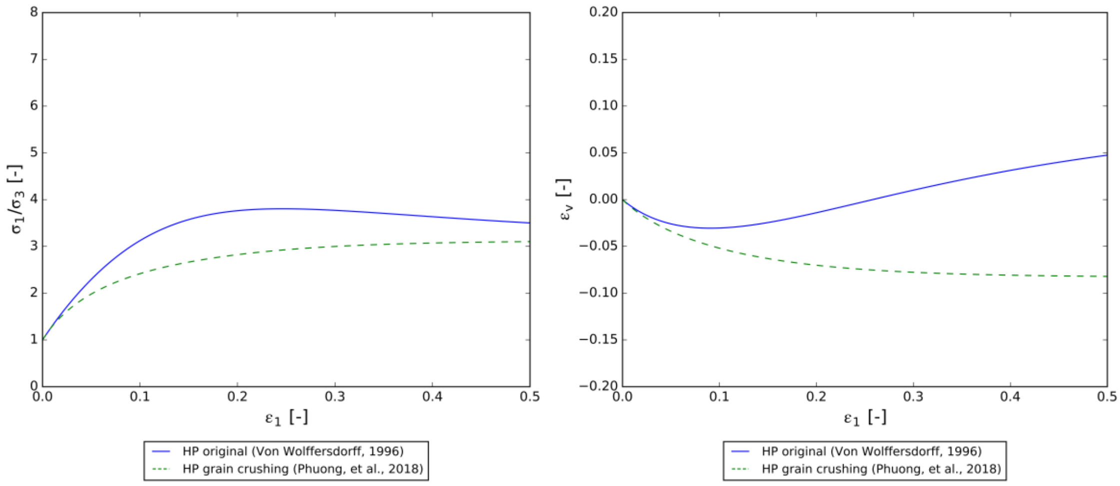

Fig. 127: Triaxial test results for material set HP 2 and σ_3 = 8000 kPa – stress ratio vs axial strain (left) and volumetric strain vs axial strain (right)

From Fig. 124 to Fig. 127 the different stress and strain development during triaxial loading can be observed between the application of the original hypoplastic model and the hypoplastic model for grain crushing. However, the final stresses (after large deformations) are similar for the original hypoplastic model and the grain crushing model.

SCE analyses and limit pressures

All the obtained pressure-expansion curves for all four analyzed cases (orig. HP 1, GC HP 1, orig. HP 2, GC HP 2) as well as the limit pressures for orig. HP 1 and GC HP 1 are presented in appendix C. The resulting limit pressures for orig. HP 2 and GC HP 2 can be seen in Tab. 30 and Tab. 31.

Tab. 30: Calculated limit pressures for orig. HP 2

	Limit pressure p_{LS} [kPa]				
p_0 \ I_D	0.0	0.1	0.2	0.3	0.4
25 kPa	514	557	605	654	726
50 kPa	828	885	953	1034	1133
100 kPa	1338	1424	1523	1641	1788
150 kPa	1776	1882	2009	2157	2335
300 kPa	2888	3048	3232	3449	3709

p_0 I_D	0.5	0.6	0.7	0.8	0.9
25 kPa	813	928	1094	1353	1840
50 kPa	1258	1436	1652	1999	2628
100 kPa	1967	2198	2515	2981	3790
150 kPa	2558	2841	3224	3778	4715
300 kPa	4026	4426	4953	5698	6908

Tab. 31: Calculated limit pressures for GC HP 2

	Limit pressure p_{LS} [kPa]				
p_0 I_D	0.0	0.1	0.2	0.3	0.4
25 kPa	514	552	599	654	722
50 kPa	828	885	952	1033	1134
100 kPa	1338	1424	1523	1641	1787
150 kPa	1775	1882	2007	2156	2335
300 kPa	2888	3047	3231	3449	3708
p_0 I_D	0.5	0.6	0.7	0.8	0.9
25 kPa	810	932	1093	1353	1851
50 kPa	1260	1424	1669	2002	2629
100 kPa	1966	2198	2515	2981	3790
150 kPa	2558	2842	3223	3778	4715
300 kPa	4026	4426	4953	5698	6908

For the materials HP 1 and HP 2 the obtained pressure-expansion curves and thus the resulting limit pressures show nearly no difference between the application of the original hypoplastic soil model and the grain crushing model. Hence, applying the original hypoplastic model or the grain crushing model delivers similar results.

KIM parameters

After the determination of the limit pressures, the KIM parameters are obtained by means of a curve fitting procedure (see Tab. 32). As expected, between the orig. HP 1 and GC HP 1 only small differences occur for the resulting KIM parameters. A reason for these small differences may also be the fact, that for GC HP 1 the full KIM analysis was executed fully automatized by python scripting (see chapter 6.6). The KIM parameters obtained for material HP 2 show also only very small differences. Hence, again it can be concluded, that for both materials (HP 1 & HP 2), there is no difference between the application of the original hypoplastic model and applying the grain crushing model (at least for these material sets).

Tab. 32: Calculated KIM parameters for different hypoplastic parameter sets

Parameter	orig. HP 1	GC HP 1	orig. HP 2	GC HP 2
a_1	1.622	1.589	2.928	2.949
a_2	-5.330	-5.434	-5.422	-5.402
a_3	-1.535	-1.540	-1.430	-1.430
b_1	0.829	0.832	0.781	0.782
b_2	0.078	0.083	0.116	0.117
b_3	-1.459	-1.480	-1.380	-1.380

The conclusion drawn before can be proved by the p_{LS}-curves shown in Fig. 128 and Fig. 129.

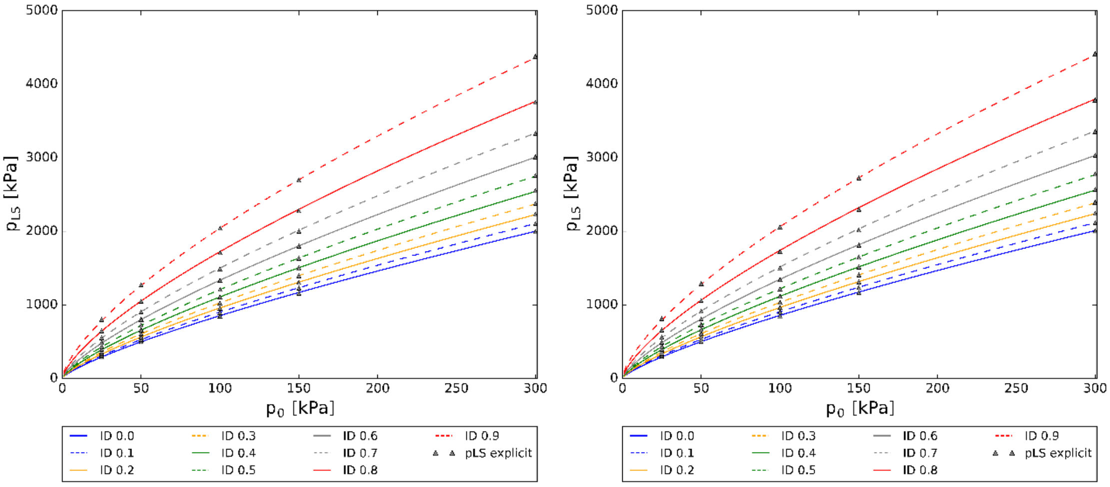

Fig. 128: p_{LS}-p_0' curves for orig. HP 1 (left) and GC HP 1 (right)

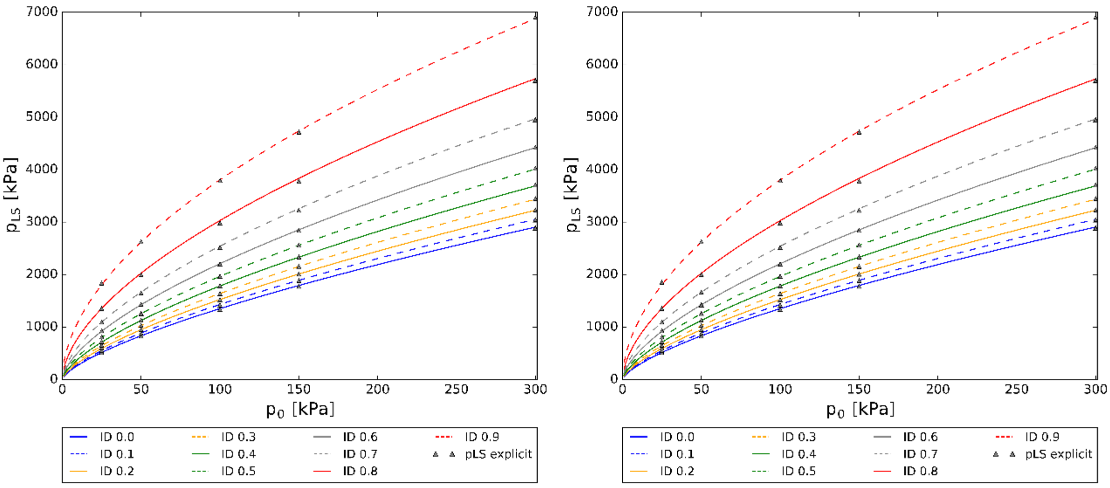

Fig. 129: p_{LS}-$p_0{}'$ curves for orig. HP 2 (left) and GC HP 2 (right)

Cone resistance

The final step of the KIM analysis consists of the determination of the cone resistance q_c and for both materials, HP 1 and HP 2, the cone resistances are compared again between the application of the original hypoplastic model and applying the grain crushing model. The results for some selected density states are presented from Fig. 130 to Fig. 133 for both materials and for the remaining relative densities I_D the results can be seen in appendix C. As expected from the previous conclusions, applying both, the original hypoplastic soil model or the grain crushing model, results in the same magnitudes for the cone resistance q_c.

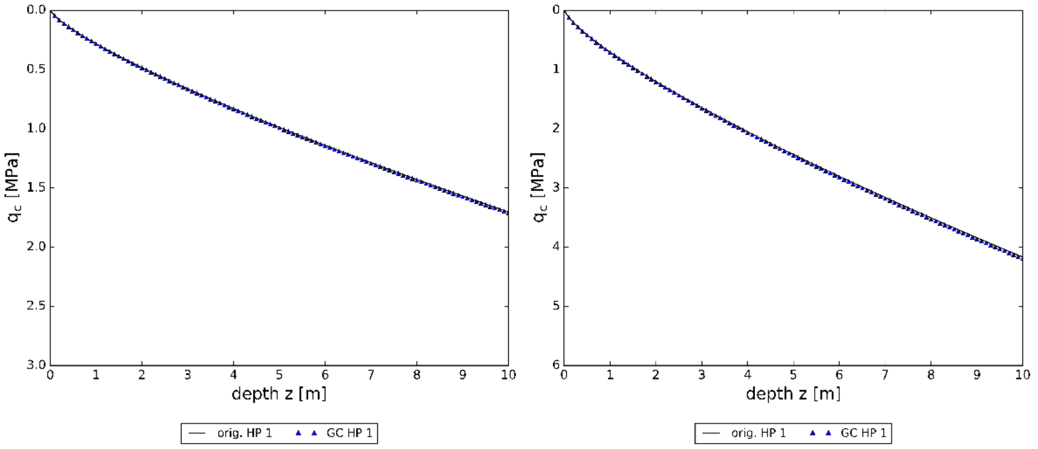

Fig. 130: q_c-curves for material HP 1 and different relative densities (I_D = 0.1 (left) and I_D = 0.3 (right))

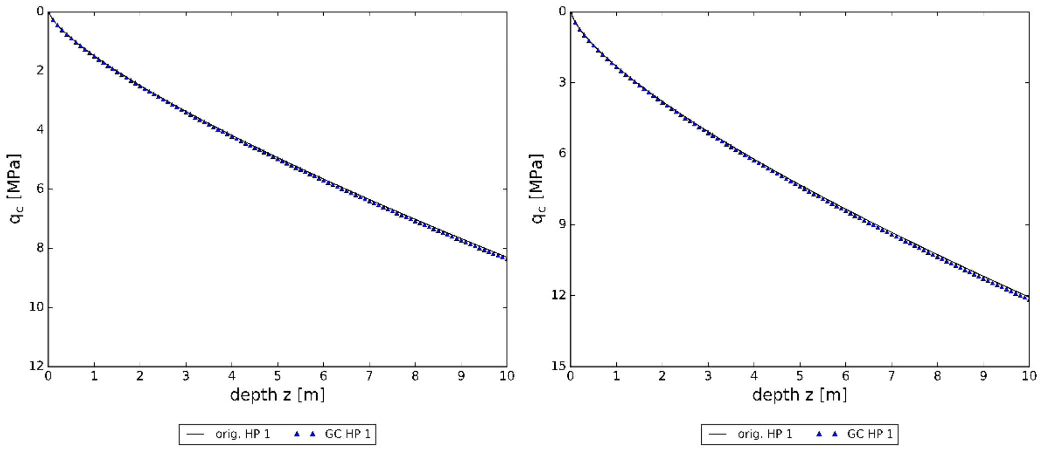

Fig. 131: q_c-curves for material HP 1 and different relative densities ($I_D = 0.6$ (left) and $I_D = 0.8$ (right))

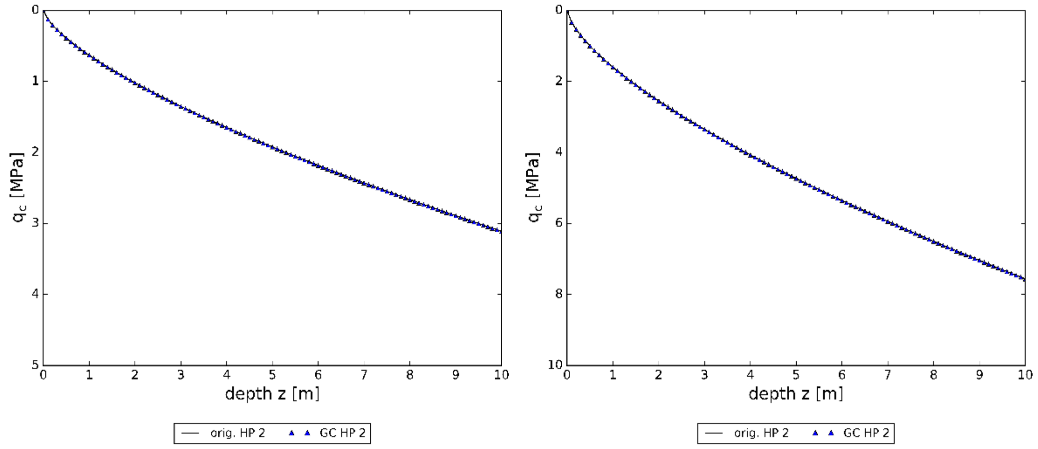

Fig. 132: q_c-curves for material HP 2 and different relative densities ($I_D = 0.1$ (left) and $I_D = 0.3$ (right))

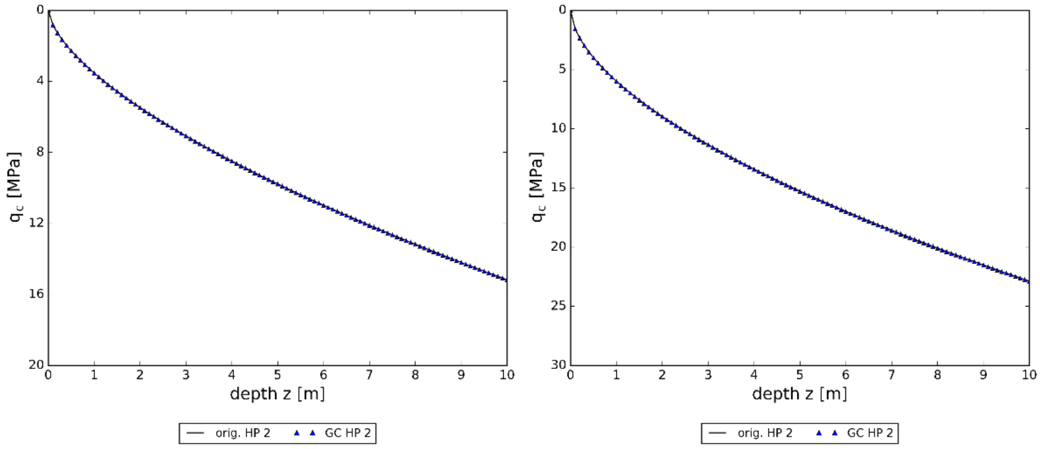

Fig. 133: q_c-curves for material HP 2 and different relative densities ($I_D = 0.6$ (left) and $I_D = 0.8$ (right))

6.6 Full automation of whole KIM analysis

Due to the fact that a full KIM analysis is very time consuming the final goal of the performed research is to develop a fully automatized KIM analyzing process. In the end, the user should only need to provide the hypoplastic parameter set within an Excel-worksheet and define the directory within the Python script. Parts of the final code can be seen within appendix C.

Winkler (2018) already automated the first step of the KIM analysis, including the automatic creation of 50 different finite element models ($I_D = 0.0$ to 0.9 and $p_0 = 25$ to 300 kPa) as well as the calculation and saving of all of these models. The respective python code can be seen in (Winkler, 2018) and was only extended slightly for the full automation. First, the hypoplastic parameters must be read in from the csv-file (see appendix C), and then the extended code from Winkler (2018) was applied in order to automatically create and calculate all 50 different finite element models.

The next step of the KIM analysis is probably the most time consuming and is related to the output of the results of the FEA. Without any automation of this process step, it was originally necessary to copy the corresponding stresses and deformations for every stress point and node (for each of the 50 FEM) manually to an Excel-worksheet, where all results were then averaged in order to obtain the pressure-expansion curves. With python remote scripting, it is possible to automate this output and save the results as txt-files in the desired directory (see appendix C).

Before determining the KIM parameters by means of a curve-fitting procedure, the pressure-expansion curves are plotted, and the limit pressures are determined and saved as txt-file for every density state and every initial effective mean pressure. An example of the determination of the limit pressure is shown in appendix C.

With the previously obtained limit pressures, the next step consists of the determination of the KIM parameters a_i and b_i. Based on a curve-fitting procedure that is provided by Winkler (2018) and executed within EXCEL, the whole process is automated with Python. The single steps of the curve-fitting procedure in Excel are detailed in (Winkler, 2018). The first step of the curve fitting procedure, which estimates the a and b values, can be seen in appendix C for the a-values. It can be seen in Tab. 33 that the automated curve-fitting procedure delivers satisfying results. The KIM parameters are obtained through python, the curve-fitting is done through EXCEL and the given KIM parameters (Thurner, et al., 2019) are compared for the parameter set HP 1.

Tab. 33: KIM parameters from (Thurner, et al., 2019), EXCEL curve-fitting & Python curve-fitting

Parameter	KIM parameters (Thurner, et al., 2019)	EXCEL	Python
a_1	1.666	1.622	1.587
a_2	-6.152	-5.330	-5.390
a_3	-1.597	-1.535	-1.540
b_1	0.835	0.829	0.833
b_2	0.073	0.078	0.084
b_3	-1.395	-1.459	-1.490

For a further verification of the python sript a full KIM analysis was performed for three materials taken from Cudmani (2000), namely Ticino sand, Toyoura sand and Hokksund sand. From Tab. 34 to Tab. 36 the KIM parameters from Cudmani (2000) are compared to the KIM parameters obtained from the automated KIM analysis by applying the python script.

Tab. 34: KIM parameters Ticino sand

	a_1	a_2	a_3	b_1	b_2	b_3
(Cudmani, 2000)	3.055	-6.686	-1.355	0.794	0.133	-1.379
Python	2.590	-6.952	-1.400	0.802	0.133	-1.350
|△|[%]	18.0	3.8	3.2	1.0	0.0	2.1

Tab. 35: KIM parameters Toyoura sand

	a_1	a_2	a_3	b_1	b_2	b_3
(Cudmani, 2000)	1.944	-6.814	-1.439	0.807	0.161	-1.377
Python	2.056	-6.342	-1.470	0.815	0.159	-1.390
|△|[%]	5.4	7.4	2.1	1.0	1.3	1.0

Tab. 36: KIM parameters Hokksund sand

	a_1	a_2	a_3	b_1	b_2	b_3
(Cudmani, 2000)	2.735	-6.347	-1.402	0.773	0.138	-1.425
Python	2.928	-5.422	-1.430	0.781	0.116	-1.380
|△|[%]	6.6	17.1	2.0	1.0	19.0	3.3

From Tab. 34 to Tab. 36 it can be seen, that the python script delivers quite good results for the KIM parameters compared to the ones given in (Cudmani, 2000). The accuracy of the Python curve-fitting procedure can be increased by increasing the number of iteration steps (within the curve fitting procedure), however, this will also cause calculation time to increase.

The last calculation step of the Python script is related to the determination of the cone resistance q_c over depth. Therefore, the equations from chapter 6.4 are applied within the script. Parts of this are shown in appendix C. Finally, for all the resulting plots of the script, the “matplotlib” package is used for plotting the q_c-curves (appendix C). The flowchart shown in Fig. 134 gives an overview of the prebviously described step-by-step procedure of a full KIM analysis. Furthermore, within appendix C, a detailed description for the correct application of the “full_automated_KIM”-script is given.

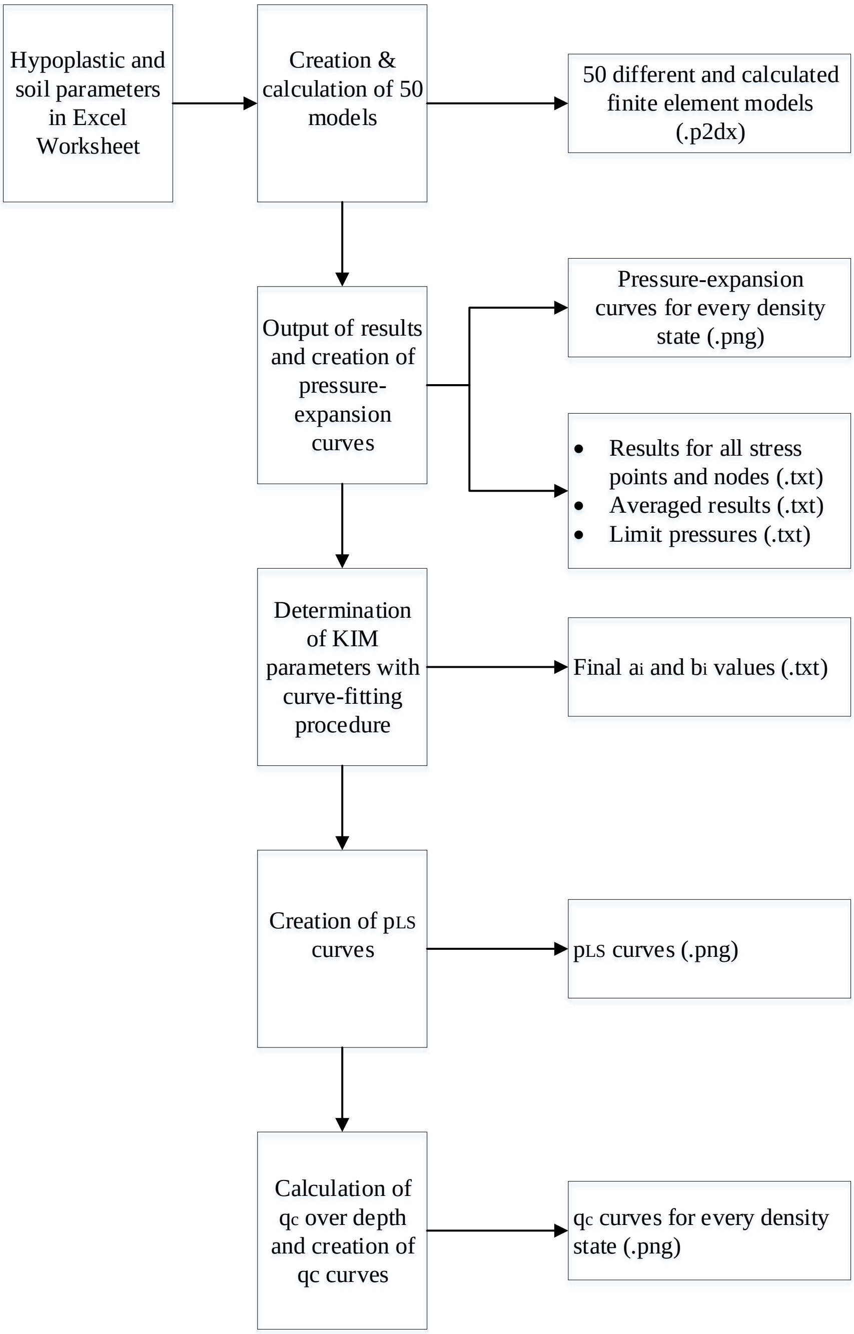

Fig. 134: Flow chart of full KIM analysis process

7 Press Replace Method

Since the Karlsruhe Interpretation Method is primary used as a correlation method for the cone resistance q_c and the relative density I_D, the aim of this chapter is to investigate another numerical technique used to model cone penetration tests (CPT), namely the Press-Replace method (PRM). First, a literature review is presented, followed by a detailed description of the implementation of the PRM within PLAXIS. Finally, the results of the finite element analyses are compared to results given in literature, and further required tasks related to the PRM are formulated.

7.1 Literature study

With the relatively novel numerical technique, known as the Press-Replace method, the penetration of an object into a continuum can be modelled by means of standard finite element analysis. The PRM was first applied by Andersen et al. (2004) in order to model the penetration of a suction pile in clays. Based on this first approach, Engin (2013) and Tehrani et al. (2016) applied the PRM to analyze the process of pile penetration. Furthermore, Xian (2017) used the Press-Replace method for numerical investigations of cone penetration tests in clays.

Numerical approaches to derive solutions for cone penetrations tests are very rare and often only possible by making simplifications to the problem, as seen by the spherical cavity expansion. It is also true that analytical approaches are very difficult to solve due to the high complicated boundary value problem. However, the results of preliminary studies regarding the application of the PRM performed by Engin et al. (2015), Tehrani et al. (2016) and Xian (2017) showed that this method is able to represent the stress situation in soil during deep penetration processes (Xian, 2017).

A key issue regarding the numerical modelling of cone penetration tests is related to mesh distortion and the interaction between the cone and the soil. To handle these problems, the initial mesh is preserved, whereas the material properties of the penetrated volume are subsequently updated at the beginning of each phase. Therefore, a change in the global stiffness matrix is caused. Compared to other numerical approaches, such as the Material Point Method (MPM) or the Coupled Eulerian Lagrangian (CEL) method, there is no need for updating of the mesh when applying the Press-Replace method. Due to this, the two big advantages of the PRM are first faster calculation times and second the possibility of applying sharp corners (Engin, et al., 2015; Tehrani, et al., 2016).

The Press-Replace technique consists of an alternating prescribed displacement phase and a geometry update, in which the penetrated soil is replaced by the cone material. The updated geometry is used to model the advance of the cone into the soil, which is numerically achieved through a change in the global stiffness matrix at the beginning of every geometry update (replace phase). In relation to the step-by-step geometry update, the PRM further comprises of a displacement boundary (Ditrichlet boundary) at every phase, which is located at the top of the cone (or pile) and causes a penetration downwards. For a better understanding, the mathematical formulas are given by equations (7.1) to (7.3), and Fig. 135 illustrates the step-by-step phases of the displacement controlled finite element analysis (Engin, et al., 2015; Tehrani, et al., 2016; Xian, 2017).

$$\begin{bmatrix} K_{11}^{i} & \cdots & K_{1,n-1}^{i} & K_{1,n}^{i} \\ \vdots & \cdots & \vdots & \vdots \\ K_{n-1,j}^{i} & \cdots & \vdots & K_{n-1,n-1}^{i} \\ K_{n,1}^{i} & \cdots & K_{n-1,n-1}^{i} & K_{n,n}^{i} \end{bmatrix} \begin{bmatrix} \Delta u_{1}^{i} \\ \vdots \\ \Delta u_{n-1}^{i} \\ \Delta u_{n}^{i} \end{bmatrix} = \begin{bmatrix} \Delta f_{1}^{i} \\ \vdots \\ \Delta f_{n-1}^{i} \\ \Delta f_{n}^{i} \end{bmatrix} \tag{7.1}$$

or

$$K^{i} \Delta u^{i,j} = \Delta f^{i,j} \tag{7.2}$$

Where K^i is the updated global stiffness matrix at phase i, $\Delta u^{i,j}$ the displacement increment of phase i and $\Delta f^{i,j}$ the load increment of phase i, which can be determined as follows:

$$\Delta f^{i,j} = f_{ex}^{i} - \int B^{T} \sigma^{j-1} dV \tag{7.3}$$

where f_{ex}^{i} is the external load vector, B^T is the matrix containing the derivations of the shape functions, and $\sigma^{i,j}$ is the stress state of phase i (where $\sigma^{i,0}$ is the stress state at the beginning of phase i).

Fig. 135 shows that the whole penetration process (replace phases) is subdivided into several slices with a certain thickness t_s. The increment of the prescribed displacement between two "Press"-phases (i and i + 1) is equal to the slice thickness t_s. Because this method is based on the small-strain theory, the global stiffness matrix only takes into account the change of material within every "Replace"-phase. For a more detailed description of the PR-technique, reference is made to Engin et al. (2015), Tehrani et al. (2016) and Xian (2017).

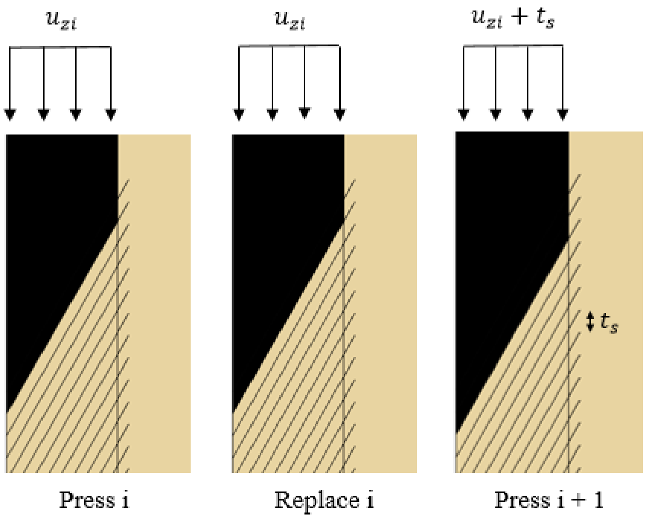

Fig. 135: Different phases of Press-Replace method

7.2 Finite element analyses

First, two finite element analyses found in literature were remodeled with PLAXIS. The buildup of a finite element model by means of the Press-Replace method has the final aims of modelling cone penetration tests and comparing the results obtained from the KIM analysis. These FEA comprise of one analysis of jacked piles (Tehrani, et al., 2016) and one CPT modelling from (Xian, 2017).

7.2.1 Pile penetration

General aspects

An axisymmetric model with 15-noded triangular elements is used and the model dimensions are shown in **Fehler! Verweisquelle konnte nicht gefunden werden.** (left). Further, continuous jacking of a circular-cross-section pile with a diameter of B = 0.3 m is considered and a surcharge layer with an unit weight of γ = 100 kN/m³ and a height of h = 0.5 m ($\sigma = 50\ kPa$) is modelled to avoid numerical problems (Tehrani, et al., 2016).

Materials and interfaces

For remodeling the FEA of Tehrani et al. (2016) the hypoplastic parameters for Baskarp sand are given in Tab. 37, and with $e_{d0} = e_{min}$ and $e_{i0} = e_{max}$, the initial void ratios e can be determined with $e = e_{max} - I_D * (e_{max} - e_{min})$ for the two considered density states ($I_D = 0.4$ & $I_D = 0.8$). Fig. 136 (right) shows a schematic representation of the interfaces with the properties given in Tab. 38.

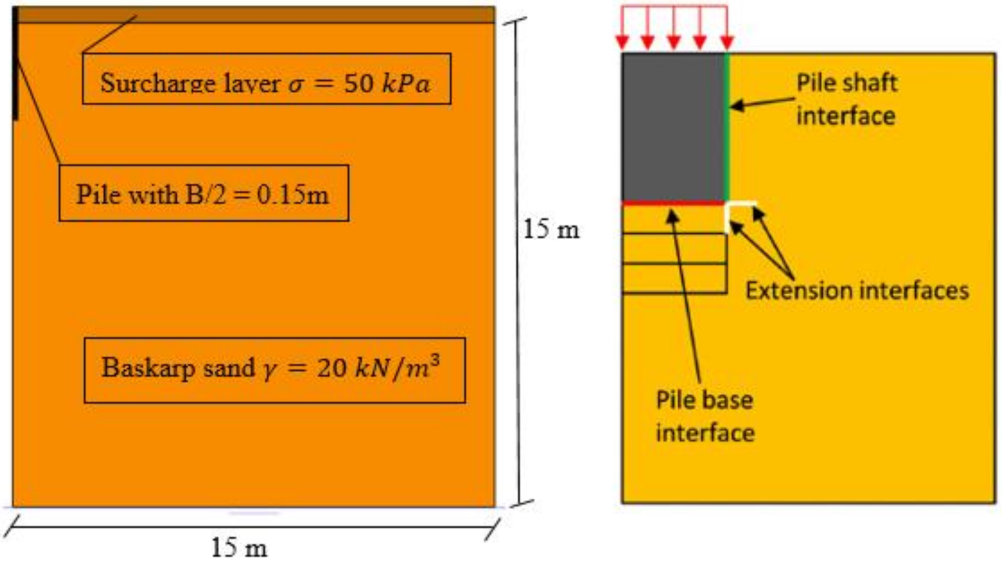

Fig. 136: Model dimension (left) and interface elements (right) (Tehrani, et al., 2016)

Tab. 37: Hypoplastic parameters for Baskarp sand

Material	φ_c [°]	h_s $[MPa]$	n [-]	e_{d0} [-]	e_{c0} [-]	e_{i0} [-]	α [-]	β [-]
Baskarp sand	30	4,000	0.42	0.548	0.929	1.08	0.12	0.96

Tab. 38: Interface properties

Material	I_D [%]	E_{oed} $[MPa]$	c_{ref} [kPa]	δ [°]	ψ [°]
Pile shaft (pile base)	40	60.88	0	27.5	0
Extension	40	75.15	1000	30.0	0
Pile shaft (pile base)	80	179.88	0	27.5	0
Extension	80	222.10	1000	30.0	0

The pile is modelled as linear-elastic with a Young's modulus of E = 30 GPa and a Poisson's ratio of $\nu = 0.3$. Tehrani et al. (2016) considers the pile base interface with the same properties as the pile shaft interface, and with regards to the extension interfaces, a cohesion of c = 1 MPa is applied to avoid any relative slippage between the extended interfaces and the nearby soil and to ensure that the shear strength (at the extension interfaces) is always higher than the shear stress in the soil (Tehrani, et al., 2016).

Construction phases

According to Engin (2013), the proposed slice thickness in the PRM ranges from B/10 to B/8, and hence in this FEA, a slice thickness of B/10 = 0.03 m is applied. In total, 100 slices are required to model the pile that has been jacked down to 10*B (3 m) below the ground level. The thickness of slices (B/10) is also equal to the displacement increment between the single “Press”-phases. For all phases, the settings were chosen as follows:

- Tolerated error of 1%
- Max load fraction per step: 0.05
- Desired min number of iterations: 6
- Desired max number of iterations: 15
- Arc-length control type: Off

The line displacement is based on the top of the pile, with displacement in the x-direction set to “fixed” and displacement in the y-direction set to “prescribed”, with negative magnitudes. At the start, the initial stresses are created by applying the K_0-procedure and deactivating all interfaces and prescribed displacements. The first few calculation phases, including the activated interfaces as well the applied displacements, are shown in Fig. 137 and Fig. 138.

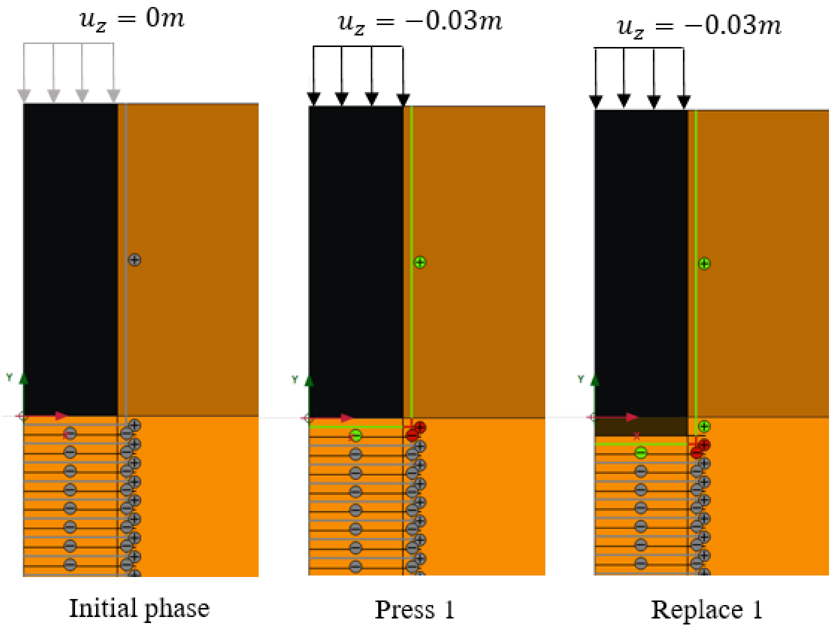

Fig. 137: Construction phases PRM

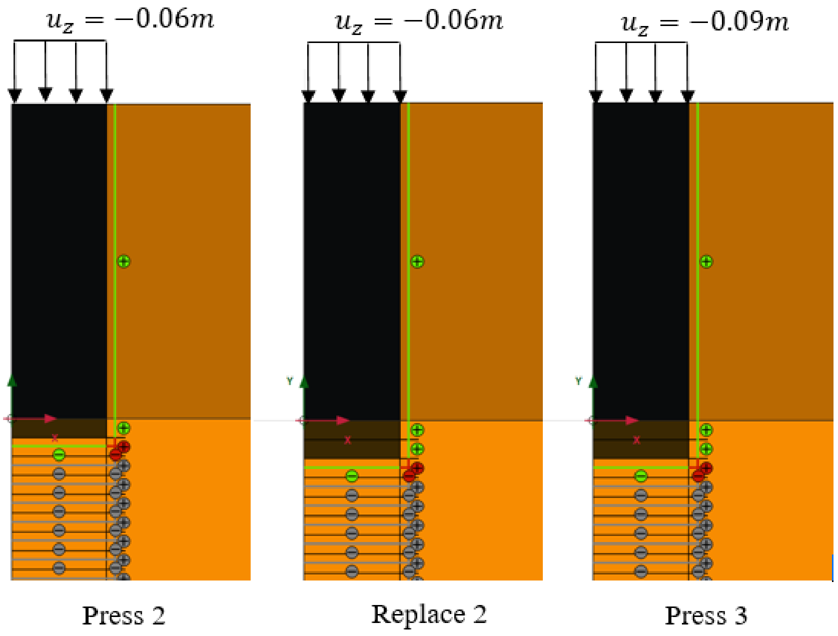

Press 2 Replace 2 Press 3

Fig. 138: Construction phases PRM

Fig. 137 and Fig. 138 show the first few construction phases, for which the extensions interfaces are colored red (see Tab. 38) and the pile shaft and pile base interfaces are colored green (see Tab. 38). Furthermore, it must be mentioned that the part of the pile within the surcharge layer is modelled with the same material parameters as described above, but with a unit weight of $\gamma = 100$ kN/m³ to provide a consistent surcharge layer for the whole model.

Results

To verify the calculations made, some results from literature (Tehrani, et al., 2016) were taken and compared with the obtained results of the FEA.

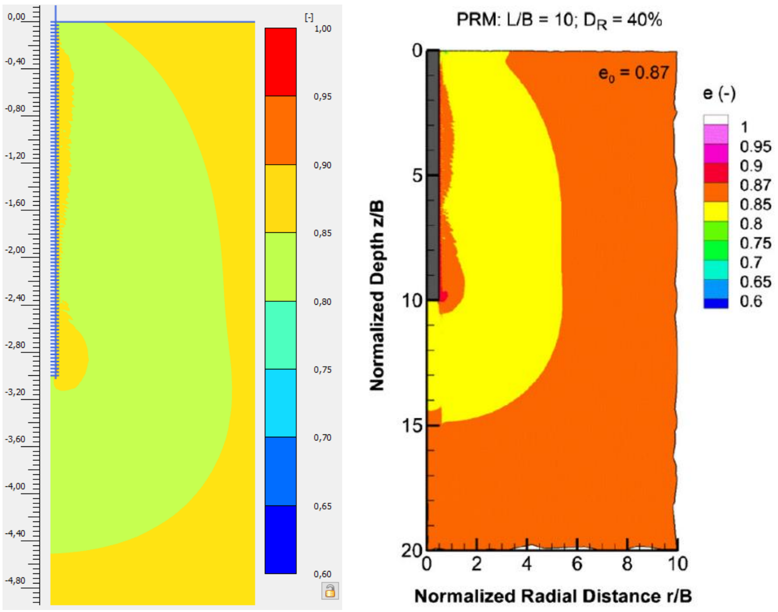

Fig. 139: Void ratio after 10B pile penetration for a relative density of $I_D = 0.4$: FEA (left) and results from literature (Tehrani, et al., 2016) (right)

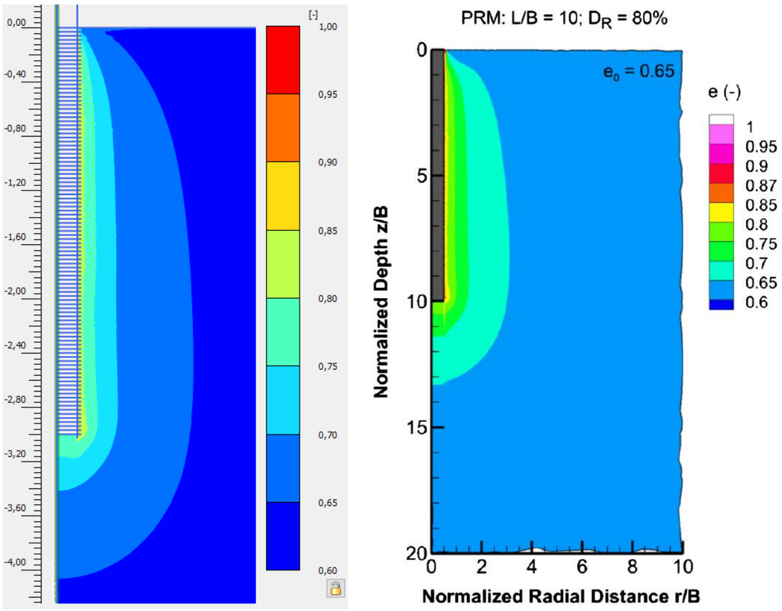

Fig. 140: Void ratio after 10B pile penetration for a relative density of $I_D = 0.8$: FEA (left) and results from literature (Tehrani, et al., 2016) (right)

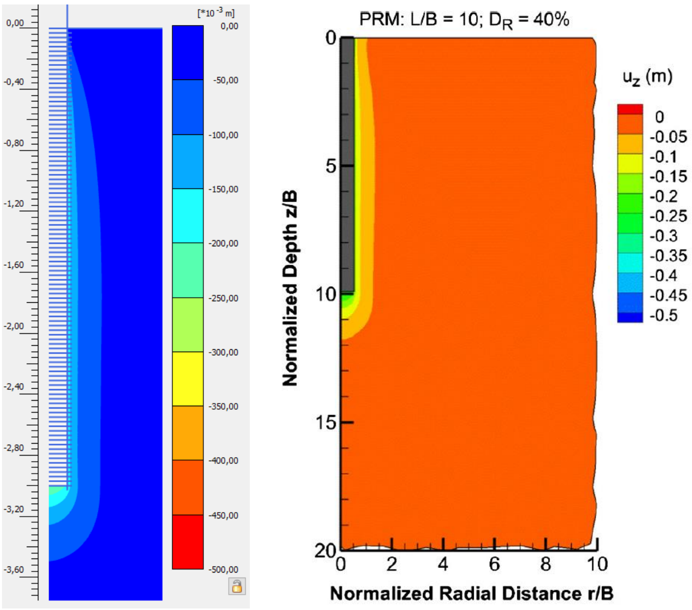

Fig. 141: Vertical displacements after 10B pile penetration for a relative density of $I_D = 0.4$: FEA (left) and results from literature (Tehrani, et al., 2016) (right)

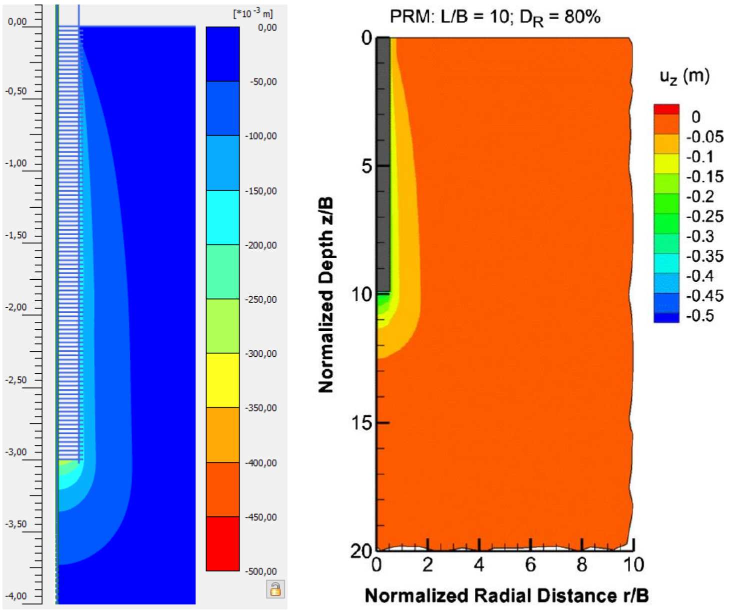

Fig. 142: Vertical displacements after 10B pile penetration for a relative density of $I_D = 0.8$: FEA (left) and results from literature (Tehrani, et al., 2016) (right)

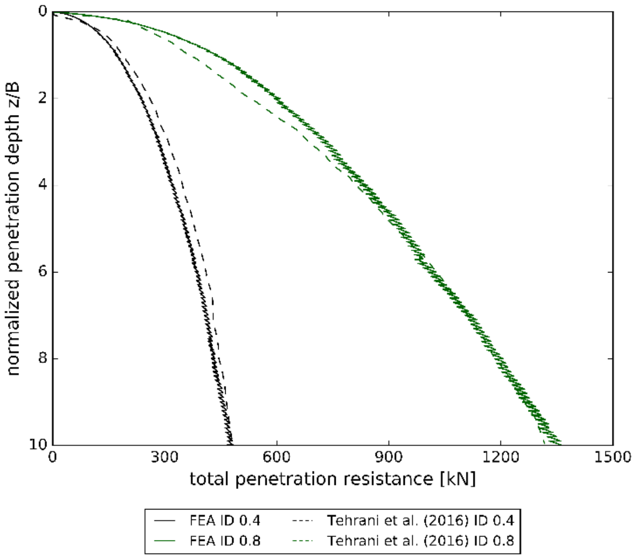

Fig. 143: Total penetration resistance during pile installation using PRM

With regards to the results presented in Fig. 139 to Fig. 143, it is shown that the results obtained from the FEA are similar to the results from literature (Tehrani, et al., 2016). Notably, the development of the total penetration resistance with the penetration depth is nearly equal. Hence, it can be concluded that the PRM was correctly implemented within PLAXIS. The next section presents the application of the PRM for the modelling of cone penetration.

7.2.2 Cone penetration

General aspects

Similarly to before, an axisymmetric model with 15-noded triangular elements is used with finite element model dimensions shown in Fig. 144. Furthermore, a cone with a diameter of D = 0.036 m is initially embedded at depth of 5D (0.18 m), and a surcharge layer with an unit weight of γ = 800 kN/m³ and a height of h = 0.05 m ($\sigma = 40\ kPa$) is modelled to create initial stresses (Xian, 2017).

Materials

The material for the soil and the interfaces, as well as the cone, are given in Tab. 39. The parts of the surcharge layer (cone$_{\text{surcharge}}$ & soil$_{\text{surcharge}}$) are modelled with the same parameters as given in Tab. 39, except that for both, a unit weight of γ = 800 kN/m³ is applied to ensure an initial stress of σ = 40 kPa. Also, the undrained shear strength of the soil$_{\text{surcharge}}$ was taken with s_u = 1 kPa into account. Different to the application of the PRM for the jacked piles, Xian (2017) does not define any properties for the extension interfaces of the material that is used for the FEA here. Usually, the extension interfaces are modelled to reduce the stress fluctuations at the intersection between the top of the cone and the bottom of the penetrometer.

To investigate the influence of the extension interfaces, finite element analyses are performed with and without extension interfaces (with the same parameters as soil material without any strength reduction).

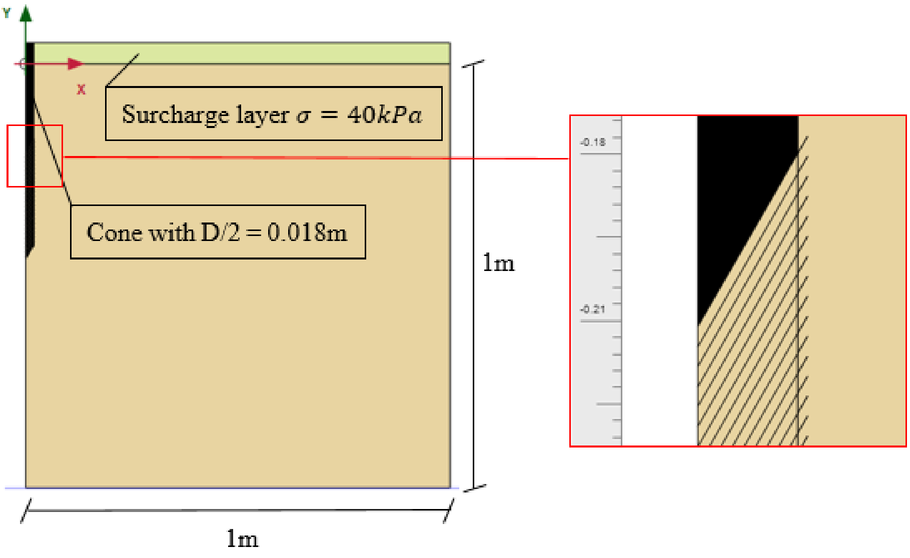

Fig. 144: Model dimensions according to Xian (2017)

Tab. 39: Parameters for FEA

	Cone	Soil	Interface shaft	Interface cone
Material model	Linear elastic	Linear elastic	Mohr-Coulomb	Mohr-Coulomb
Drainage	Non-porous	Non-porous	Undrained	Undrained
γ [kN/m³]	0	0	0	0
E' [GPa]	200	-	-	-
ν' [-]	0.1	-	-	-
G [MPa]	-	3	3	3
ν_u [-]	-	0.49	0.49	0.49
s_u [kPa]	-	20	0	20
K_{0T} [-]	1.0	1.0	1.0	1.0

Construction phases

The slice thickness (displacement increment) is again considered with D/10 (0.0036 m), and a penetration of the cone from a depth of 6D to a depth of 11D is modeled. Therefore, 60 slices are required, and unlike the FEA of jacked piles, Xian (2017) does not separate the “Press”- and the “Replace”-phase. He instead combined both, meaning that only 60 phases are required instead of 120. To see if any influence comes from combining both phases, the same FEA was also performed with separated phases (see Fig. 137 and Fig. 138). Furthermore, for all phases, the default iteration parameters were chosen, and the line displacement is based, again, at the top of the penetrometer with displacement in the x-direction set to “fixed” and displacement in the y-direction set to “prescribed”, with negative magnitudes. Initial stresses are created by applying the K_0-procedure and deactivating all interfaces and line displacements. In Fig. 145 and Fig. 146, the first 5 calculation phases are illustrated with the shaft interfaces colored blue and the cone interfaces colored green.

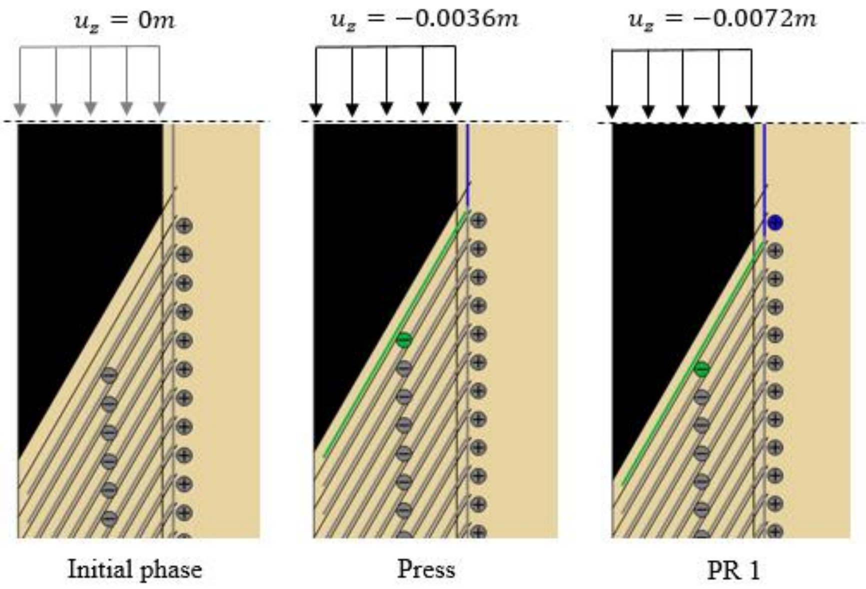

Fig. 145: Construction phases PRM

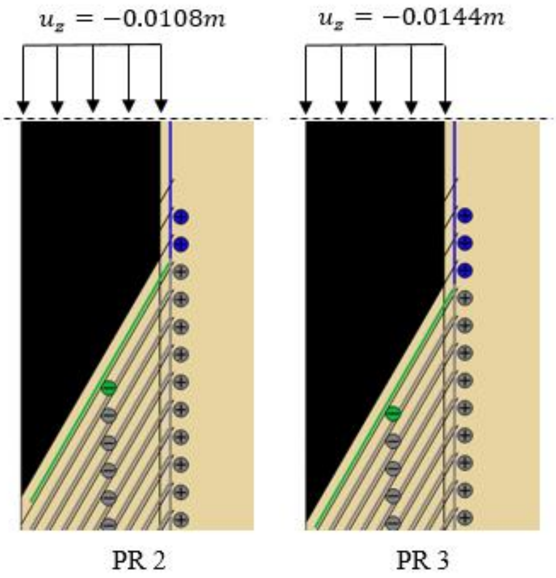

Fig. 146: Construction phases PRM

Results

Firstly, the results obtained from the FEA are compared to the results from literature (Xian, 2017) for the two analyzed cases (rough cone / smooth shaft and smooth cone / smooth shaft). For the latter case, smooth cone / smooth shaft, the undrained shear strength s_u for the cone interface (see Tab. 39) was changed to 0 kPa. According to Xian (2017) the cone tip resistances q_t are obtained by taking the stresses across the cone, as exemplified in Fig. 147.

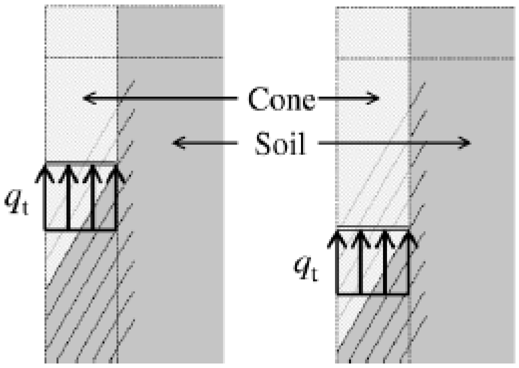

Fig. 147: Determination of cone tip resistances q$_t$ (Xian, 2017)

Furthermore, it is necessary to determine the theoretical cone factor N$_c$ in order to enable a comparison with the results from (Xian, 2017). Therefore, the corrected cone resistance q$_t$ (see Fig. 147), the initial vertical stress σ_{v0} and the undrained shear strength of the soil s$_u$ are required to calculate N$_c$, as shown in equation (7.4).

$$N_c = \frac{q_t - \sigma_{v0}}{s_u} \tag{7.4}$$

Due to a shortage of time at the end of the thesis, the corrected cone resistances q$_t$ in the PLAXIS Output were obtained through the application of a new cross section for each calculation phase at the appropriate depth and the use of the vertical stresses. This step (determination of corrected cone resistance) may be not accurate enough and therefore, this issue must be improved in further research. For each calculation phase, the corrected cone resistance was then obtained by taking the average of all stresses obtained from the appropriate cross section. However, regarding the obtained results from the cross section, it can be seen that there are some very high stress peaks, which may influence the average. Therefore, the results for the theoretical cone factor are presented once for all results (considering whole cross section) and once with the elimination of the highest stress peaks (not considering the whole cross section). Furthermore, as previously stated, the FEA were performed with and without applying extension interfaces, and for the following presented results, the following denotation is valid:

- Rough cone / smooth shaft → r.c. / s.s.
- Smooth cone / smooth shaft → s.c. / s.s.
- With extension interfaces → w.e.i.
- Without extension interfaces → wo.e.i.

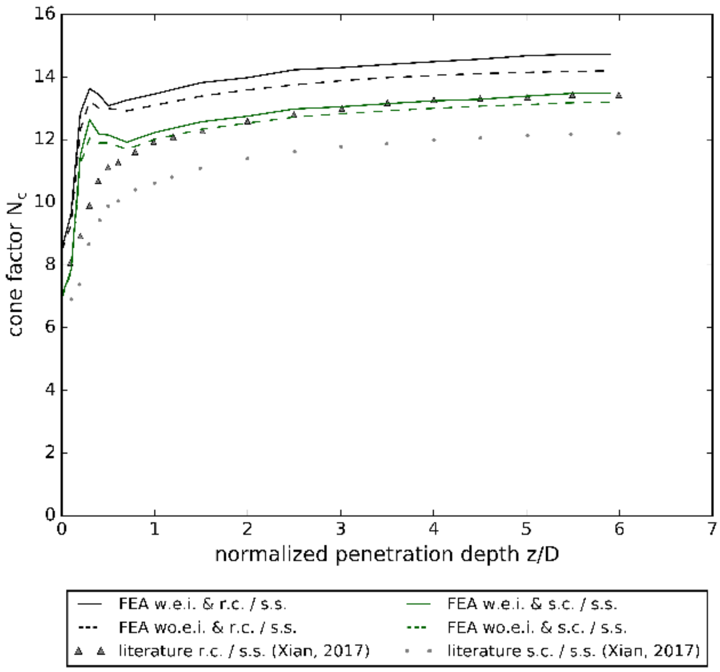

Fig. 148: Results for the cone factor N_c without eliminating outliers compared with results from literature (Xian, 2017)

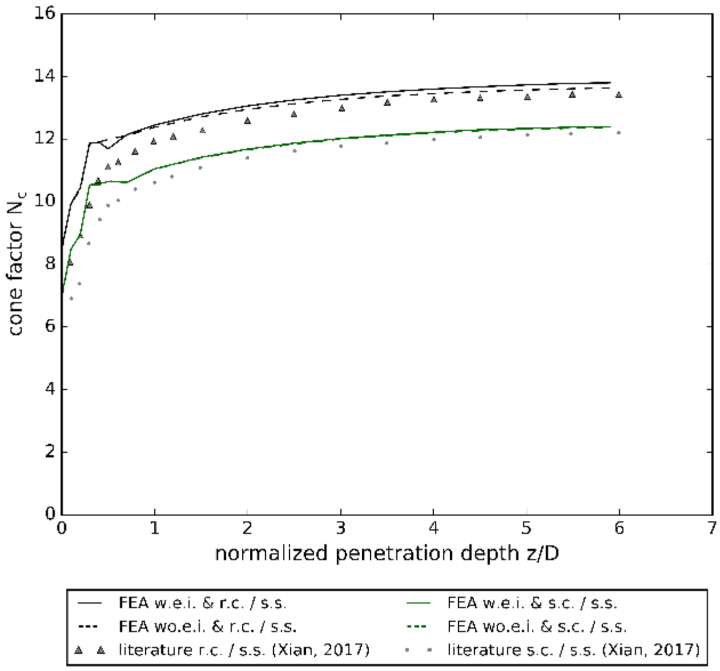

Fig. 149. Results for the cone factor N_c with eliminating outliers compared with results from literature (Xian, 2017)

Fig. 149 (left) clearly shows that just using the stresses from the appropriate cross section does not deliver satisfying results. It also can be seen that for the analysis of the case rough cone / smooth shaft, the application of extension interfaces shows some effects on the results when compared to the FEA without extension interfaces, whereas with regards to the case smooth cone / smooth shaft, there is almost no difference. In Fig. 149 (right), it can be seen that with the elimination of the biggest outliers, the results obtained from the FEA are very similar to the results from (Xian, 2017), and, furthermore, there is no difference between the results when applying extension interfaces and neglecting them. Hence, it can be concluded that the application of extension interfaces may have an influence on the stress peaks. However, to only neglect outliers and take the remaining results is not a satisfying process, and, therefore, further investigations with respect to the output must be performed. Besides the investigations regarding the output, several issues must be considered in order to finally come up with a finite element model, which enables a good comparison to the results obtained from a KIM analysis (see chapter 8.2). Finally, Fig. 150 shows that there is no difference between the results when the “Press”- and “Replace”-phases are combined and when they are seerated.

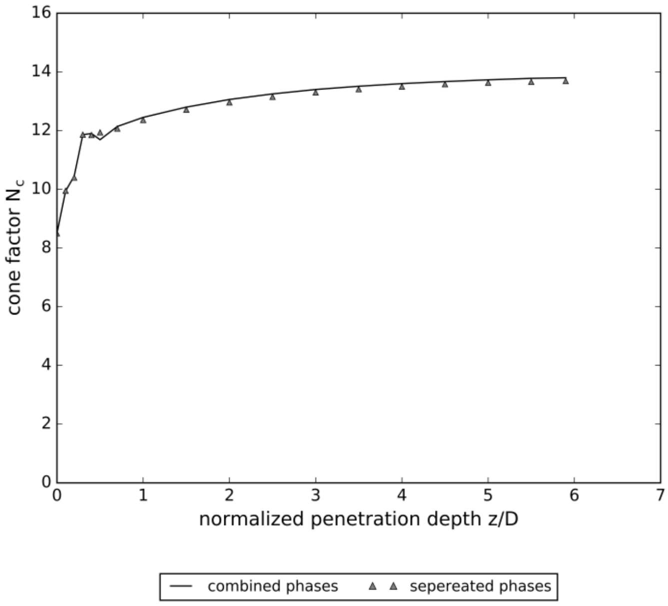

Fig. 150: Comparison between combining “Press”- and “Replace”-phases and separating them

7.2.3 Automatic model creation with Python-scripting

With more than 100 calculation phases and several hundred interfaces, the model creation is very time consuming, and, furthermore, for different investigations with the same FEM, changes must be implemented in every single phase. Therefore, the automatic model creation with python scripting is a good option, because when the overall model is established, changes can be implemented by simply changing the code. For the FEM presented in chapter 7.2.1, a code for the automatic model was created and is shown within appendix D. This code can be easily adapted to apply the PRM to cone penetration.

8 Conclusion and Outlook

This final chapter briefly summarizes the performed investigations. This is followed by a detailed outlook for further research regarding the main issues of the Karlsruhe Interpretation Method.

8.1 Conclusion

The aim of this thesis was to further investigate the Karlsruhe Interpretation Method both by means of analyzing and improving the finite element analysis of the spherical cavity expansion problem and by investigating different constitutive soil models.

Because up until now the Karlsruhe Interpretation Method is used mainly as a correlation method between the cone resistance q_c and the relative density I_D related to land reclamation using calcareous sands, the thesis starts by shortly introducing these issues. Following that, the main parts of the KIM are introduced to the reader, namely the hypoplastic soil model and the spherical cavity expansion problem. Regarding the hypoplastic soil model according to Von Wolffersdorff (1996), the standard calibration process of the constitutive soil parameters is presented with the aim to evince the difficulties and uncertainties of the calibration procedure.

Preliminary performed studies showed a significant influence of single hypoplastic parameters on the results of a spherical cavity expansions, and, thus, for the results of a KIM analysis as well. Therefore, several investigations regarding the automatic calibration tool ExCalibre were performed, and it could be shown that ExCalibre is a very helpful tool for determining the input parameters for the hypoplastic soil model. However, based on the investigations, it turned out that the number and the type of laboratory tests (provided to the ExCalibre input file) have a significant influence on the resulting hypoplastic parameters. It was also discovered that ExCalibre reacts very sensitively to the provided initial void ratios within the input file. Additionally, with regards to the original hypoplastic soil model, a hypoplastic soil model for crushable sand was investigated, and it was shown that applying this new constitutive soil model results in a significantly different soil behavior in the case of very high stresses.

In order to investigate the finite element analysis of the spherical cavity expansion problem, the influence of the dilatancy angle and the initial stress field for the Mohr-Coulomb and the Hardening Soil model was deeply analyzed. Regarding the dilatancy angle it could be shown that generally, a decreasing amount of non-associativity causes the pressure-expansion curves to increase, and hence higher limit pressures are reached. With an increasing dilatancy angle, the pressure-expansion curves also tend to increase further, even though large strains are applied to the model, and, thus, a well defined limit pressure could not be defined when using the Mohr-Coulomb model. For the Hardening Soil model, this issue can be controlled by applying the dilatancy-cut-off option. The comparison of the Hardening Soil model with the hypoplastic soil model (regarding SCE results) indicated that the Hardening Soil model is capable to provide satisfying results, but due to the fact that this constitutive soil model does not take pyknotropy into account for each density state, a new Hardening Soil parameter set must be generated for each density state. Thus, a great amount of effort is required to perform a full KIM analysis.

Performing a full KIM analysis for both a parameter set obtained from a standard calibration process and for one obtained from the automatic calibration of ExCalibre showed that most of the input parameters optimized by means of ExCalibre are in agreement with the "experienced-based" parameter determination of the hypoplastic soil model. However, the performed studies showed a significant deviation between "classical" parameter determination and ExCalibre for the input parameter α, which controls the material's peak friction angle, and hence the dilatancy behavior of the material. The studies regarding the final results of a full KIM analysis indicated the high sensitivity of the KIM to certain input parameters of the hypoplastic soil model but also showed the potential of the automatic parameter calibration with ExCalibre. The results from chapter 6.5 showed, that applying the original hypoplastic soil model results in the same cone resistances as for the application of the grain crushing model.

The full automation of the KIM analysis with Python scripting makes the practical application of the KIM much easier because the user only has to provide the hypoplastic input parameters, and after a successful run of the script, all of the results from a full KIM analysis are provided.

Finally, an alternative approach for numerical modelling of cone penetration tests is presented by means of the Press-Replace method. Two examples found in literature have been validated by means of FEA, and, furthermore, a Python code for an automatic model creation was developed.

8.2 Outlook

With this thesis the advantages of the KIM were shown. However, it can be seen that further research concerning the KIM and all of its considered parts is necessary to improve the accuracy of this interpretation method. The following main topics should be considered in future research:

- **Shape factor**

  Regarding the accuracy of the KIM, the shape factor may be the element containing the largest uncertainties, and, therefore, it should be investigated to see if it is accurate enough to only depend on the relative density.

- **Calibration of hypoplastic soil parameters**

  With respect to the calibration of the hypoplastic soil parameters, both procedures, namely the standard manual calibration and the automatic calibration with ExCalibre must be investigated simultaneously in order to improve both. It must be investigated which laboratory test results should be taken for the parameter calibration, and, which and how many lab-tests should be provided in the ExCalibre input file. Hence, it is suggested to do a manual calibration of the hypoplastic parameter for several soils based on the appropriate lab-tests, and then use the same lab-tests and perform an automatic calibration with ExCalibre. From the results based on a wide range of materials, it is possible that the ExCalibre code must be adapted slightly or, otherwise, some aspects of the manual calibration procedure should be executed differently.

- **Hypoplastic soil model for crushable sand**

  This constitutive soil model should be applied different materials, and then it should be compared to original lab-test results as well as results obtained when applying the original hypoplastic soil model. Furthermore, the development of the hypoplastic soil model for crushable sand is only based on the results obtained from tests performed on different silica sands. Therefore, the stress dependency of the certain parameters must also be defined for calcareous sands.

- **Improving simulation series of SCE**

  Regarding the first step of a full KIM analysis, improvement of the simulations series of the spherical cavity expansion problem is required. So far, 50 different FEA are created and calculated, and then the results are used for the determination of the KIM parameters. The number of FEA could be reduced, however, the accuracy of determining the KIM parameters should not be affected.

- **KIM analysis with more materials**

  A full KIM analysis must be performed both for more materials and for the same materials, but with a different parameter calibration approaches (as done in chapter 6). Furthermore, it is necessary to compare the results obtained from a KIM analysis with real test data or other numerical approaches.

- **Automation of KIM analysis**

  The script for the full automation of the KIM analysis was developed on the basis of just a few hypoplastic materials and pre-determined KIM results. Also, there are some numerical problems within the SCE that will make both the resulting KIM parameters and the obtained cone resistances useless. Therefore, the code must be extended to account for and react to numerical problems during the finite element analysis of the SCE problem. Additionally, the accuracy of the other parts within the code must be improved, and, furthermore, a code for the automatic creation of the original PLAXIS model can be added.

- **Press-Replace method**

  Regarding the Press-Replace method, it is important to adapt the pre-created finite element models of chapter 6 to enable a good representation of cone penetration tests, and also a possible comparison to the results obtained from a KIM analysis. The adaption should include investigations of the interface properties in order to account for a realistic soil-cone interaction (especially stiffness and strength parameters), sensitivity analyses related to structural issues (model dimensions, boundary conditions and so on) and finding a proper solution for the output.

9 Bibliography

Andersen, K. H., Andersen, L., Jostad, H. P. & Clukey, E. C., 2004. Effect of skirt-tip geometry on set-up outside suction anchors in soft clay. *ASME Conference Proceedings 2004,* pp. 1035-1044.

Baldi, G. et al., 1986. IOnterpretation of CPTs and CPTUs, 2nd part: drained penetration of sands. In: *4th International Geotechnical Seminar, Field Instrumentaion and In-Situ Measurements.* s.l.:s.n., pp. 143-155.

Bauer, E., 1996. Calibration of a Comprehensive Hypoplastic Model for Granual Materials. *Soils and Foundations, Vol. 36, No. 1,* pp. 13-26.

Bolton, M., 1986. The strength and dilatancy of sands. *Geotechnique, Vol. 36,* pp. 65-78.

Brinkgreve, R. B. J. et al., 2018. *PLAXIS 2018. Finite element code for soil and rock analysis, User Manual.* Delft: Plaxis bv..

Brinkgreve, R. B. J., Swolfs, W. M. & Engin, H. K., 2010. *PLAXIS 2D 2010 - Users Manual.* Delft, The Netherlands: Plaxis bv.

Clark, A. R. & Walker, B. F., 1977. A proposed scheme for the classification and nomemclature for use in the engineering description on Middle Eastern sedimentary rocks.. *Geotechnique, Vol. 27, No. 1,* pp. 93-99.

Colliat-Dangus, J. L., Desrues, J. & Foray, P., 1988. Triaxial testing of granular soil under elevated cell pressure. In: *Advanced triaxial testing of soil and rock.* s.l.:ASTM International, pp. 290-310.

Cudmani, R., 2000. *Statische, alternierende und dynamische Penetration in nichtbinidigen Böden, Ph.D. Thesis.* Karlsruhe: University Fridericiana.

Cudmani, R. & Osinov, V. A., 2001. The cavity expansion problem for the intepretation of cone penetration and pressuremeter tests. *Canadian Geotechnical Journal, Vol. 38,* pp. 622-638.

Daouadji, A. & Hicher, P. Y., 2010. An enhanced constitutive model for crushable granular materials. *International journal for numerical and analytical methods in geomechanics, Vol. 34, No. 6,* pp. 555-580.

Engin, H. K., 2013. *Modelling pile installation effects: A numerical approach, Ph.D. Thesis.* Delft: Technical University Delft.

Engin, H. K., Brinkgreve, R. B. J. & Van Tol, A. F., 2015. Simplified numerical modelling of pile penetration–the press-replace technique, Vol. 39, No. 15. *International Journal for Numerical and Analytical Methods in Geomechanics,* pp. 1713-1734.

Engin, H. K., Jostad, H. P. & Rohe, A., 2014. On the modelling of grain crushing in hypopalsticity. *Numerical Methods in Geotechnical Engineering*, pp. 33-38.

Grecu, S., 2018. *Behaviour of Axially Loaded Bucket Foundations in Sand, Master's Thesis.* Aalborg: Aalborg University.

Gudehus, G. et al., 2008. The soilmodels.info project. *International Journal for Numerical and Analytical Methods in Geomechanics, Vol. 32, No. 12*, pp. 1571-1572.

Herle, I., 2000. Granulometric limits of hypoplastic models. *Task quaterly, Vol. 4, No. 3*, pp. 389-407.

Herle, I. & Gudehus, G., 1999. Determination of parameters of a hypoplastic constitutive model from properties of grain assemblies. *Mechanics of Cohesive-frictional Materials: An International Journal on Experiments, Modelling and Computation of Materials and Structures, Vol. 4, No. 5*, pp. 461-486.

Jaky, J., 1944. The coefficient of earth pressure at rest. *(In Hungarian: A nyugalmi nyomas tenyezoje). Journal of the Society of Hungarian Architects and Engineers, Vol. 78, No. 22*, pp. 355-358.

Loung, M. T. & Touati, A., 1983. Sols grenus sous fortes contraints. *Revue Francaise de Géotechnique 24*, pp. 51-63.

Marcher, T., Vermeer, P. A. & Von Wolffersdorff, P. A., 2000. Hypopalstic and elastoplastic modelling - a comprehensive with test data. In: D. Kolymbias, Hrsg. *Constitutive Modelling of Granular Materials.* Berlin: Springer, pp. 353-374.

Masin, D., 2010. *Plaxis implementation of hypoplasticity, Technical Report.* s.l.:s.n.

Masin, D., 2019. *Modelling of Soil Behaviour with Hypoplasticity: Another Approach to Soil Constitutive Modelling.* 1 Hrsg. s.l.:Springer International Publishing.

Meier, T., 2007. *Application of Hypoplastic and Viscoplastic Constitutive Models for Geotechnical Problems, Ph.D. Thesis.* Karlsruhe: University Fridericiana.

Meigh, A. C., 1987. *Cone penetration testing.* 1 Hrsg. s.l.:Butterworth-Heinemann.

Miura, N. & Yamanouchi, T., 1973. Compressibility and drained shear characteristics of a sand under high confinig pressures. In: *Technology reports of the Ymaguchi University, Vol. 1, No. 2.* s.l.:s.n., pp. 271-290.

Nakata, Y., Hyodo, M. & Hyde, A., 2001. Microscopic particle crushing of sand subjected to high pressure one-dimensional compression. *Soils and Foundations, Vol. 41, No. 1*, pp. 69-83.

Niemunis, A. & Herle, I., 1997. Hypoplastic model for cohesionless soils with elastic strain range. *Mechanics of Cohesive-frictional Materials: An International Journal on Experiments, Modelling and Computation of Materials and Structures, Vol. 2, No. 4*, pp. 279-299.

Ohde, J., 1939. *Zur Theorie der druckverteilung im baugrund.* s.l.:s.n.

Phuong, N. T. V., 2018. *Numerical Modelling Of Pile Installation Using Material Point Method, Ph. D. Thesis.* Delft: Technical University Delft.

Phuong, N. T. V., Rohe, A., Brinkgreve, R. B. J. & van Tol, A. F., 2018. Hypoplastic model for crushable sand. *Soil and Foundations, Vol. 58, No. 3*, pp. 615-626.

Reinisch, J., 2018. *Estimating the relative density in calcareous sands with the Karlsruhe Interpretation Method, Masters' Thesis.* Graz: University of Technology Graz.

Schanz, T. & Vermeer, P., 1996. Angles of friction and dilatancy of sand. *Géotechnique, Vol. 46, No. 1*, pp. 145-152.

Schanz, T. & Vermeer, P., 1998. On the stiffness of sands. *Géotechnique, Vol. 48*, pp. 383-387.

Schanz, T., Vermeer, P. A. & Bonnier, P. G., 1996. The hardening soil model: Formulation and verification. In: *Beyond 2000 in Computational Geotechnics.* Rotterdam: Balkema, pp. 281-296.

Schmertmann, J. H., 1976. *An Updated Correlation Between Relative Density Dr and Fugro-Type Electric Cone Bearing, qc, Contract Report DACW 39-76 M 6646 WES.* Wicksburg, Mississippi: s.n.

Slawik, S., 2018. *Numerical Studies on KIM employing the Cavity Expansion Method, Master's Thesis.* Gdansk: Gdansk University of Technology.

Tehrani, F. S., Nguyen, P., Brinkgreve, R. B. J. & Van Tol, A. F., 2016. Comparison of Press-Replace Method and Material Point Method for analysis of jacked piles. *Computers and Geotechnics, Vol. 78*, pp. 38-53.

Thurner, R., Johannes, R. & Tschuchnigg, F., 2019. Influence of the carbonate Content on CPT-Results and Practical Relevance for the Soil Improvement Works on Major Land Reclamation Projects. In: H. Shehata & H. Poulos, Hrsg. *Latest Thoughts on Ground IMprovement Techniques, GeoMEast 2018. Sustainable Civil Infrastructures.* Cham: Springer, pp. 122-131.

Tschuchnigg, F., 2012. *Finite Element Modelling of Deeo Foundations Emplyoing an Embedded Pile Formulation, Ph.D. Thesis.* Graz: University of Technology Graz.

Tschuchnigg, F., Reinisch, J. & Thurner, R., 2018. Estimation of the relative Density in Calcareous Sands using the Karlsruhe Interpretation Method. In: W. Wu & H. Yu, Hrsg. *Proceedings of China-Europe Conference on Geotechnical Engineering.* Cham: Springer, pp. 734-738.

Tschuchnigg, F. & Winkler, M. B., 2019. KIM - Numerical studies on the spherical cavity expansion problem. *European Conference on Soil Mechanics and Geotechnical Engineering, Reykjavik*, pp. 1-6.

Uhlig, M. & Herle, I., 2015. Bestimmung der Porenzahl aus Drucksondierungen. In: T. Schanz & A. Hettler, Hrsg. *Aktuelle Forschung in der Bodenmechanik 2015.* Berlin, Heidelberg: Springer Vieweg, pp. 85-100.

Von Wolffersdorff, P., 1996. A hypoplastic relation for granular materials with predefined limit state surface. *Mechanics of Cohesive_frictional Materials, Vol. 1*, pp. 251-271.

Winkler, M. B., 2018. *KIM - Investigation of spherical cavity expansion emplying different constitutive models, Master's Thesis.* Graz: Technical University Graz.

Xian, L. Y., 2017. *Numerical Study of Cone Penetration Test in Clays using Press-Replace Method, Ph.D. Thesis.* Singapore: Technical University of Singapore.

Xu, X., 2007. *Investigation of the End Bearing Performances of Displacement Piles in Sand, Ph.D. Thesis.* s.l.:University of Western Australia.

Yu, H. & Houlsby, G., 1991. Finite cavity expansion in dilatant soils: loading analysis. *Geotechniqeu, Vol. 41, No. 2*, pp. 173-183.

Appendix A for chapter 4

A-Tab. 1 Differences between b and a and c and a – Rohatec sand

Rohatec sand				
Input sets				
Hypoplastic parameters	Set b	Δab [%]	Set c	Δac [%]
φ_c[°]	34.3	0	33.9	-1.2
hs [MPa]	222880	+263.1	223026	+263.4
n [-]	0.366	-20.8	0.336	-27.3
ed0 [-]	0.382	+0.8	0.382	+0.8
ec0 [-]	0.764	+0.9	0.764	+0.9
ei0 [-]	0.917	+0.9	0.917	+0.9
α [-]	0.1	-9.1	0.09	-18.2
β [-]	2.8	-15.2	2.4	-27.3

A-Tab. 2: Differences between d and a and e and a – Rohatec sand

Rohatec sand				
Input sets				
Hypoplastic parameters	Set d	Δad [%]	Set e	Δae [%]
φ_c[°]	34.5	+0.6	34.2	-0.3
hs [MPa]	221341	+260.6	228990	+273.1
n [-]	0.342	-26.0	0.368	-20.3
ed0 [-]	0.385	+1.6	0.382	+0.8
ec0 [-]	0.770	+1.7	0.763	+0.8
ei0 [-]	0.924	+1.7	0.916	+0.8
α [-]	0.11	0	0.1	-9.1
β [-]	3.4	+3.0	2.6	-21.2

A-Tab. 3: Differences between f and a and g and a – Rohatec sand

Rohatec sand				
Input sets				
Hypoplastic parameters	Set f	Δaf [%]	Set g	Δag [%]
φ_c[°]	35.8	+4.4	33.4	-2.6
hs [MPa]	207644	+238.3	236823	+285.8
n [-]	0.315	-31.8	0.371	-19.7
ed0 [-]	0.389	+2.6	0.381	+0.5
ec0 [-]	0.779	+2.9	0.762	+0.7
ei0 [-]	0.935	+2.9	0.915	+0.7
α [-]	0.18	+63.6	0.08	-27.3
β [-]	4.8	+45.5	1.7	-48.5

A-Tab. 4: Differences between h and a and i and a – Rohatec sand

Rohatec sand				
	Input sets			
Hypoplastic parameters	Set h	Δah [%]	Set i	Δai [%]
φ_c [°]	34.4	+0.3	33.9	-1.2
hs [MPa]	219677	+257.9	76674	+24.9
n [-]	0.363	-21.4	0.432	-6.5
ed0 [-]	0.382	+0.8	0.380	+0.3
ec0 [-]	0.765	+1.1	0.76	+0.4
ei0 [-]	0.917	+0.9	0.912	+0.3
α [-]	0.11	0	0.1	-9.10
β [-]	3.2	-3.0	2.8	-15.2

A-Tab. 5: Differences between j and a and k and a – Rohatec sand

Rohatec sand				
	Input sets			
Hypoplastic parameters	Set j	Δaj [%]	Set k	Δak [%]
φ_c [°]	34.5	+0.6	34.2	-0.3
hs [MPa]	58276	-5.1	68499	+11.6
n [-]	0.438	-5.2	0.464	+0.4
ed0 [-]	0.381	+0.5	0.378	-0.3
ec0 [-]	0.761	+0.5	0.756	-0.1
ei0 [-]	0.914	+0.6	0.908	-0.1
α [-]	0.13	+18.2	0.1	+9.1
β [-]	4.1	+24.2	3.1	-6.1

A-Tab. 6: Differences between l and a and m and a – Rohatec sand

Rohatec sand				
	Input sets			
Hypoplastic parameters	Set l	Δal [%]	Set m	Δam [%]
φ_c [°]	35.8	+4.4	33.4	-2.6
hs [MPa]	59181	-3.6	76783	+25.1
n [-]	0.401	-13.2	0.5	+8.2
ed0 [-]	0.384	+1.3	0.376	-0.8
ec0 [-]	0.769	+1.6	0.752	-0.7
ei0 [-]	0.922	+1.4	0.902	-0.8
α [-]	0.18	+63.6	0.08	-27.3
β [-]	5.2	+57.6	1.8	-45.5

A-Tab. 7: Differences between n and a – Rohatec sand

Rohatec sand		
	Input sets	
Hypoplastic parameters	Set n	Δan [%]
φ_c [°]	35.8	+4.4
hs [MPa]	59181	-3.6
n [-]	0.401	-13.2
ed0 [-]	0.384	+1.3
ec0 [-]	0.769	+1.6
ei0 [-]	0.922	+1.4
α [-]	0.18	+63.6
β [-]	5.2	+57.6

A-Tab. 8: Differences between b and a and c and a – Kralupy sand

Kralupy sand				
		Input sets		
Hypoplastic parameters	Set b	Δab [%]	Set c	Δac [%]
φ_c [°]	36.3	0	39.5	+8.8
hs [MPa]	1926	-49.4	2322	-39.1
n [-]	0.152	-7.9	0.154	-6.7
ed0 [-]	0.802	+5.8	0.786	+3.7
ec0 [-]	1.604	+5.7	1.573	+3.7
ei0 [-]	1.925	+5.8	1.887	+3.7
α [-]	0.18	+50.0	0.28	+133.3
β [-]	4.6	+7.0	4.4	+2.3

A-Tab. 9: Differences between d and a and e and a – Kralupy sand

Kralupy sand				
		Input sets		
Hypoplastic parameters	Set d	Δad [%]	Set e	Δae [%]
φ_c [°]	35.6	-1.9	36	-0.8
hs [MPa]	1515	-60.2	2237	-41.3
n [-]	0.145	-12.1	0.159	-3.6
ed0 [-]	0.831	+9.6	0.782	+3.2
ec0 [-]	1.663	+9.6	1.564	+3.1
ei0 [-]	1.995	+9.6	1.877	+3.1
α [-]	0.16	+33.3	0.15	+25.0
β [-]	4.6	+7.0	2.9	-32.6

A-Tab. 10: Differences between f and a and g and a – Kralupy sand

Kralupy sand				
Input sets				
Hypoplastic parameters	Set f	Δaf [%]	Set g	Δag [%]
φ_c[°]	41.2	+13.5	39	+7.4
hs [MPa]	1894	-50.3	2226	-41.6
n [-]	0.147	-10.9	0.149	-9.7
ed0 [-]	0.808	+6.6	0.797	+5.1
ec0 [-]	1.616	+6.5	1.594	+5.1
ei0 [-]	1.939	+6.5	1.913	+5.1
α [-]	0.23	+91.7	0.28	+133.3
β [-]	4.8	+11.6	4	-7.0

A-Tab. 11: Differences between h and a and i and a – Kralupy sand

Kralupy sand				
Input sets				
Hypoplastic parameters	Set h	Δah [%]	Set i	Δai [%]
φ_c[°]	35.1	-3.3	39.5	+8.8
hs [MPa]	2439	-36.0	2947	-22.7
n [-]	0.157	-4.8	0.151	-8.5
ed0 [-]	0.781	+3.0	0.794	+4.7
ec0 [-]	1.561	+2.9	1.587	+4.6
ei0 [-]	1.874	+3.0	1.905	+4.7
α [-]	0.13	+8.3	0.21	+75.0
β [-]	2.7	-37.2	4.3	0

A-Tab. 12: Differences between j and a and k and a – Kralupy sand

Kralupy sand				
Input sets				
Hypoplastic parameters	Set j	Δaj [%]	Set k	Δak [%]
φ_c[°]	35.6	-1.9	36	-0.8
hs [MPa]	4935	+29.5	2925	-23.2
n [-]	0.18	+9.1	0.151	-8.5
ed0 [-]	0.723	-4.6	0.797	+5.1
ec0 [-]	1.446	-4.7	1.594	+5.1
ei0 [-]	1.735	-4.7	1.913	+5.1
α [-]	0.11	-8.3	0.1	-16.7
β [-]	4.2	-2.3	2.5	-41.9

A-Tab. 13: Differences between l and a and k and a – Kralupy sand

Kralupy sand				
Input sets				
Hypoplastic parameters	Set l	Δal [%]	Set m	Δam [%]
φ_c[°]	41.2	+13.5	39	+7.4
hs [MPa]	5130	+34.6	4533	+19.0
n [-]	0.147	-10.9	0.16	-3.0
ed0 [-]	0.772	+1.8	0.756	-0.3
ec0 [-]	1.543	+1.7	1.511	-0.4
ei0 [-]	1.852	+1.8	1.814	-0.3
α [-]	0.14	+16.7	0.19	+58.3
β [-]	3	-30.2	3.8	-11.6

A-Tab. 14: Differences between n and a

Kralupy sand		
	Input sets	
Hypoplastic parameters	Set n	Δan [%]
φ_c[°]	35.1	-3.3
hs [MPa]	4416	+15.9
n [-]	0.164	-0.6
ed0 [-]	0.753	-0.7
ec0 [-]	1.507	-0.7
ei0 [-]	1.808	-0.7
α [-]	0.09	-25.0
β [-]	2.3	-46.5

A-Tab. 15: Initial void ratios of set 1 and set 2 – Dobrany sand

	Initial void ratios		
Test	Input dataset (set 1)	ExCalibre output (set 2)	Difference [%]
Triax 50 kPa	0.524	0.510	-2.7
Triax 100 kPa	0.545	0.530	-2.8
Triax 200 kPa	0.588	0.627	+6.6

A-Tab. 16: Initial void ratios of set 2 and set 3 – Dobrany sand

	Initial void ratios		
Test	Input dataset (set 2)	ExCalibre output (set 3)	Difference [%]
Triax 50 kPa	0.510	0.511	+0.2
Triax 100 kPa	0.530	0.531	+0.2
Triax 200 kPa	0.627	0.622	-0.8

A-Tab. 17: Initial void ratios of set 3 and set 4 – Dobrany sand

	Initial void ratios		
Test	Input dataset (set 3)	ExCalibre output (set 4)	Difference [%]
Triax 50 kPa	0.511	0.511	0
Triax 100 kPa	0.531	0.530	-0.2
Triax 200 kPa	0.622	0.621	-0.2

A-Tab. 18: Hypoplastic parameters for input set 1 and 2 – Dobrany sand

Set (input)	φ_c [°]	h_s $[kPa]$	n [-]	e_{d0} [-]	e_{c0} [-]	e_{i0} [-]	α [-]	β [-]
Set a (set 1)	36.5	49846	0.243	0.530	1.144	1.372	0.09	4.5
Set b (set 2)	36.5	49401	0.174	0.635	1.271	1.525	0.10	4.1
Difference [%]	0	-0.9	-28.4	+19.8	+11.1	+11.2	+11.1	-8.9

A-Tab. 19: Hypoplastic parameters for input set 2 and 3 – Dobrany sand

Set (input)	φ_c [°]	h_s $[kPa]$	n [-]	e_{d0} [-]	e_{c0} [-]	e_{i0} [-]	α [-]	β [-]
Set b (set 2)	36.5	49401	0.174	0.635	1.271	1.525	0.10	4.1
Set c (set 3)	36.5	47540	0.170	0.640	1.281	1.537	0.10	4.2
Difference [%]	0	-3.8	-2.3	+0.8	+0.8	+0.8	0	+2.4

A-Tab. 20: Hypoplastic parameters for input set 3 and 4 – Dobrany sand

Set (input)	φ_c [°]	h_s $[kPa]$	n [-]	e_{d0} [-]	e_{c0} [-]	e_{i0} [-]	α [-]	β [-]
Set c (set 3)	36.5	47540	0.170	0.640	1.281	1.537	0.10	4.2
Set d (set 4)	36.5	46432	0.168	0.644	1.287	1.545	0.10	4.3
Difference [%]	0	-2.3	-1.2	+0.1	+0.5	+0.5	0	+2.4

A-Tab. 21: Settings for oedometric compression test – Dobrany sand

Soil test	e_{init}	Pressure-steps [kPa]
Oedometer 1	0.996	8 – 10 – 20 – 40 – 80 – 150 – 300 – 600 – 1200 – 600 – 150 – 40 - 10

A-Tab. 22: Settings for triaxial compression test – Dobrany sand

Soil test	e_{init}	Confining pressure $\sigma_3 [kPa]$
Triax 1	0.510	50
Triax 2	0.530	100
Triax 3	0.627	200

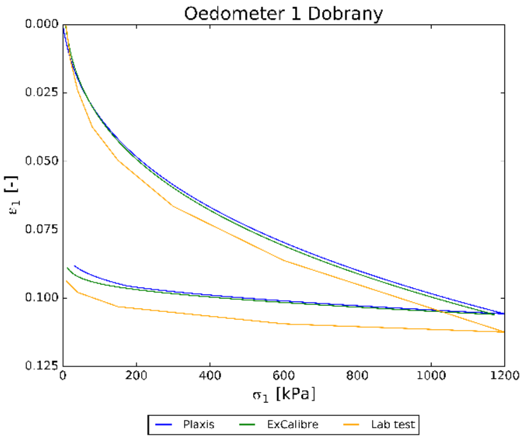

A-Fig. 1: Oedometric compression tests – Dobrany sand

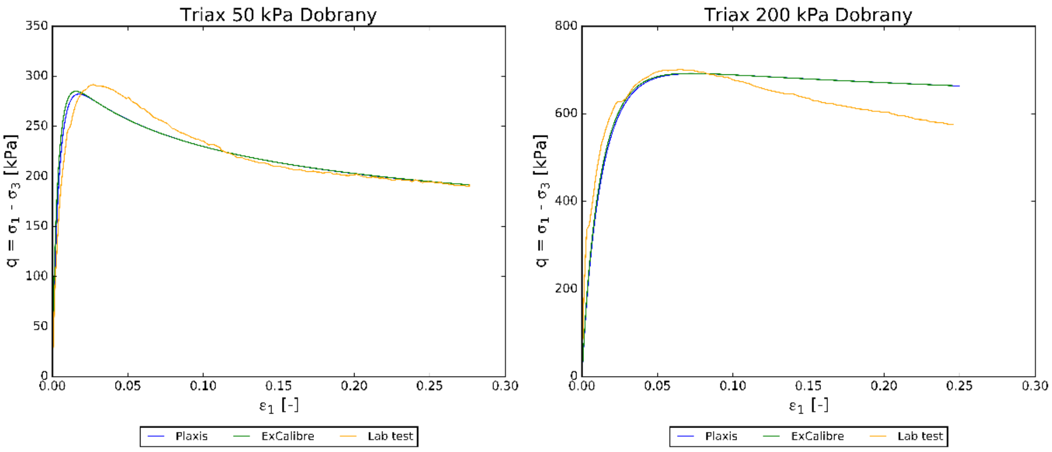

A-Fig. 2: Triaxial compression tests (q-ε_1-diagrams) – Dobrany sand

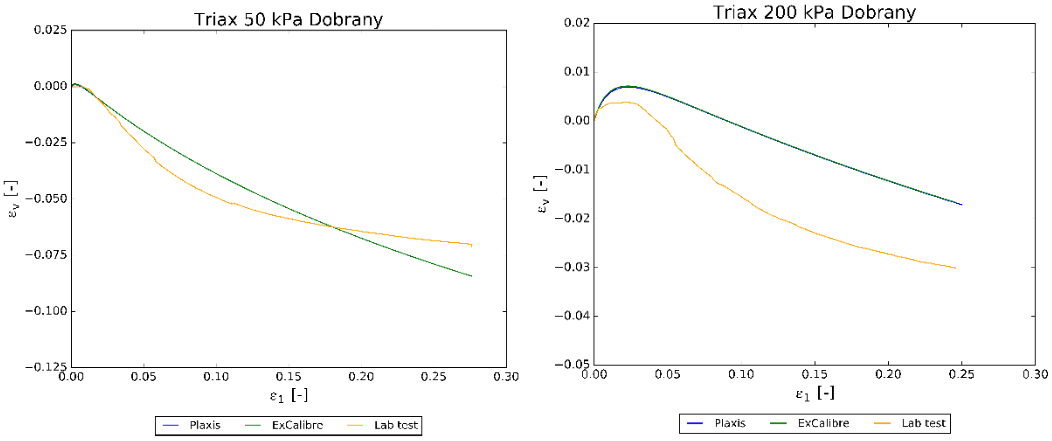

A-Fig. 3: Triaxial compression tests (ε_v-ε_1-diagrams) – Dobrany sand

Appendix B for chapter 5

Initial stress conditions ($\boldsymbol{p', \sigma_1'}$ & $\boldsymbol{\sigma_3'}$) for $\mathbf{K_0 = 1.0}$ / non-uniform

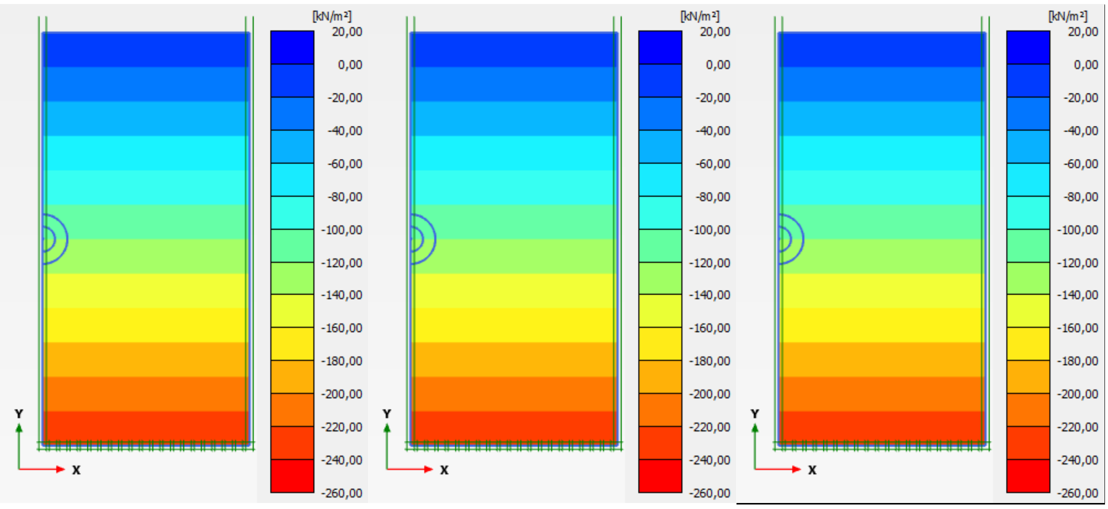

A-Fig. 4: Initial stress situation (p', σ_1' & σ_3') for boundary condition 1 (left), boundary condition 2 (middle) and boundary condition 3 (right)

Final stresses ($\boldsymbol{p', q}$ & $\boldsymbol{\sigma_1'}$) and deformations ($\boldsymbol{|u|}$) for $\mathbf{K_0 = 1.0}$ / non-uniform

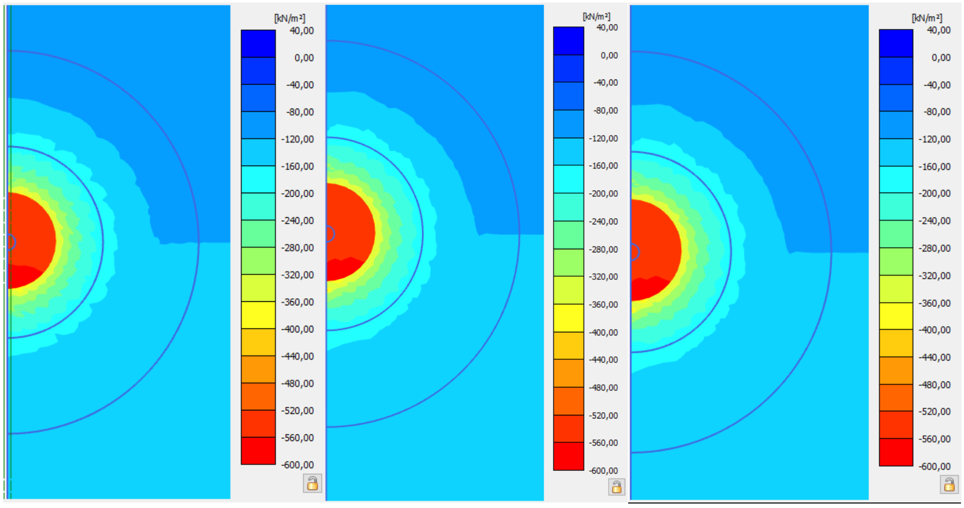

A-Fig. 5: Final p' for boundary condition 1 (left), boundary condition 2 (middle) and boundary condition 3 (right)

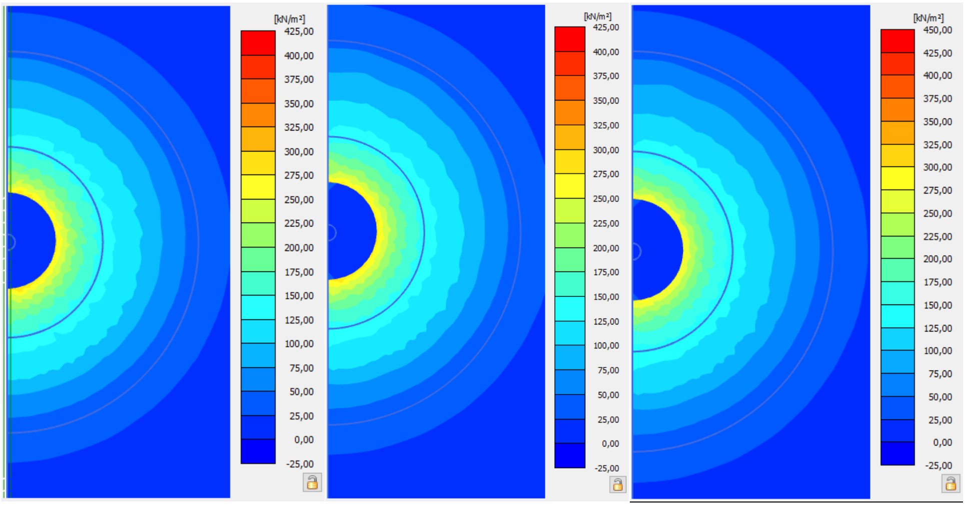

A-Fig. 6: Final q for boundary condition 1 (left), boundary condition 2 (middle) and boundary condition 3 (right)

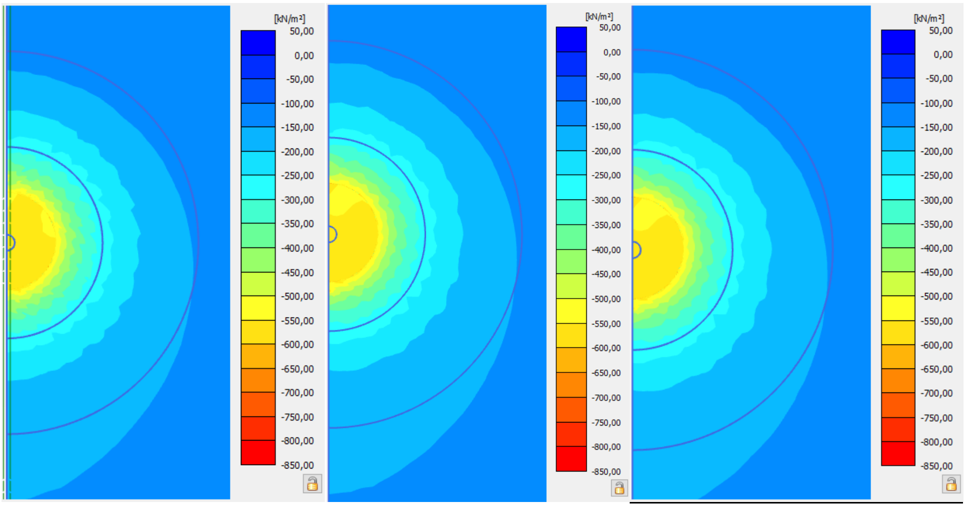

A-Fig. 7: Final σ_1' for boundary condition 1 (left), boundary condition 2 (middle) and boundary condition 3 (right)

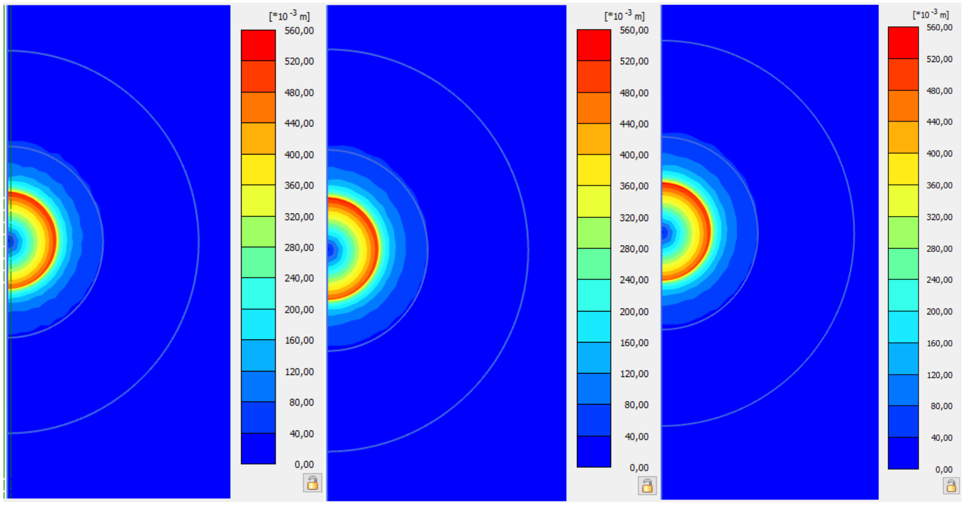

A-Fig. 8: Final $|u|$ for boundary condition 1 (left), boundary condition 2 (middle) and boundary condition 3 (right)

Pressure-expansion curves for K_0 = 1.0 / non-uniform

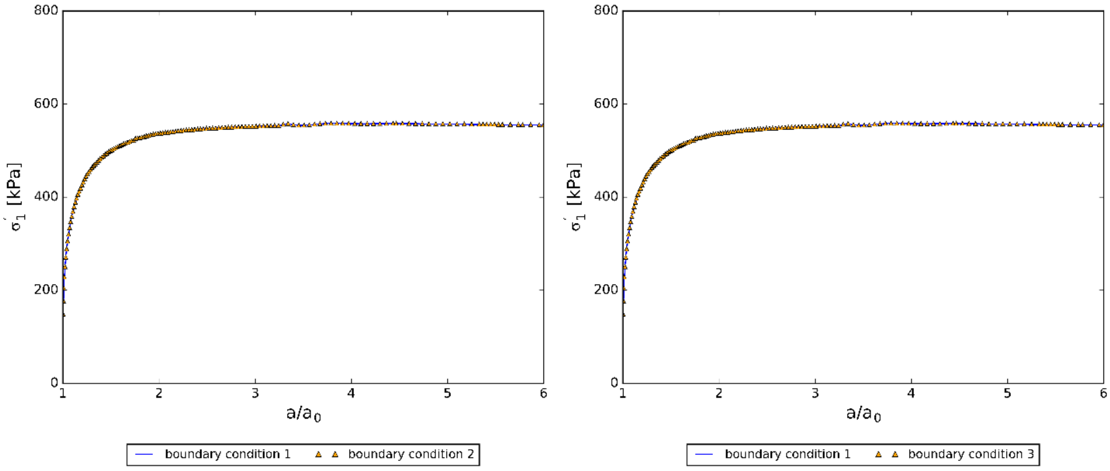

A-Fig. 9: Pressure-expansion curves for boundary condition 2 (left) and boundary condition 3 (right) compared to boundary condition 1

HS contour plots for σ_1'

- K_0 = 1.0 / non-uniform / ψ = 0°

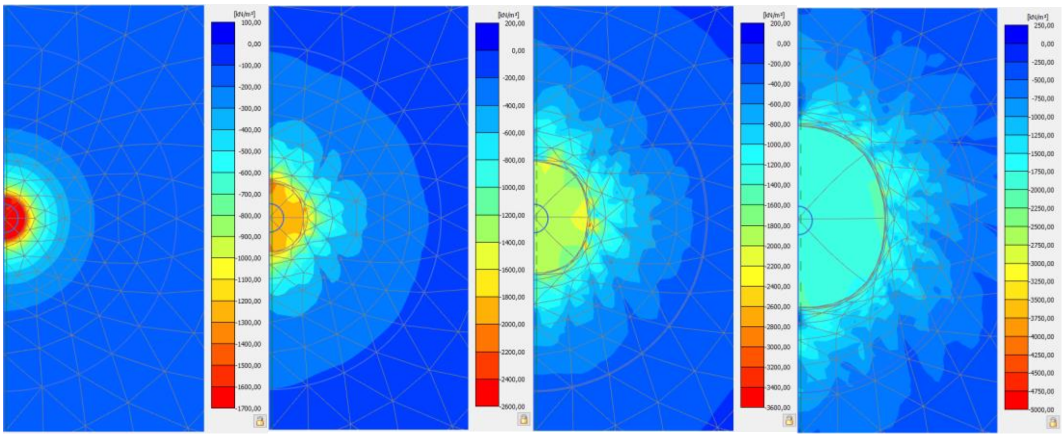

A-Fig. 10: Contour plots for σ_1': HS 1 material set, K_0 = 1.0, ψ = 0°, non-uniform (from phase 1 to phase 4)

- K₀ = 0.36 / same p_0' / uniform / $\psi = 0°$

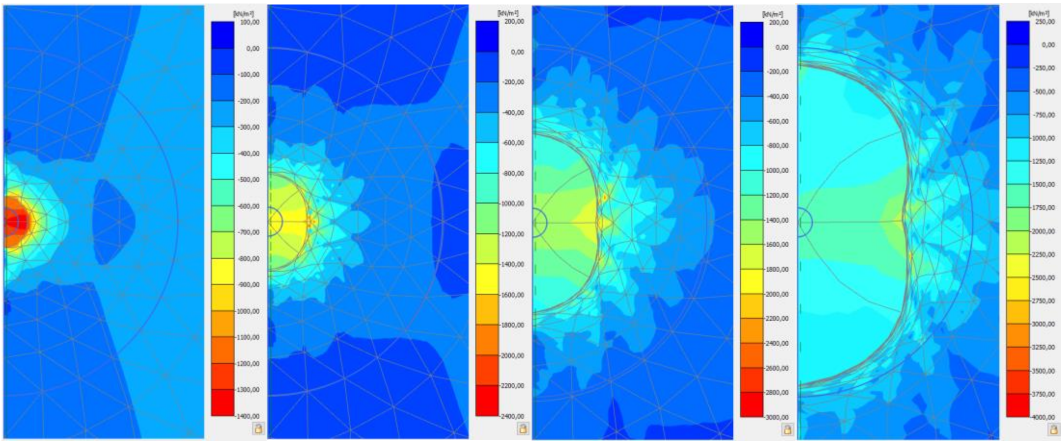

A-Fig. 11: Contour plots for σ_1': HS 1 material set, K₀ = 0.36, same p_0', $\psi = 0°$, uniform (from phase 1 to phase 4)

- K₀ = 0.36 / same p_0' / uniform / $\psi = 40°$

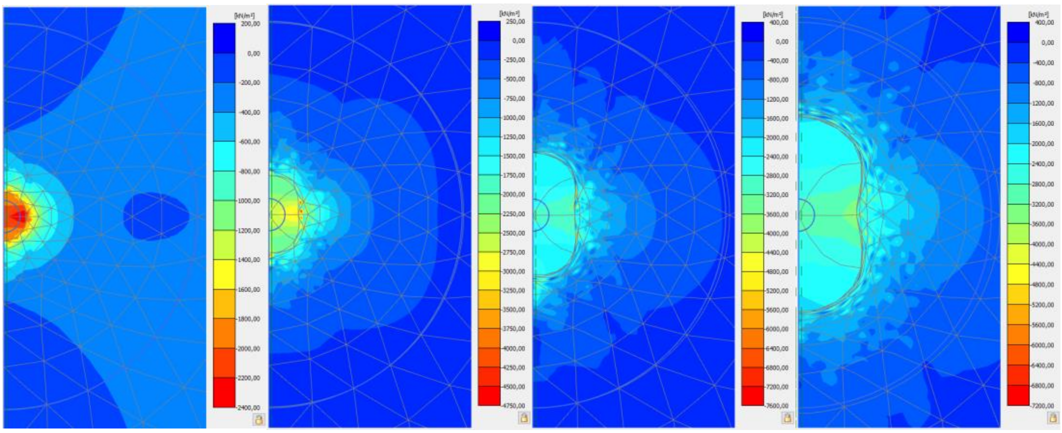

A-Fig. 12: Contour plots for σ_1': HS 1 material set, K₀ = 0.36, same p_0', $\psi = 40°$, uniform (from phase 1 to phase 4)

- K₀ = 0.36 / same p_0' / non-uniform / $\psi = 0°$

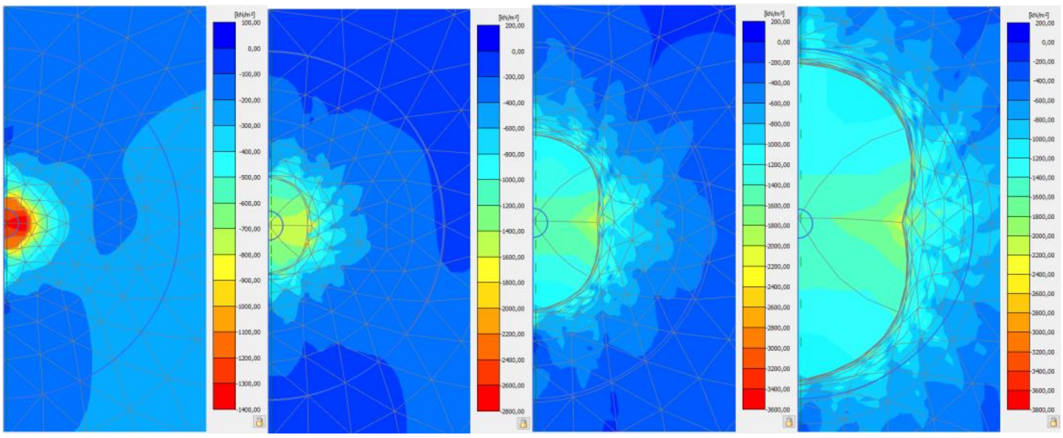

A-Fig. 13: Contour plots for σ_1': HS 1 material set, K₀ = 0.36, same p_0', $\psi = 0°$, non-uniform (from phase 1 to phase 4)

- $K_0 = 0.36$ / same p_0' / non-uniform / $\psi = 40°$

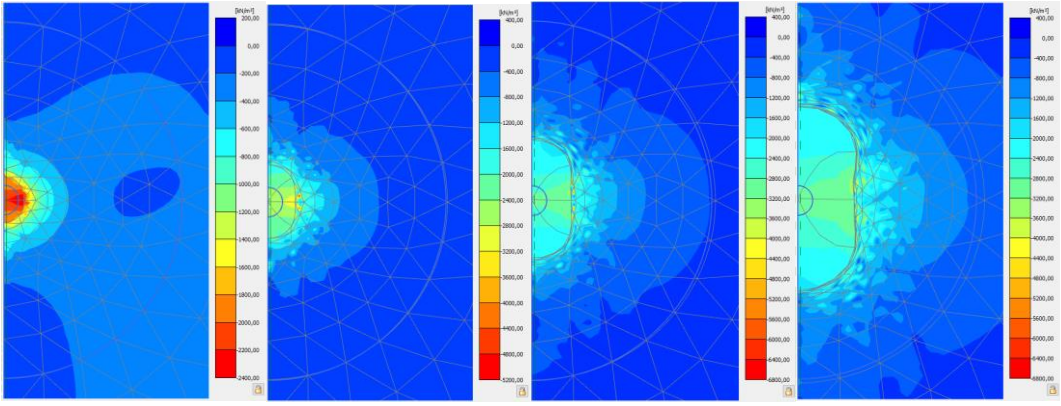

A-Fig. 14: Contour plots for σ_1': HS 1 material set, $K_0 = 0.36$, same p_0', $\psi = 40°$, non-uniform (from phase 1 to phase 4)

Hardening Soil model / contour plots for u_{tot}

- $K_0 = 1.0$ / non-uniform / $\psi = 0°$

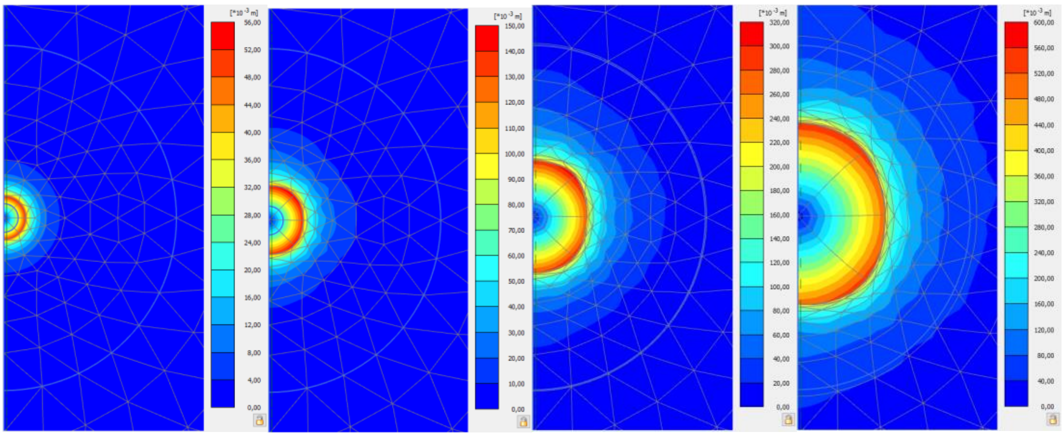

A-Fig. 15: Contour plots for u_{tot}: HS 1 material set, $K_0 = 1.0$, $\psi = 0°$, non-uniform (from phase 1 to phase 4)

- $K_0 = 0.36$ / same p_0' / uniform / $\psi = 0°$

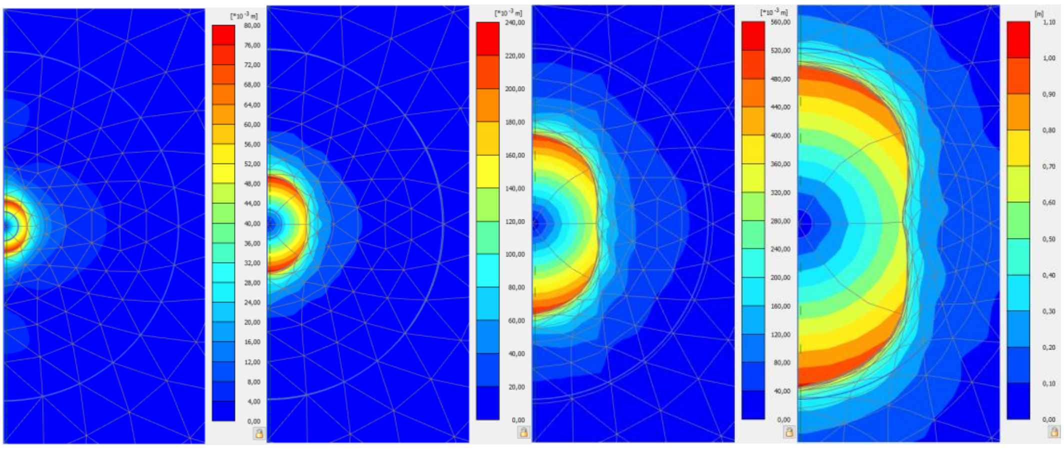

A-Fig. 16: Contour plots for u_{tot}: HS 1 material set, $K_0 = 0.36$, same p_0', $\psi = 0°$, uniform (from phase 1 to phase 4)

- $K_0 = 0.36$ / same p_0' / uniform / $\psi = 40°$

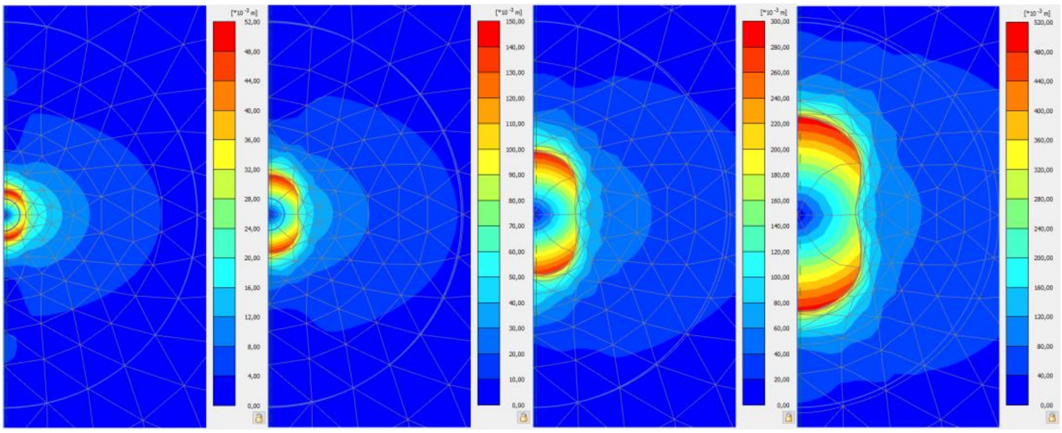

A-Fig. 17: Contour plots for u_{tot}: HS 1 material set, $K_0 = 0.36$, same p_0', $\psi = 40°$, uniform (from phase 1 to phase 4)

- $K_0 = 0.36$ / same p_0' / non-uniform / $\psi = 0°$

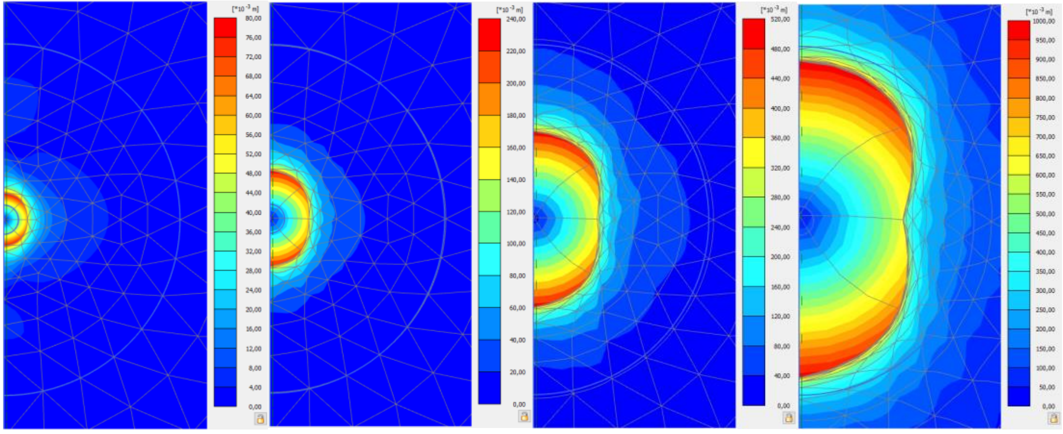

A-Fig. 18: Contour plots for u_{tot}: HS 1 material set, $K_0 = 0.36$, same p_0', $\psi = 0°$, non-uniform (from phase 1 to phase 4)

- $K_0 = 0.36$ / same p_0' / non-uniform / $\psi = 40°$

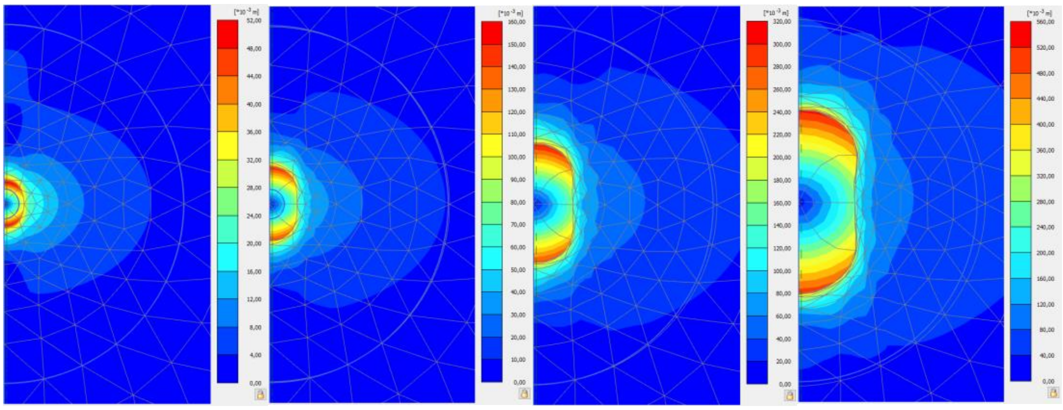

A-Fig. 19: Contour plots for u_{tot}: HS 1 material set, $K_0 = 0.36$, same p_0', $\psi = 40°$, non-uniform (from phase 1 to phase 4)

Appendix C for chapter 6

A-Tab. 23: Hypoplastic parameter set for different input files in ExCalibre

Material	φ_c [°]	h_s $[MPa]$	n [-]	e_{d0} [-]	e_{c0} [-]	e_{i0} [-]	α [-]	β [-]
Ex. 1	32.7	35.17	0.436	0.610	1.220	1.463	0.49	2.30
Ex. 2	34.2	34.01	0.464	0.606	1.213	1.455	0.32	2.00
Ex. 3	30.9	113.91	0.721	0.400	0.800	0.960	0.10	0.10
Ex. 4	34.2	35.72	0.452	0.607	1.215	1.458	0.30	2.00
Ex. 5	31.3	28.78	0.369	0.625	1.250	1.500	0.30	5.90
Ex. 6	33.8	27.10	0.368	0.626	1.251	1.501	0.01	6.90
Ex. 7	33.8	79.33	0.505	0.405	0.809	0.971	0.01	8.00
Ex. 8	33.8	30.12	0.420	0.613	1.227	1.472	0.17	3.70

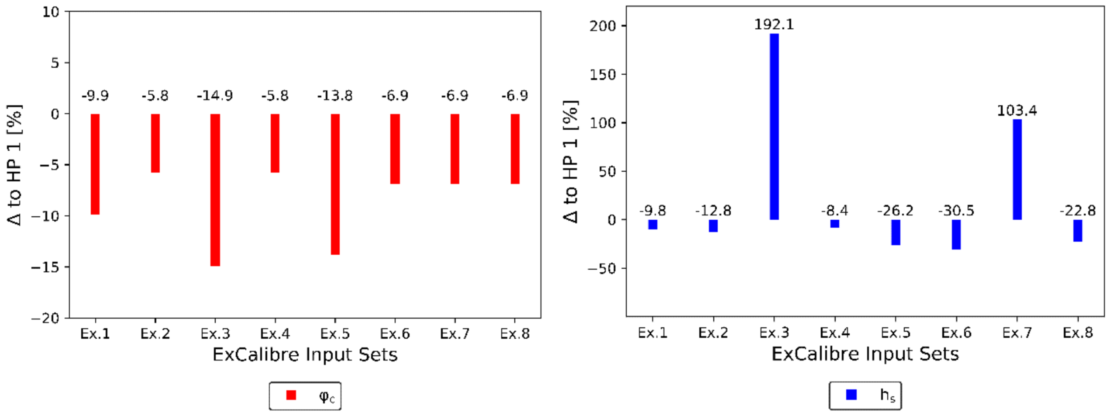

A-Fig. 20: Differences between HP 1 and ExCalibre results (for φ_c (left) and h_s (right))

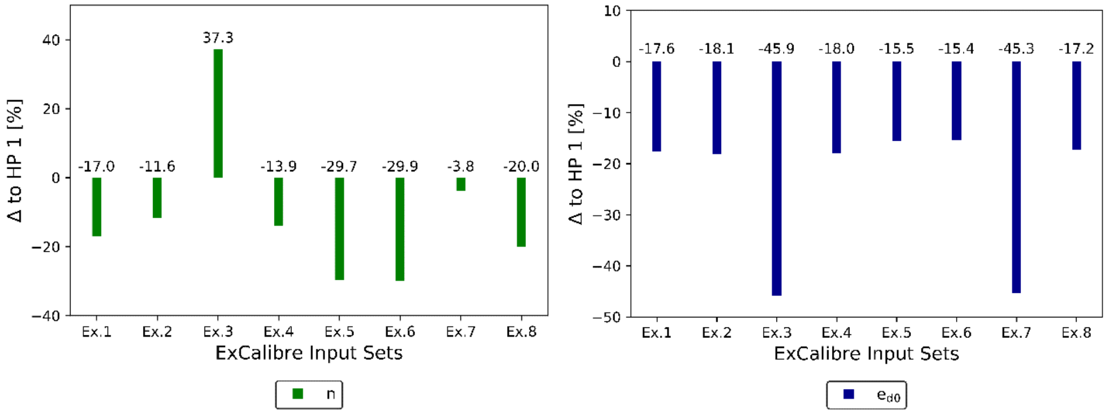

A-Fig. 21: Differences between HP 1 and ExCalibre results (for n (left) and e_{d0} (right))

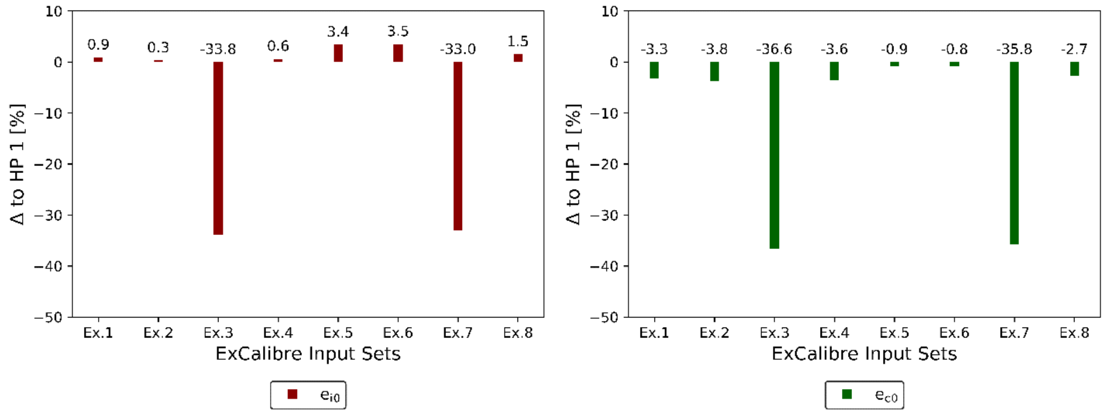

A-Fig. 22: Differences between HP 1 and ExCalibre results (for e_{i0} (left) and e_{c0} (right))

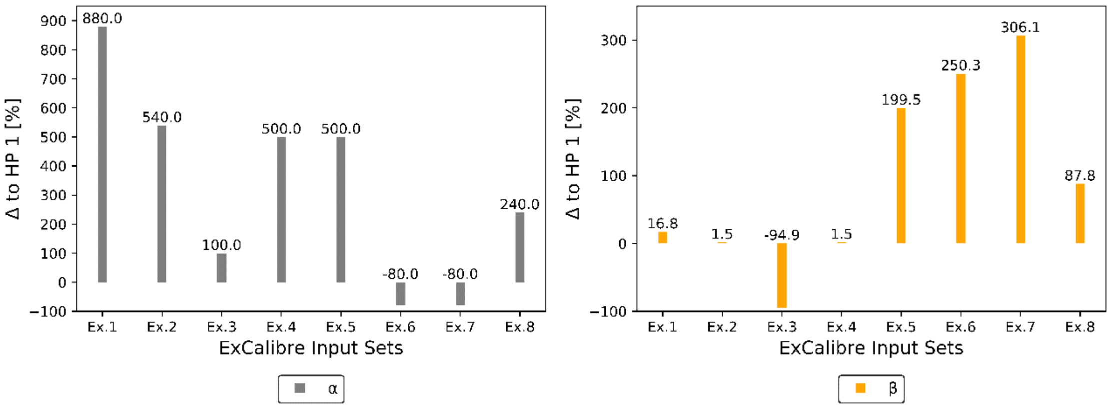

A-Fig. 23: Differences between HP 1 and ExCalibre results (for α (left) and β (right))

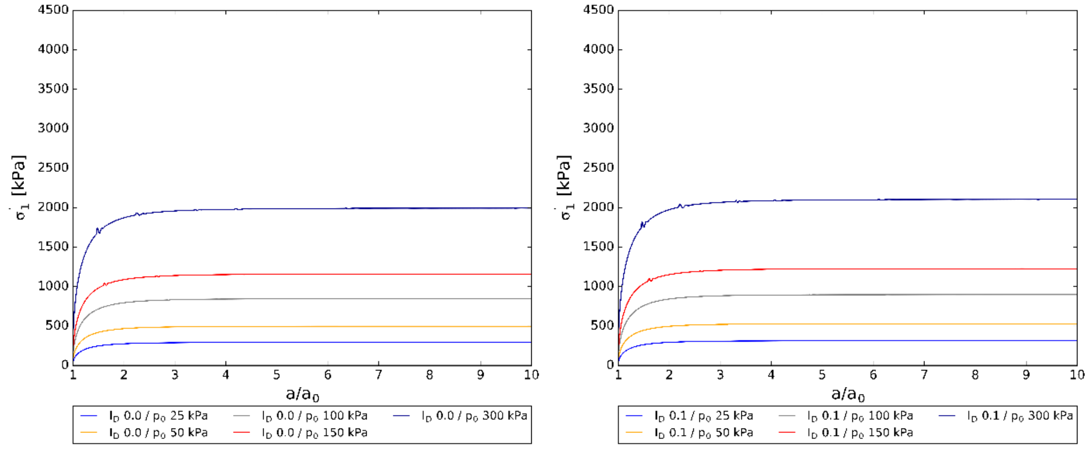

A-Fig. 24: Pressure-expansion curves for parameter set HP 1 and different density states (I_D 0.0 (left) and I_D 0.1 (right))

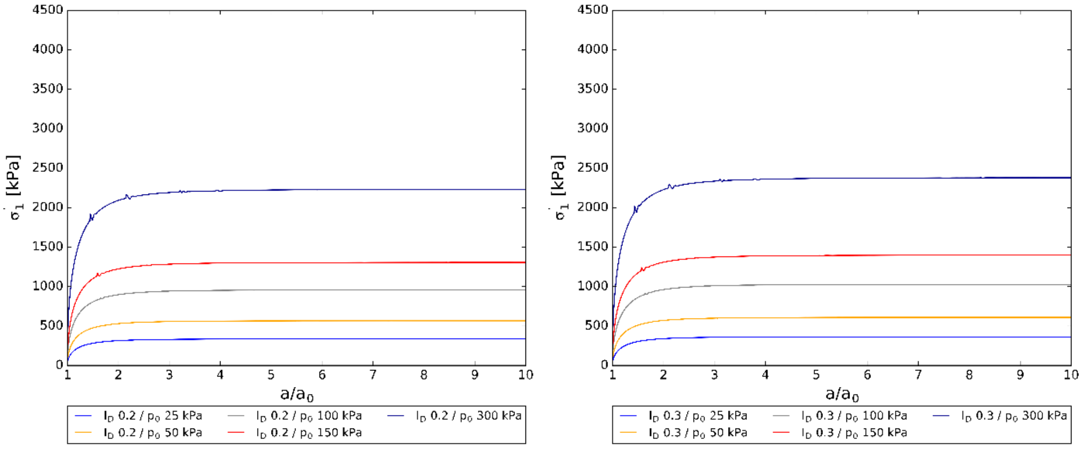

A-Fig. 25: Pressure-expansion curves for parameter set HP 1 and different density states (I_D 0.2 (left) and I_D 0.3 (right))

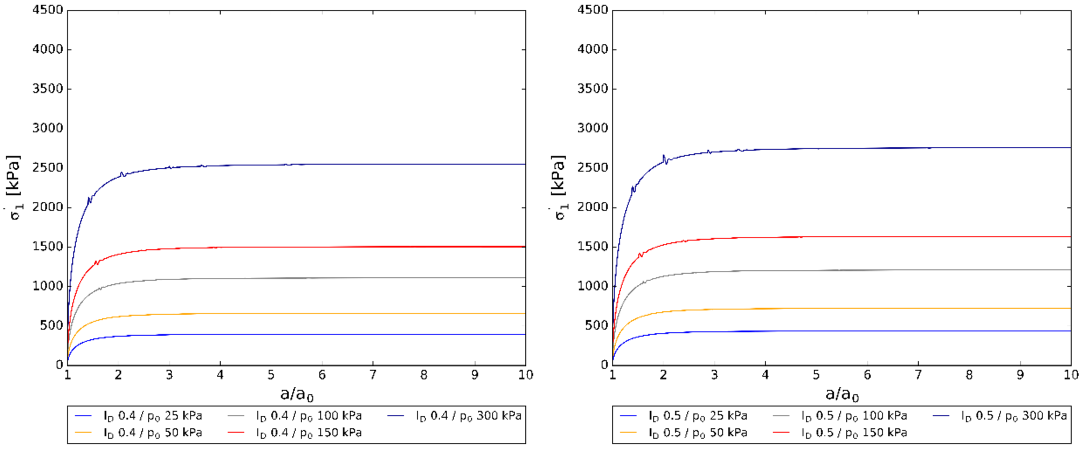

A-Fig. 26: Pressure-expansion curves for parameter set HP 1 and different density states (I_D 0.4 (left) and I_D 0.5 (right))

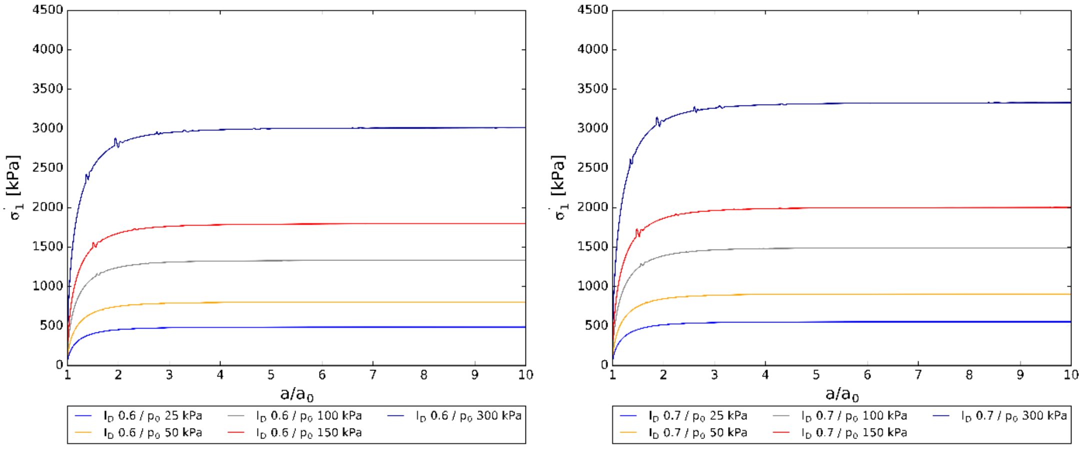

A-Fig. 27: Pressure-expansion curves for parameter set HP 1 and different density states (I_D 0.6 (left) and I_D 0.7 (right))

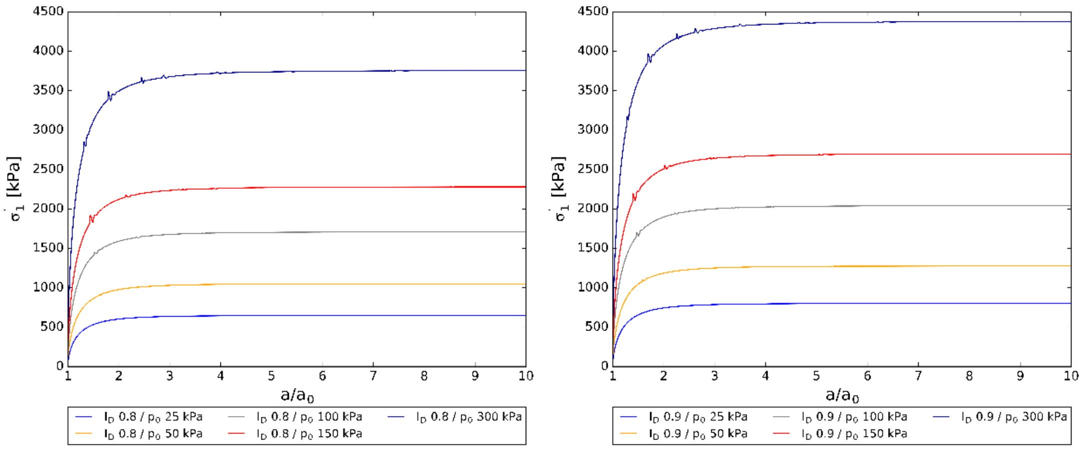

A-Fig. 28: Pressure-expansion curves for parameter set HP 1 and different density states (I_D 0.8 (left) and I_D 0.9 (right))

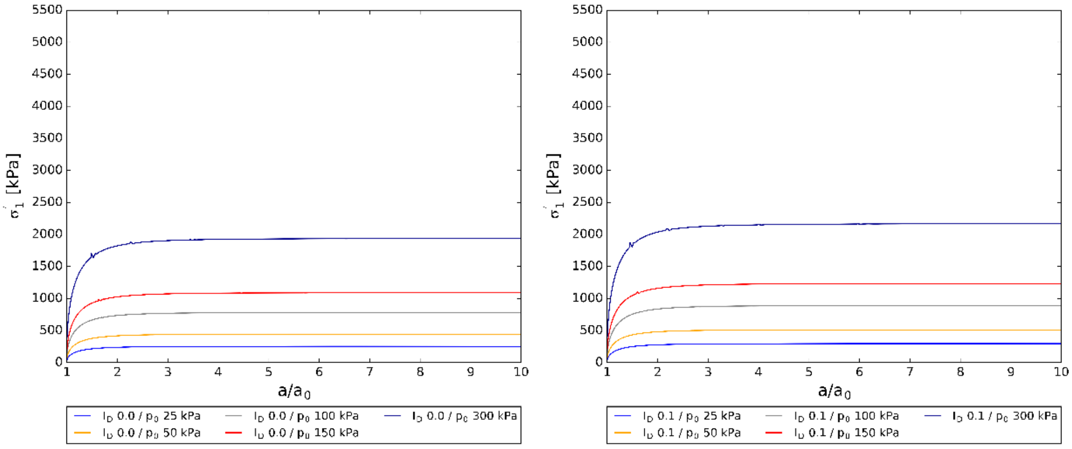

A-Fig. 29: Pressure-expansion curves for parameter set Ex. 4 and different density states (I_D 0.0 (left) and I_D 0.1 (right))

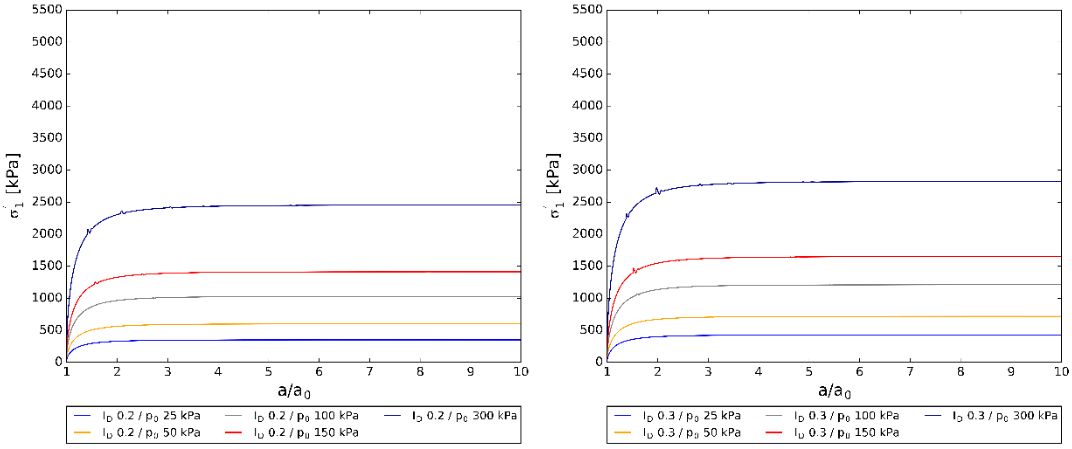

A-Fig. 30: Pressure-expansion curves for parameter set Ex. 4 and different density states (I_D 0.2 (left) and I_D 0.3 (right))

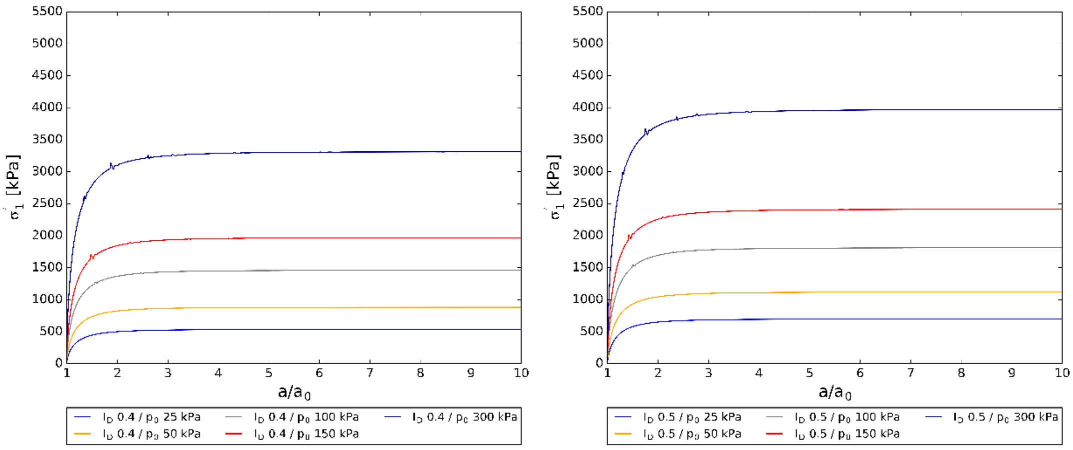

A-Fig. 31: Pressure-expansion curves for parameter set Ex. 4 and different density states (I_D 0.4 (left) and I_D 0.5 (right))

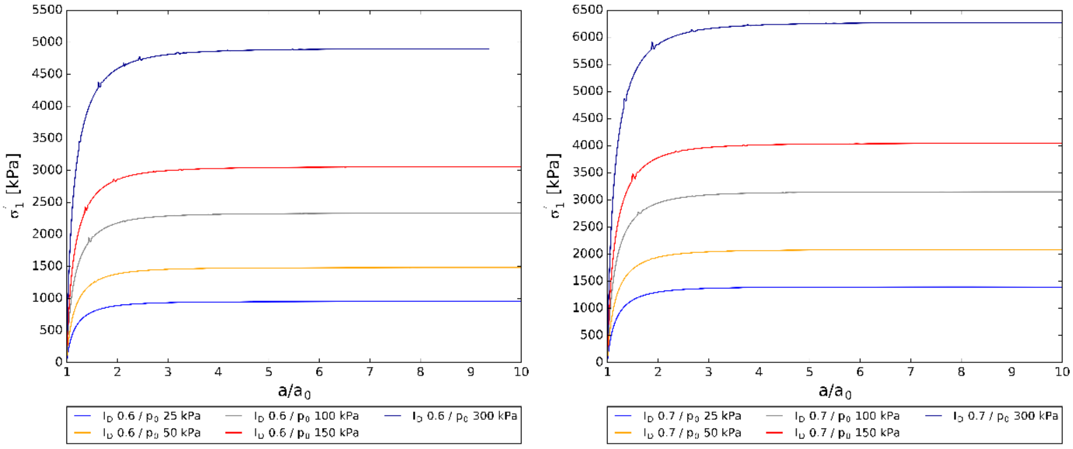

A-Fig. 32: Pressure-expansion curves for parameter set Ex. 4 and different density states (I_D 0.6 (left) and I_D 0.7 (right))

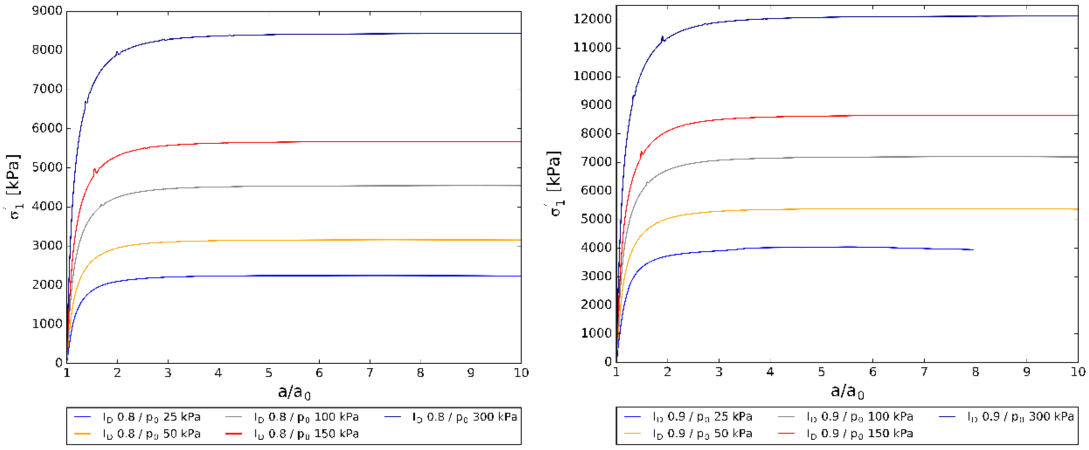

A-Fig. 33: Pressure-expansion curves for parameter set Ex. 4 and different density states (I_D 0.8 (left) and I_D 0.9 (right))

A-Tab. 24: Calculated limit pressures for parameter set HP 1

	Limit pressure p_{LS} [kPa]				
p_0 \ I_D	0.0	0.1	0.2	0.3	0.4
25 kPa	293	313	336	363	396
50 kPa	497	529	566	609	661
100 kPa	846	898	957	1027	1109
150 kPa	1159	1227	1306	1398	1506
300 kPa	1994	2105	2233	2380	2553
p_0 \ I_D	0.5	0.6	0.7	0.8	0.9
25 kPa	436	487	554	648	802
50 kPa	724	803	906	1050	1275
100 kPa	1209	1333	1492	1709	2042
150 kPa	1636	1797	2003	2280	2698
300 kPa	2760	3012	3331	3755	4379

A-Tab. 25: Calculated limit pressures for parameter set Ex. 4

	Limit pressure p_{LS} [kPa]				
p_0 \ I_D	0.0	0.1	0.2	0.3	0.4
25 kPa	254	296	352	428	536
50 kPa	445	512	599	717	882
100 kPa	782	890	1029	1212	1460
150 kPa	1091	1233	1415	1652	1970
300 kPa	1937	2167	2455	2825	3312
p_0 \ I_D	0.5	0.6	0.7	0.8	0.9
25 kPa	697	954	1396	2248	4045
50 kPa	1119	1483	2082	3163	5383
100 kPa	1812	2332	3151	4547	7202
150 kPa	2413	3055	4044	5674	8654
300 kPa	3971	4899	6275	8431	12122

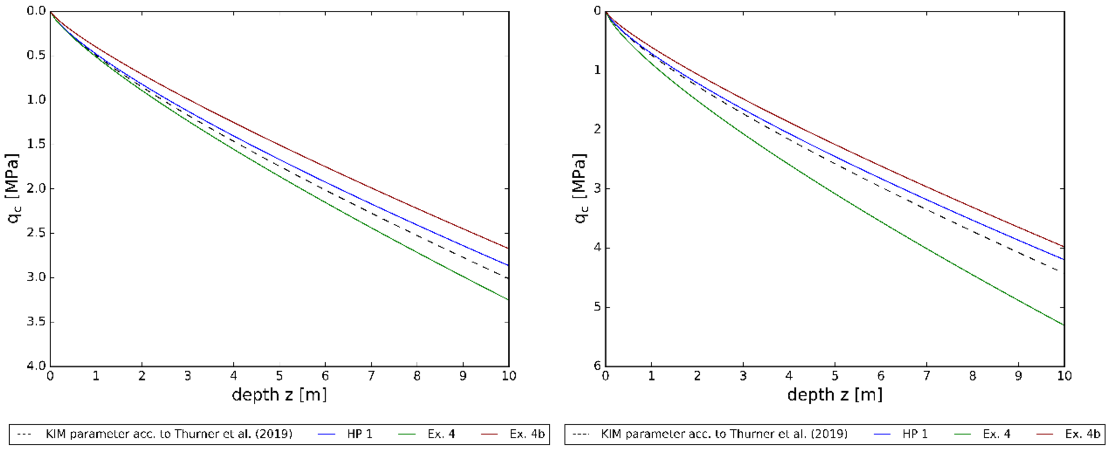

A-Fig. 34: q_c curves for relative densities $I_D = 0.2$ (left) and $I_D = 0.3$ (right)

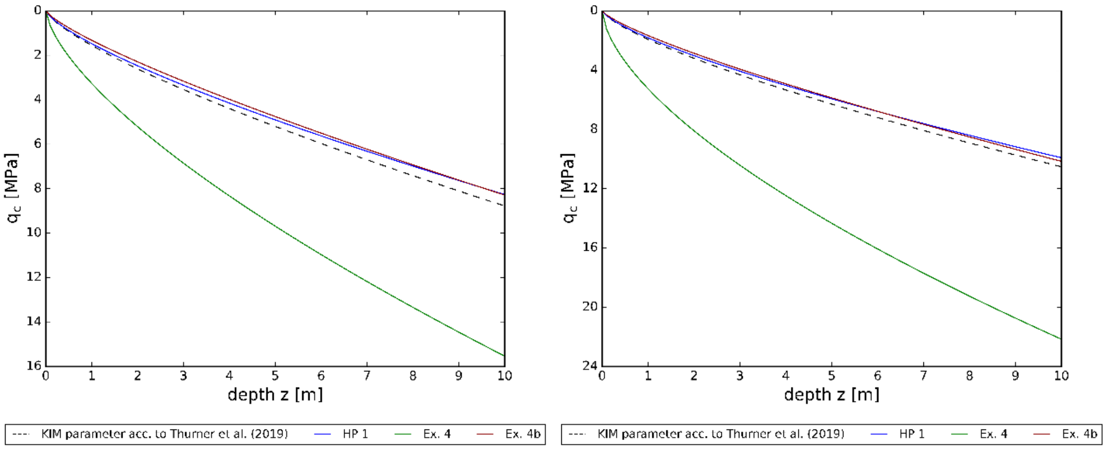

A-Fig. 35: q_c curves for relative densities $I_D = 0.6$ (left) and $I_D = 0.7$ (right)

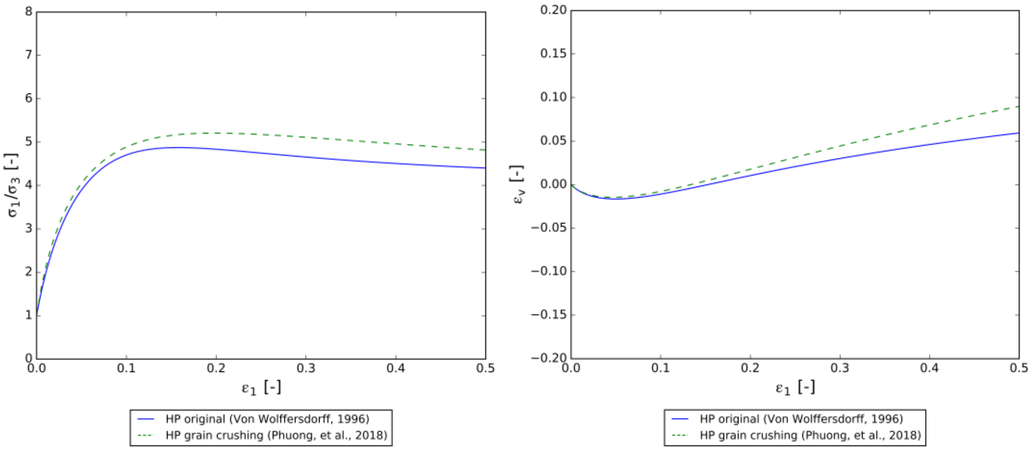

A-Fig. 36: Triaxial test results for material set HP 1 and σ_3 = 500 kPa – stress ratio vs axial strain (left) and volumetric strain vs axial strain (right)

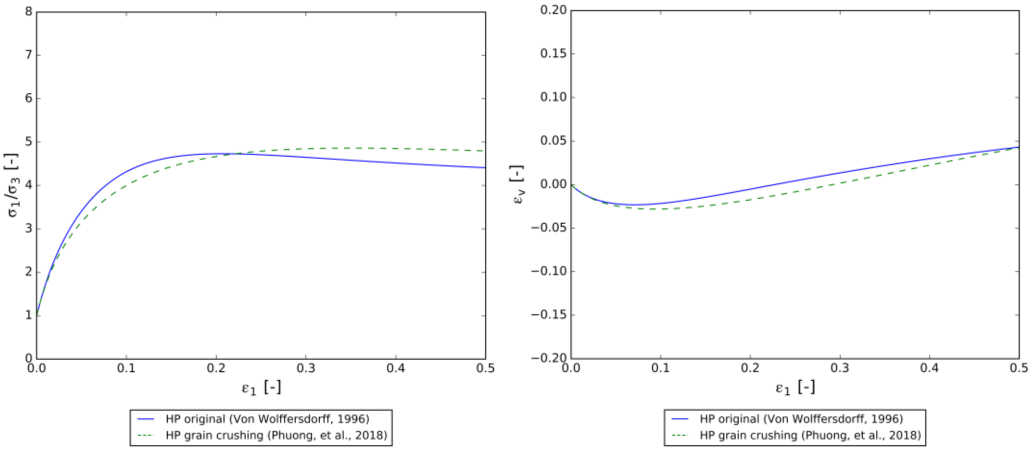

A-Fig. 37: Triaxial test results for material set HP 1 and σ_3 = 1000 kPa – stress ratio vs axial strain (left) and volumetric strain vs axial strain (right)

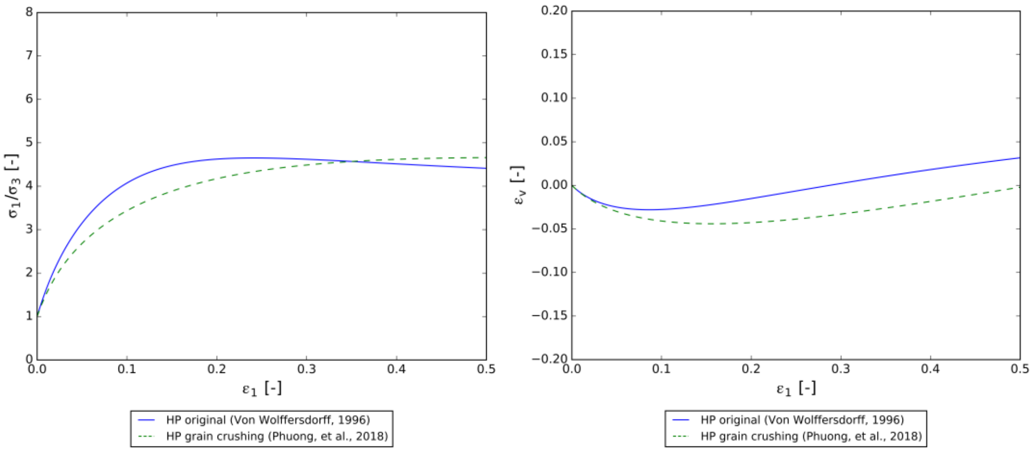

A-Fig. 38: Triaxial test results for material set HP 1 and σ_3 = 1500 kPa – stress ratio vs axial strain (left) and volumetric strain vs axial strain (right)

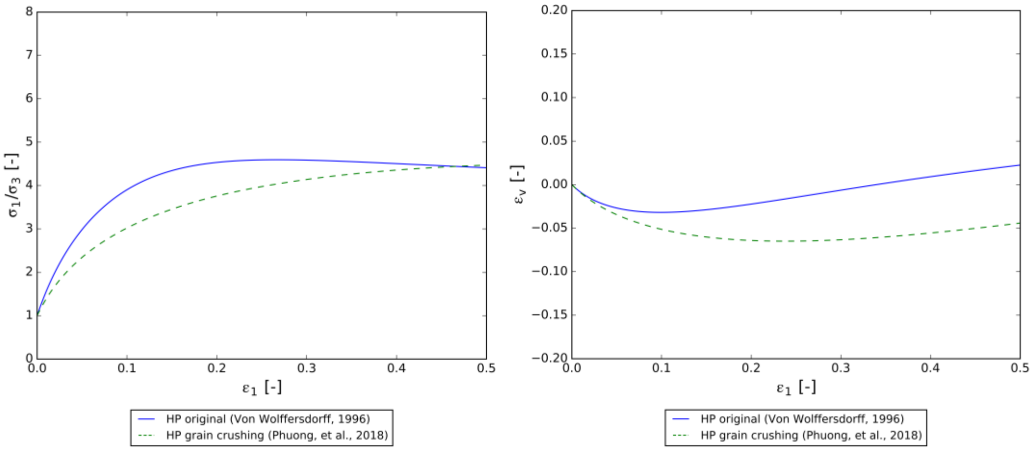

A-Fig. 39: Triaxial test results for material set HP 1 and σ_3 = 2000 kPa – stress ratio vs axial strain (left) and volumetric strain vs axial strain (right)

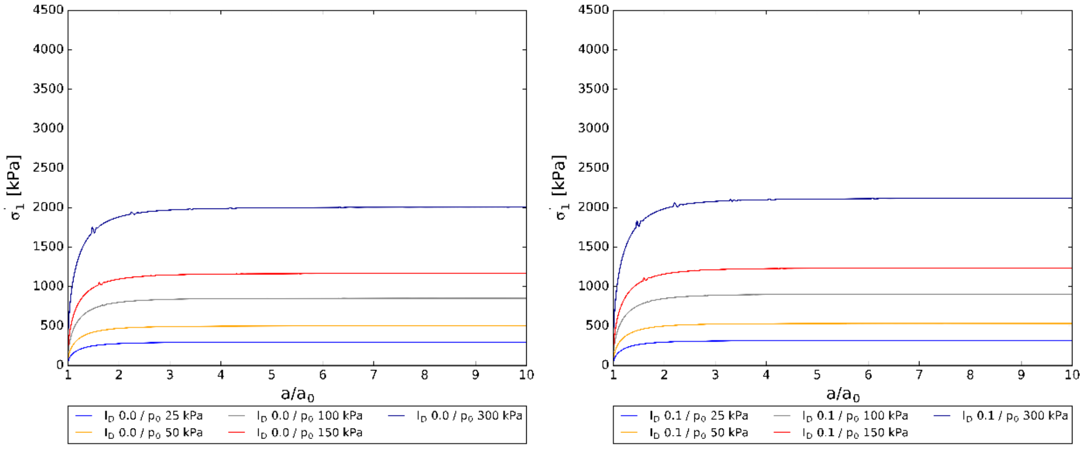

A-Fig. 40: Pressure-expansion curves for GC HP 1 and different density states (I_D 0.0 (left) and I_D 0.1 (right))

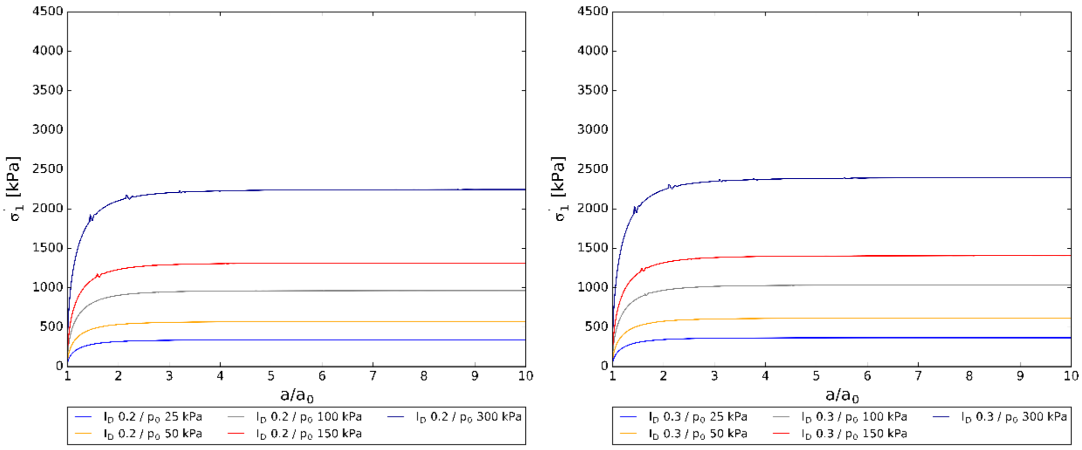

A-Fig. 41: Pressure-expansion curves for GC HP 1 and different density states (I_D 0.2 (left) and I_D 0.3 (right))

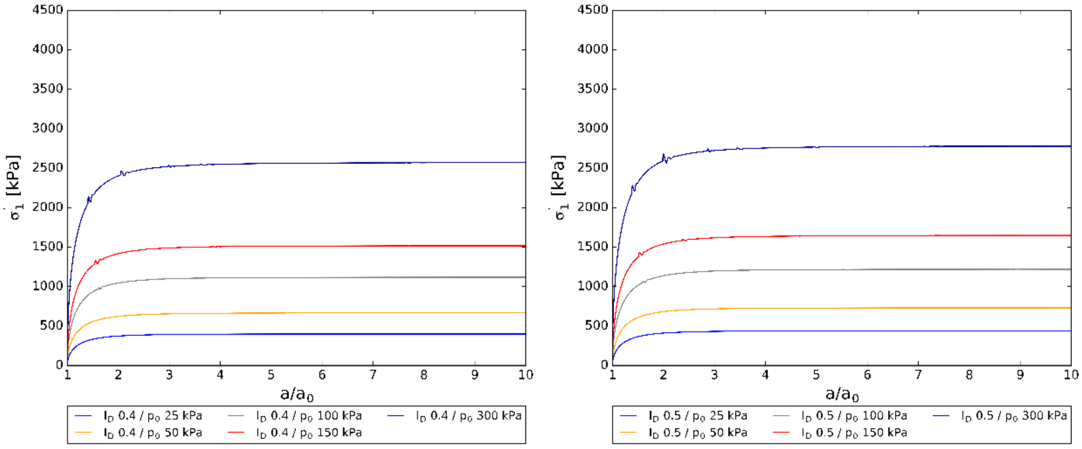

A-Fig. 42: Pressure-expansion curves for GC HP 1 and different density states (I_D 0.4 (left) and I_D 0.5 (right))

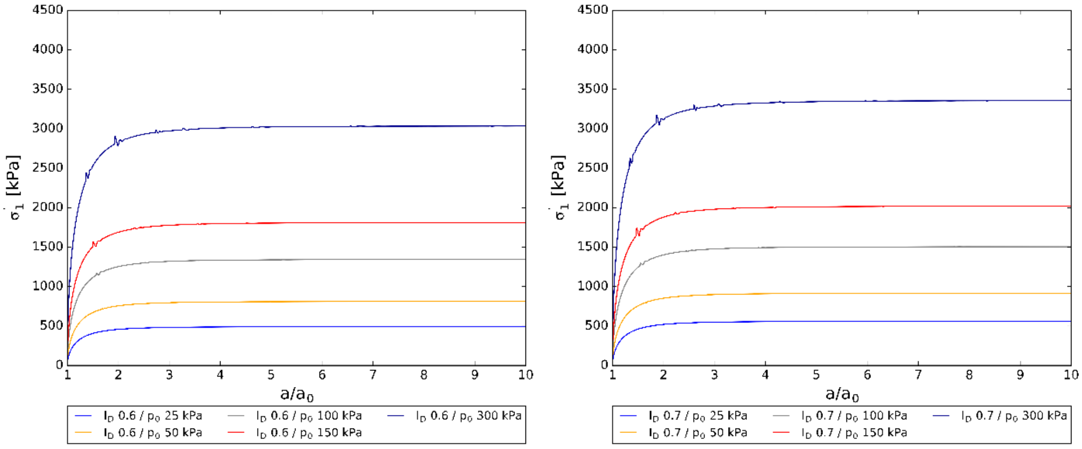

A-Fig. 43: Pressure-expansion curves for GC HP 1 and different density states (I_D 0.6 (left) and I_D 0.7 (right))

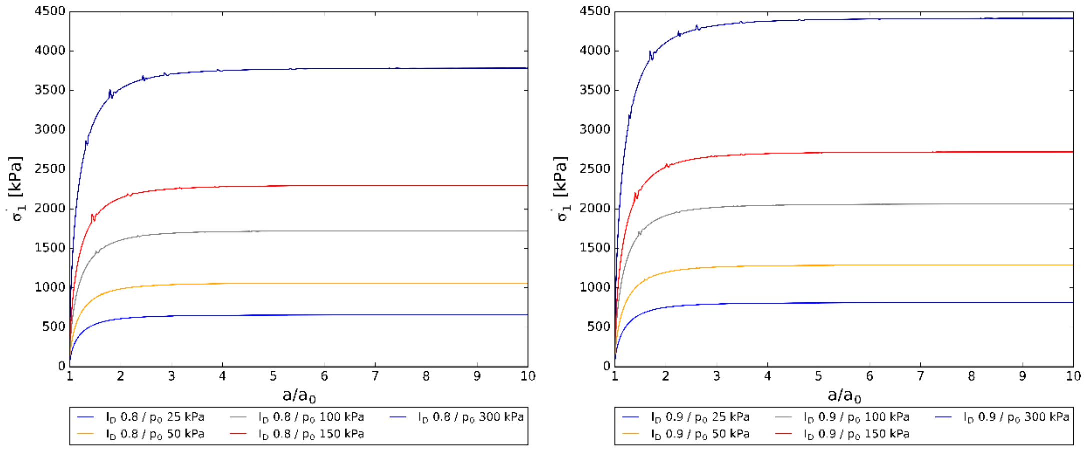

A-Fig. 44: Pressure-expansion curves for GC HP 1 and different density states (I_D 0.8 (left) and I_D 0.9 (right))

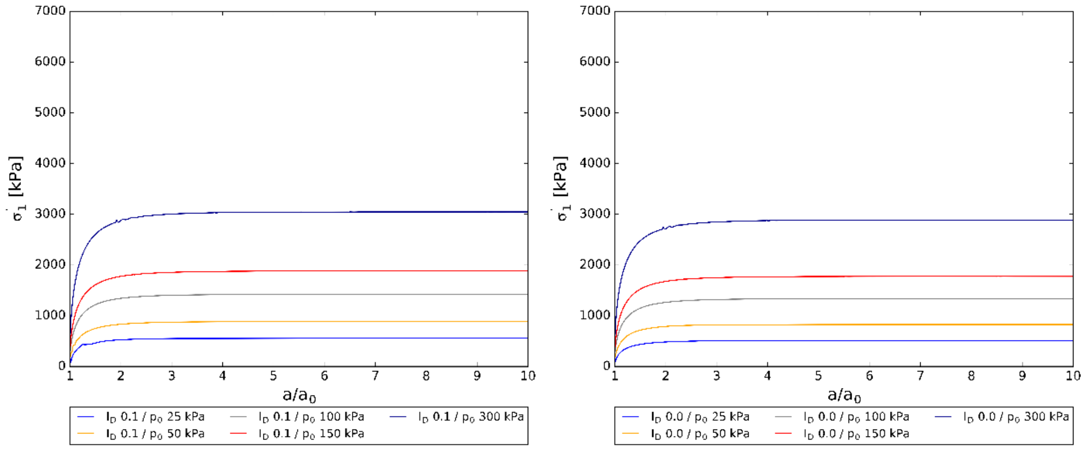

A-Fig. 45: Pressure-expansion curves for orig. HP 2 and different density states (I_D 0.0 (left) and I_D 0.1 (right))

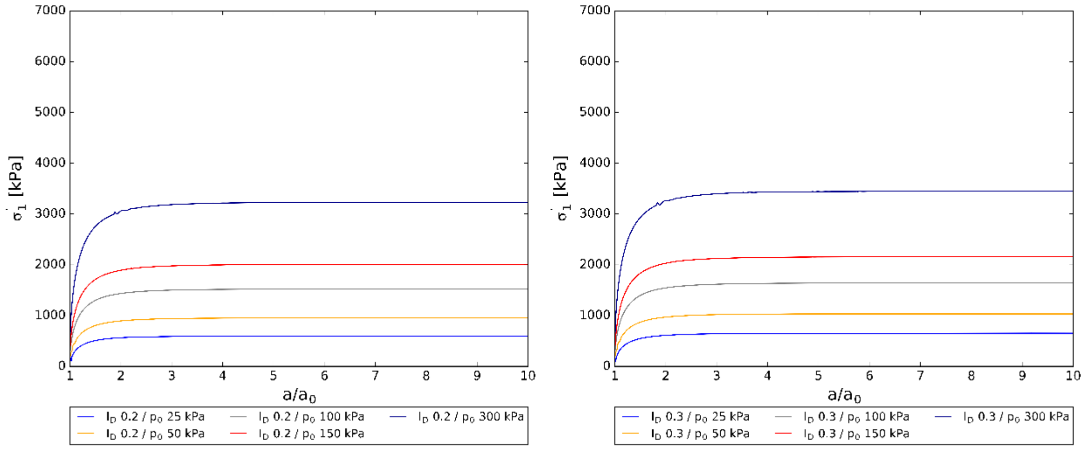

A-Fig. 46: Pressure-expansion curves for orig. HP 2 and different density states (I_D 0.2 (left) and I_D 0.3 (right))

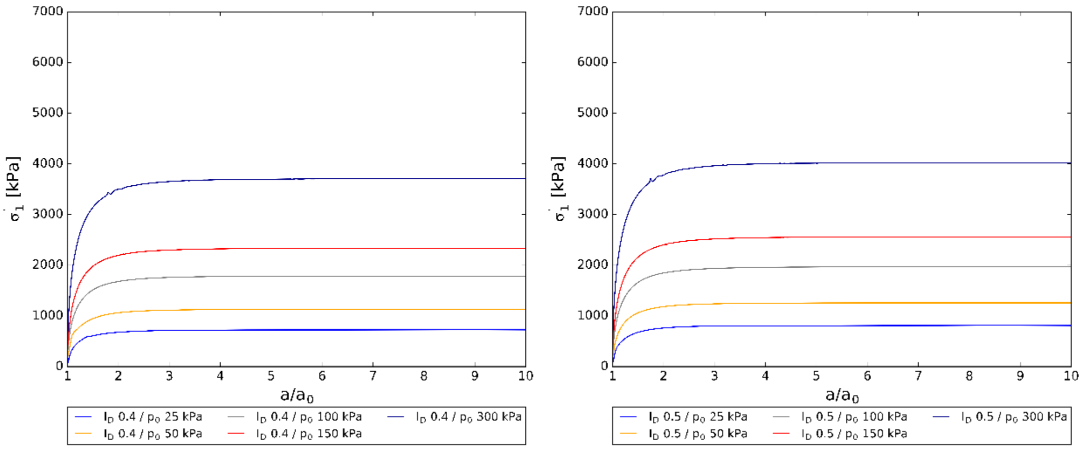

A-Fig. 47: Pressure-expansion curves for orig. HP 2 and different density states (I_D 0.4 (left) and I_D 0.5 (right))

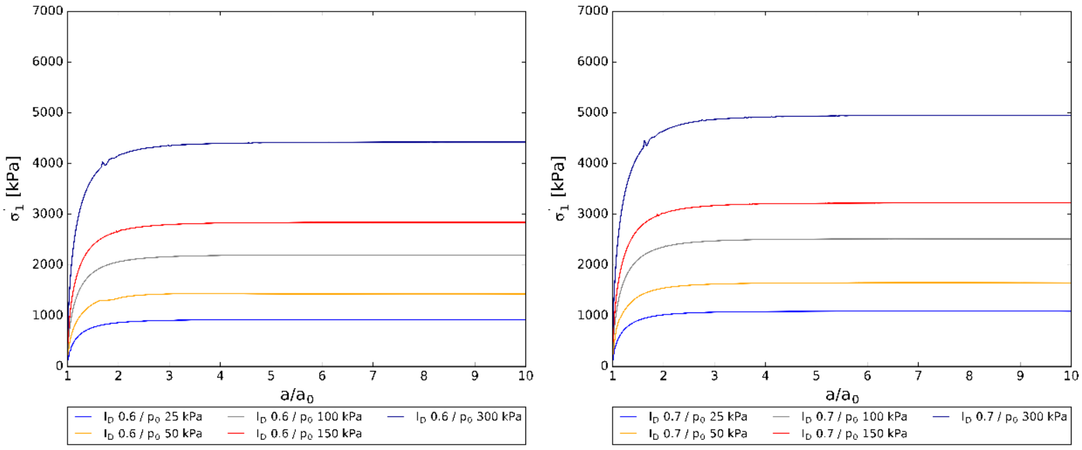

A-Fig. 48: Pressure-expansion curves for orig. HP 2 and different density states (I_D 0.6 (left) and I_D 0.7 (right))

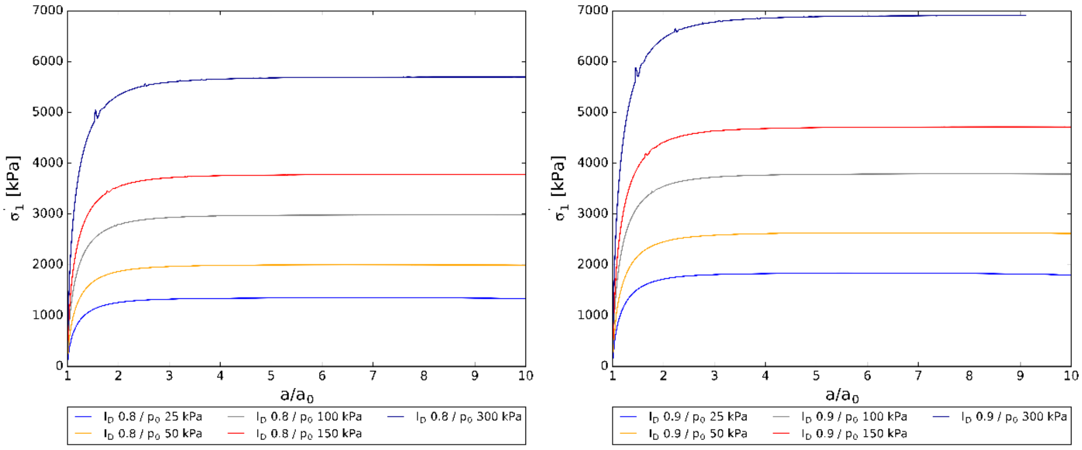

A-Fig. 49: Pressure-expansion curves for orig. HP 2 and different density states (I_D 0.8 (left) and I_D 0.9 (right))

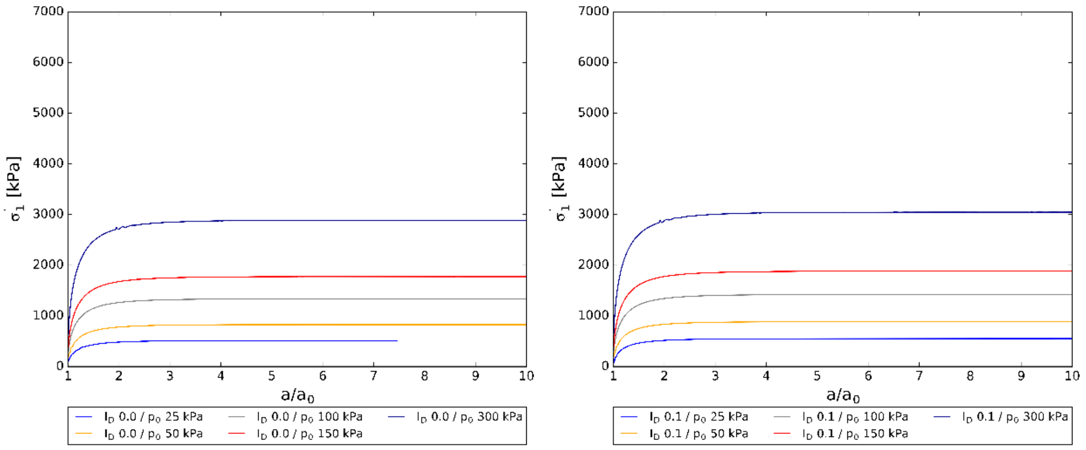

A-Fig. 50: Pressure-expansion curves for GC HP 2 and different density states (I_D 0.0 (left) and I_D 0.1 (right))

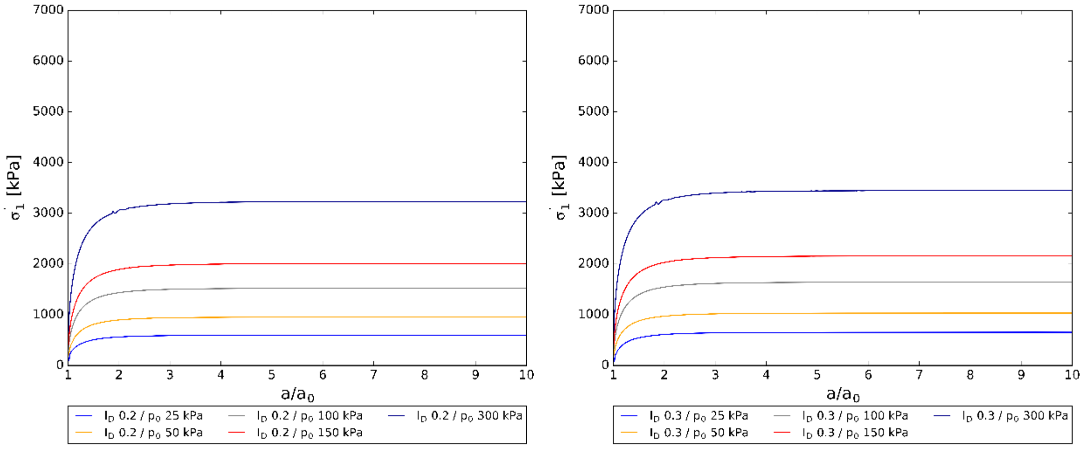

A-Fig. 51: Pressure-expansion curves for GC HP 2 and different density states (I_D 0.2 (left) and I_D 0.3 (right))

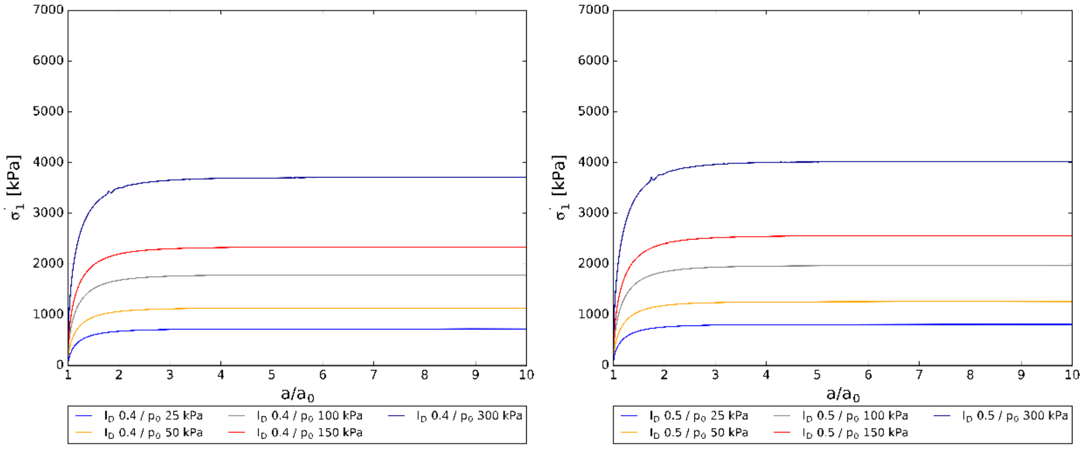

A-Fig. 52: Pressure-expansion curves for GC HP 2 and different density states (I_D 0.4 (left) and I_D 0.5 (right))

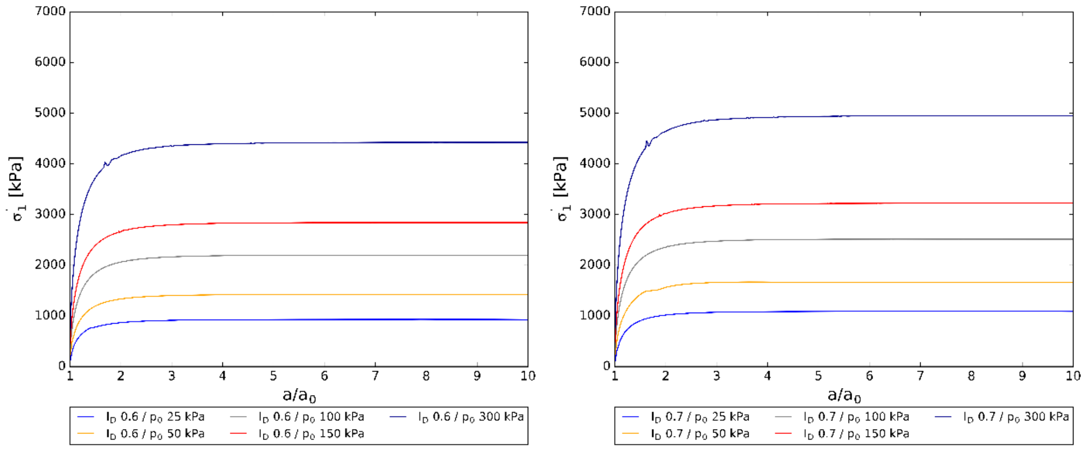

A-Fig. 53: Pressure-expansion curves for GC HP 2 and different density states (I_D 0.6 (left) and I_D 0.7 (right))

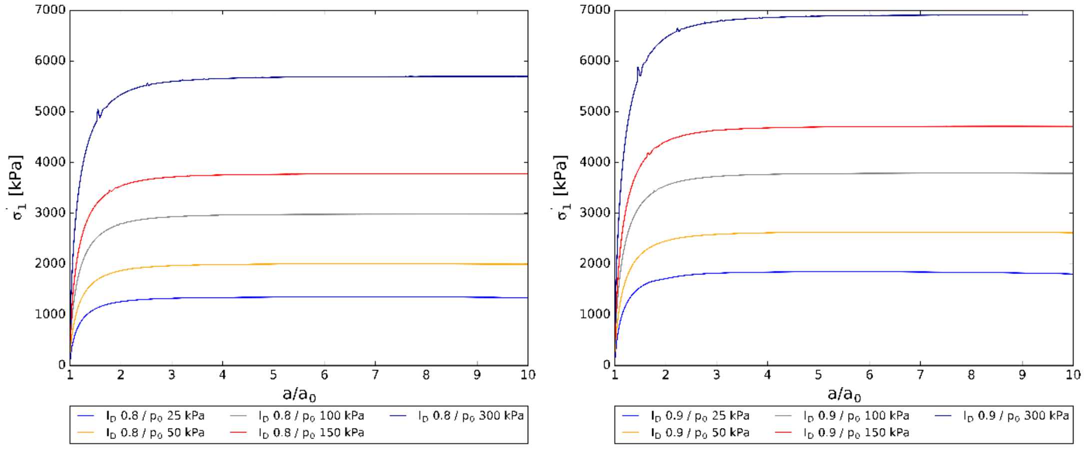

A-Fig. 54: Pressure-expansion curves for GC HP 2 and different density states (I_D 0.8 (left) and I_D 0.9 (right))

A-Tab. 26: Calculated limit pressures for GC HP 1

	Limit pressure p_{LS} [kPa]				
p_0 \ I_D	0.0	0.1	0.2	0.3	0.4
25 kPa	296	316	339	336	399
50 kPa	500	533	570	614	666
100 kPa	852	904	964	1034	1118
150 kPa	1166	1235	1314	1407	1517
300 kPa	2006	2118	2246	2395	2570
p_0 \ I_D	0.5	0.6	0.7	0.8	0.9
25 kPa	440	491	559	655	811
50 kPa	730	810	915	1060	1288
100 kPa	1219	1344	1505	1725	2061
150 kPa	1648	1811	2019	2299	2723
300 kPa	2779	3034	3357	3786	4416

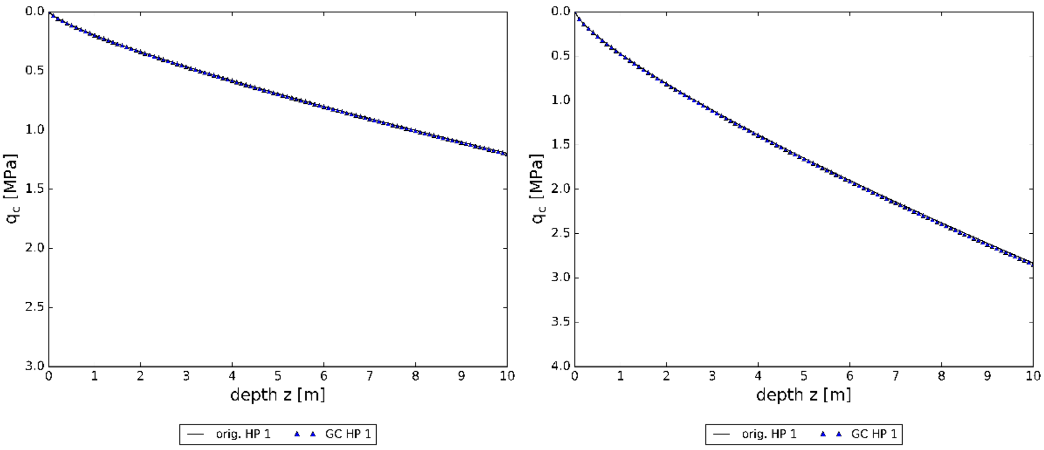

A-Fig. 55: q_c-curves for material HP 1 and different relative densities (I_D = 0.0 (left) and I_D = 0.2 (right))

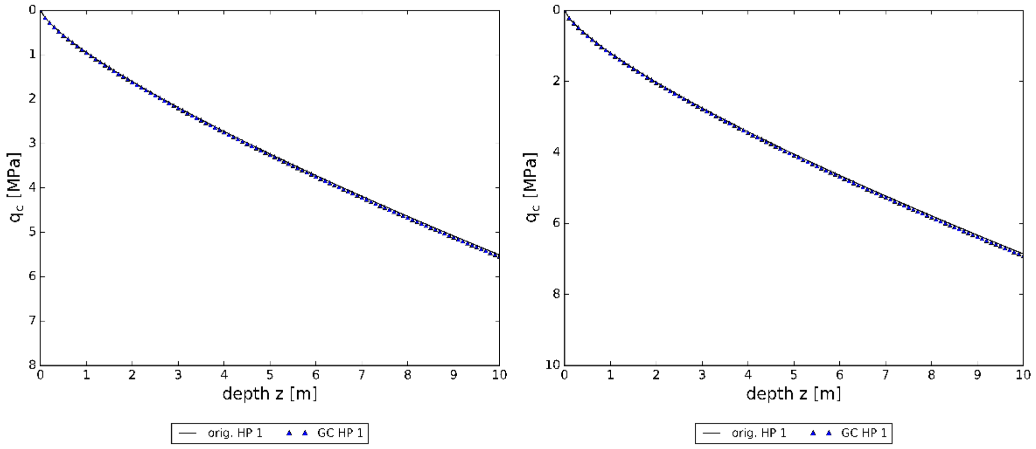

A-Fig. 56: q_c-curves for material HP 1 and different relative densities (I_D = 0.4 (left) and I_D = 0.5 (right))

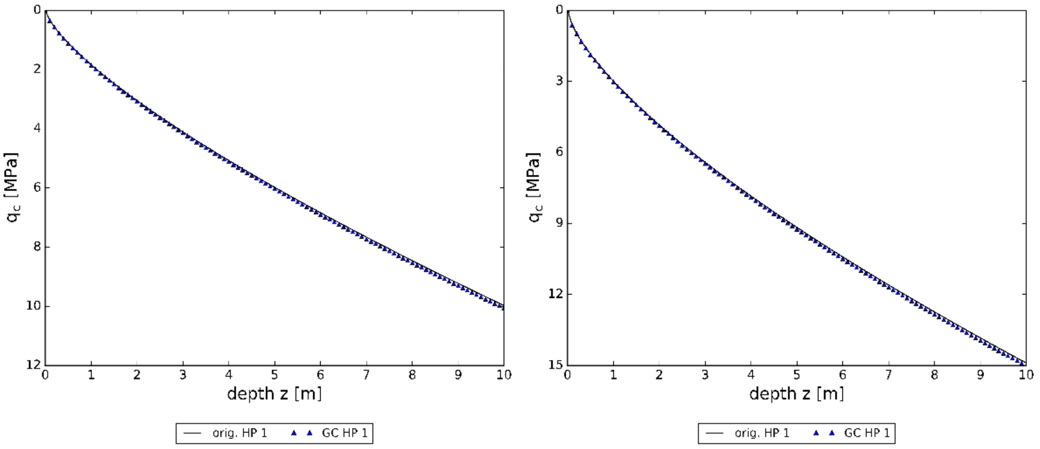

A-Fig. 57: q_c-curves for material HP 1 and different relative densities (I_D = 0.7 (left) and I_D = 0.9 (right))

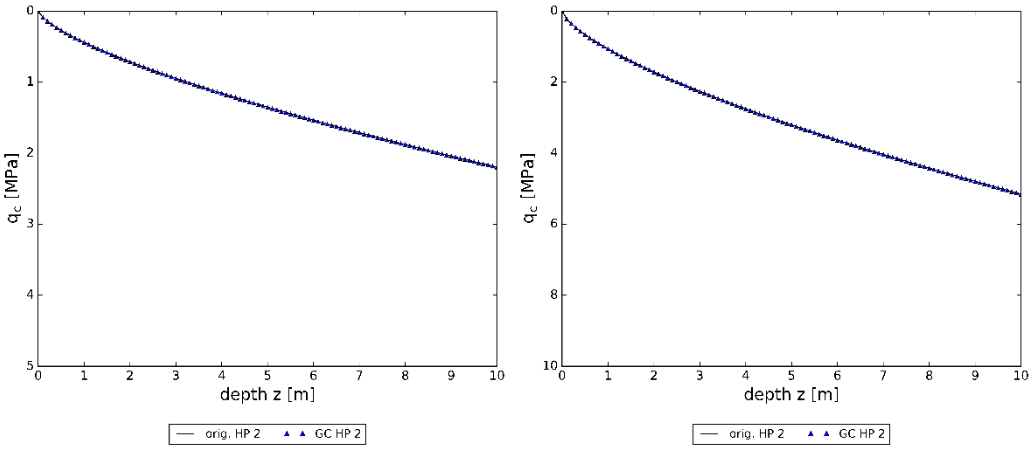

A-Fig. 58: q_c-curves for material HP 2 and different relative densities (I_D = 0.0 (left) and I_D = 0.2 (right))

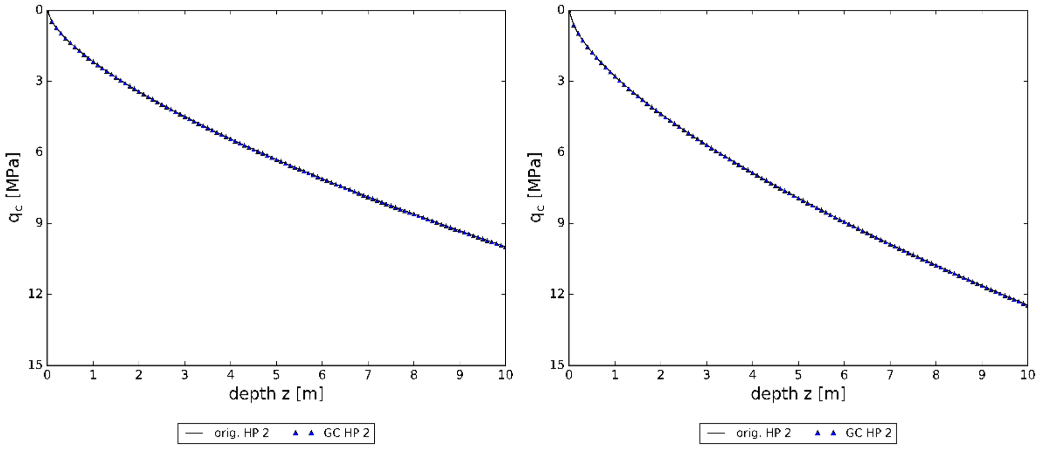

A-Fig. 59: q_c-curves for material HP 2 and different relative densities (I_D = 0.4 (left) and I_D = 0.5 (right))

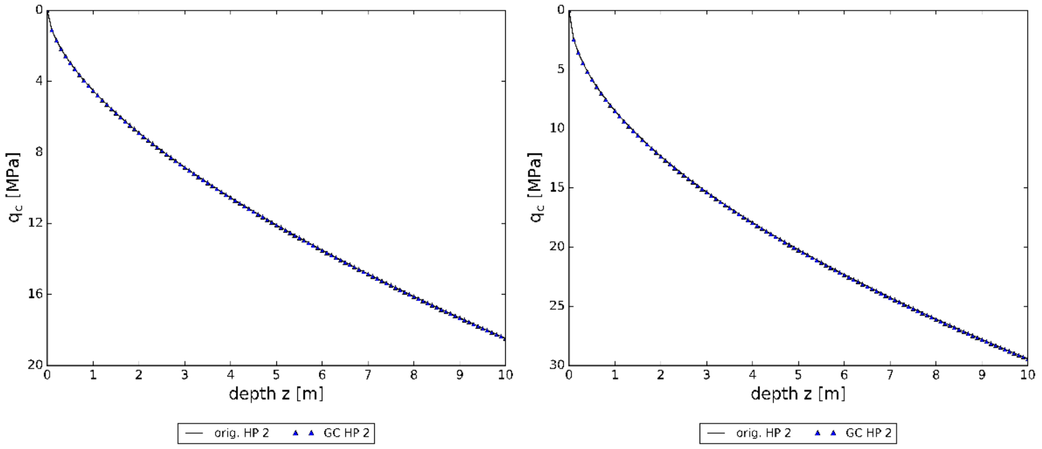

A-Fig. 60: q_c-curves for material HP 2 and different relative densities (I_D = 0.7 (left) and I_D = 0.9 (right))

Parts of the python code for reading and assigning the hypoplastic parameters

```
#  load csv-file with hypoplastic parameters

array = np.loadtxt('path', delimiter=';', skiprows = 3)
np.savetxt('path',array,fmt ='%0.6f')

#  assign hypoplastic parameters

phi_c = array[0]
p_t = array[1]
h_s = array[2]
n = array[3]
ed0 = array[4]
...

#  assign hypoplastic parameters in the Plaxis-file

g_i.Materials[i].setproperties('MaterialName', 'XXX',
                    'Colour', 'XXX',
                    'SoilModel', 'XXX',
                    'UserDLLName','udsm_hps64.dll',
                    'UserModel','Hypoplas.-sand',
                    'K0Primary', 'XXX',
                   'User1', phi_c,            #phi_c
                   'User2', p_t,              #p_t
                   'User3', h_s,              #h_s
                   'User4', n,                #n
                   'User5', ed0,              #e_d0
                    ...
```

Parts of the python code for the automatic output of the FEA results

```
for j in range (0,len(p0)):

    for i in range(0,len(ID)):

        IDstring = str(ID[i])
        p0stringNoZeros = str(p0[j])
        p0string=p0stringNoZeros[::-1].zfill(5)[::-1]
        print(p0string)
        name = '\ID_0' + IDstring[2] + '_p0_' + p0string[2:] + '.p2dx'
        name2 = '\ID_0' + IDstring[2] + '_p0_' + p0string[2:] + '.txt'
        s_i.open(path_plaxis + name)

        # determining number of succesfully calculated phases
        a = 0
        for k in range (1,'number of phases + 1 '):
            if g_i.Phases[k].CalculationResult == g_i.Phases[k]\
            .CalculationResult.ok:
                a = a + 1
            else:
                ()

        g_i.view(g_i.InitialPhase)
        stepids = []
        sig2 = []
        uz2 = []
        sig3 = []
        uz3 = []
        sig4 = []
        uz4 = []
        ...

        # output of desired results
        z = 0
        for z in range (0,a):
            z = z + 1
            steplist = g_o.Phases[z].Steps[0:len(g_o.Phases[z].Steps)]
            x = g_o.Phases[z].Steps[0].ID

            for k in range(len(steplist)):
                stepids.append(str('Step_{}'.format(x)))
                sig2.append(g_o.getcurveresults(g_o.CS_2, steplist[k],
                                            g_o.Soil.SigmaEffective1))
                uz2.append(g_o.getcurveresults(g_o.CN_2, steplist[k],
                                            g_o.Soil.Utot))
                ...
                x+=1

            # saving results as txt-file
            with open(save_path,'w') as file:
                    for 'X' in zip('sig2,uz2, ...'):
                        file.writelines(['{}, ...'.\
                                         format('x')])
```

Parts of the python code for the averaging process and the determination of the limit pressures

```
a0 = 0.1
def mean_stress(value_array):
    nr_rows = len(value_array)
    nr_cols = len(value_array[0])
    mean_stress_vec = []
    for i in range(nr_rows):
        temp_vec = value_array[i][0:nr_cols:2]
        mean_stress_vec.append(np.mean(temp_vec)*-1)
    return mean_stress_vec

def mean_u(value_array):
    nr_rows = len(value_array)
    nr_cols = len(value_array[0])
    mean_u_vec = []
    for i in range(nr_rows):
        temp_vec = value_array[i][1:nr_cols:2]
        mean_u_vec.append(np.mean(temp_vec)/a0+1)
    return mean_u_vec

u_max = []

for i in range (0,len(ID)):

    results_pLS = []
    for j in range(0,len(p0)):


        # file names & paths
        IDstring = str(ID[i])
        p0stringNoZeros = str(p0[j])
        p0string=p0stringNoZeros[::-1].zfill(5)[::-1]
        name = '\ID_0' + IDstring[2] + '_p0_' + p0string[2:] + '.txt'
        name_pls = '\pls_ID_0' + IDstring[2] + '.txt'
        'different paths'

        # results average
        array = np.loadtxt('path', delimiter=',')
        stress = mean_stress(array)
        u = mean_u(array)

        # results pLS
        pls = np.max(stress)
        results_pLS.append(pls)

    np.savetxt('path', results_pLS, fmt ='%0.6f')
```

Parts of the python code for the curve-fitting procedure

```
# defining arrays
...
for i in range (0,1500):
    a = a + 0.01
    b = b + 0.001
    a_vec.append(a)
    b_vec.append(b)

for i in range (0,len(a_vec)):

    for j in range (0,len(b_vec)):

        for k in range (0,len(p0_1)):

            pls_est = a_vec[i] * p0_1[k] ** b_vec[j]
            pLS_est.append(pls_est)

for i in range (0,len(ID_1)):

    'path'
    pLS2 = np.loadtxt('path')/1000

    for i in range (0,int(len(pLS_est)/5)):

        for j in range(0,5):

            a = a + 1
            error = (pLS_est[a] - pLS2[j])**2
            error_sum.append(error)

        i = np.sum(error_sum)
        sum_e.append(i)

    l = np.min(sum_e)
    fehler.append(l)
    u = int(len(sum_e))

    for i in range (0,u):

        if sum_e[i] == l:
            pos = i
        else:
            ()

    for i in range (0,len(a_vec)):

        for j in range (0,len(b_vec)):
            a = a + 1

            if a == pos:
                a_est.append(a_vec[i] - 0.05)
                b_est.append(b_vec[j] - 0.005)
            else:
                ()

np.savetxt('path', a_est, fmt = '%0.1f')
np.savetxt('path', b_est, fmt = '%0.2f')
```

Parts of the python code for the calculation of the cone resistances over depth

```
#  defining paths & loading KIM parameters
...
ai = np.loadtxt('path')
bi = np.loadtxt('path')


# computation of shape factor
for h in range (0,len(ID)):
    kq = (1.5 + (5.8*ID[h]*ID[h])/(ID[h]*ID[h]+0.11))
    kqID.append(kq)

# create array for depth z & defining water content
a = -0.1
for j in range (0,101):
    a = a + 0.1
    z.append(a)

w = 'x'

# computation of a & b parameters for different relativ densities
for h in range (0,len(ID)):
    a = ai_3[0] + ai_3[1]/(ai_3[2]+ID[h])
    b = bi_3[0] + bi_3[1]/(bi_3[2]+ID[h])
    a_ID.append(a)
    b_ID.append(b)

# computation of K0 and qc
K0 = 1 - m.sin(phi_c*m.pi/180)

for j in range (0,len(ID)):

    for i in range (...):
        ...

    for i in range (...):

        sigmaV = (1 + w/100)*(roh_s/(1+ecZ[i-1]-ID[j]*(ecZ[i-1]-edZ[i-
1])))
        *9.81*z[i-1]
        sigmaVZ.append(sigmaV)
        p= (1/3)*sigmaVZ[i]*(1+2*K0)
        pZ.append(p/1000)
        ec = ec0*m.e**(-((3*pZ[i-1]*1000/h_s)**n))
        ecZ.append(ec)
        ed= ed0*m.e**(-((3*pZ[i-1]*1000/h_s)**n))
        edZ.append(ed)

        qc = kqID[j]*a_ID[j]*pZ[i-1]**b_ID[j]
        qcZ.append(qc)
```

Parts of the python code for plotting the cone resistance q_c over depth

```
if np.max(qcZ) < 5:
    max_y = 5
    ticks_y = 1

elif ...

IDstring = str(ID['i'])
params = {'mathtext.default': 'regular'}
plt.rcParams.update(params)

plt.title('q$_{c}$-z diagram' + ' {}'.format('name') + 'ID 0.'+
          IDstring[2], fontsize = 15)
plt.ylabel('$q_c [MPa]$', fontsize = 13)
plt.xlabel("$depth z [m]$", fontsize = 13)

plt.axis([0,10, 0, max_y])
plt.gca().invert_yaxis()
major_ticks_x = np.arange(0, 11, 1)
major_ticks_y = np.arange(0, max_y + ticks_y, ticks_y)
plt.xticks(major_ticks_x)
plt.yticks(major_ticks_y)

line = mlines.Line2D([], [], color = 'blue', linestyle = '-',
                       label='{}'.format('name')+' ID_0.' +
IDstring[2] )

plt.legend(handles=[line],\
               loc = 'lower center', bbox_to_anchor =(0,-
0.18,1,2),ncol = 4,
               borderaxespad = 0, fontsize = 9)

plt.plot(z, qcZ, linewidth = 1, color = 'blue', linestyle = '-')
plt.savefig('path' + '/qc_curve_ID_0.' + IDstring[2] + '.png',
            bbox_inches = 'tight', dpi = 1200)
plt.figure()
```

Application of “full_automated_KIM”- script

At first, the folder “KIM” has to be transferred to any desired directory of your computer and then the folder arrangement within the “KIM” which must not be changed at all is shown in figure A-Fig. 61:

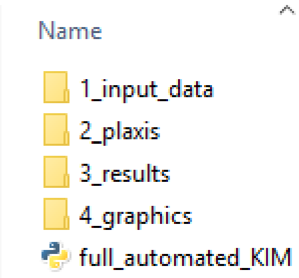

1_input_data
2_plaxis
3_results
4_graphics
full_automated_KIM

A-Fig. 61: folder arrangement within the folder „KIM“

The first step then is to assign the soil-model parameters in the input file KIM/1_input_data/input_soil_parameter.xlsx and save this file as a .csv-file at the same directory. **Note**: before saving the file, the decimal separator has to be changed from “,” to “.” and it is proposed to use a very small value for “p_t” like e.g.
$1*10^{-5}$. An already correctly filled input-file can be seen in A-Fig. 62.

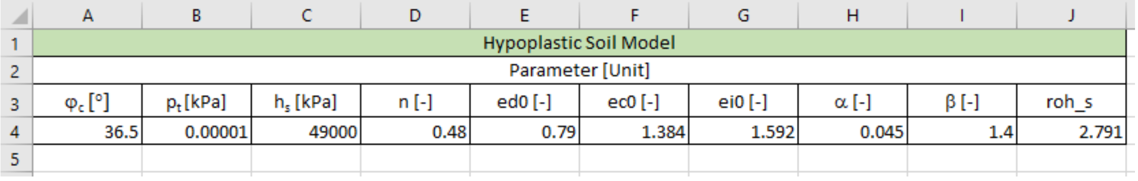

	A	B	C	D	E	F	G	H	I	J
1	Hypoplastic Soil Model									
2	Parameter [Unit]									
3	φ_c [°]	p_t [kPa]	h_s [kPa]	n [-]	ed0 [-]	ec0 [-]	ei0 [-]	α [-]	β [-]	roh_s
4	36.5	0.00001	49000	0.48	0.79	1.384	1.592	0.045	1.4	2.791
5										

A-Fig. 62: Example for a correctly filled input-file

In the next step, the script (“full_automated_KIM”) has to be opened with any program (e.g. Spyder or Notepad++) and **only** the lines 16, 19 and 23 must be changed. In line 16 and 19 the directory of the “KIM”-folder has to be added. Both lines include the same directory but with different separations. In line 23 the desired material must be added. Furthermore, in line 3 and 4 a desired password has to be determined (same password for line 3 and 4). Exemplary the “KIM”-folder is copied on the desktop and therefore the correctly filled script is shown in A-Fig. 63 for an applied material name of “Hostun Sand”. It is important to save the python script “full_automated_KIM” with the file-extension “.py”.

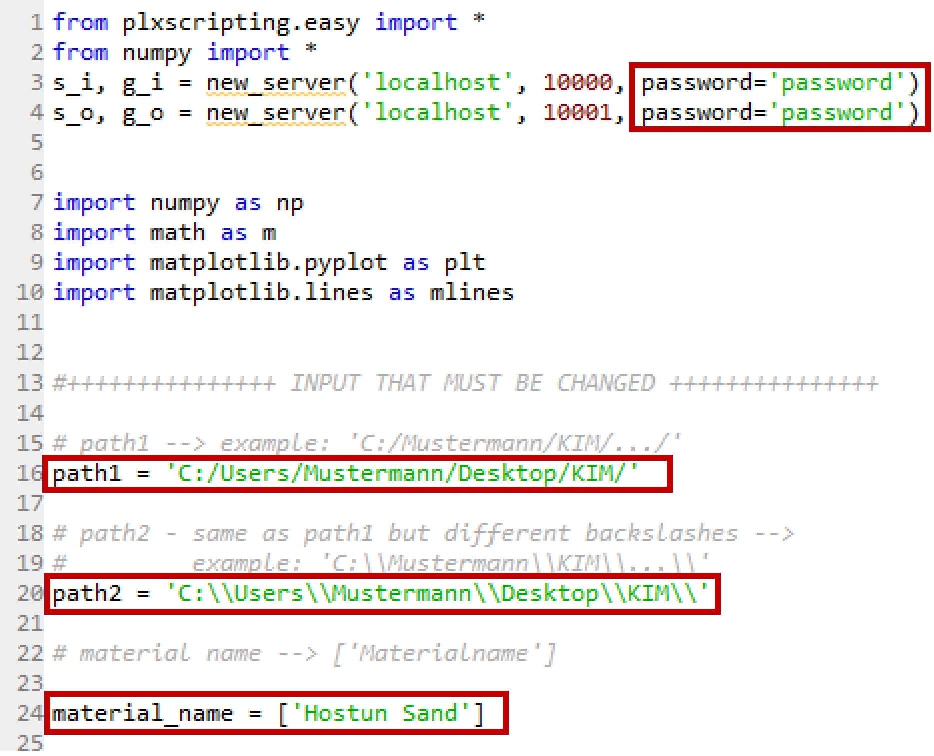

```
from plxscripting.easy import *
from numpy import *
s_i, g_i = new_server('localhost', 10000, password='password')
s_o, g_o = new_server('localhost', 10001, password='password')


import numpy as np
import math as m
import matplotlib.pyplot as plt
import matplotlib.lines as mlines


#+++++++++++++++ INPUT THAT MUST BE CHANGED +++++++++++++++

# path1 --> example: 'C:/Mustermann/KIM/.../'
path1 = 'C:/Users/Mustermann/Desktop/KIM/'

# path2 - same as path1 but different backslashes -->
#         example: 'C:\\Mustermann\\KIM\\...\\'
path2 = 'C:\\Users\\Mustermann\\Desktop\\KIM\\'

# material name --> ['Materialname']

material_name = ['Hostun Sand']

```

A-Fig. 63: Exemplary final python script

After saving the python script correctly with the extension ".py", the original finite element model has to be opened with PLAXIS 2018 within the directory /KIM/2_plaxis/1_original_file/original_file.p2dx. Then the remote scripting server must be configured within PLAXIS and the previously determined password has to be filled in as shown in A-Fig. 64 and A-Fig. 65.

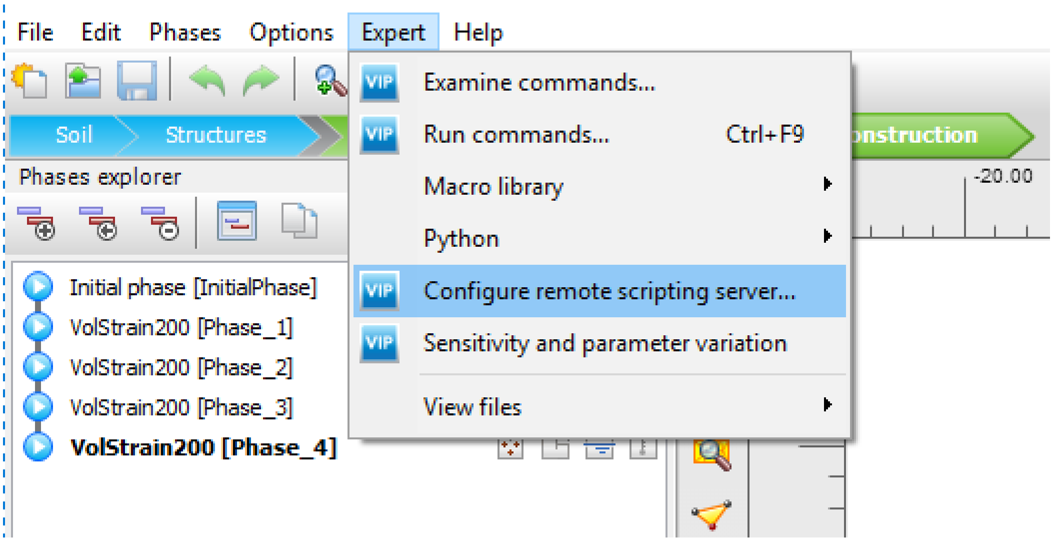

A-Fig. 64: Configuration of remote scripting server

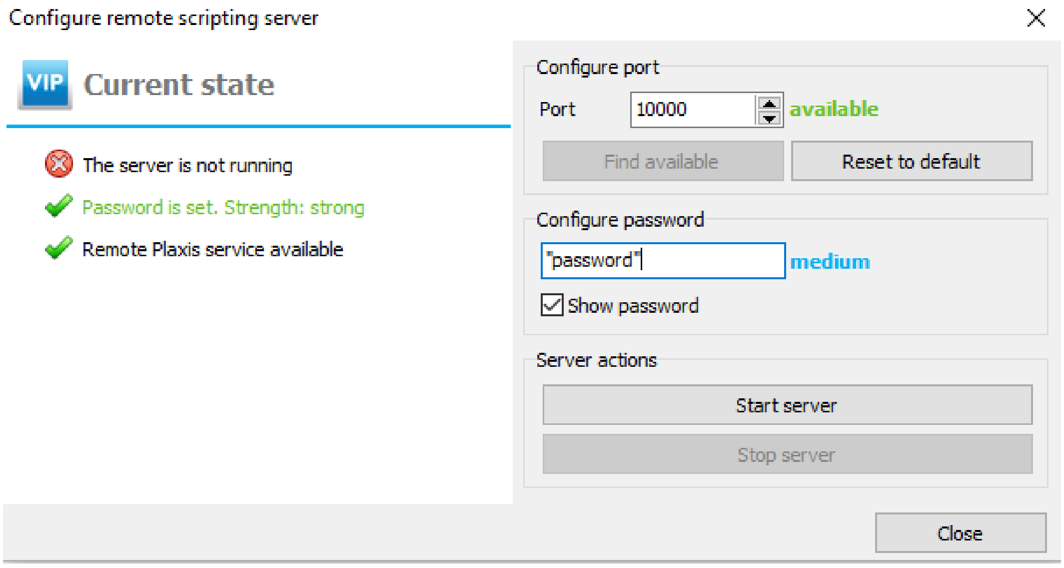
Configure remote scripting server

Current state

- The server is not running
- Password is set. Strength: strong
- Remote Plaxis service available

Configure port

Port: 10000 available

Configure password

"password" medium

☑ Show password

A-Fig. 65: Adding the previously determined password for the remote scripting server

After a successful configuration of the remote scripting server, only the python script “full_automated_KIM” has to be started as shown in A-Fig. 66.

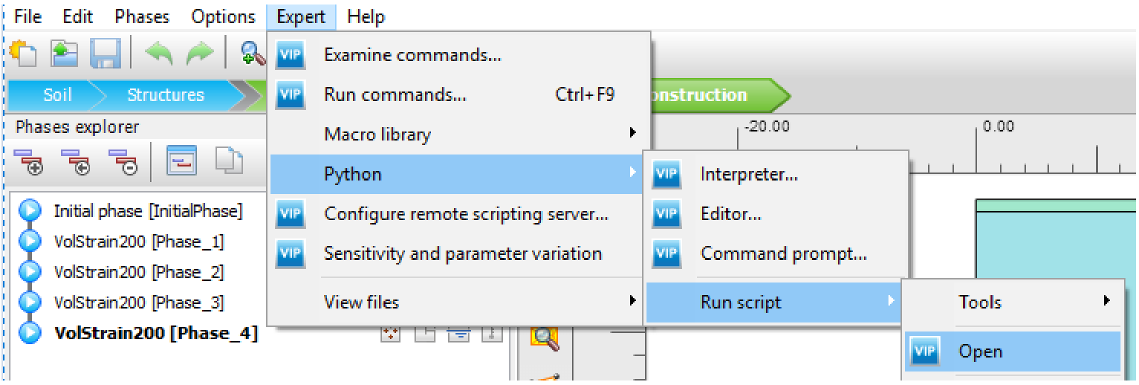

A-Fig. 66: Running the python script

The full KIM analysis is finished, when the last q_c-curve over depth for a density state of $I_D = 0.9$ is saved at the correct directory and the python-execution window is closed.

Appendix D for chapter 7

Python code for automatic model creation for a PRM analysis

```
# requirements for remote scripting within PLAXIS

plaxis_path = r'C:\Program Files\Plaxis\PLAXIS 2D\python\Lib\site-packages'
import imp
found_module =imp.find_module('plxscripting', [plaxis_path])
plxscripting =imp.load_module('plxscripting', *found_module)
from plxscripting.easy import*

# port info
localhostport = 9999

# connect to plaxis application with password
s_i, g_i = new_server('localhost', localhostport, password = '')

# Start a new project
s_i.new()


# set model and element properties
g_i.setproperties('Title', 'Press-Replace-Technique_Python','ModelType','axisymmetry','ElementType','15-Noded','UnitForce','kN')
g_i.SoilContour.initializerectangular(0, -15, 15, 0.5)


# define new materials
ground = g_i.soilmat()
ground1 = g_i.soilmat()
ground2 = g_i.soilmat()
ground3 = g_i.soilmat()
ground4 = g_i.soilmat()

ground.setproperties('MaterialName', 'Sand HP Dr40',
                     'Colour', 101623,
                     'SoilModel', 100,
                     'UserDLLName','udsm_hps64.dll',
                     'UserModel','Hypoplas.-sand',
                                        'einit', 0.83,
                                        'emin', 0.548,
                                        'emax', 1.018,
                                        'Pref' , 100,
                                        'User1', 30,            #phi_c
                                        'User2', 0.01,          #p_t
                                        'User3', 4000E6,        #h_s
                                        'User4', 0.42,          #n
                                        'User5', 0.548,         #e_d0
                                        'User6', 0.929,         #e_c0
                                        'User7', 1.08,          #e_i0
                                        'User8', 0.12,          #alpha
                                        'User9', 0.96,          #beta
                                        'User16', 1.0677,       #e_0
                                        'EoedRef', 75152,       #int.
                                        'cref', 0,              #int.
                                        'phi', 30,              #int.
                                        'psi', 0,               #int.
                                        'Gref', 6832)           #int.
```

```
ground1.setproperties('MaterialName', 'Pile Shaft Interface',
                    'Colour', 124262,
                    'SoilModel', 100,
                    'UserDLLName','udsm_hps64.dll',
                    'UserModel','Hypoplas.-sand',
                                      'einit', 0.83,
                                      'emin', 0.548,
                                      'emax', 1.018,
                                      'Pref' , 100,
                                      'User1', 30,           #phi_c
                                      'User2', 0.01,         #p_t
                                      'User3', 4000E6,       #h_s
                                      'User4', 0.42,         #n
                                      'User5', 0.548,        #e_d0
                                      'User6', 0.929,        #e_c0
                                      'User7', 1.08,         #e_i0
                                      'User8', 0.12,         #alpha
                                      'User9', 0.96,         #beta
                                      'User16', 1.0677,      #e_0
                                      'EoedRef', 60876,      #int.
                                      'cref', 0,             #int.
                                      'phi', 27.5,           #int.
                                      'psi', 0,              #int.
                                      'Gref', 5534)          #int.


ground2.setproperties('MaterialName', 'Extension Interface',
                    'Colour', 136136,
                    'SoilModel', 100,
                    'UserDLLName','udsm_hps64.dll',
                    'UserModel','Hypoplas.-sand',
                                      'einit', 0.83,
                                      'emin', 0.548,
                                      'emax', 1.018,
                                      'Pref' , 100,
                                      'User1', 30,           #phi_c
                                      'User2', 0.01,         #p_t
                                      'User3', 4000E6,       #h_s
                                      'User4', 0.42,         #n
                                      'User5', 0.548,        #e_d0
                                      'User6', 0.929,        #e_c0
                                      'User7', 1.08,         #e_i0
                                      'User8', 0.12,         #alpha
                                      'User9', 0.96,         #beta
                                      'User16', 1.0677,      #e_0
                                      'EoedRef', 75152,      #int.
                                      'cref', 1000,          #int.
                                      'phi', 30,             #int.
                                      'psi', 0,              #int.
                                      'Gref', 6832)          #int.
```

```
ground3.setproperties('MaterialName', 'Pile',
                      'Colour', 141370,
                      'SoilModel', 1,
                      'DrainageType','Drained',
                      'gammaUnsat',0,
                      'gammaSat',0,
                      'einit',0,
                      'Eref', 30000000,
                      'Gref', 11.54E6,
                      'nu', 0.3)


ground4.setproperties('MaterialName', 'Surcharge Layer',
                      'Colour', 158137,
                      'SoilModel', 1,
                      'DrainageType','Drained',
                      'gammaUnsat',100,
                      'gammaSat',100,
                      'einit',0,
                      'Eref', 75152,
                      'Gref', 28900,
                      'nu', 0.3)



# definition of boreholes to define soillayers with different
materials

borehole = g_i.borehole(0) # creation of a new borehole at x = 0
borehole.setproperties('Head',-15) # set the waterhead at y = -15


g_i.soillayer(15) # add a soillayer
g_i.Soils[0].Material = ground # assign a material


# go to the structures section in Plaxis
g_i.gotostructures()


# polygon for surcharge layer
polygon_surcharge_layer = g_i.polygon(0,0,15,0,15,0.5,0,0.5)
g_i.Soil_2.Material = ground4


# prescribed displacements
g_i.line(0,0,0.15,0)
g_i.linedispl(g_i.line_1)
g_i.linedisplacement_1.setproperties('displacement_x', 'fixed',
                                     'uy_start', -0.03)
```

```
# create interfaces
a = 0
for i in range(0,100):
    a = a - 0.03
    g_i.neginterface(0,a,0.15,a)

a = 0
for i in range(0,100):
    a = a - 0.03
    g_i.neginterface(0.15,a,0.18,a)

a = 0.03
for i in range(0,101):
    a = a - 0.03
    g_i.posinterface(0.15,a,0.15,a-0.03)


# go to mesh section and mesh the model
g_i.gotomesh()
g_i.mesh()

# go to staged construction
g_i.gotostages()


# add and modify Phases
g_i.InitialPhase.DeformCalcType = 'K0 procedure'
g_i.Soil_2.activate(g_i.Phases[0])
g_i.phase(g_i.InitialPhase) # add phase after initial Phase
g_i.linedisplacement_1.activate(g_i.Phases[1])
g_i.Soil_2.activate(g_i.Phases[1])


# creation of desired amount of phases
a = 0
for i in range (0,199):
        a = a + 1
        g_i.phase(g_i.Phases[a])

# settings for first phase
a = 0
for a in range(0,4):
        a = a + 1
        g_i.lines[a].activate(g_i.Phases[2])

a = -1
for i in range (0,2):
        a = a + 1
        g_i.set(g_i.Interfaces[a].MaterialMode,(g_i.Phases[2]),
                                               'Custom')
        g_i.set(g_i.Interfaces[a].Material, (g_i.Phases[2]),ground1)

a = 1
for i in range (0,2):
        a = a + 1
        g_i.set(g_i.Interfaces[a].MaterialMode,(g_i.Phases[2]),
                                              'Custom')
        g_i.set(g_i.Interfaces[a].Material, (g_i.Phases[2]),ground2)
```

```
# incresing prescribed displacements in every "Press"-phase
# replace of soil in every "Replace"-phase

a = -1
b = 0
c = 0
d = 0
for i in range(0,100):
               a = a + 2
               b = b + 2
               c = c + 1
               d = d - 0.03
               g_i.set(g_i.linedisplacement_1_1.uy_start,
(g_i.Phases[a]), d)
               g_i.set(g_i.Soils[c].Material, (g_i.Phases[b]),ground3)
#or with: g_i.set(g_i.Soils[c].Material, (g_i.Phases[b]),
g_i.Materials[3])


# activating and deactivating of interfaces
a = -1
b = 2
c = 2
d = 0
e = 4
f = 3
for i in range(0,99):
        a = a + 3
        b = b + 3
        c = c + 2
        d = d + 3
        e = e + 3
        f = f + 3
        g_i.lines[a].deactivate(g_i.Phases[c])
        g_i.lines[b].activate(g_i.Phases[c])
        g_i.lines[d].deactivate(g_i.Phases[c])
        g_i.lines[e].activate(g_i.Phases[c])
        g_i.lines[f].activate(g_i.Phases[c])
```

```
# assing materials to interfaces
a = 2
b = 0
c = 3
d = 2
e = 1
for i in range(0,99):
        a = a + 2
        b = b + 3
        c = c + 3
        d = d + 3
        e = e + 3
        g_i.set(g_i.Interfaces[b].MaterialMode,(g_i.Phases[a])
                                              'Custom)
        g_i.set(g_i.Interfaces[b].Material, (g_i.Phases[a]),ground1)
        g_i.set(g_i.Interfaces[c].MaterialMode,(g_i.Phases[a]),
                                              'Custom')
        g_i.set(g_i.Interfaces[c].Material, (g_i.Phases[a]),ground2)
        g_i.set(g_i.Interfaces[d].MaterialMode,(g_i.Phases[a]),
                                               'Custom')
        g_i.set(g_i.Interfaces[d].Material, (g_i.Phases[a]),ground2)
        g_i.set(g_i.Interfaces[e].MaterialMode,(g_i.Phases[a]),
                                               'Custom')
        g_i.set(g_i.Interfaces[e].Material, (g_i.Phases[a]),ground1)


# rename phases
a = -1
for i in range(0,100):
               a = a + 2
               g_i.Phases[a].Identification = 'Press_{}'.format(i+1)

a = 0
for i in range (0,100):
               a = a + 2
               g_i.Phases[a].Identification = 'Replace_{}'.format(i+1)


# change settings of all phases
a = 0
for i in range (0,200):
        a = a + 1
        g_i.Phases[a].Deform.UseDefaultIterationParams = False
        g_i.Phases[a].Deform.ArcLengthControl = 'Off'
        g_i.Phases[a].Deform.DesiredMinIterations = 6
        g_i.Phases[a].Deform.DesiredMaxIterations = 15
        g_i.Phases[a].Deform.MaxSteps = 1000
        g_i.Phases[a].Deform.MaxLoadFractionPerStep = 0.05

g_i.calculate() #calculate all phases

save_path = r'path'
g_i.save(save_path) #Save the project under the defined path
```